Doctoral Program in Bioengineering
Organic Chemistry Area

DOCTORAL THESIS

Synthesis of Diketopyrrolopyrrole Derivatives and their use in Singlet Fission, Solar Cells Applications, and Induction of Chirality

MEMORY TO OBTAIN THE DEGREE OF DOCTOR PRESENTED BY:

Maria João Álvaro Albuquerque Martins

Under the direction of:

Prof. Dra. Ángela Sastre Santos

UNIVERSIDAD MIGUEL HERNÁNDEZ DE ELCHE

INSTITUTO DE BIOINGENIERÍA

Elche, 2021

UNIVERSITAS
Miguel Hernández

Indicios de Calidad

La tesis doctoral titulada "**Synthesis of Diketopyrrolopyrrole Derivatives and their use in Singlet Fission, Solar Cells Applications, and Induction of Chirality**", realizada por Dña Maria João Álvaro Albuquerque Martins, con NIE: Y5859346-H, bajo la dirección de la Prof. Dra. Ángela Sastre Santos, se presenta bajo la modalidad de Tesis Convencional con los siguientes índices de calidad según el campo de evaluación de la ANEP de Química:

Publicaciones científicas:

1. Ilias Papadopoulos, Maria João Álvaro-Martins, Desire Molina, Patrick M. McCosker, Paul A. Keller, Timothy Clark, Ángela Sastre-Santos, Dirk M. Guldi, Solvent-dependent singlet fission in diketopyrrolopyrrole dimers – a mediating charge transfer versus a trapping symmetry-breaking charge separation, *Adv. Energy Mater.*, **2020**, *10*, 2001496; doi.org/10.1002/aenm.202001496; FI: 29.368 área de conocimiento: Chemistry Physical; puesto que ocupa/total de revistas en el área: 5/162.

2. Maria J. Álvaro-Martins, José G. Sánchez, Giulia Lavarda, Desiré Molina, Josep Pallarès, Tomás Torres, Lluis F. Marsal, Ángela Sastre-Santos, Subphthalocyanine-Diketopyrrolopyrrole Conjugates: 3D Star-Shaped Systems as Non-Fullerene Acceptors in Polymer Solar Cells with High Open-Circuit Voltage, *ChemPlusChem*, **2021**, *86*, 1-9; doi.org/10.1002/cplu.202100103; FI: 2.863; área de conocimiento: Chemistry, Multidisciplinary; puesto que ocupa/total de revistas en el área: 98/216.

UNIVERSITAS
Miguel Hernández

Programa de Doctorado en Bioingeniería

Dña. Ángela Sastre Santos, Catedrática del área de Química Orgánica, perteneciente al Departamento de Farmacología, Pediatría y Química Orgánica y Directora del Instituto de Bioingeniería de la Universidad Miguel Hernández de Elche, director de la tesis doctoral titulada "**Synthesis of Diketopyrrolopyrrole Derivatives and their use in Singlet Fission, Solar Cells Applications, and Induction of Chirality**"

Informa:

Que Maria João Álvaro Albuquerque Martins ha realizado bajo mi supervisión el trabajo titulado "**Synthesis of Diketopyrrolopyrrole Derivatives and their use in Singlet Fission, Solar Cells Applications, and Induction of Chirality"** conforme a los términos y condiciones definidos en su Plan de Investigación y de acuerdo con el Código de Buenas Prácticas de la Universidad Miguel Hernández de Elche, cumpliendo los objetivos previstos de forma satisfactoria para su defensa pública como tesis doctoral.

Lo que firmo para los efectos oportunos, en Elche a 20 de julio de 2021

Fdo.: Prof. Dra. Ángela Sastre Santos

Directora de la tesis

UNIVERSITAS
Miguel Hernández

Programa de Doctorado en Bioingeniería

Dña. Piedad Nieves de Aza Moya, Catedrática del área de Ciencia de los Materiales e Ingeniería Metalúrgica y Coordinadora de la Comisión Académica del Programa de Doctorado en Bioingeniería de la Universidad Miguel Hernández de Elche.

Informa:

Que Maria João Álvaro Albuquerque Martins con NIE: Y5859346-H ha realizado bajo la supervisión de nuestro Programa de Doctorado el trabajo titulado "**Synthesis of Diketopyrrolopyrrole Derivatives and their use in Singlet Fission, Solar Cells Applications, and Induction of Chirality**", bajo la dirección de la Prof. Dra. Ángela Sastre Santos, conforme a los términos y condiciones definidos en su Plan de Investigación y de acuerdo con el Código de Buenas Prácticas de la Universidad Miguel Hernández de Elche, cumpliendo los objetivos previstos de forma satisfactoria para su defensa pública como tesis doctoral.

Lo que firmo para los efectos oportunos, en Elche a 20 de julio de 2021

Fdo.: Prof. Dra. Piedad Nieves de Aza Moya

Coordinadora del Programa de Doctorado en Bioingeniería

Financiación

La realización de la tesis que aquí se presenta ha sido posible gracias a la financiación obtenida que se indica a continuación:

1. Beca Santiago Grisolía: Grisoliap 2017715.

“Eles não sabem, nem sonham,

que o sonho comanda a vida.

Que sempre que um homem sonha

o mundo pula e avança**”**

António Gedeão –Pedra Filosofal

Acknowledgements

The culmination of this Thesis is due to personal effort, but also to external help I received along the path. That´s why I want to thank these people.

First of all, I would like to thank Prof. Dr. Ángela Sastre Santos for giving me the opportunity to carry out my Doctoral Thesis in her group and for having been my Thesis Director during these four years. Muchas gracias por la ayuda y libertad que me has dado para realizar los proyectos a que nos propusimos.

The Generalitat Valenciana for funding with the support of Santiago Grisolia Project that allowed me to carry out this work with funding.

To the DYSMOL group that without them my life as a doctoral student would be much more difficult:

A ti Belén que eres la que nos levanta el ánimo y que haces que el laboratorio no explote dando siempre tus consejos de seguridad. Porque antes de todo lo importante es la seguridad de todos.

Javi, muchas gracias por todas las dudas que me quitaste y por toda la ayuda que siempre me has dado cuando te la pedí.

A Fernando por la ayuda principalmente en la revisión del manuscrito. Muchas gracias.

A mis compañeros de laboratorio que hicieron que los momentos más intensos se suavizarán. Principalmente a ti Jorge por toda la ayuda que me has dado con todos los papeles y burocracia y claro por tus enseñanzas de castellano. A Desi por todas las “discusiones” que tuvimos de cómo mejorar los rendimientos de las reacciones de los DPP y de cómo tenemos pena de que no sean tan buenos como nos gustaría. A Adrián por ser el mejor compañero de despacho y por todas las bromas que nos inventamos, los de 94 unidos por el mismo sentido de humor. A Ana, Nathalie y Jose por compartir tantos momentos divertidos y por la ayuda que me han dado siempre que les pedí.

I would also like to thank Prof. Dario Bassani and Prof. Reiko Oda for allowing me to do a 3-month internship and thus increase my knowledge in chemistry. Thank you for letting me stay longer than expected (caused by the confinement). And, off course, their respective groups, NEO and CMA groups, from which I had the privilege to learn during these months.

And also all project collaborators, namely Prof. Dr Guldi, Prof. Dr. Timothy Clark, Prof. Dr. Paul A. Keller, Prof. Dr. Tomás Torres, Prof. Dr. Lluis Marsal, for having collaborated in the elaboration of the projects.

Thank you very much to the people I have met randomly over these 4 years abroad, as it is not always easy to come to a new country and meet wonderful people like you, especially you Lupi for your support and fun times we had during your stay in Elche and for making me discover a bit of Latin culture. For you too Fabrizio, even though it's a recent “discovery”, you've already made me look at a world in a different way and you made Elche so much more fun.

And to all the people who came with me before embarking on this adventure. Principalmente a ti, Christophe que me deste sempre o teu apoio incomdicional e mesmo longe fizeste com que tudo fosse mais fácil. Durante este tempo de mais stress foste o meu super heroí. Muito obrigada.

E por último, queria agradecer à minha família que é a minha base de suporte e que sem eles não poderia ter chegado onde cheguei. Aos meus pais por me terem apoiado em todas as decisões, principalmente, nesta de vir para o estrangeiro e realizar este sonho. Aos meus irmãos por estarem sempre presente em todos os momentos, sentido mesmo longe estamos perto. E por último, aos meus avós por tudo que fizeram por mim.

Index

Symbols and Abbreviations

λ	Wavelength
δ	Chemical shift
^{1}H-NMR	Proton Nuclear Magnetic Resonance
^{13}C-NMR	Carbon-13 Nuclear Magnetic Resonance
^{11}B-NMR	Boron-11 Nuclear Magnetic Resonance
A_G	Acceptor Group
Å	Angstrom
Abs	Absorbance
AcOH	Acetic acid
A_D	Absorption of Left
AFM	Atomic Force Microscopy
A_L	Absorption of right
AM	Air Mass
APTES	(3-aminopropyl)triethoxysilane
a.u.	Arbitrary unit
BHJ	Bulk Heterojunction Solar Cell
Bz	Benzonitrile
°C	Degree Celsius
CD	Circular Dichroism
CDCA	Chenodeoxycholic acid
CPL	Circularly Polarized Luminescence
CR	Charge Recombination
CS	Charge Separation
CT	Charge Transfer
CV	Cyclic Voltammetry

D_G	Donor Group
D	Left side
d	Doublet
dd	Doublet of doublets
DFT	Density Functional Theory
DH	Left Handed Helix
DMF	*N*,*N*-Dimethylformamide
DMSO	Dimethyl sulfoxide
DNA	Deoxyribonucleic acid
DPP	Diketopyrrolopyrrole
DPV	Differential Pulse Voltammetry
DR	Left Handed Ribbon
DSSC	Dye-Sensitized Solar Cell
ε	Molar Extinction Coefficient
E_{gap}	Band Gap Energy
$E_{gap,\ CV}$	Electrochemical Band Gap Energy
$E_{gap,opt}$	Optical Band Gap Energy
EH	Ethylhexyl chain
EJ	Exajoule (10^{18} Joules)
E_{ox}	Oxidation Potential
EQE	External Quantum Efficiency
E_{red}	Reduction Potential
ET	Electronic Transfer
ETM	Electron Transporting Materials
EU	European Union
eV	Electronvolt

Fc/Fc^+	Ferrocene/ferrocenium redox couple
FF	Fill Factor
Fluor.	Fluorescence
FQY	Fluorescence Quantum Yield
FT-IR	Fourrier-Transform Infra-Red
fsTA	Femtoseconds Transient Absorption Spectroscopy
g_{abs}	Absorption Dissymmetry Factor
H	Proton
h	hour
HOMO	Highest Occupied Molecular Orbital
HR-MS	High Resolution Mass Spectrometry
HTM	Hole Transporting Materials
InterSF	Intermolecular Singlet Fission
IntraSF	Intramolecular Singlet Fission
IPCE	Incident Photon-to –Current Efficiency
ITO	Indium Tin Oxide
J	Coupling Constant
J_{SC}	Short-Circuit Current
LH	Right handed helix
LR	Right handed ribbon
LUMO	Lowest Unoccupied Molecular Orbital
m	*Meta* position
m	Multiplet
MEG	Multiexciton Generation
min	Minute
Norm.	Normalized

m/z	Mass-to-charge ratio
NBS	*N*-Bromosuccinimide
NFA	Non-Fullerene Acceptor
nm	Nanometer
NMP	*N*-Methyl-2-pyrrolidone
ns	Nanosecond (10^{-9} seconds)
nsTA	Nanoseconds Transient Absorption Spectroscopy
o	*Ortho* position
OD	Optical Density
OSC	Organic Solar Cell
p	*Para* position
PCE	Power Conversion Efficiency
PDI	Perylene diimide
PEDOT:PSS	Poly(3,4-ethylenedioxythiophene) polystyrene sulfonate
PEM	Photoelectric Modulator
PHJ	Planar Heterojunction Solar Cell
POM	Polyoxometalate
ppm	Parts per million
PSC	Perovskite Solar Cell
ps	Picosecond (10^{-12} seconds)
PV	Photovoltaic Technology
Ref	Reference
rt	Room Temperature
s	singlet
S*	Exited Sensitizer

SF	Singlet Fission
SEC	Spectroelectrochemical
SubPc	Subphthalocyanine
t	Triplet
T	Triplet state
TEM	Transmission Electron Microscopy
TEOS	tetraethylorthosilicate
TMEDA	*N*,*N*,*N*',*N*'-tetramethylethylenediamine
V	Volt
vs	*versus*
V_{OC}	Open-Circuit Voltage
UV-vis	Ultraviolet-visible spectroscopy

Abstract

Light can generate a chain of reactions that, knowing how to use them, allows us to improve and develop new technological systems that overcome some current issues.

One of them is associated with the uncontrolled use of fossil resources making them increasingly scarce. Thus, having the advantage of using for free the largest existing light source, Solar Energy, several alternatives were taken into consideration to try to fix or mitigate some of the damage generated by this desperate consumption of resources that are not infinite. And for this, it is not only important to test new materials that are more efficient in the use of photovoltaics, but also to understand the phenomena that occur whenever light is absorbed by these materials, and thus make an investigation from the core. This means that it is essential to know the photophysical properties of the materials to be used in order take advantage of the solar energy as much as possible.

For this task is necessary to join forces among several areas of knowledge. And it is here that organic chemistry brings many advantages due to the possibility to carry out a rational and systematic modification of the chemical structure of the molecules, thus generating a deep understanding of the structure-property relationship that can allow the fine tuning of the optical/electronic levels of the materials to achieve the best photovoltaic result possible.

In this sense, this Thesis is a compilation of some developed works, which are divided into three chapters. The first two share the same essence of studying molecules to improve photovoltaic performance, although the first one is more focused on the study of singlet fission as a photophysical property itself, rather than to its application photovoltaics. The knowledge of this intrinsic property of materials can be used as an asset in this area as it allows to surpass the *Schockley-Queisser theoretical efficiency limit*. In contrast, Chapter 2 is devoted to the application of several examples of DPP derivatives in OSCs. Finally, Chapter 3, which is not aimed at photovoltaic energy, makes its contribution to the study of the chirality transfer between different moieties, specifically between a chiral inorganic structure and an achiral organic molecule. to improve the problem that sometimes arises in synthesis of the chiral compounds.

Specifically, Chapter 1 deals with the design and synthesis of three DPP dimers for application in singlet fission (SF). The molecules differ from each other in the relative position of two diketopyrrolopyrrole (DPP) moieties on the phenylene group (*ortho*, *meta* and *para*), allowing to study the influence of the position of one DPP in relation to the other (**Figure 1**). Furthermore, the influence of solvent polarity was also studied using benzonitrile as polar solvent and toluene as non-polar one, verifying that SF is strongly influenced by the solvent. As a result, no

triplet states were detected in toluene, while in benzonitrile for derivatives ***o*-DPP 1** and ***m*-DPP 3** it was possible to populate these states from the $(S_0S_1)_{CT}$ state. ***o*-DPP 1** showed the highest SF efficiency due to a greater electronic interaction between the DPP moieties.

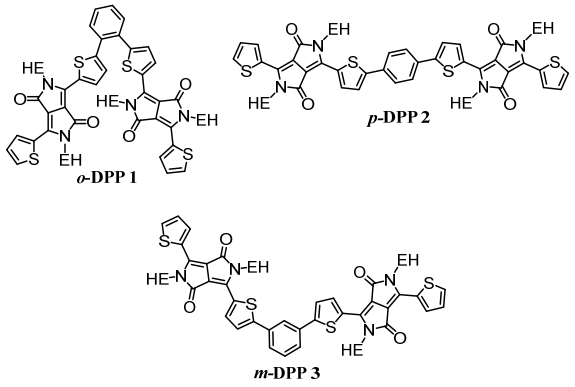

Figure 1- *Structures of the target compounds in Chapter 1. EH- ethylhexyl chain.*

Chapter 2 focused on the application of DPP derivatives in photovoltaic cells. Two different approaches were taken into account, namely the use in dye sensitized solar cells (DSSCs) and in bulk heterojunction solar cells (BHJs). For the first approach, three DPP- acid derivatives were synthesized and characterized (**Figure 2**). Two of these molecules had a carboxylic acid as an anchoring group in *meta* or *para* position in the phenylene moiety in relation with the DPP core, ***p*-DPP acid 9** and ***m*-DPP acid 10**, and the third molecule contained two DPP units on a benzoic acid moiety [**$(DPP)_2$ acid 11**]. With the increment of DPP moieties it was pretended to increase the photovoltaic performance due to the existence of an intramolecular singlet fission effect. Our expectations were not fulfilled, as the first preliminary tests showed low efficiencies. However, ***p*-DPP acid 9** was the one that presented the best performance, due to a greater electronic interaction.

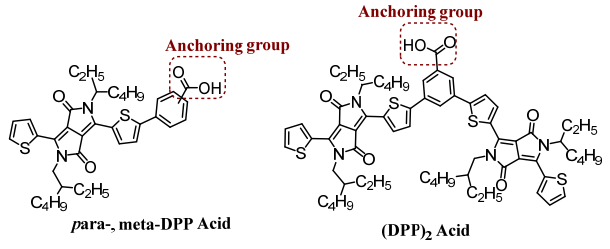

Figure 2- *Structures of DPP-sensitizer synthetized in Chapter 2.*

Regarding to the second approach, four new SubPc-DPP derivatives were synthesized for its study as non-fullerene acceptors (NFAs) in inverted-BHJs. The molecules have a conical shape using the SubPc as a core, and three DPPs linked by acetylene bridges as wings (**Figure 3**). The best efficiency was reached with the

PBDB-T:***C*$_1$-SubPc(DPP)$_3$-OPh 18** couple with a PCE of 3.17%. However, the most surprising and unexpected result was the high V_{OC} values that were obtained for all derivatives which probably makes these derivatives good candidates for ternary OSCs.

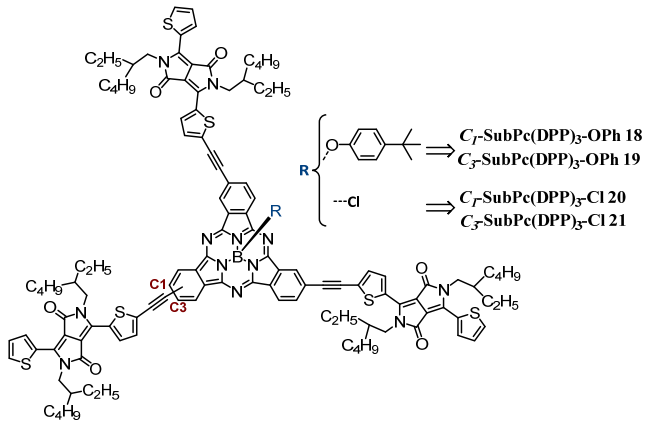

***Figure 3-** Structures of SubPc-(DPP)$_3$ acceptors used in BHJs, Chapter 2.*

Chapter 3 does not follow the spirit of the other chapters having its own meaning as it is an approach in order to combat the problem that exists when synthesizing and purifying chiral compounds (**Figure 4**). This is based on chirality transfer from nanostructures with chiral morphology to achiral DPP derivatives. Thus, three DPP linked to *ortho*-, *para*- and *meta*-benzoic acids were synthesized, while on the other hand silica nanostructures (helices and ribbons) were developed by a sol-gel method. The link between both systems was made by amide bonding. The optical properties of the linked systems were observed by UV-vis and fluorescence, detecting a red-shift of the spectra. Finally, the chirality was determined with the aid of the absorption dissymmetry factor, $g_{abs,}$ verifying that the greater the distance between the nanostructure and the DPP unit, the greater the value of dissymmetry and the greater the induction of chirality.

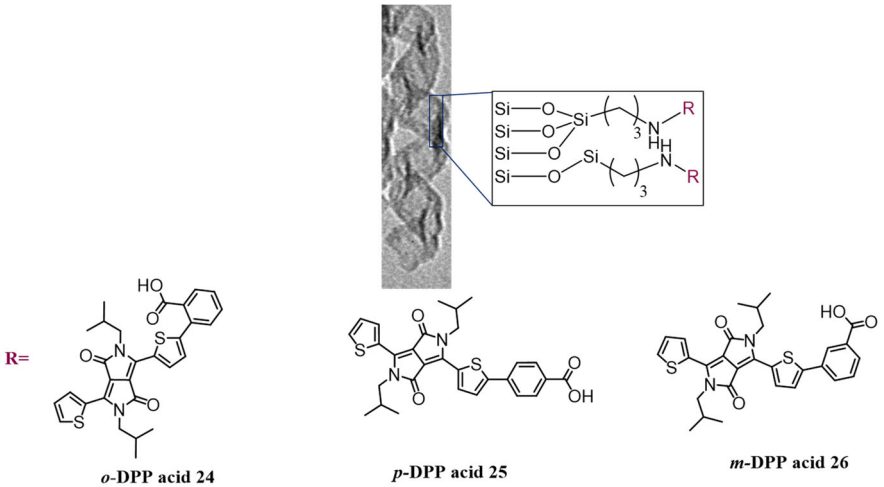

Figure 4- *General scheme of dyes-silica nanostructures in Chapter 3.*

Resumen

La luz puede generar una cadena de reacciones que, sabiendo utilizarlas, nos permite mejorar y desarrollar nuevos sistemas tecnológicos que superen algunos problemas actuales.

Uno de ellos está asociado con el uso descontrolado de recursos fósiles que los hace cada vez más escasos. Así, teniendo la ventaja de utilizar de forma gratuita la mayor fuente de luz existente, la Energía Solar, se tomaron en consideración varias alternativas para intentar reparar o mitigar parte de los daños que genera este desesperado consumo de recursos que no son infinitos. Y para ello, no sólo es importante probar nuevos materiales que sean más eficientes en el uso de la energía fotovoltaica, sino también comprender los fenómenos que ocurren siempre que la luz es absorbida por estos materiales, y así hacer una investigación desde el núcleo. Esto significa que es fundamental conocer las propiedades fotofísicas de los materiales a utilizar para aprovechar al máximo la energía solar.

Para esta tarea es necesario unir fuerzas entre varias áreas del conocimiento. Y es aquí donde la química orgánica presenta muchas ventajas debido a la posibilidad de llevar a cabo una modificación racional y sistemática de la estructura química de las moléculas, generando así un conocimiento profundo de la relación estructura-propiedad que puede permitir el ajuste fino de las propiedades ópticas/electrónicas de los materiales para conseguir el mejor resultado fotovoltaico posible.

En este sentido, esta Tesis es una recopilación de algunos trabajos desarrollados, los cuales se dividen en tres capítulos. Los dos primeros comparten la misma esencia de estudiar moléculas para mejorar el rendimiento fotovoltaico, aunque el primero está más centrado en el estudio de la fisión singlete como una propiedad fotofísica en sí misma, que en su aplicación fotovoltaica. El conocimiento de esta propiedad intrínseca de los materiales se puede utilizar como un activo en esta área ya que permite superar el límite de eficiencia teórico de Schockley-Queisser. Por el contrario, el Capítulo 2 está dedicado a la aplicación de varios ejemplos de derivados de diketopyrrolopyrrole (DPP) en células solares organicas (OSC). Finalmente, el Capítulo 3, que no está dirigido a la energía fotovoltaica, hace su contribución al estudio de la transferencia de quiralidad entre diferentes unidades, específicamente entre una estructura inorgánica quiral y una molécula orgánica aquiral. para mejorar el problema que a veces surge en síntesis de los compuestos quirales.

Concretamente, el Capítulo 1 trata del diseño y síntesis de tres dímeros DPP para su aplicación en la fisión singlete (SF). Las moléculas difieren entre sí en la posición relativa de dos grupos DPP en el grupo fenileno (posiciones *orto*, *meta* y

para), lo que permite estudiar la influencia de la posición de un DPP en relación con el otro (**Figura 1**). Además, también se estudió la influencia de la polaridad del disolvente utilizando benzonitrilo como disolvente polar y tolueno como no polar, verificando que la SF está fuertemente influenciada por el disolvente. Como resultado, no se detectaron estados triplete en tolueno, mientras que en benzonitrilo para los derivados ***o*-DPP 1** y ***m*-DPP 3** fue posible poblar estos estados desde el estado $(S_0S_1)_{CT}$. El compuesto ***o*-DPP 1** mostró la mayor eficiencia de SF debido a una mayor interacción electrónica entre las unidades de DPP.

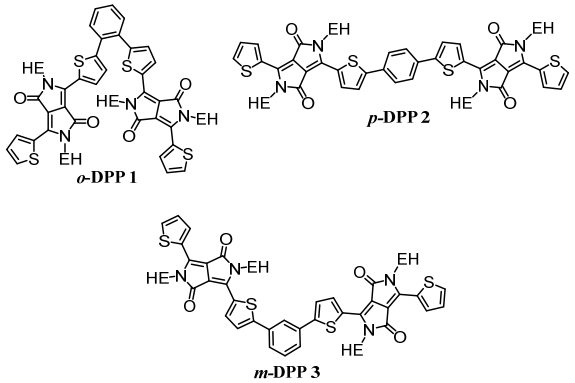

Figura 1- *Estructuras de los compuestos objetivo del capítulo 1. EH- cadena de etilhexilo.*

El Capítulo 2 se centra en la aplicación de derivados de DPP en células fotovoltaicas. Se tuvieron en cuenta dos enfoques diferentes, en el primero, el uso en células solares sensibilizadas por colorante (DSSC) y en el segundo en células solares de heterounión masiva (BHJ). Para el primer enfoque, se sintetizaron y caracterizaron tres acidos carboxílicos derivados de DPP (**Figura 2**). Dos de estas moléculas poseían un ácido carboxílico como grupo de anclaje en posición *meta* o *para* en el fenileno en relación con el núcleo de DPP, ***p*-DPP 9 ácido** y ***m*-DPP 10 ácido**, la tercera molécula contenía dos unidades DPP en una unidad de ácido benzoico [**$(DPP)_2$ ácido 11**]. Con el incremento de unidades de DPP se pretendió incrementar el rendimiento fotovoltaico debido a la existencia de un efecto de fisión singlete intramolecular. Nuestras expectativas no se cumplieron, ya que los estudios llevados a cabo mostraron bajas eficiencias. Sin embargo, el ***p*-DPP ácido 9** fue el que mejor presentó mejores propiedades, atribuido a una mayor interacción electrónica.

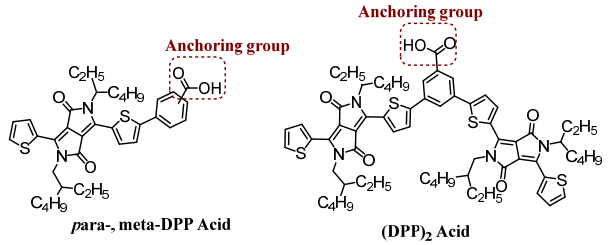

Figura 2- *Estructuras de los sensibilizadores sintetizados de DPP del Capítulo 2.*

Con respecto al segundo enfoque, se sintetizaron cuatro nuevos compuestos de SubPc-DPP para su estudio como aceptores de electrones no-fulerénicos (NFAs) en células BHJ invertidas. Las moléculas tienen una forma cónica utilizando la SubPc como núcleo y tres DPP unidos por puentes de acetileno en los extremos (**Figura 3**). La mejor eficiencia se alcanzó con el par PBDB-T:***C1*-SubPc (DPP)3-OPh 18** con un PCE del 3,17%. Sin embargo, el resultado más sorprendente e inesperado fueron los altos valores de V_{OC} que se obtuvieron para todas las derivadas, lo que probablemente las convierte en buenas candidatas para OSC ternarias.

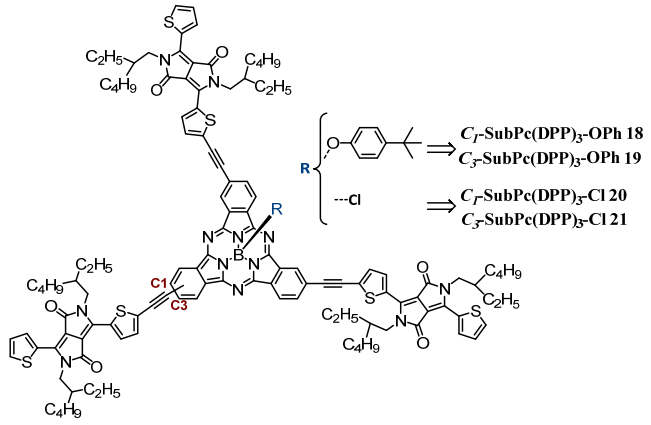

Figura 3- *Estructuras de los aceptores SubPc-(DPP)3 utilizados en BHJ, Capítulo 2.*

El Capítulo 3 no sigue el objetivo de los demás capítulos, ya que es un enfoque para combatir el problema que existe al sintetizar y purificar compuestos quirales (**Figura 4**): se trata de estudiar la transferencia de quiralidad de nanoestructuras con morfología quiral a derivados de DPP aquirales. Así, se sintetizaron tres DPP unidos a ácidos *orto*-, *para*- y *meta*-benzoicos, mientras que por otro lado se desarrollaron nanoestructuras de sílice (hélices y cintas) mediante un método sol-gel. El vínculo entre ambos sistemas se realizó mediante unión amida. Las propiedades ópticas de los sistemas enlazados se observaron mediante UV-vis y fluorescencia, detectando un desplazamiento hacia al rojo. Finalmente, se determinó la quiralidad con ayuda del factor de disimetría de absorción, g_{abs},

verificando que a mayor distancia entre la nanoestructura y la unidad DPP, mayor valor de disimetría y mayor inducción de quiralidad.

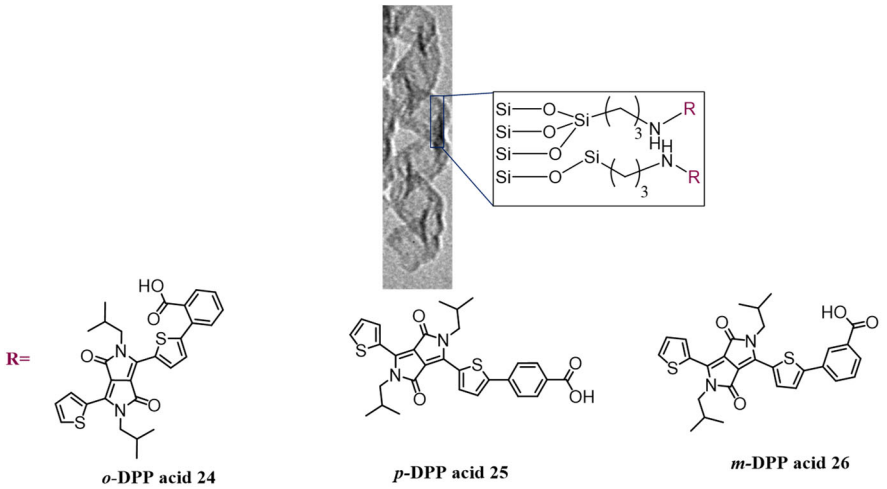

Figura 4- *Esquema general de nanoestruturas de sílica-colorantes del Capítulo 3.*

Introduction

Depletion of fossil fuels

The modern industrial society has been using fossil resources, such as coal, oil and gas, as if they were infinite. The financial growth of this society is based on the overuse of these resources leading to depletion as they are consumed.[1] The concerns surrounding this problematic have persisted for decades. The most famous prognosis of this depletion of fossil fuels was reported in 1956 by Hubbert with the *Hubbert´s Peak Theory* or just *Hubbert´s Curve*. The model consisted in the prediction of a bell-shaped curve, in which the production of fossil fuels increased due to the improvement of the extraction methods, reaching the maximum and, later, decreasing until the depletion of resources.[2] The model predicted that the United States oil production would peak in the 1970s what proved to be true (**Figure 1**).

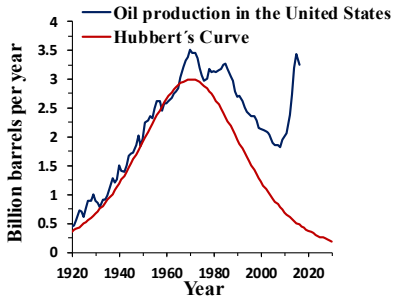

***Figure 1**- Annual oil production in the United States compared with the Hubbert´s curve. Adapted from Ritchie.[3] Sources of the original data: U.S. Energy Information Administration.[4]*

Maintaining exaggerated and disproportionate consumption will lead, sooner or later, to the fossil resources run out. However, a new scenario started when the new technologies made possible to extract oil from more difficult places, thus enabling the use of these resources for a longer time, although at a higher cost. On the other hand, the extensive use of these resources brought as additional problem an increase of the atmospheric CO_2 level and, consequently, the climate change, being one of the most important reasons for changing the energy production system. The concentration of CO_2 in the atmosphere has increased from approximately 277 ppm to 407.38 ppm between 1750, beginning of the Industrial Era, and 2018.[5] However, the CO_2 emission as anthropogenic emission became dominant from 1950 to the

[1] A. J. Cavallo, *Natural Resources Research*, **2004**, *13*, 211–221.
[2] M. K. Hubbert, *Nuclear Energy and the Fossil Fuel*, 1956.
[3] H. Ritchie, *How Long Before We Run Out of Fossil Fuels?*, **2017**,https://ourworldindata.org/how-long-before-we-run-out-of-fossil-fuels#note-2, accessed 30/04/2020.
[4] *U.S. Energy Information Administration, U.S. Field Production of Crude Oil*, **2019**, https://www.eia.gov/dnav/pet/hist/LeafHandler.ashx?n=pet&s=mcrfpus1&f=a, accessed 30/04/2019.
[5] P. Friedlingstein, *et. al. Earth Syst. Sci. Data*, **2019**, *11*, 1783–1838.

present, having increased by about 2.2% per year in the period 2005-2015.[6] In 2015, 195 countries, signed the *Paris Agreement*, adopting measures with the aim to keep the increase in global average temperature well below 2 °C above pre-industrial levels, in order to reduce the climate change.[7] Since the increase of environmental protection concerns in the whole world, the renewable energies such as wind, geothermal and solar energies have gained great relevance. Nowadays, in Portugal the domestic primary energy is based in a high percentage renewable energy sources, ranking in fifth place compared to other countries of the EU-28, in 2017, with a great contribution of renewable energies in the production of electricity energy (54.2%) according to REA State of the Environment Portal Portugal ("*Relatório do Estado do Ambiente (REA)"* in the *"Portal do Estado do Ambiente Portugal"*), behind Austria (72.17%), Sweden (65.89%), Denmark (60.36%) and Latvia (54.36%).[8a] Spain appeared in eighth place with 36.34%. In 2018, 55.2% of the overall electricity production in Portugal was of renewable origin, with the hydroelectric and the wind energies occupying the highest places, (**Figure 2a)**.[8] However, over the years, the production of energy from solar power has grown due to the implementation of photovoltaic panels in several areas. In Spain, just as in Portugal the implementation of measures in favour of renewable energies has increased over time, with 46.7% of the total energy in 2018 coming from renewable energies (**Figure 2b**).[9]

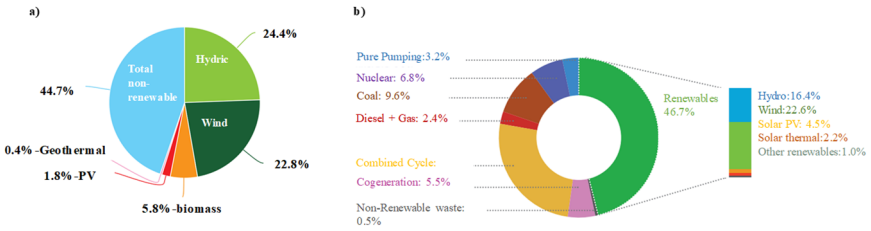

Figure 2- a) *Percentage of total energy produced in Portugal in 2018. Data obtained in REA.*[8] ***b)*** *Percentage of total energy produced in Spain in 2018 according the REE.*[9]

Among all renewable energy sources, sunlight is the most abundant, approximately 430 EJ of sunlight energy impinge on the Earth per hour, being enough energy to supply the whole world.[10] However, the proper use of solar energy still brings one of the biggest challenges to be overcome, the collection, conversion and

[6] C. Le Quéré, J. I. Korsbakken, C. Wilson, J. Tosun, R. Andrew, R. J. Andres, J. G. Canadell, A.Jordan, G. P. Peters, D. P.van Vuuren, *Nat. Clim. Chang.*, **2019**, *9*, 213–217.

[7] *United Nations, Paris Agreement*, **2015**, https://unfccc.int/process-and-meetings/the-paris-agreement/the-paris-agreement, accessed 01/05/2021.

[8] a) *State of the Environment Portal Portugal*, https://rea.apambiente.pt/, Accessed in 01/05/2020. b) *APREN Yearbook* **2019**, *Associação de Energias Renováveis* (APREN), https://www.apren.pt/, Accessed 01/05/2021.

[9] *Electrical Network of Spain*, Red Electrica de España (REE), https://www.ree.es/en/datos/publications/renewable-energy-report/2018-report, Accessed in 01/05/2021.

[10] A. J. Carrillo, J. G.-Aguilar, M. Romero, J. M. Coronado, *Chem. Rev.*, **2019**, *119*, 4777-4816.

distribution, are part of the greatest difficulties. The solar energy could be use in several applications namely photothermic, photocatalytic, photovoltaic (PV) technology.[11] The mainly attraction in the use of PV systems is that the solar energy, a free inexhaustive source of energy, is converted into electricity without harming the environment.[12] Regardless of the nature of solar cells, they all share the same conceptual working principle, that consists in the absorption of the incoming photon by the semiconductor material generating an electron-hole pair, the exciton. Then, this pair of charge carriers dissociates, with electrons moving to the negative electrode and holes to the positive one. Under normal conditions, only photons with energy equal or greater than the band gap ($E_{band\ gap}$) will generate an electron-hole pair.[13] In this process, apart from carrier recombination and parasitic resistance-related losses, two other mechanisms derivate from an energy mismatch may contribute to solar energy dissipation.[14] One of them occurs when the energy of the incident photons is too low to excite electrons across the band gap ($h\upsilon < E_{gap}$), called the sub-band gap losses, (**Figure 3**). In the case of crystalline silicon solar cells (c-Si), these losses can reach around 20% of the sun energy (AM 1.5 solar spectrum).[15] On the other hand, the incident photons with energy higher than the band gap give rise to energy losses in the form of heat (**Figure 3**).[15,16] The latter process is designated as lattice thermalization loss and causes that, 35% of the solar spectrum cannot be harvested in crystalline silicon devices.[15]

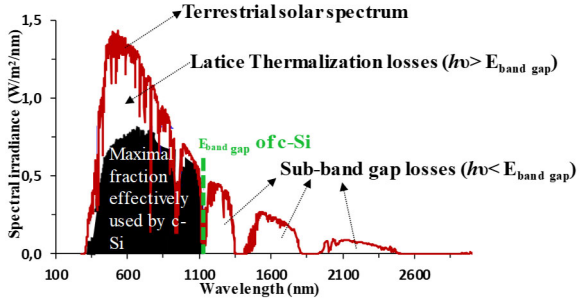

Figure 3- *Spectral distribution of the AM 1.5 G solar irradiance (official standard spectrum for PV performance evaluation defined by the American Society for Testing and Materials (ASTM) of ASTM G173-03: Global 37 deg South Facing Tilt) with the band gap of crystalline silicon solar cells ($E_{band\ gap}$= 1.1 eV).*

[11] a) N. S. Lewis, *Science*, **2007**, 315, 9. b) J. Gong, C. Li, M. R. Wasielewski, *Chem. Soc. Rev.,* **2019**, *48*, 1862-1864.
[12] G.K. Singh, *Energy*, **2013**, *53*, 1-13.
[13] A. Shah, P. Torres, R. Tscharner, N. Wyrsch, H. Keppner, *Sciences*, **1999**, 285.
[14] D. M. Bagnall, M. Boreland, *Energy Policy*, **2008**, *36*, 4390-4396.
[15] A. Ivaturi, H. Upadhyaya, in A Comprehensive Guide to Solar Energy Systems. With Special focus on Photovoltaic Systems, ed. T. M. Letcher, V. M. Fthenakis, Elsevier, **2018**, ch. Upconversion and Downconversion Processes for Photovoltaics, pag. 279–298.
[16] T. F. Schulzea, T. W. Schmidt, *Energy Environ. Sci.,* **2015**, *8*, 103–125.

Besides these two energy loss processes inherent to the absorber material, other losses related to the electronic properties of solar cells need to be taken into account, representing approximately 15% of the energy of the solar spectrum.[17] These extraction losses can be due to contact voltage losses, recombination losses (poor interface or material quality), junction losses, reflection losses from interfaces, among other.[15] These losses make that the maximum thermodynamic efficiency for single junction devices that can be obtained is approximately 30%. This limitation is called *Schockley-Queisser theoretical efficiency limit*.[18]

To overpass this limitation, several investigations are carried out either studding the physical properties of the compounds such as the singlet fission (SF) or developing new molecules for solar cells. It is in this sense that this doctoral thesis focuses on the one hand, on the study of the different intrinsic physical properties of organic compounds, but also on the study of PV in new derivatives. Therefore, the relation between light and matter is the physical basis of all the work. But the core of this investigation is based on a particular family of compounds, the diketopyrrolopyrroles (DPPs), which will be studied later.

So, following this line of thought, it is necessary to describe several physical processes that occur when a light beam incides in an organic compound, and this is what will be discovered next.

Theoretical considerations on photophysical phenomena

The light-matter interaction starts with light absorption giving rise to several phenomena. When an organic compound absorbs light, it goes from the ground state (S_0), which is usually singlet in nature, to an electronically singlet excited state with higher energy (S_1, S_2, …S_n). According to the Franck-Condon principle, this transition occurs without changing the multiplicity (the initially populated excited state has the same spin). Nevertheless, the excited state is not stable. However, during the decay it is possible to invert the spin of an electron leading to the formation of a triplet state (the sum of electron spin is one).

After the absorption of energy, a series of events are triggered to bring back the molecule to the ground state, such events can be mapped by the Jablonski diagram, (**Figure 4)**. The basic requirement for the absorption process is that the energy provided by the photon should be equal or greater than the energy needed by the system to go from the ground state to the first excited state, which corresponds to an electron transition from the highest occupied molecular orbital (HOMO) to the lowest unoccupied molecular orbital (LUMO). Then, the return to the fundamental state can occur either by radiative transition, emitting photons, or by a non-radiative

[17] A. Rao, R. H. Friend, *Nat. Rev. Mater.,* **2017**, *2*, 17063.
[18] W. Shockley, H. J. Queisser, *J. Appl. Phys.*, **1961**, *32*, 510.

transition, *e.g.* generating heat. Thus, the return to the fundamental state can occur by a radioactive process. There are two radiative processes, the fluorescence and the phosphorescence. Fluorescence is based on a decay from the excited singlet state S_1 to the ground state S_0, green arrow in **Figure 4**. This happens on a 10^{-9}-10^{-7} seconds timescale. Furthermore, the photon emission occurs at a greater wavelength (lower energy) than that of the absorption. In the case of phosphorescence decay, the time required to reach the ground state is much longer (10^{-6}-10^{-3} seconds) because there must be an intersystem crossing (*vide infra*) between the singlet excited state S_1 and a triplet excited state of lower energy T_1 (which is a forbidden process as it implies a change in multiplicity spin) and later the relaxation (photon emission) to the ground state, grey arrow in **Figure 4**. The non-radiative transitions can be separated in two processes, the internal conversion and the intersystem crossing. The internal conversion occurs when the system relaxes from a vibrational level of a certain excited state to a high vibrational level of an excited state of lower energy, blue arrow in **Figure 4**. Finally, when the system transits from a vibrational state to another with different multiplicity is called intersystem crossing, orange arrow in **Figure 4**.

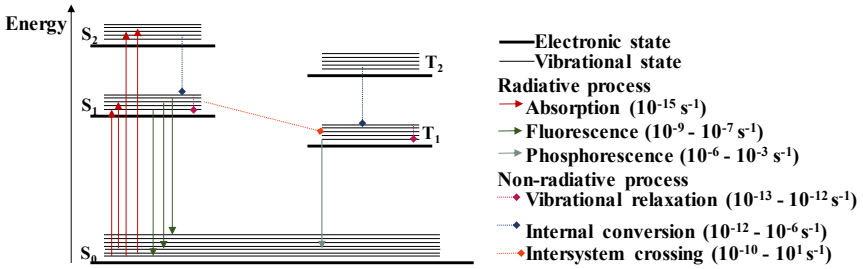

Figure 4- *Jablonski diagram.*

An excimer or excited dimer can be produced when one molecule in its excited state interacts with other molecule of the same species in the ground state (A---A)*. This interaction is only stable in the excited state because in the ground state the molecules are closed-shell systems. Once an excimer is formed, it can relax to the ground state by radioactive process, obtaining broad and featureless emission spectra.[19] In the case that the interacting molecules are different, the system is called exciplex (**Figure 5**).

[19] Klán, P. & Wirz, J. *Photochemistry of Organic Compounds*., John Wiley & Sons, Ltd, **2009**, Pag 60-69.

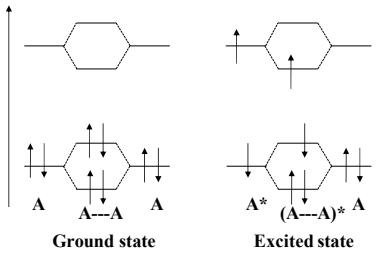

Figure 5- *Orbital diagram for the interaction between two molecules.*

However, in the ground state it is also possible to observe intermolecular interactions. Depending on the molecule structure it could be possible to originate Van der Walls interactions, H-bonding, π-π stacking. In some cases, the new interactions make possible the appearance of new electronic transitions derived from the aggregates, which are not observed in the monomers.[20] The arrangement of the aggregates can occur in different ways and the extreme cases are J-aggregates ("head-to-tail" where a bathochromic shift is observed) or H-aggregates ("side-by-side", where a hypsochromic shift is noted).

- **Photoinduced electron transfer**

In a system that consists of a donor group (D_G) and an acceptor group (A_G), the absorption of electromagnetic radiation leads to an exited state. In this state, two pathways are possible for returning to the ground sate. One of them consists in a radiative process with a velocity constant K_D. In the other one, an electronic transfer (ET) from D_G to A_G can occur, leading to separated (CS) state ($D_G^{\cdot+}$- $A_G^{\cdot-}$, where $D_G^{\cdot+}$ is the radical cation of the donor, and $A_G^{\cdot-}$ is the radical anion of the acceptor), with a velocity constant K_{ET}. After charge recombination (CR) the system can return to the ground state by a radiative or non-radiative process (**Figure 6**).

[20] N. J. Hestand, F. C. Spano, *Chem. Rev.*, **2018**, *118*, 7069−7163.

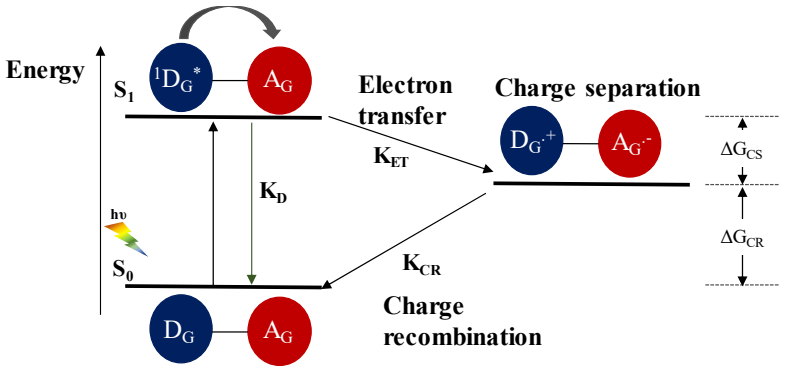

Figure 6- *Energy diagram of a donor-acceptor system.*

According to the Marcus theory, which describes the electron transfer process, K_{ET} can be express as:[21]

$$K_{ET} = \frac{4\pi^2|V|^2}{h}\left(\frac{1}{4\pi\lambda k_B T}\right)^{1/2} \exp\left(-\frac{(\Delta G^0 + \lambda)^2}{4\lambda k_B T}\right) \qquad \textit{Eq. 1}$$

where h is the Planck constant, λ is the reorganization energy (energy needed to structurally reorganize the donor, the acceptor and their solvation spheres after electron transfer), k_B is the Boltzman constant, T is the absolute temperature, V is the electronic coupling of functions between products and reagents (that is, between the charge separated state and the excited molecule) and ΔG^0 is the Gibbs free energy change for the electron transfer reaction between the two states.

In the normal region of Marcus's parabola ($|\Delta G^o| < \lambda$), the rate constant of an electron transfers increases with increasing free energy of the process. When the free energy equals the rearrangement energy ($|\Delta G^o| = \lambda$), the reaction rate is maximum and is directly related to the electronic coupling between the donor and the acceptor. Interestingly, in the inverted region of Marcus's parabola ($|\Delta G^o| > \lambda$), an increase in the free energy of the process produces a decrease in the rate of electron transfer (**Figure 7**).

[21] W. W. Parson, *J. Chem. Phys.*, **2020**, *152*, 184106.

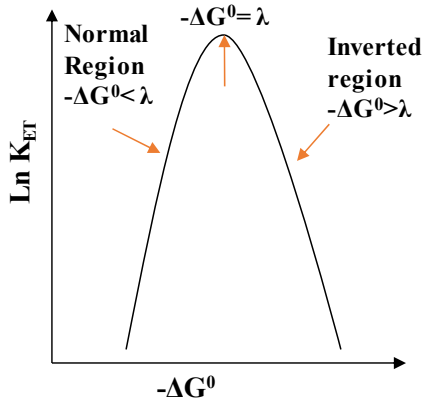

Figure 7-*Marcus's parable of electronic transfer processes.*

The value of λ is the key to modulate the appearance and the maximum of Marcus' parabola. The best donor-acceptor systems are those that have a low reorganization energy. As a result, rapid electron transfer processes occur as the charge recombination process becomes more difficult, because ΔG^o is much larger than the reorganization energy. The main factor affecting the magnitude of ΔG_{CS}^o and ΔG_{CR}^o is the stability of the charge separeted state. This depends on the oxidation potential of the donor, the reduction potential of the acceptor and the electrostatic attraction between cation and anion, which is a function of the distance between them and the dielectric constant of the solvent.[21]

Diketopyrrolopyrroles

After having briefly discussed several concepts that will be important in the course of this work, now it is important to focus the attention on the protagonists of this thesis, the diketopyrrolopyrroles.

Diketopyrrolopyrrole or DPP is a heterocyclic structure consisting of a conjugated bicyclic π dilactam. DPPs have great chemical versatility, allowing several structural changes, in positions 3 and 6 by different types of aromatic rings which provides different optical properties, and also in the lactam nitrogen's, 2 and 5 positions, with alkyl, acyl or aryl chains, in order to improve solubility in organic solvent (**Figure 8**).

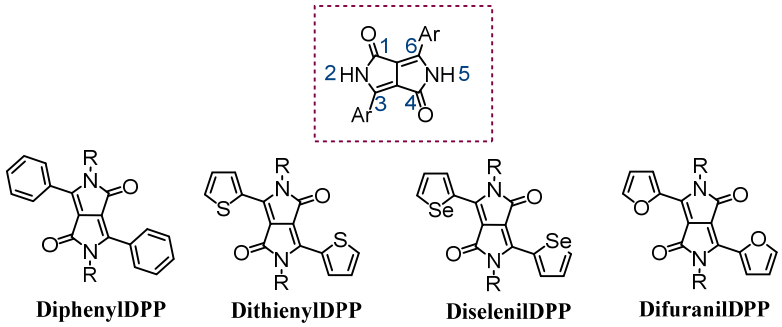

Figure 8-*General structure and the atoms numeration of DPPs. R represents an alkyl, aryl or acyl chain.*

DPPs were discovered by chance in 1974 when Farnum was tried to synthesize a β-lactam (4-phenylazet-2(1H)-one) by a Reformatsky reaction, that result in the formation of the diphenylDPP, **Scheme 1**.[22]

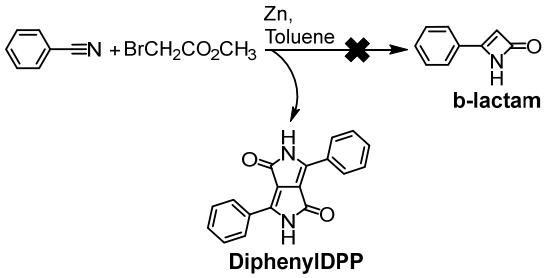

Scheme 1- *First synthesis of a DPP.*

This DPP presented several characteristics, such as high melting point (mp >350 °C), insolubility in volatile solvents, and a bright red colour, receibing soon attention from Ciba-Geigy company which studied these molecules as pigments and introduced the first DPP pigment in the market in 1986.[23] After this event, other DPPs have been developed and introduced in the market for application like paints, plastics, fibers and inks. Years later, DPPs have received increasing attention in other fields as in photovoltaic technologies as discussed later.

- **Diketopyrrolopyrrole synthesis**

The DPP recognition has sparked major studies in order to improve the synthetic yield of DPP core. In the literature there are several synthetic routes leading to the DPP skeleton in high yields. Some examples of these routes will be presented below.

[22] D. G. Farnum, G. Mehta, G. G. I. Moore, F. P. Siegal, *Tetrahedron Lett*., **1974**, *29*, 2549.
[23] Z. Hao, A. Iqbal, *Chem. Soc. Rev*., **1997**, *26*, 203-213.

1. Reformatsky route

In 1988, a mechanism was proposed for Farnum`s synthesis of DPP. The first step involves a condensation of the Reformatsky reagent with benzonitrile to achieve the intermediate **II**. Then, the C-alkylation by bromoacetate and ring closure leads to intermediate **IV**. Condensation with a second benzonitrile and subsequent cyclization of intermediate **V** gives rise to **DPP I** (**Scheme 2**).[24]

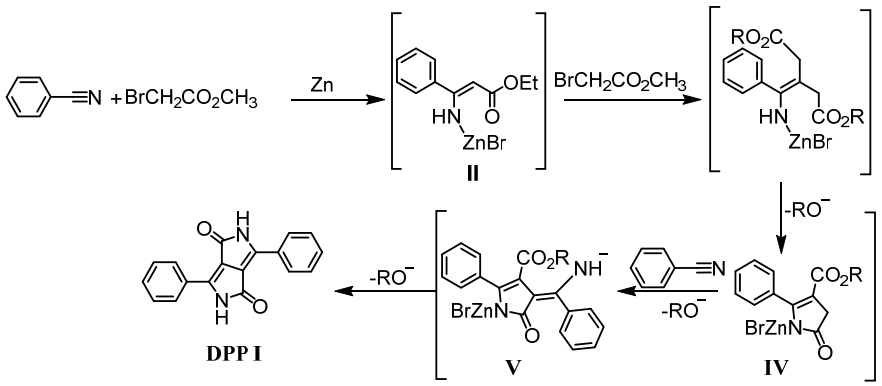

Scheme 2- *Reformatsky reaction pathway.*

2. Succinic ester route

In 1983 it was described the reaction of a succinic ester with an aromatic nitrile in the presence of strong base in a pseudo-Stobbe condensation to give rise to the DPP (**Scheme 3a**). **Scheme 3b** show the mechanism where the enaminoester **VI** cyclizes to the pyrrolidinone ester **VII**, which reacts with other molecule of benzonitrile under basic conditions, and after ring closure affords the **DPP**.[24] Under this conditions it is possible to obtain the DPP with a very good yield being the reaction more used nowadays.

[24] A. Iqbal, M. Jost, R. Kirchmayr, J. Pfenninger, A. Rochat, O. Wallquist, *Bull. Soc. Chim. Belg.*, **1988**, *97*, 615-644.

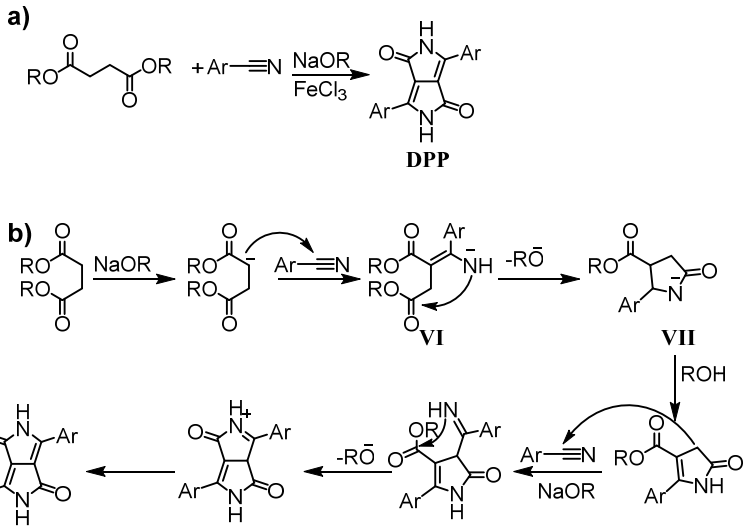

Scheme 3- a) *Succinic ester route.* ***b)*** *Mechanism of DPP formation via succinic ester route. Noted that Ar represents an aromatic moiety.*

3. Succinamide route

Other synthetic route to the DPP moiety was published by Gompper using the succinamide in the presence of *N*,*N´*-dimethylbenzamide diethyacetal, affording a mixture DPP and compound **VIII**. The later can react with *t*-BuOK yielding DPP (**Scheme 4**).[25] This route leads to lower yields than the succinic ester route.

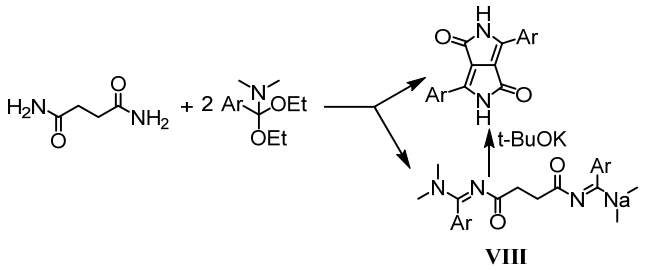

Scheme 4- *Synthesis of DPP via succinamide route.*

4. Varied routes

There are ways for the direct preparation of *N*,*N´*-disubstituted DPPs. Thus, for example, Langhals described the condensation of the diketofurofurane **IX** with two equivalents of aniline in the presence of dicyclohexylcarbodiimide (DCC), to yield **DPP II** (**Scheme 5a**).[26]

[25] F. Gloss, R. Gompper, *Angew. Chem.*, **1987**, *99*, 566.
[26] H. Langhals, T. Grundei, T. Potrawa, K. Polborn, *Liebigs Ann.*, **1996**, *5*, 679–682.

The synthesis of *N*,*N´* diaryl **DPP III** with different substituents in the aryl moieties has been described using the classic Stobbe condensation followed by an oxidation with 2,3-dichloro-5,6-dicyanobenzoquinone (DDQ) (**Scheme 5b**).[27] Later, a new approach for the synthesis of **DPP III** was reported, wherein a ketoamide and its bromo derivative were condensed and, after a ring closure, formed the DPP system (**Scheme 5c**).[28]

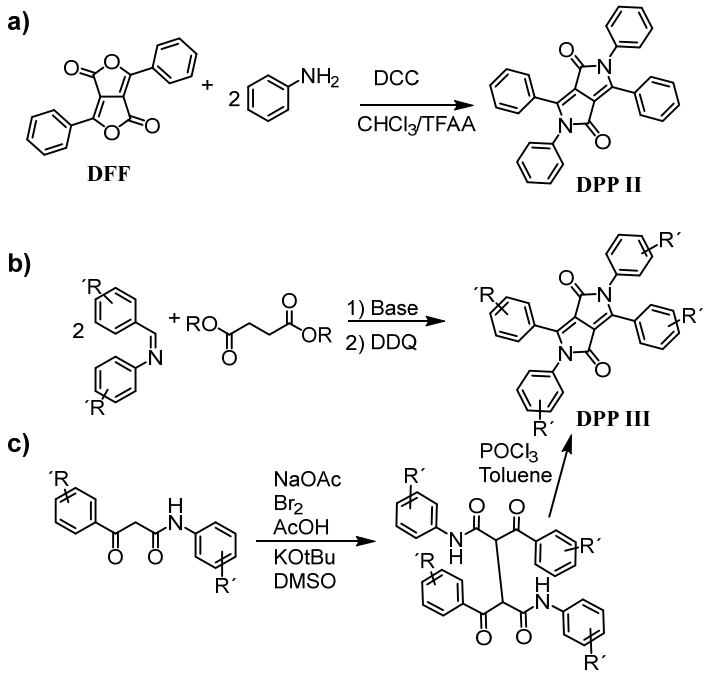

Scheme 5-*Miscellaneous DPP synthetic routes.*

- **Reactivity of diketopyrrolopyrroles**

The DPP structure contains several reactive positions being prone to electrophilic attack, such as oxygen and nitrogen atoms in the amide group, double bonds in DPP core and aromatic rings at the 3 and 6 positions. Also, nucleophilic attack can occur, *e.g.* on the carbonyl carbon atom and the α,β-unsaturated system present in the DPP core. **Figure 9** illustrates the potentially reactive centers in the diphenylDPP.

[27] M. Jost, A. Iqbal, A. C. Rochat, US 4585878 (29.04.1986).
[28] T.R. Chamberlain, C. Thornley, WO 02/068422 (06.09.2002).

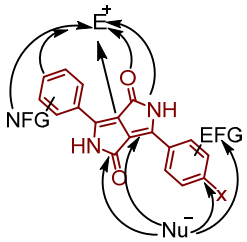

EFG: Electrophilic funtional group (e.g.CN, COOR);
NFG: Nucleophilic functional group (e.g. OH, SH, NHR)
X: e.g. halogen
E: Electrophile
Nu: Nucleophile

Figure 9- *Reactive centers in a diphenylDPP.*

In the following several examples of reactions will be presented.

1. *N*-alkylation

The lactams of the DPP under basic conditions react in the same way as an amide, meaning that can be deprotonated to give ambidentate anions, in which the negative charge is distributed between the oxygen and nitrogen atoms (**Scheme 6a**). The possibility of the oxygen atoms having the negative charge difficult the *N*-alkylation because the *O*-alkylation reaction competes with this. This secondary compound was described by Frebort.[29] As the DPP consists in two fused lactams, the charge can be shifted to the second oxygen atom. The low solubility of the DPP unit caused by the strong intermolecular hydrogen interactions, difficults the reaction and to combat this problem it is necessary to use polar, aprotic solvents like DMF, NMP [30] or nitrobenzene [31] which allows to increase the temperature (**Scheme 6b**). Thus, using for example potassium carbonate or alkoxides (*t*-BuOK, MeONa)[32] and the alkylating agent it is possible to obtain the *N*-alkylation of the DPP.[33] Besides to these reagents, in the literature there are examples of reaction where a phase transfer catalyst such as quaternary ammonium salts were used.[34]

[29] Š. Frebort, Z. Eliáš, A. Lyčka, S. Luňák Jr., J. Vyňuchal, L. Kubáč, R. Hrdina, L. Burgert, *Tetrahedron Lett.* **2011**, *52,* 5769.
[30] a) A. R. Rabindranath, Y. Zhu, I. Heim, B. Tieke, *Macromolecules,* **2006**, *39*, 8250. b) G. Zhang, K. Liu, Y. Li, M. Yang, *Polym. Int.,* **2009**, *58*, 665.
[31] M. Jost, A. Iqbal, A. C. Rochat, (Ciba-Geigy AG), Eur. Pat. Appl. 133156, **1984**.
[32] M. Vala, M. Weiter, J. Vynuchal, P. Toman, S. Lunák Jr., *J. Fluoresc.,* **2008**, *18*, 181.
[33] G. Colonna, T. Pilati, F. Rusconi, G. Zecchi, *Dyes Pigm.,* **2007**, *75*, 125.
[34] a) M. Kirkus, L. Wang, S. Mothy, D. Beljonne, J. Cornil, R. A. J. Jannsen, S. C. J. Meskers, *J. Phys. Chem. A,* **2012**, *116*, 7927. b) M. Grzybowski, E. Glodkowska-Mrowka, T. Stoklosa, D. T. Gryko, *Org. Lett.,* **2012**, *14*, 2670. c) M. Grzybowski, V. Hugues, M. Blanchard-Desce, D. T. Gryko, *Chem. Eur. J.,* **2014**, *20,* 12493.

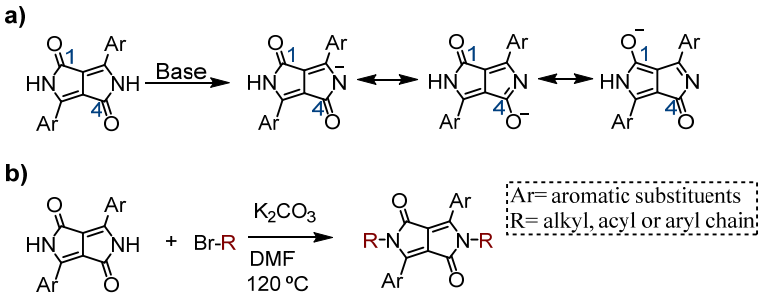

Scheme 6- a) *Mesomeric structures of a deprotonated DPP.* ***b)*** *General scheme of an N-alkylation reaction.*

The introduction of the chain in the DPP increases abruptly the solubility in organic solvents because it is no longer possible to form intermolecular hydrogen bonds. The solubility increases with the size and branching of the alkyl group.

2. Electrophilic and nucleophilic aromatic substitutions

Together with *N*-alkylation, the reactions on the aromatic substituents at the 3 and 6 positions have been vastly studied. In particular, the aromatic electrophilic and nucleophilic aromatic substitution reactions. An example of electrophilic aromatic substitution reaction is the sulfonation of diphenylDPP with fuming sulfuric acid (**Scheme 7a**). On the same way as fuming sulfuric acid, the reaction with bromine originates the substitutions at the *para* position of benzene rings (**Scheme 7b**).[35] Depending on the substituents on the aromatic ring, the nucleophilic aromatic substitution can also take place, for example the **DPP V** can react with amines at high temperatures giving rise to **DPP VI** (**Scheme 7c**).[36]

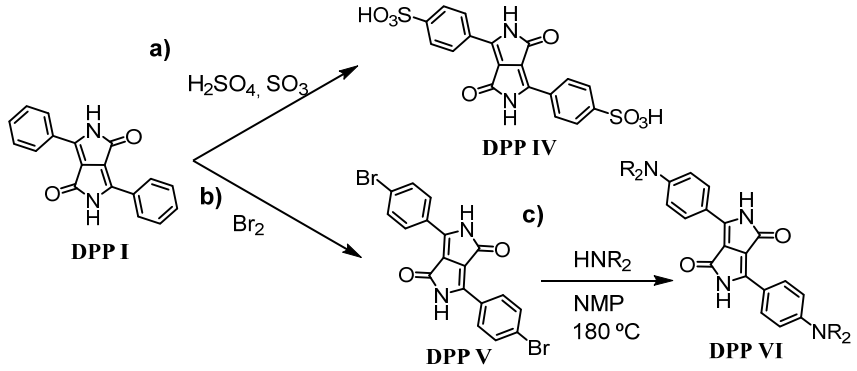

Scheme 7- a) *and* ***b)*** *Examples of electrophilic aromatic substitutions reaction.* ***c)*** *Example of a nucleophilic aromatic substitution reaction.*

[35] M. Grzybowski, D. T. Gryko, *Adv. Opt. Mater.*, **2015**, *3*, 280–320.
[36] A. C. Rochat, O. Wallquist, A. Iqbal, J. Mizuguchi, J., EP 353184 (Ciba-Geigy,31.01.1990).

This reaction allowed to investigate other type of pigments, but nowadays the DPP derivatives have been investigated in several applications such as photovoltaic technology among other, being *N*-alkylation an essential step due to the importance of solubility property to synthetize more complex DPPs.

3. Other reactions

The bromination reaction of *N,N´*-disubstituted-3,6-diheteroarylDPPs has great importance with regard to the use of these intermediates for carbon-carbon couplings. The high electron density of the heterocycles allows the bromination of α positions through an aromatic electrophilic substitution in the presence of *N*-bromosuccinimide (NBS)[37] and with Br_2 in the case of furan[38] and thiophene[39] derivatives (**Scheme 8**).

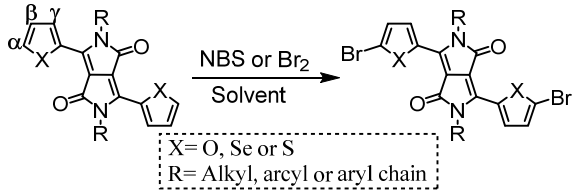

Scheme 8- *General scheme of bromination.*

The carbon-carbon coupling is a term for a variety of reactions, usually catalysed by palladium derivatives, leading to the linkage of two moieties trough a carbon-carbon single bond. There are different types of coupling depending on the nature of the reagents, thus for example, the Stille coupling used tin derivatives, the Suzuki-Miyaura coupling boronates, the Heck reaction alkenes, and the Sonogashira reaction alkynes, for examples. In the literature exists an extensive library of DPP derivatives synthesized using Pd-catalysed cross-coupling reactions. **Scheme 9** shows a general scheme of the diverse couplings and some recent bibliography where there are examples of each coupling.

These coupling reactions are an optimal synthetic via because they usually proceed in high yields and allow to obtain infinite wide variety of DPP derivatives. In this way it is possible to study the diverse optical properties of this family of compound and introduce them in several applications.

[37] a) L. Huo, J. Hou, H.-Y. Chen, S. Zhang, Y. Jiang, T. L. Chen, Y. Yang, *Macromolecules,* **2009**, *42*, 6564. b) J. Lee, A-R. Han, J. Hong, J. H. Seo, J. H. Oh, C. Yang, Adv. *Funct. Mater.,* **2012**, *22*, 4128. c) Y. Suna, J. Nishida, Y. Fujisaki, Y. Yamashita, *Org. Lett.,* **2012**, *14*, 3356. d) J. C. Bijleveld, B. P. Karsten, S. G. J. Mathijssen, M. M. Wienk, D. M. de Leeuwb, R. A. J. Janssen, *J. Mater. Chem.* **2011**, *21*, 1600. e) C. H. Woo, P. M. Beaujuge, T. W. Holcombe, O. P. Lee, J. M. J. Fréchet, *J. Am. Chem., Soc.* **2010**, *132*, 15547. f) M. Shahid, T. M.-Ward, J. Labram, S. Rossbauer, E. B. Domingo, S. E. Watkins, N. Stingelin, T. D. Anthopoulos., M. Heeney, *Chem. Sci.,* **2012**, *3*, 181.
[38] Y Li, P. Sonar, S. P. Singh, W. Zeng, M. S. Soh, *J. Mater. Chem.,* **2011**, *21*, 10829.
[39] B. Y. Li, S. P. Singh, P. Sonar, *Adv. Mater.,* **2010**, *22*, 4862.

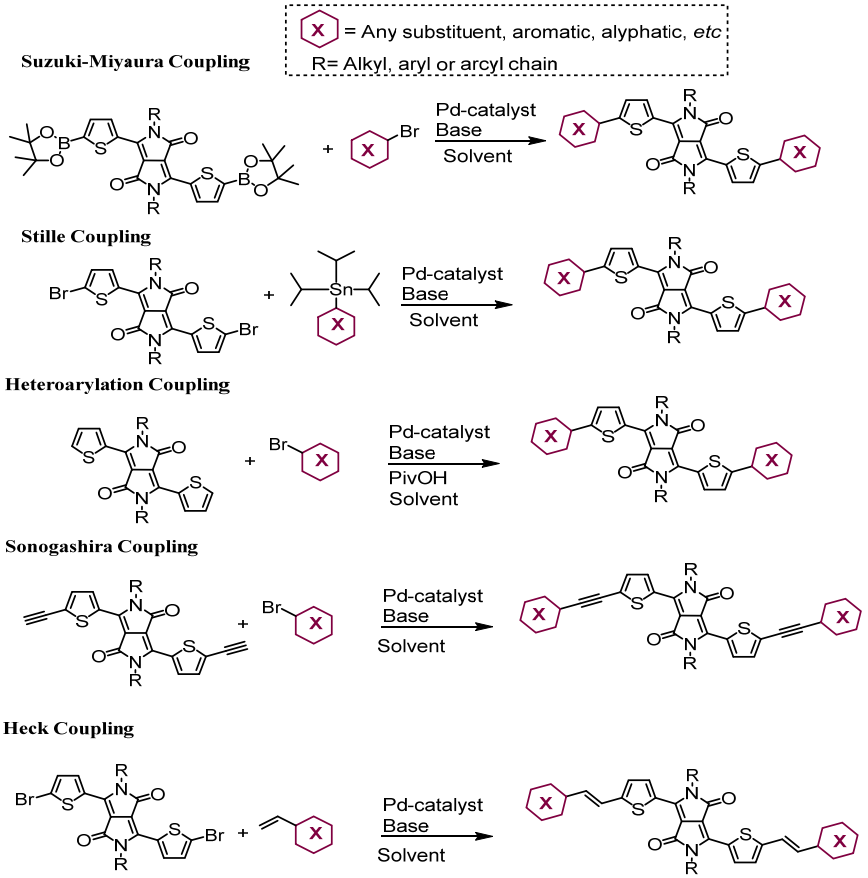

Scheme 9- General scheme of: **a)** Suzuki-Miyaura coupling[40] **b)** Stille coupling[41] **c)** Heteroarylation coupling[42] **d)** Sonogashira coupling[43] **e)** Heck coupling.[44]

[40] a) G. K. Dutta, S. Kasthuri, G. Marappan, S. V. Jayaraman, Y. Sivalingam, C. D. Natalee, V. Nutalapati, *J. Mater. Chem. C*, **2019**,*7*, 9954-9965. b) R. W. Jadhav, R. V. Hangarge, M. D. Aljabri, K. S. More, J.-Y. Chen, L. A. Jones, R. A. Evans, J.-L. Li, S. V. Bhosale, A. Gupta, *Mater. Chem. Front.*, **2020**, *4*, 2176. c) F. Wu, L. Wang, H. Tang, D. Cao, *Anal. Chem.*, **2019**, *91*, 5261−5269. d) A. K. Hundal, S. Ali, M. Jameel, L. Jones, N. Kaur, R. A. Evans, J.-L. Li, S. J. Langford, A. Gupta, *Mater. Chem. Front*, **2020**, *4,* 3209. e) M. L. Agazzi, V. A. S. Almodovar, N. S. Gsponer, S. Bertolotti, A. C. Tomé, E. N. Durantini, *Org. Biomol. Chem.*, **2020**, *18*, 1449-1461.

[41] a) S.-H. Wang, T.-W. Wang, H.-C. Tsai, P.-C. Yang, C.-F. Huang, R.-H. Lee, *RSC Adv.*, **2020**, *10*, 9525. b) Y.-C. Lin, C.-K. Chen, Y.-C. Chiang, C.-C. Hung, M.-C. Fu, S. Inagaki, C.-C. Chueh, T. Higashihara, W.-C. Chen, *ACS Appl. Mater. Interfaces*, **2020**, *12*, 33014−33027. c) X. Liua, L. Kong, H. Dua, Y. Zhanga, J. Zhaoa, Y. Xie, *Org. Electron.*, **2019**, *64*, 223–235. d) D. Xia, F. Yang, J. Li, C. Li, W. Li, *Mater. Chem. Front*., **2019**, *3*, 1565.

[42] a) M. Mainville, M. Leclerc, *ACS Appl. Polym. Mater.,* **2021**, *3*, 2-13. b) T. H Nguyen, L. T Nguyen, H. T. Nguyen, N.-L. T Phan, V. Q Nguyen, L.-Thu T Nguyen, M. H Hoang, H. Le Tran, P. T Mai, H. Murata, M. Zaidan, A. Aziz, M. Akaborie, H. T Nguyen, *Polym. Int.*, **2019**, *68,* 1776–1786.

[43] a) L. Yin, Q. Yuan, Y. Li, *New J. Chem*., **2020**, *44*, 13319. b) F. Cheng, X. He, L. Yin, B. Xie, Y. Li, *Dyes Pigm.*, **2020**, *176*, 108211. c) D. Giri, S. K. Raut, S. K. Patra, *Dyes Pigm.*, **2020**, *174,* 108032.

[44] a) A. Rahmanudin, L. Yao, A. Sekar, H.-H. Cho, Y. Liu, C. R. Lhermitte, K. Sivula, *ACS Macro Lett.*, **2019**, *8*, 134−139. b) V. A. S. Almodôvar, A. C. Tomé, *J. Porphy. Phthalocyanines*, **2019**, *23*, 1–24.

The introduction of different substituents changes the optical properties of DPPs, it means that the UV-vis spectra of these extended DPPs are usually batho-and hyperchromically shifted relative to the starting brominated DPP.

- **Optical properties of *N,N´*-dialkylated diketopyrrolopyrrole**

The introduction of substituents on the nitrogen atoms of the lactams leads to changes in the physical properties, not only in the solubility, as explained before, but also in the optical properties because these new constituents affect the electron density on nitrogen atoms and increase the steric hindrance on the aromatic substituents at the 3 and 6 positions, meaning that they can rotate out of the plane of the chromophores. However, the alkylation does not significantly change the fluorescence quantum yield.[45] Therefore, the π-conjugation between the molecular parts is weakened. Thus, the nature and the size of the substituents influence the dihedral angle (τ) between the DPP core and the plane of the aromatic group. Some dihedral angle values based on X-ray data are presented in **Table 1**. In the first two examples **A** and **B**, the influence of the alkylation of the lactams on the τ value is evidenced: the τ value for **B** is almost five times larger than the one for **A**. Comparing the τ values for **DPP B** with the vales for the other three examples (**C**, **D** and **E**) it is visible that the angle reduces significantly when smaller aryl substituents such a furan, thiophene and selenophene are present. In these three cases it is possible to establish intramolecular interactions between the X_4 and the hydrogen of the metyl group (H_1) and between the oxygen atom of the carbonyl group (O_3) and the H_2 (**Figure 10**), however they are more stronger in the case of the furan derivatives because the oxygen is smaller and more electronegative than sulphur and selenium.

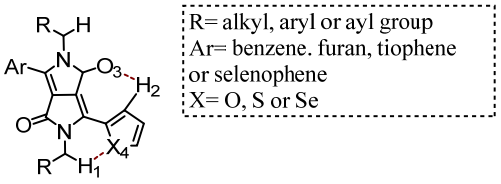

Figure 10- *Intramolecular interaction.*

[45] M. Vala, M. Weiter, J. Vyňuchal, P. Toman, S. Luňák Jr., *J Fluoresc.*, **2008**, *18*, 1181–1186.

Table 1-Dihedral angle comparison of different DPPs.

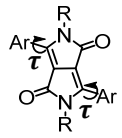

DPP	Ar	R	τ(°)	Ref.
A		H	7.1	[46]
B		C_6H_{13}	34.2	[47]
C		C_6H_{13}	10.1	[48]
D		C_6H_{13}	12.0	[47]
E	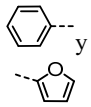	Me	31.1/0.9	[49]

Hence, the π- conjugation is weakened changing the UV-vis spectra, and the higher tendency for a rotation of aryl substituents results in a broader absorption and emission spectra, increasing the Stokes shifts. Generally, the UV-vis spectrum of DPPs present two bands, one between 300 and 450 nm, while the other lies between 500 and 700 nm. The comparison between UV-vis in solid state and in solution shows some differences in the shape and position, usually in solid state the spectra are broader and red-shifted. These differences are related with the intermolecular interaction in solid state (π-π interaction, Van der Waals force or hydrogen bond). **Figure 11a** presents the comparison between solid state and solution spectra of 2,5-bis(2`-octyldodecyl)-3,6-di(thiene-2-yl)-2,5-dihydropyrrolo[3,4-*c*]pyrrole-1,4-dione (DPP-$(OD)_2$). DPP is also known to have high quantum fluorescence yields that can reach over 90%.[50] **Figure 11b** shows the absorption and emission spectra of DPP-$(OD)_2$.

[46] J. Mizuguchi, A. Grubenmann, G. Wooden, *Acta Cryst. B*, **1992**, *48*, 696-700.
[47] J. Dhar, N. Venkatramaiah, A. Anitha, S. Patil, *J. Mater. Chem C*, **2014**, *2*, 3457.
[48] M. A. Naik, N. Venkatramaiah, C. Kanimozhi, S. Patil, *J. Phys. Chem. C,* **2012**, *116*, 26128–26137.
[49] C. J. H. Morton, R. Gilmour, D. M. Smith, P. Lightfoot, A. M. Z. Slawin, E. J. MacLean, *Tetrahedron*, **2002**, *58*, 5547-5565.
[50] M Kaur, D. H. Choi, *Chem. Soc. Rev*., **2015**, *44*, 58.

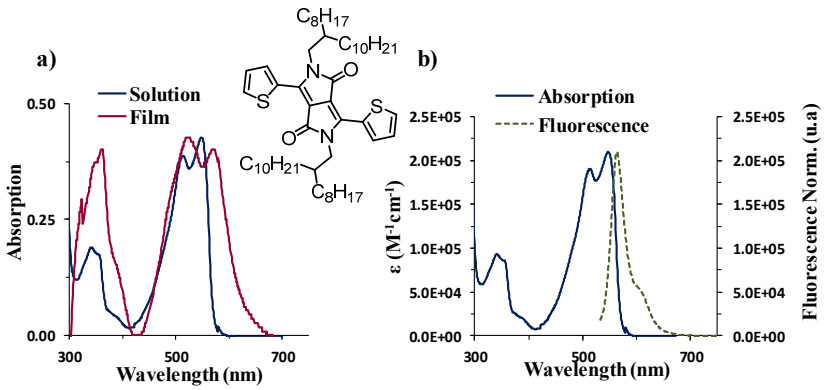

Figure 11- a) *Absorption spectra of* ***DPP-(OD)$_2$*** *in solution (blue line) and in solid state (red line).* ***b)*** *Absorption (blue line) and fluorescence (green line) spectra of* ***DPP-(OD)$_2$***.

- **Application of diketopyrrolopyrrole**

Currently, DPPs are widely studied for their properties and chemical versatility. But this interest arose in 2008 when the first study was reported, where a DPP was used as a semiconductor for OFETs and not as a pigment.[51] Due to their chemical versatility they can be applied in the form of polymers or simply in the form of single molecules. This feature allows the application of DPP in a wide range of applications. Namely DPPs are considered promising building blocks to construct high-performance semiconducting materials for various electronic devices. There are several review reports that compile the studies that justified this sentence. In this sense, DPPs are widely used in solar cells, both in dye sensitised solar cell, bulk heterojunction solar cell or perovskite solar cells,[52] OEFTS,[53] chemical sensors,[53,54] photodetectors,[53,55] memory devices[53,56].

But not all studies follow this technological path, there are several articles that describe DPP for biological applications[50], being as a molecular chemodosimeter or even for photodynamic therapy.[57]

[51] L. Burgi, M. Turbiez, R. Pfeiffer, F. Bienewald, H.-J. Kirner, C. Winnewisser, *Adv. Mater.,* **2008**, *20*, 2217–2224.
[52] C. Zhao, Y. Guo, Y. Zhang, N. Yan, S. You, W. Li, *J. Mater. Chem. A*, **2019**, *7*, 10174-10199.
[53] Q. Liu, S. E. Bottle, P. Sonar, *Adv. Mater.,* **2020**, *32*, 1903882.
[54] M. Kaur, D. H. Lee, D. S. Yang, H. A. Um, M. J. Cho, J. S. Kang, D. H. Choi, *Chem. Commun.* **2014**, *50*, 14394.
[55] L. Zhang, T. Yang, L. Shen, Y. Fang, L. Dang, N. Zhou, X. Guo, Z. Hong, Y. Yang, H. Wu, J. Huang, Y. Liang, *Adv. Mater.* **2015**, *27*, 6496.
[56] Y. Li, H. Li, H. Chen, Y. Wan, N. Li, Q. Xu, J. He, D. Chen, L. Wang, J. Lu, *Adv. Funct. Mater.* **2015**, *25*, 4246.
[57] a) W. Qua, L. Yanga, Y. Hanga, X. Zhanga, Y. Qub, J. Hua, *Sensors Actuators B*, **2015**, *211*, 275–282. b) J. Schmitt, V. Heitz, A. Sour, F. Bolze, H. Ftouni, J.-F. Nicoud, L. Flamigni, B. Ventura, *Angew. Chem.*, **2015**, *127*, 171–175.

Chapter 1

Synthesis and Characterization of Diketopyrrolopyrrole Dimers for their Study in Singlet Fission

1.1. Introduction

The *Schockley-Queisser theoretical efficiency limit* is the biggest challenge to overcome and enhance the PV performance, as mentioned before.[16] Multijunction solar cells are one example to minimize thermalization losses, that consist in several subcells with different band gaps concerted by tunnel diodes.[58] So far the maximum efficiency obtained for this type of devices was 46%, however, in a perfect system with infinite subcells the maximum efficiency that could be obtained is 68%.[59] Although better efficiencies are achieved with this type of devices than with silicon solar cells. It is not a viable alternative because the production cost is very high. Hence, it is necessary to develop other solutions to combat losses. A strategy to overcome sub-band gap losses, can be using the upconversion process, which consists in an anti-Stokes type nonlinear optical emission, in which one high-energy photon is emitted from two or more low-energy photons.[60] On the other hand, thermalization losses can be limited using semiconductors nanostructures that efficiently undergo multiple exciton generation (MEG). So, devices cheaper than multijunction solar cells can be developed. In this process, there is a conversion from a high-energy photon into multiple electron-hole pairs if the energy of the hot excitons generated by the absorption of the photons is bigger than two times the bandgap at least, $E_{photon} > 2\times E_{gap}$.[61] In the case that the photon possesses an energy bigger than the bandgap but smaller than twice the band gap this excess energy, $\Delta E = h\upsilon - E_{gap},$. is unavoidably lost.[61] However, the maximum theoretical efficiency that can be obtained for solar cells based in MEG is 45% under AM 1.5 standard spectrum.[62] The MEG process is used in semiconductor quantum dots, however the analogue process for organic semiconductors is dominated by singlet exciton fission or singlet fission (SF).[63] This process is the down-conversion of one singlet exciton ($E(S_1)$) into two triplet excitons with approximately half the initial singlet energy ($E(T_1) \approx {}^{1}/_{2} E(S_1)$).[64] However, in contrast with the MEG process, the SF process needs two different

[58] a) M. K. Siddiki, J. Li, D. Galipeau, Q. Qiao, *Energy Environ. Sci*., **2010**, *3*, 867–883. b) F. Dimroth, S. Kurtz, *MRS Bull.*, **2007**, *32,* 230-235.
[59] a) R. M. France, J. F. Geisz, I. García, M. A. Steiner, W. E. McMahon, D. J. Friedman, T. E. Moriarty, C. Osterwald, J. S. Ward, A. Duda, M. Young, W. J. Olavarria, *IEEE J. Photovolt.*, **2016**, *6*, 2. b) A. D. Vos, *J. Phys. D: Appl. Phys.*, **1980**, *13*, 839-846.
[60] F. Auzel*, Chem. Rev*., **2004**, *104*, 139−173.
[61] a) M. C. Beard, J. M. Luther, O. Semonin, A. J. Nozik, *Acc. Chem. Res.*, **2013**, *46*, 1252–1260. b) S. Kolodinski, J. H. Werner, T. Wittchen, H. J. Queisser, *Appl. Phys. Lett.*, **1993**, *63*, 17.
[62] M. C. Hanna, A. J. Nozik, *J. Appl. Phys.*, **2006**, *100*, 074510.
[63] a) M. B. Smith, J. Michl, *Chem. Rev*., **2010**, *110*, 6891–6936. b) I. Paci, J. C. Johnson, X. Chen, G. Rana, D. Popovic, D. E. David, A. J. Nozik, M. A. Ratner, J. Michl, *J. Am Chem. Soc*., **2006**, *128*, 16546-16553.
[64] E. C. Greyson, B. R. Stepp, X. Chen, A. F. Schwerin, I. Paci, M. B. Smith, A. Akdag, J. C. Johnson, A. J. Nozik, J. Michl, M. A. Ratner, *J. Phys. Chem. B*, **2010**, *114*, 14223–14232.

absorbers, one SF sensitizer combined in optical series with one ordinary sensitizer.[63]

The motivation to apply SF chromophores in solar cells can be attributed to Hanna and Nozik in 2006[65] that reported the concept of carrier multiplication solar cells, however, Dexter was the one which described for the first time the sensitization of conventional solar cells by SF chromophores in 1979.[66] The application of SF chromophores in solar cells mitigates energy losses due to the conversion of the kinetic-energy excess from the hot carrier into a second exciton, whenever the solar photons have energy of at least twice the band gap of the semiconductor. Part of the excitation energy excess is harvested as increased photocurrent and the theoretical power conversion efficiency is enhanced to 44%.[67] But, it is important to note that, to exceed the *Schockley-Queisser limit*, SF solar cells requires two or more light capturing components, a SF material capable to absorb high energy photons and a chromophore responsible for converting lower energy solar radiation into a single electron-holes pair per solar photons.[68]

1.1.1. Singlet fission

Singlet fission was a mechanism proposed in 1960, in order to justify the reduction of fluorescence yields in anthracene and tetracene crystals.[69] It is defined as a spin-allowed process in which an organic chromophore in an excited singlet state (S_1) shares its excitation energy with a neighbouring ground-state (S_0) chromophore and then, both are converted into a pair of spin-correlated triplets $^1(T_1T_1)$, and then which later splits into two independent triplet states (T_1+T_1).[63] Therefore, the SF process can be described as a sequence of internal conversion and intersystem crossing as:

$$S_0 + S_1 \leftrightarrows {}^1(T_1T_1) \leftrightarrows (T_1+T_1) \qquad \textit{Eq. 1.1}$$

The first step represents an internal conversion process, and the second step is an intersystem crossing process. According to **Eq. 1.2**, SF is a reverse process of triplet-triplet annihilation, where two triplets excitons collide and fuse into a singlet exciton.[70] The thermodynamic requirement for SF is:

$$E(S_1) \geq 2\,E(T_1) \qquad \textit{Eq. 1.2}$$

From the point of view of energetic losses, there are three possible situations. When $2E(T_1) \approx E(S_1)$ the molecules may be appropriated for efficient SF. When $2E(T_1)$-

[65] M. C. Hanna, A. J. Nozik, *J. Appl. Phys.,* **2006***, 100*, 074510.
[66] D. L. Dexter, *J. Lumin.,* **1979**, *18*, 779−784.
[67] K. Miyata, Y. Kurashige, K. Watanabe, T. Sugimoto, S. Takahashi, S. Tanaka, J. Takeya, T. Yanai, Y. Matsumoto, *Nat. Chem.*, **2017**, *9*, 983-989.
[68] D. Casanova, *Chem. Rev.*, **2018**, *118*, 7164−7207.
[69] a) S. Singh, J. Jones, W. Siebrand, B. P. Stoicheff, G. Schneider, *J. Chem.Phys.*, **1965**, *42*, 330–342. b) C. E. Swenberg, W.T. Stacy, *Chem. Phys. Lett.*, **1968**, *2*, 327–328.
[70] B.J. Walker, A. J. Musser, D. Beljonne, R. H. Friend, *Nat. Chem.*, **2013**, *5*, 1019-1024.

$E(S_1)>0$ occurs an exothermic SF, the process is expected to undergo efficiently from the energetic point of view. Endothermic SF occur when $2E(T_1)-E(S_1)<0$, there may be an energy barrier to be overcome by thermal excitation.[71] Endothermic SF with a barrier up to 200 meV is also highly efficient.[72] In addition, the energy level of the second triplet excited state should be twice the energy of the lowest-lying triplet excited state to reduce the triplet-triplet annihilation process, $2E(T_1) <E(T_2)$. However, molecules that do not fulfill the condition described in the **Eq. 1.2** can also present SF, but the fast relaxation processes will reduce the SF yield and it is complicate to determine the SF mechanism.[73] When the chromophores are identical, the SF is called homofission, and when the chromophores are different from each other, the SF is known as heterofission.[63]
The energetic stint is not the only parameter to be taken into consideration to determine the SF rate and yield. The electronic coupling between the two neighbouring compounds play also a key role.[74] To avoid competition between SF and vibrational deactivation, the ideal chromophores for SF need to meet the following requirements: an absorption onset near 2 eV; a high absorption coefficient above the absorption onset; obey to the thermodynamic requirement defined in **Eq. 1.2**, to assume a high efficiency and a fast rate of singlet fission and a slow rate of the reverse re-fusion process.[73]
Depending on the system used, SF can be either intermolecular SF or intramolecular SF.

1.1.1.1. Mechanisms of singlet fission[75]

For what is known nowadays, SF occurs in two steps. In the first one there is the formation of the singlet-correlated triplet pair, $^1(T_1T_1)$, and in the second one the $^1(T_1T_1)$ split into two independent triplet pairs, $T_1\cdots T_1$. For the first step of SF, the spin–conserving internal conversion from (S_1S_0) to $^1(T_1T_1)$, there are in the literature three different mechanisms that describe this step: the quantum coherent mechanism, the direct and the CT-mediated mechanism (**Figure 1.1**).[76] In the case of the quantum coherent mechanism, a quantum superposition state $[(S_1S_0) \leftrightarrow {}^1(T_1T_1)_n]$ is formed directly when (S_1S_0) is excited, with a spin-correlated triplet pair $^1(T_1T_1)_n$ (**Figure 1.1a**).[77]

[71] S. Itoa, T. Nagami, M. Nakano, *J. Photochem. and Photobiol. C: Photochem. Rev.,* **2018**, *34*, 85–120.
[72] M. H. Futscher, A. Rao, B. Ehrler, *ACS Energy Lett.,* **2018**, *3*, 10, 2587-2592.
[73] V. Balzani, P. Ceroni, A. Juris, *Photochemistry and Photophysics: Concepts, Research, Applications*, Wiley-VCH, **2014**, pag 449-451.
[74] F. Mirjani, N. Renaud, N. Gorczak, F. C. Grozema, J. *Phys. Chem. C*, **2014**, 118, 14192−14199.
[75] Short notations were adopted in order to lighten the text, however where $^1(S_0S_0)$ is read, $/A(S_0)C(S_0)>$ should be read. Where $^1(S_1S_0)$ is read, $/A(S_1)C(S_0)>$ or $/A(S_0)C(S_1)>$ should be read. Where $^n(T_1T_1)$ is read, $/A(T_1)C(T_1)>$ should be read. And where $(T_1 +T_1)$ is read. $/A(T_1) >+/C(T_1)>$ should be read.
[76] B. S. Basel, C. Hetzer, J. Zirzlmeier, D. Thiel, R. Guldi, F. Hampel, A. Kahnt, T. Clark, D. M. Guldi, R. R. Tykwinski, *Chem. Sci.*, **2019**, *10*, 3854–3863.
[77] A. M. Alvertis, S. Lukman, T. J. H. Hele, E. G. Fuemmeler, J. Feng, J. Wu, N. C. Greenham, A. W. Chin, A. J. Musser, *J. Am. Chem. Soc.*, **2019**, *141*, 17558−17570.

There are observations in the literature indicating that sometimes the coherent superposition includes a CT state, in other words: $[(S_1S_0) \leftrightarrow CT \leftrightarrow {}^1(T_1T_1)_n]$. The spin-correlated triplet pair can still be localized on two neighbouring molecules or may already be diffused apart evolving eventually into two independent triplet states.[67,78] Following the proposal of Scholes[79] SF can be described in a three-step process:

$$S_1 + S_0 \leftrightarrows : [(S_1S_0) \leftrightarrow {}^1(T_1T_1)_n] \leftrightarrows {}^1(T_1T_1) \leftrightarrows T_1 + T_1 \qquad \textit{Eq. 1.4}$$

When the coupling between $^1(S_1S_0)$ and $^1(T_1T_1)_n$ is weak and the electronic coherence is lost in a short timescale, SF can be treated as an incoherent two-electron–transfer process from (S_1S_0) to $^1(T_1T_1)$. The incoherent SF can occur without any contribution of CT state, denominated direct mechanism, or can occur mediated by CT state, known asCT-mediated mechanism (**Figure 1.1b)**.

In the direct mechanism, after the excitation of the $^1(S_0S_0)$ state of the chromophores, the $^1(S_1S_0)$ is populated as the final state. After that, a multiexciton state (ME) is formed, $^n(T_1T_1)$, dissociating into two individual triplet states $(T_1 + T_1)$.[63] In contrast to the direct mechanism, the CT-mediated SF postulates that a single electron transfer from an intermolecular excited singlet state, S_1S_0, produces a higher-lying |AC> or |CA> state, the CT state, which can strongly couple to the correlated triplet state pair, the ME state, and after dissociation leads to the triplet pair state $(T_1 + T_1)$.[80]

[78] K. Miyata, F. S. C.-Burton, F. L. Geyer, X.-Y. Zhu, *Chem. Rev.*, **2019**, *119*, 4261−4292.
[79] R. D. Pensack, E. E. Ostroumov, A. J. Tilley, S. Mazza, C. Grieco, K. J. Thorley, J. B. Asbury, D. S. Seferos, J. E. Anthony, G. D. Schole, *J. Phys. Chem. Lett.*, **2016**, *7*, 2370−2375.
[80] T. C. Berkelbach, M. S. Hybertsen, D. R. Reichman, *J. Chem. Phys.*, **2013**, *138*, 114103.

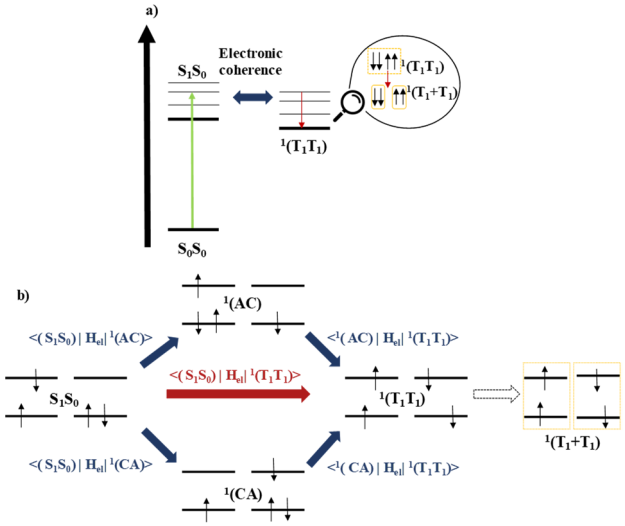

Figure 1.1- a) *Schematic kinetic model of quantum coherent mechanism.* ***b)*** *Schematic of SF incoherent mechanisms: direct mechanism illustrated by the red arrow and the mediated mechanism represented by the blue arrows, adapted of [63]. CT configurations are indicated as anion-cation $^1(AC)$ and cation-anion $^1(CA)$ spin singlets.*

In the second step of the SF, the spin-decorrelated one, the triplet pair losses its spin coupling and becomes two independent triplet states with random orientations. This step is induced by spin-dependent Hamiltonians, such as dipole-dipole interaction between electronic spins and the electron nuclear spin interaction. [81] The Hamiltonians mix the singlet-coupled triplet pair state $^1(T_1T_1)$ with the triplet $^3(T_1T_1)$ (if symmetry allowed) and the quintet-coupled $^5(T_1T_1)$ analogs.[81] In a π-stacked solid the initial correlated triplet pair is strongly coupled and the exchange interaction between both triplets is too large so the $^1(T_1T_1)$ does not mix with $^5(T_1T_1)$. In the case of a weakly coupled triplet pair $^1(T_1\cdots T_1)$ the exchange interaction is small enough for singlet quintet $^5(T_1\cdots T_1)$ mixing to happen via spin dipole-dipole interaction between the two triplets and then the direct formation of two independent triplet states occurs (**Figure 1.2**).[82]

[81] A. Japahuge, T. Zeng, *ChemPlusChem*, **2018**, *83*, 146-182.
[82] B. S. Basel, J. Zirzlmeier, C. Hetzer, B. T. Phelan, M. D. Krzyaniak, S. R. Reddy, P. B. Coto, N. E. Horwitz, R. M. Young, F. J. White, F. Hampel, T. Clark, M. Thoss, R. R. Tykwinski, M. R. Wasielewski, D. M. Guldi, *Nat. Commun.*, **2017**, *8*, 15171.

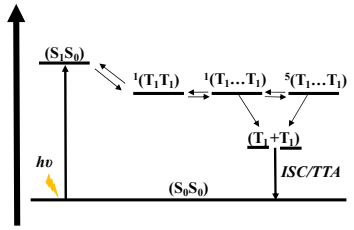

Figure 1.2- *Kinetic model of the triplet decorrelation in crystal, films, and aggregates. The mechanism of* $^{1}(T_1T_1)$ *was not considered.*

In the case of the dimers, two different possibilities are taken into account, a strongly coupled dimer and a weakly coupled dimer (**Figure 1.3**). In the first situation, the quintet state is not formed for same reason presented for the strong coupled in crystal. In the second case, quintet triplet mixing is possible the $^{3}(T_1T_1)$. However, the $^{3}(T_1T_1)$ does not facilitate the formation of the individual triplets (**Figure 1.3**).[83]

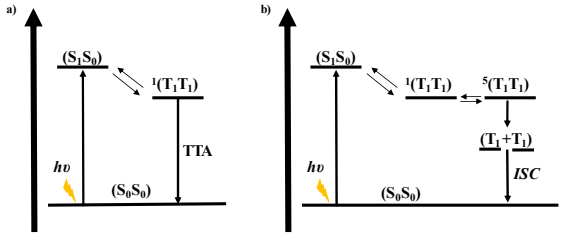

Figure 1.3- *Kinetic models of the triplet decorrelation in covalent dimers.* ***a)*** *Strongly coupled system, there is not singlet-quintet mixing.* ***b)*** *Singlet fission in a weakly coupled system singlet-quintet mixing.*

1.1.2. Singlet fission chromophores

SF can be studied in two different modalities, the intermolecular SF (interSF), that occurs in crystalline samples, and the intramolecular SF (intraSF), that can be studies in covalent dimers. The intermolecular SF was the first one to be studied using anthracene, tetracene, pentacene and hexacene crystals. However, data analysis and interpretation are complicated, and beyond that, it is impossible to control the intermolecular arrangement of chromophores in a crystalline sample. These were the reasons that boosted the intraSF study. Within these systems the orientation and the distance of the chromophores can be controlled. Moreover, in intraSF it is possible to tune the intermolecular interaction while in crystalline samples the interaction occurs through space. These advantages bring the possibility to deep understand the SF mechanism and study several chromophores

[83] M. Chena, M. D. Krzyaniaka, J. N. Nelsona, Y. J. Baea, S. M. Harveya, R. D. Schallera, M. Younga, M. R. Wasielewsk, *Proc. Natl. Acad. Sci. U.S.A.*, **2019**, *116*, 8178–8183.

that are capable to undergo SF. For example, chromophores like heteroacenes,[84] acene-thiophenes,[84] diphenylisobenzofurans,[85] , rylenesdiimides [86] and DPPs were studied in intraSF.

Several examples of DPP derivatives studied in interSF and intraSF will be presented in **Section 1.2**.

1.2. Background

1.2.1. Intermolecular singlet fission in diketopyrrolopyrroles

In 2016 Harnett explored for the first time the SF phenomena on DPP derivatives, **PhDPP**, **TDPP** and **PhTDPP** (**Figure 1.4**) [87] By transient absorption spectra, the authors observed that SF occurred only in **TDPP** and in **PhTDPP** thin films, while in **PhDPP** thin films or in disordered **TDPP** and **PhTDPP** aggregates was not observed. This conclusion is supported by the fact that triplet formation in CH_2Cl_2 solution was not detected, contrary to the rapid triplet formation in **TDPP** and **PhTDPP** films, τ_{SF}=220±50 ps and τ_{SF}=220±20 ps, respectively. The triplet yield for **PhTDPP** was 210±35% and 165±30% estimated by singlet depletion and energy transfer methods, respectively. However, for **TDPP** it was not determined the same way due to the weak transient signal. It was not clear why this signal was weak, however, the authors justified that this could be due to the lack of vibronic structure in the **TDPP** thin film. This study demonstrated also that DPP is highly sensitive to the electronic coupling between adjacent chromophores, which was correlated with the greater degree of π-overlap and closer π-stacking in **TDPP** (3.50 Å) and **PhTDPP** (3.59 Å) relative to **PhDPP** (3.90 Å).

[84] Y.-D. Zhang, Y. Wu, Y. Xu, Q. Wang, K. Liu, J.-W. Chen, J.-J. Cao, C. Zhang, H. Fu, H.-L. Zhang, *J. Am. Chem. Soc*., **2016**, *138*, 6739−6745.
[85] J. C. Johnson, A. J. Nozik, J. Michl, *J. Am. Chem. Soc.*, **2010**, *132*, 16302-16303.
[86] a) C. Mauck, K. Brown, N. Horwitz, M. R. Wasielewski, *J. Phys. Chem. A*, **2015**, *119*, 5587–5596. b) S. W. Eaton, L. E. Shoer, S. D. Karlen, S. M. Dyar, E. A. Margulies, B. S. Veldkamp, C. Ramanan, D. A. Hartzler, S. Savikhin, T. J. Marks, et al., *J. Am. Chem. Soc.,* **2013**, *135*, 14701–14712. c) A. K. Le, J. A. Bender, S. T. Roberts, B. J. A. Le A. K. Roberts S. T., J. A. B. Aaron, K. Le Sean T. Roberts, *J. Phys. Chem. Lett.,* **2016**, *7*, 4922–4928. d) K. Nagarajan, A. R. Mallia, V. S. Reddy, M. Hariharan, *J. Phys. Chem. C*, **2016**, *120*, 8443–8450. e) Y. V. Aulin, K. M. Felter, D. D. Günbas, R. K. Dubey, W. F. Jager, F. C. Grozema, *Chempluschem*, **2018**, *83*, 230–238. f) A. K. Le, J. A. Bender, D. H. Arias, D. E. Cotton, J. C. Johnson, S. T. Roberts, *J. Am. Chem. Soc.,* **2018**, *140*, 814–826. g) C. Schierl, A. Niazov-Elkan, L. J. W. Shimon, Y. Feldman, B. Rybtchinski, D. M. Guldi, *Nanoscale,* **2018**, *10*, 20147–20154.
[87] P. E. Hartnett, E. A. Margulies, C.M. Mauck, S. A. Miller, Y. Wu, Y. L. Wu, T. J. Marks, M. R. Wasielewski, *J. Phys. Chem. B*, **2016**, *120*, 1357−1366.

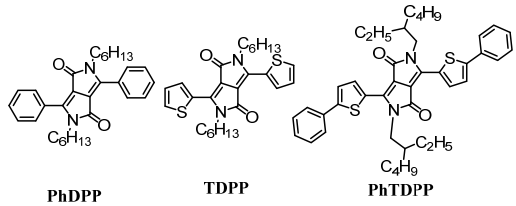

Figure 1.4- *Chemical structures of* ***PhDPP****,* ***TDPP*** *and* ***PhTDPP****.*

The same group later synthesized several thiophene-DPP derivatives with different aliphatic chains at the 2,5-positions of the DPP, namely methyl (**Me**), n-hexyl (**C6**), triethylene glycol (**TEG**), and 2-ethylhexyl (**EH**), and studied the influence of excimers on the SF process (**Figure 1.5**).[88] The different intermolecular packing produced a variable intermolecular charge transfer interaction in thin films. SF from the eximers state of **Me**, **C6**, **TEG** and **EH** were τ_{SF}=22, 336, 195 and 1200 ps, respectively giving a triplet yield of 200%, 110%, 110% and 70%, respectively.

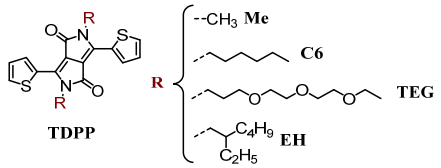

Figure 1.5- *Chemical structures of* ***Me****,* ***C6****,* ***TEG*** *and* ***EH****.*

In 2017, SF in **PhTDPP** nanoparticles in water was reported (**Figure 1.4**). Having observed that the SF process was faster in small **PhTDPP** nanoparticles, due to the higher surface area volume ratio, which allows more molecules to be exposed to the high dielectric aqueous environment.[89] The author attributed the dependence of the nanoparticles size with the speed of the SF process to the dielectric stabilization of a high-lying virtual charge transfer state, which engages in an increased superexchange interaction with the $^1(S^1S^0)$ and $^1(T^1T^1)$ states. However, it was also concluded that the greater the domain of nanoparticles, the more easily triplet excitons can diffuse away, thus yielding the longest lifetimes in the largest nanoparticles.

Li designed several DPP derivatives with varied aromatic substitution (**Figure 1.6**).[90] After this intensive study, the author concluded that a good DPP-based in SF sensitizer should have one or two aromatic rings bearing weak electron-donating or withdrawing substituents, like F, Cl and Me.

[88] C. M. Mauck, P. E. Hartnett, E. A. Margulies, L. Ma, C. E. Miller, G. C. Schatz, T. J. Marks, M. R. Wasielewski, *J. Am. Chem. Soc.*, **2016**, *138*, 11749−11761.
[89] C. M. Mauck, P. E. Hartnett, Y.-L. Wu, C. E. Miller, T. J. Marks, M. R. Wasielewski, *Chem. Mater.*, **2017**, *29*, 6810−6817.
[90] L. Shen, Z. Tang, X. Wang, H. Liu, Y. Chen, X. Li**,** *Phys. Chem. Chem. Phys.*, **2018**, *20*, 22997-23006.

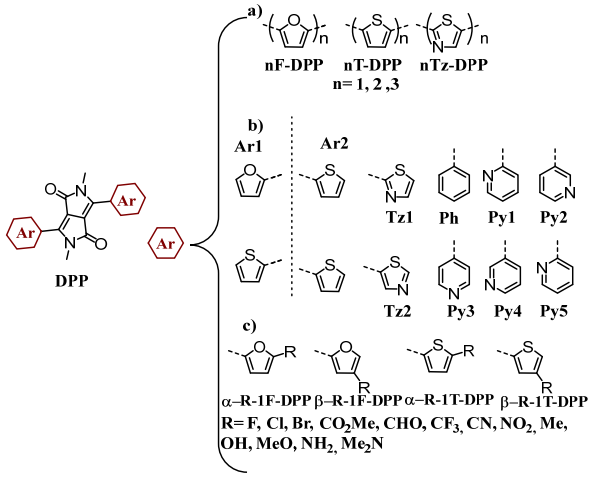

Figure 1.6- *Chemical structures of the compounds described by Li.*

More recently, Braunschweig described six DPP-rylene thin film superstructures, making different mixtures of one out of two DPP and three rylenes (**Figure 1.7**).[91] The six superstructures were assembled by orthogonal H-bonding and π-π stacking. The solid-state packing of the compounds undergo SF. Consistent results with a quasi-selective excitation of DPP were obtained. fsTA and nsTA spectroscopies of the thin films and the monomers in solution, and triplet-triplet sensitization experiments demonstrated that the DPPs undergo SF and subsequent triplet decorrelation via exciton diffusion through the heterosuperstructures.

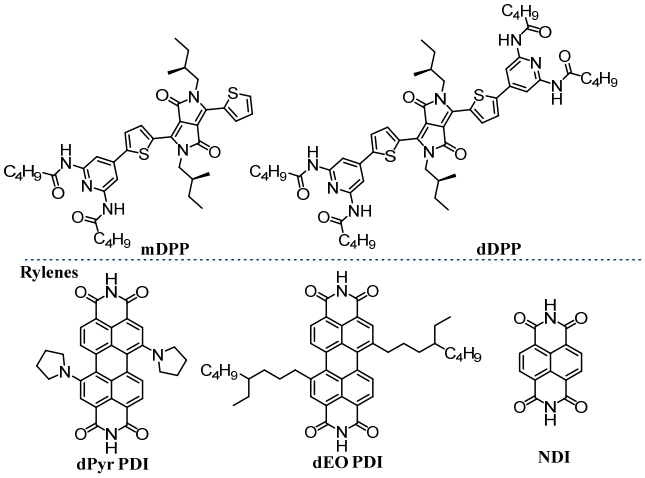

Figure 1.7- *Structure of the DPP and the rylenes.*

[91] A. M. Levine, C. Schierl, B. S. Basel, M. Ahmed, B. A. Camargo, D. M. Guldi, A. B. Braunschweig, *J. Phys. Chem. C*, **2019**, *123*, 1587−1595.

1.2.2. Intramolecular singlet fission in diketopyrrolopyrroles

As previously mentioned, DPP can undergo intermolecular SF thanks to the charge transfer character of their excitations, making them also possible candidates for intramolecular SF. There are more studies dealing with interSF in monomers than with intraSF in dimers. Nevertheless, the following two works describe DPPs undergoing intraSF.

Patil described the design of two thiopheneDPP molecules with a vinyl bridge to control the interchromophoric coupling (**Figure 1.8**).[92] The interaction between the two DPP was observed by UV-vis analysis, while photoluminescence spectroscopy showed a non-emissive character. The transient absorption measurements were performed on **TDPP-V-TDPP** in solution and in one polystyrene matrix. In both cases an initial "bright" excited state appeared rapidly decaying to a dark and extremely short-lived $2A_g$ type singlet. No triplet or charge formation were observed, maybe due to a conformational change driving the rapid excited-state deactivation.

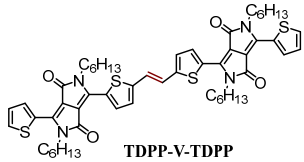

TDPP-V-TDPP

Figure 1.8- *Structure of the* ***TDPP-V-TDPP****.*

This study did not allow to report a triplet state for this compound while opening the doors for further studies on DPPs undergoing intramolecular SF. Wasielewski described a system with two thiopheneDPP derivative linked to a 2,7-di-*tert*-butyl-9,9-dimethylxanthene (XAN), **DPP-Xan-DPP**, which conferred a cofacial arrangement to the compound (**Figure 1.9**).[93] The π-π interaction between the two chromophores mediated by the bridge mimic the interchromophor interaction in thin films. In all tested solvents, the authors observed a pseudoequilibrium between S_1S_0 and the charge transfer state, which leads to monomer-like fluorescence. However, the formation of either the $^1(T_1T_1)$ or free triplet state for the dimer was not observed.

[92] T. Mukhopadhyay, A. J. Musser, B. Puttaraju, Joydeep Dhar, R. H. Friend, S. Patil, *J. Phys. Chem. Lett.,* **2017**, *8*, 984-991.
[93] C. M. Mauck, Y. J. Bae, M. Chen, N. P.-Riggs, Y.-L. Wu, M. R. Wasielewski, *ChemPhotoChem*, **2018**, *2*, 223-233.

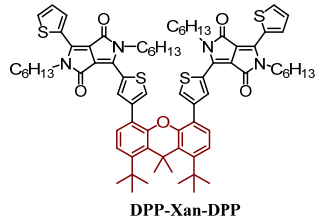

Figure 1.9- *Chemical structure of* ***DPP-Xan-DPP****.*

1.3. Goal

The improvement of renewable energies, especially photovoltaics, is one of the most urgent challenges of the mankind.

Therefore, previously explained, SF could be a very interesting way for solar cell improvement. For this reason, and inspired by the two previous reports, we propose the synthesis of three DPP dimers, linked via different dithienylphenylene spacers, ***ortho*-DPP 1**, ***para*-DPP 2** and ***meta*-DPP 3** (**Figure 1.10**), to study their ability to generate intramolecular SF. Thus, we intend to study the influence of the position of one DPP in relation to the other.

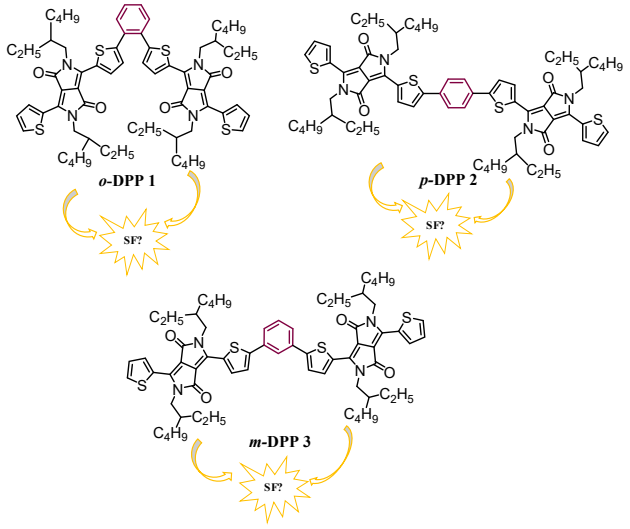

Figure 1.10- *Representative image of the objectives of this chapter.*

The SF studies were carried out by Prof. Dr Dirk M. Guldi and Prof. Dr. Timothy Clark of the Department of Chemistry & Pharmacy, Interdisciplinary Center for Molecular Materials (ICMM), Friedrich-Alexander-Universität Erlangen-Nürnberg (FAU) and the theoretical studies were developed by Prof. Dr. Paul A. Keller of the School of Chemistry & Molecular Bioscience, Molecular Horizons, Illawarra Health & Medical Research Institute, University of Wollongong.

1.4. Results and discussion

1.4.1. Synthesis and characterization of the intermediate compounds

The target compounds were successfully obtained as indicating in the following. Intermediates compounds were synthetized following reported procedures and characterized by ^{1}H NMR. The first step was to obtain **DPP 4** by the succinic ester route, as described in **Scheme 1.1**.[94]

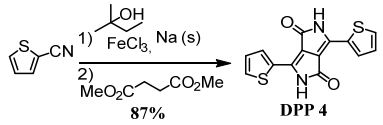

Scheme 1.1- *Synthetic route to* ***DPP 4****.*

In the presence of sodium metal and *tert*-amyl alcohol, in a process that can take up to 12 hours, sodium amylate was obtained *in situ*, which reacts with 2-thiophenenitrile and with dimethyl succinate giving **DPP 4** in 87% yield as a red-marron solid, which is insoluble in the common volatile organic solvents. The ^{1}H NMR shows two doublets of doublets and one triplet belonging to the thiophene units and one singlet corresponding to the NH of the lactams (**Figure 1.11**). The product was used for the next reactional step without more purification than two washes with hot water and acidic methanol.

[94] A. T. Yiu, P. M. Beaujuge, O. P. Lee, C. H. Woo, M. F. Toney, J. M. J. Frechet, *J. Am. Chem.Soc.*, **2012**, *134*, 2180−2185.

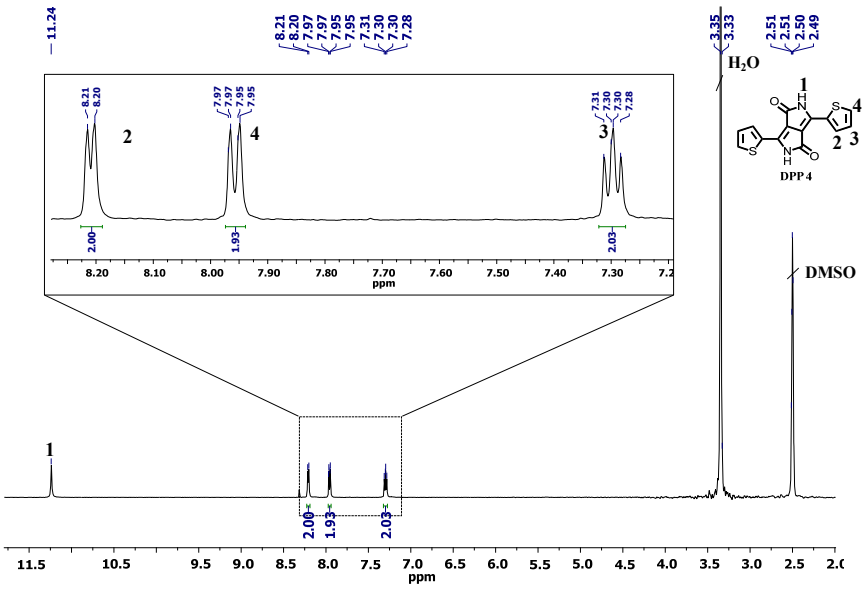

Figure 1.11- a) *^{1}H NMR of **DPP 4** in DMSO-d_6 at 25°C and the respective chemical structure.* ***b)*** *^{1}H NMR zoom in the aromatic zone.*

The second step was the *N*-alkylation to form **DPP 5**, reaching a maximum yield of 49%.[95] The yield of this reaction was not as good as expected due to *O*-alkylation side reaction which competes with the intended *N*-alkylation. Some changes in the reaction conditions were made in order to achieve the best yield, namely, various bases were tested such as NaH (29%), K_2CO_3 (20%), Cs_2CO_3 (49%), change of the reaction solvent (DMF or NMP) and the temperature. However, the best conditions were obtained using DMF as the solvent, Cs_2CO_3 as a base at 110 °C (**Scheme 1.2**) obtaining the product in a purple-red solid. The alkyl chains dramatically increased the solubility of the DPP.

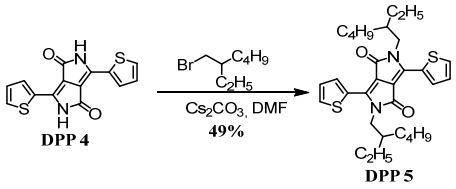

Scheme 1.2- *Synthetic route to **DPP 5**.*

DPP 5 was characterized by ^{1}H NMR in $CDCl_3$ (**Figure 1.12**). The spectrum showed some differences in the chemical shifts of the aromatic protons when compared to **DPP 4** due to the change of solvent. However, the most notable differences were the presence of four protons in the aliphatic zone, that belong to

[95] L. Huo, J. Hou, H.-Y. Chen, S. Zhang, Y. Jiang, T. L. Chen, Y. Yang, *Macromolecules*, **2009**, *42*, 6564–6571.

the aliphatic chains. These signals did not show good resolution because the ethylhexyl chain is a racemic mixture and therefore all the signals appeared in the form of multiplets. The first signal appears at 4.09-3.96 ppm, which was attributed to **H1**. The second one at 1.86-1.84 ppm corresponds to **H2** which fits perfectly because this signal integrates for 2 protons. The **H3** and **H4** protons appeared at 1.38-1.22 ppm and 0.90-0.83 ppm, respectively.

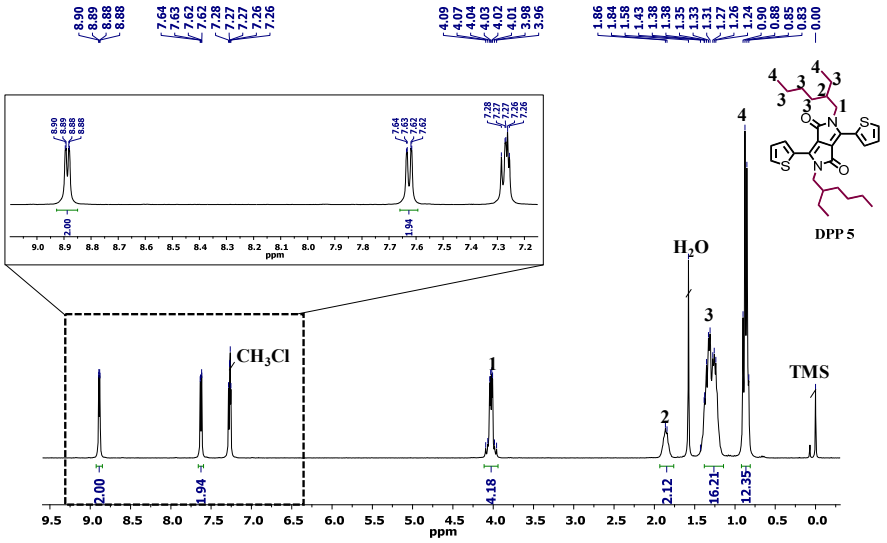

Figure 1.12-a) *^{1}H NMR of* ***DPP 5*** *in $CDCl_3$ at 25 °C and the chemical structure.* ***b)*** *^{1}H NMR zoom in the aromatic zone.*

The last step before the final coupling was an electrophilic aromatic substitution on **DPP 5** using *N*-bromosuccinimide (NBS), which gave rise to 3-monobrominated **DPP 6** with a 45% yield (**Scheme 1.3**).

Due to the low solubility of NBS in chloroform, it had to be dissolved in the minimum amount of acetic acid. Thus, **DPP 5** was dissolved in chloroform with 1 mL of acetic acid and then the NBS was added dropwise to the previous solution at 0 °C, protecting the system from light. **DPP 5** has two positions with the same reactivity that can be brominated, for this reason, under these conditions, a mixture of monobromo **DPP 6**, dibromoDPP (**DPP 7**) and unreacted **DPP 5** was obtained. **DPP 6** was characterized by ^{1}H NMR and the chemical shifts coincided with those described in the bibliography.[96]

[96] D. Sahu, C.-H. Tsai, H.-Y. Wei, K.-C. Ho, F.-C. Chang, C.-W. Chu, *J. Mater. Chem.*, **2012**, *22*, 7945–7953.

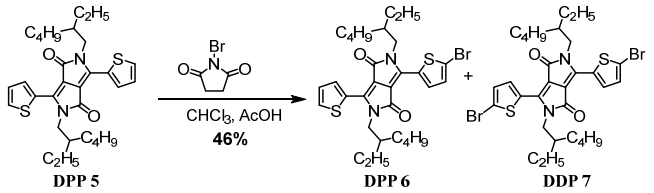

Scheme 1.3- *Synthesis of* ***DPP 6****.*

Comparing **DPP 5** and **DPP 6** spectra it was possible to verify the appearance of two new doublets at 8.62 ppm and 7.23 ppm belonging to the protons **H4** and **H5**, respectively, indicating the disappearance of symmetry in **DPP 6** by the introduction of one bromo substituent (**Figure 1.13**). In turn, the proton of the monosubstituted thiophene ring in **DPP 6** did not show considerable variation in chemical shifts when compared with the **DPP 5** chemical shift values.

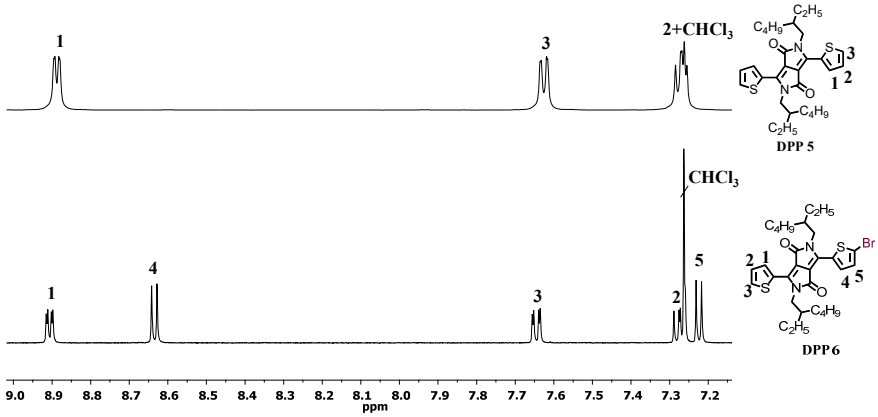

Figure 1.13- *^{1}H NMR of* ***DPP 5*** *and* ***DPP 6*** *in $CDCl_3$ at 25 °C and the chemical structure.*

In addition to the DPP intermediates, boronic ester **8b** was also prepared so that the desired **DPP 2** could be synthesized. **Scheme 1.4** shows the synthesis, which was reproduced in the same way as described in the literature.[97] 1,4-phenylenediboronic acid was condensed with propane-1,3-diol in toluene giving rise the desire compound with a 76% yield. The ^{1}H NMR spectrum of compound **8b** was identical with the spectrum described in the literature (**Figure 1.14**).

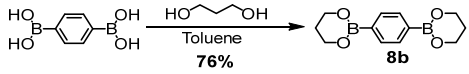

Scheme 1.4- *Synthetic route for compound* ***8b.***

[97] a) K. Watanabe, Z. Sun, K. Akagi, *Chem. Mater*., **2015**, *27*, 2895−2902.

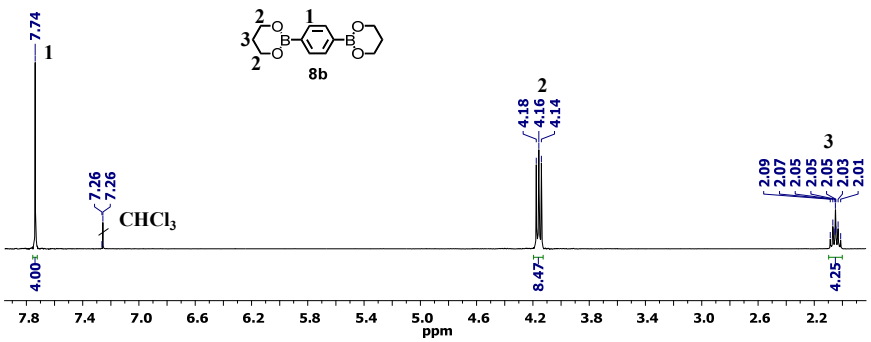

Figure 1.14- *^{1}H NMR of compound **8b** in $CDCl_3$ at 25 °C and the chemical structure.*

1.4.2. Synthesis and structural characterization of the DPP dimers

The dimers ***o*-DPP 1**, ***p*-DPP 2** and ***m*-DPP 3** were obtained by a Suzuki-Miyaura coupling between **DPP 6** and the boronic esters **8a**, **8b** [97] and **8c**, in 53%, 36% and 43% yield, respectively (**Scheme 1.5**).

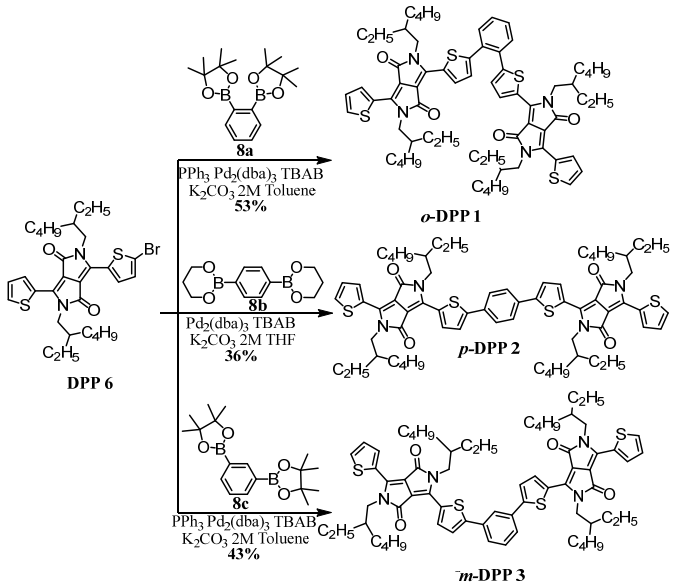

Scheme 1.5-*Synthetic route of **o-DPP 1**, **p-DPP 2** and **m-DPP 3**.*

***p*-DPP 2** was previously synthesized by a Suzuki-Miyaura coupling[98] and an analogue with a different alkyl chain by a direct heteroarylation.[99]. Comparing the yields of the Suzuki-Miyaura reaction described in the literature (45%) and the one

[98] D. Yu, Y. Liu, M. Xiao, Q. Fan, W. Su, X. Li, H. Tan, Y. Wang, R. Yang, W. Zhu, *Dyes Pigm.*, **2016**, *125*, 151-158
[99] S.-Y. Liu, D.-G. Wang, A.-G. Zhong, H.-R. Wen, *Org. Chem. Front.* **2018**, *5*, 653–661.

developed in this work (36%), it appears that we obtained lower yields, which may be due to the use of a different palladium catalysts [tetrakis(triphenylphosphine)palladium ($Pd(PPh_3)_4$ was used in the literature], a different boronic esters or even by experimental conditions. For the synthesis of ***o*-DPP 1** and ***m*-DPP 3** dimers, PPh_3 was used as a ligand to form the $Pd(PPh_3)_4$ *in situ*, and the tetramethyl boronic ester was used. With these changes the yields improved compared to ***p*-DPP 2** yield. The three dimers showed good solubility in common organic solvents, such as toluene, CH_2Cl_2, $CHCl_3$ and chlorobenzene. All dimers were completely characterized by ^{1}H-NMR (**Figure A1**, **A4** and **A6**), ^{13}C NMR (**Figure A2** and **A7**), UV-vis (**Figure 1.17**), FT-IR (**Figure A3**, **A5** and **A8**) spectroscopies and by MALDI-TOF mass spectrometry (**Figure 1.16**). ^{13}C-NMR of the ***p*-DPP 2** was not acquired because it was already described in the literature. The analysis of the ^{1}H NMR spectra of the three dimers showed some differences, namely in the protons of the benzene rings, **Figure 1.15** shows the comparison of the ^{1}H NMR spectra of the three compounds. ***p*-DPP 2** is a symmetrical compound so, for that, and as expected, only one singlet at 7.73 ppm corresponding to the benzene ring appeared. In the case of ***o*-DPP 1** there were two signals centered at 7.50-7.47 ppm and 7.15 ppm, belonging to **HB** and **HA**, respectively. Finally, in ***m*-DPP 3** spectrum, two resonances corresponding to the three distinct protons of the benzene ring appeared. At 7.93 ppm a signal belonging to **HA** can be observed and at 7.53-7.49 ppm a multiplet corresponding to the two protons **HB** and **HC**.

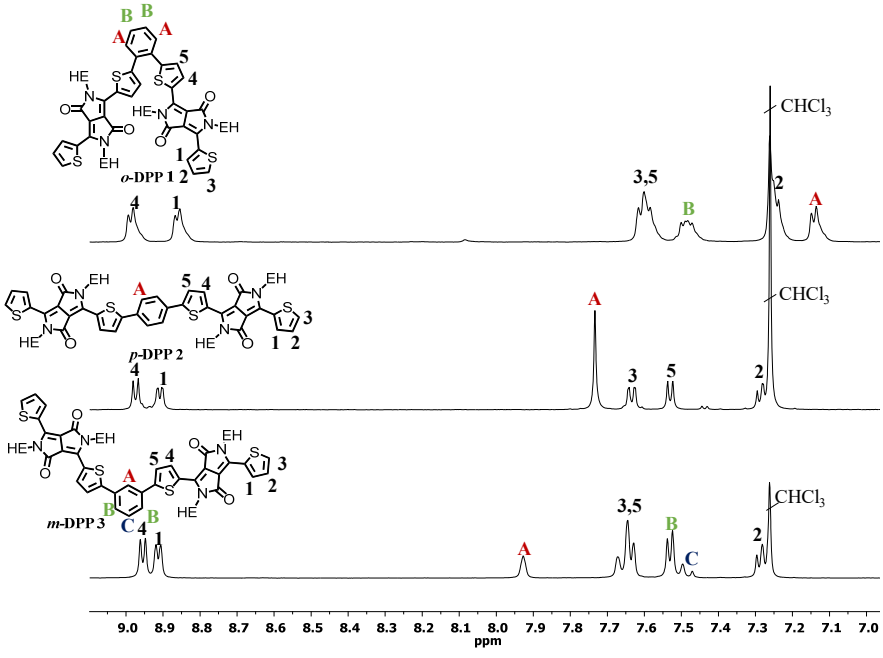

Figure 1.15- *Expansion of ^{1}H NMR in the aromatic zone of the three dimers,* ***o-DPP 1****,* **p-*DPP 2*** *and* **m-*DPP 3*** (CDCl$_3$ at 25 °C), EH= ethylhexyl chain.

Beyond the NMR spectra, the theoretical isotopic pattern of the molecular ion, $[M]^-$, for the three compounds also coincides with the experimental isotopic pattern (**Figure 1.16**).

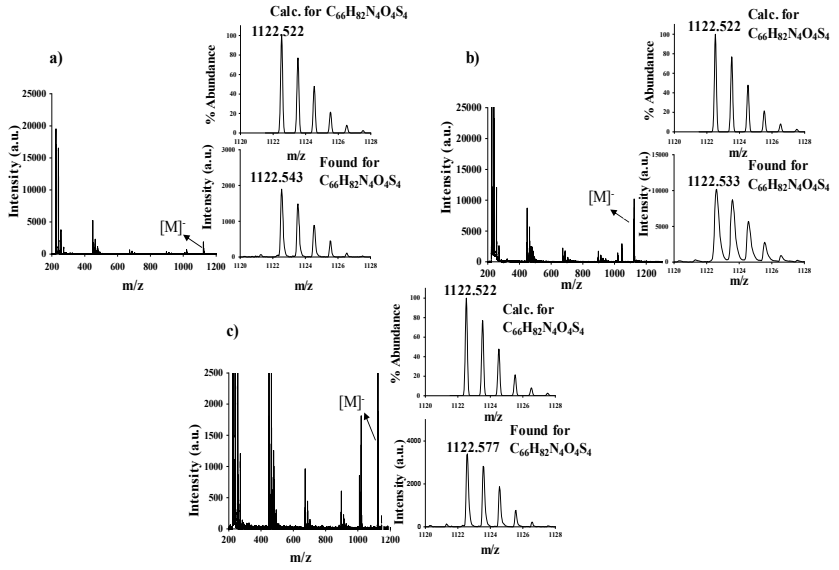

Figure 1.16- *HR-MALDI-TOF of* ***a) o-DPP 1***, ***b) p-DPP 2*** *and* ***c) m-DPP 3****. The peaks that appear in the range between 200-1010 are dithranol used as a matrix.*

The ground-state of the DPPs was explored through the study of the UV-vis spectra (**Figure 1.17**) and the optical parameters are summarized in **Table 1.1**. They were studied in two solvents with different polarities (toluene and benzonitrile) in order to investigate the influence on SF mechanism and its dynamics. In this Thesis only the results in toluene will be presented since the results in benzonitrile are similar, although in some cases it will be necessary to compare the two solvents.

Figure 1.17a present the UV-vis spectra in toluene solution of **DPP-Ref**[100], ***o*-DPP 1**, ***p*-DPP 2** and ***m*-DPP 3** in order to do a comparison among them. The dimers and **DPP-Ref** revealed several differences in their UV-vis spectra. The spectrum of **DPP-Ref** showed a set of well-resolved maxima between 400 and 600 nm, which represent the transitions to the lowest singlet excited states. In addition, maxima were seen between 300 and 400 nm, representing the corresponding transitions to higher singlet excited states.

In the spectrum of ***o*-DPP 1** two peaks with the same intensity could be observed, they were reminiscent of the absorption pattern of H-aggregates, suggesting sizeable interactions between the two DPPs. Besides that, a red-shift of roughly 20

[100] From this part on **DPP 5** will be called **DPP-Ref** because it was the reference used to compare with the dimers.

nm could be appreciated. ***p*-DPP 2** exhibited broad and featureless absorption peaks, which were roughly 60 nm red-shifted compared to **DPP-Ref**. Finally, the shape of the ***m*-DPP 2** spectrum is more like the shape of the **DPP-Ref** spectrum, despite the observation of a 30 nm red-shift. A smaller molar extinction coefficient was obtained for **DPP-Ref** (30000 $M^{-1}cm^{-1}$) while for dimers values of 65000 $M^{-1}cm^{-1}$, 96000 $M^{-1}cm^{-1}$ and 93000 $M^{-1}cm^{-1}$ were determined for ***o*-DPP 1**, ***p*-DPP 2** and ***m*-DPP 3**, respectively. In the case of optical absorption spectra in film (**Figure 1.17b**), the maximum absorption peaks for ***p*-DPP 2**, ***m*-DPP 3** and ***o*-DPP 1** were at 613 nm, 577 nm and 583 nm, respectively. Comparing these maximum peak values with the solution values, it was possible to observe that ***o*-DPP 1** suffered a larger red shift, 12 nm, while ***p*-DPP 2** and ***m*-DPP 3** did not shift significantly. In the spectrum of ***p*-DPP 2** appeared an additional shoulder at 681 nm which is indicative of a strong intermolecular packing in solid state.[101]

To provide a first look at the differences in the excited state, steady-state fluorescence measurements were made. For **DPP-Ref**, the fluorescence maximum lies between 500 and 750 nm with a fluorescence quantum yield (FQY) of 69.5% in toluene and 66.7% in benzonitrile. All the dimers underwent hypsochromic shifts, which coalesced with respective shifts seen in the absorption measurements (**Figure 1.17c**), and a significant FQY quenching. ***p*-DPP 2** suffered the strongest quenching presenting a FQY of 1.4%, while ***o*-DPP 1** presented a FQY of 12.1%. The ***m*-DPP 3** FQY was 46.6% suggesting moderated inter-DPP interactions. In contrast to **DPP-Ref,** changing the solvent from toluene to benzonitrile resulted in a further FQY quenching: 5.3% (***m*-DPP 3**), 2.1% (***o*-DPP 1**), 1.2% (***p*-DPP 2**).

[101] D. Yua, Y. Liu, M. Xiao, Q. Fan, W. Su, X. Li, H. Tan, Y. Wang, R. Yang, W. Zhu, *Dyes Pigm.*, **2016**, *125*, 151-158.

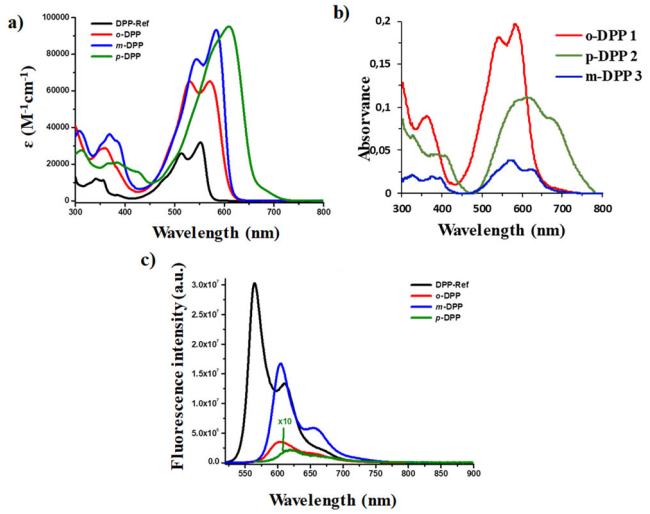

Figure 1.17- a) *Room-temperature absorption spectra of* ***DPP-Ref*** *(black),* ***o-DPP 1*** *(red),* ***p-DPP 2*** *(green) and* ***m-DPP 3*** *(blue), in toluene. b) Room-temperature absorption spectra of* ***DPP-Ref*** *(black),* ***o-DPP 1*** *(red),* ***p-DPP 2*** *(green) and* ***m-DPP 3*** *(blue) in film. c) Fluorescence spectra in toluene following photoexcitation at 545 nm for* ***o-DPP 1*** *and* ***m-DPP 3****, 550 nm for* ***p-DPP 2,*** *and 505 nm for* ***DPP-Ref****.*

Table 1.1- *Optical parameters of* ***DPP-Ref*** *and the dimers in toluene.*

Compound	$\lambda_{abs}^{solution}$/ λ_{abs}^{film} (nm)	ε ($M^{-1}cm^{-1}$)	λ_{em} (nm)	FQY (%)
DPP-Ref	552/-	31 900	565	69.5
***o*-DPP 1**	571/583	65 200	604	12.1
***p*-DPP 2**	610/613	96 150	618	1.4
***m*-DPP 3**	584/577	93 300	605	46.6

The steady-state absorption and fluorescence measurements indicated that for ***o*-DPP 1** the intensity of the absorption spectra increase was accompanied by a quenched FQY, when compared to **DPP-Ref**. Such trends were in line with intramolecular forces between slightly displaced, parallel arranged DPPs as in H-type aggregates. The solvent dependent FQYs suggested an excited state deactivation involving either the formation of a CT or a CS state. Involvement of a CT/CS state induces red-shift in the H-type aggregates, which usually feature blue-shifts.[102] Similarly, a deactivation via CT and/or CS states in H-aggregates were reported when a xanthene bridge was employed in DPP-dimers.

[102] a) H. Yamagata, C. M. Pochas, F. C. Spano, *J. Phys. Chem. B*, **2012**, *116*, 14494−14503; b) N. J. Hestand, F. C. Spano, *Chem. Rev.*, **2018**, *118*, 7069−7163.

For ***p*-DPP 2**, the broadened absorption parallels with the most strongly quenched fluorescence among the DPP-dimers. Again, the quenched and, more importantly, the solvent dependent, albeit weak, FQYs suggested the involvement of either a CT or a CS state. The broadening of the absorption features was attributed to the free and unhindered rotation of the DPPs, due to the minimal steric interaction of the *para*-position. Finally, for ***m*-DPP 3** both absorption and fluorescence resemble to what was seen for the **DPP-Ref**. The overall strength of the interaction was expected to be the weakest among the DPP-dimers, as the phenyl linker asserts better electronic communication in case of *ortho*- and *para*-substitutions.[103]

Electrochemical properties of the three dimers were examined by cyclic voltammetry (CV) using CH_2Cl_2 as solvent containing 0.1 M tetrabutylammonium hexafluorophosphate ($TBAPF_6$) as supporting electrolyte (**Figure 1.18**, **Table 1.2**).

A similaritud in the band gaps of all dimers were observed owing to the fact that the electron donor and the acceptor fragments are the same. However, ***p*-DPP 2** had the lowest E_g^{cv} among the three different dimers, due to their push-pull structure. **DPP-Ref** presented the largest bandgap with a value of 2.2 eV when compared to the DPP-dimers, which are between 2.0 and 2.1 eV.

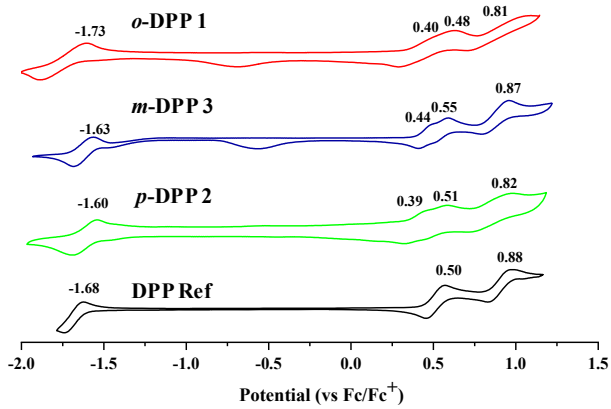

Figure 1.18. *Cyclic voltammograms of* ***o-DPP 1***, ***p-DPP 2***, ***m-DPP 3***, *and* ***DPP-Ref*** *in* CH_2Cl_2 *containing 0.1 M* $TBAPF_6$ *as supporting electrolyte and measured against* Fc/Fc^+.

[103] N. V. Korovina, J. Joy, X. Feng, C. Feltenberger, A. I. Krylov, S. E. Bradforth, M. E. Thompson, *J. Am. Chem. Soc.*, **2018**, *140*, 10179−10190.

Table 1.2. *Electrochemical parameters of* ***o-DPP 1****,* ***p-DPP 2****,* ***m-DPP 3*** *and* ***DPP-Ref****.*

Compound	E_{red1} (eV)	E_{oxi1} (eV)	$E_{g,opt}$[a]/$_{EC}$[b] (eV)	HOMO[c]	LUMO[d]
***o*-DPP 1**	-1.73	0.40	2.11/2.03	-5.20	-3.17
***p*- DPP 2**	-1.60	0.39	2.02/1.99	-5.19	-3.20
***m*-DPP 3**	-1.63	0.44	2.09/2.07	-5.24	-3.17
DPP-Ref	-1.68	0.50	2.23/2.18	-5.30	-3.12

The energy positions of the HOMOs were estimated from the onset values for the oxidation potentials: a) $E_{g,opt}$ (eV) was determined from the intersection of normalized absorption and emission spectra registered in CH_2Cl_2. b) $E_{g,EC}=E_{red1} - E_{oxi1.}$ c) $HOMO=-|E_{ox1}(vs.\ Fc/Fc^{+}) + 4.8|$. d) The LUMO values were calculated by $LUMO=HOMO+ E_{g,EC}$ (eV).

In order to study the singlet fission phenomena in the DPP dimers, spectroelectrochemical (SEC) and time-resolved transient absorption spectroscopy on the femto- (fsTAS) and nanosecond (nsTAS) timescales techniques were used in order to understand what happen when a compound absorbs a photon.

Regarding SEC, the study was based on the optical properties of DPP after one-electron reduction reduction and oxidation. A toluene/acetonitrile mixture (4/1 v/v) with 0.1 M $TBAPF_6$ as supporting electrolyte were the conditions used to perform these experiments. The result of this study was similar for the three dimers. Analyzing only the case of ***o*-DPP 1**, when a positive potential of +1.0 V was applied, it resulted in fully reversible spectroscopic features of its one-electron oxidized form in the 650 to 1000 nm range with maxima at 780 and 900 nm. However, when a negative potential of -1.5 V was applied, it resulted in the formation of its semi-stable one-electron reduced form with only a single maximum at approximately 480 nm, that was superimposed with the ground state absorption (**Figure 1.19**).

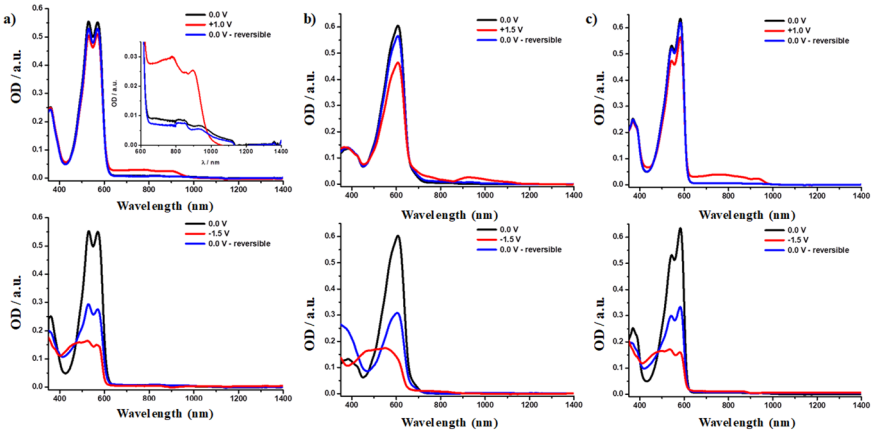

Figure 1.19. *Spectroelectrochemical features of the (**a**-up) one-electron oxidized and (**a**-down) one-electron reduced forms of **o-DPP 1**; (**b**-up) one-electron oxidized and (**b**-down) one-electron reduced forms of **p-DPP 2**; (**c**-up) one-electron oxidized and (**c**-down) one-electron reduced forms of **m-DPP 3**.*

The time-resolved transient absorption spectroscopy on the femto- (fsTAS) and nanosecond (nsTAS) timescales technique consists of sending two laser pulses through the sample. The first one gives rise to the excitation of the molecule and the second one, with a low energy that prevents the excitation of the molecule, is sent after a certain time to evaluate the excitation or relaxation processes obtained from the first pulse. Lasers used range from femtoseconds to nanoseconds. The experiments were conducted at excitation wavelengths of 530 nm (lifetimes were obtained using GloTarAn target analyses). The use of solvents with different polarities (toluene and benzonitrile) led to different results with the same sample, *vide infra*.

In the case of **DPP-Ref**, a simple and similar kinetic model was obtained for both solvents. After the excitation, the excited state S1 started to be populated, however an increase in the solvation energy led to the formation of the $(S_1)_{solv}$ state and after a reorganization the ground state was recovered (**Figure 1.20**).

In the case of dimers different results were obtained with toluene and benzonitrile. In toluene similar results were obtained for the three derivatives. The same initial singlet excited state (S_1S_0) was observed with lifetimes of 9.9, 15.5 and 7.8 ps for ***o*-DPP 1**, ***p*-DPP 2**, and ***m*-DPP 3**, respectively. The solvent reorganization lead to the formation of a new state, the $(S_1S_0)_{Sol}$ with lifetimes of 576 ps (***o*-DPP 1**), 372 ps (***m*-DPP 3**), and 77 ps (***p*-DPP 2**). These shorter lifetimes reflected the strength of intramolecular DPP-interactions in the dimers. In addition to these two states the ***o*-DPP 1**, ***p*-DPP 2**, and ***m*-DPP 3** populate yet another third state, corresponding

to the CT state [$(S_1S_0)_{CT}$], and lead to the quantitative ground-state recovery.[104] So, in toluene was not appreciable any triplet excited state. The only notable differences between the dimers were the shifts in the ground state bleach (GSB) and selective excitation (SE) features.

On the other hand, the results changed significantly when the study was made in benzonitrile. The values of FQYs showed the strong impact of solvent polarity, suggesting a subtle interplay between the different states in the excited state deactivation of the dimers. In the case of ***p*-DPP 2** no triplet excited state was populated, however, the strong SEC signal and the low FQY value inferred a symmetry-breaking charge separation (SBCS) state instead of CT formation. The SBCS acted as a trap that prevented the infraSF.

Regarding ***o*-DPP 1** and ***m*-DPP 3** derivatives, both possessed a triplet excited state character, $^1(T_1T_1)$ and (T_1+T_1), corroborating intraSF. The analysis of GloTarAn target analysis was necessary as the triplet excited state was overlapped with their GSB, making it difficult to determine TQYs. Nevertheless, TQYs of 40% and 11% for ***o*-DPP 1** and ***m*-DPP 3**, respectively, were determined. ***m*-DPP 3** presented lower TQYs perhaps due to weaker electronic communication of the DPP in *meta*-position. So, the increase of solvent polarity allowed to stabilize the intermediate $(S_1S_0)_{CT}$ and allowed the triplet states being populated in ***o*-DPP 1** and ***m*-DPP 3**.

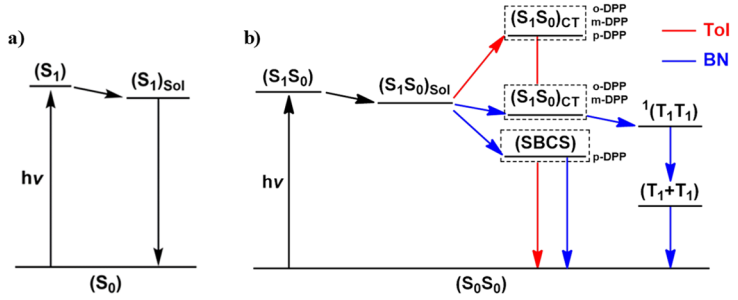

Figure 1.20. a) *Kinetic model used to fit the transient absorption data of* ***DPP-Ref*** *in toluene and benzonitrile.* ***b)*** *Kinetic models used to fit the transient absorption data of the dimers in toluene (red) and benzonitrile (blue).*

[104] M. Chen, Y. J. Bae, C. M. Mauck, A. Mandal, R. M. Young, M. R. Wasielewski, *J. Am. Chem. Soc.*, **2018**, *140*, 9184−9192.

1.5. Conclusions

A set of three dimers of DPP linked via dithienylphenylene spacers in different positions (***o*-DPP 1**, ***p*-DPP 2**, and ***m*-DPP 3**), was synthesized, characterized, and examined in light of intraSF.

A synthetic 5-step reaction pathway was used in which the last step was a Suzuki-Miyaura coupling allowing the coupling between **DPP 6** and the boronic esters **8a**, **8b** and **8c**, thus obtaining the desired compounds with yields of 53%, 36% and 43% for ***o*-DPP 1**, ***p*-DPP 2** and ***m*-DPP 3**, respectively.

The structures and properties of these materials were analyzed by usual techniques such as ^{1}H and ^{13}C NMR, mass spectrometry, UV-vis and fluorescence emission and the LUMO and HOMO values were calculated from cyclic voltammetry. In addition, time-resolved transient absorption spectroscopy and the spectroelectrochemistry were also used.

Steady-state absorption and fluorescence measurements indicated the involvement of a charge-transfer and/or charge-separated state along the SF-cascade with a strong dependence on solvent polarity. For ***o*-DPP 1** the increase of absorption intensity was accompanied by a quenched FQY comparing with **DPP-Ref**. For ***p*-DPP 2**, the broadened absorption parallels with the most strongly quenched fluorescence among the DPP-dimers. For ***m*-DPP 3** both absorption and fluorescence resemble to what was seen for **DPP-Ref**.

With the time-resolved transient absorption spectroscopy analysis in toluene for the three dimers was not possible to observe any excited triplet states. However, in contrast, in benzonitrile the population of $^{1}(T_1T_1)$ and subsequent (T_1+T_1) was enabled. Furthermore, the spatial arrangement of the DPPs was a very important factor to reach this triplet state, it means the closer the DPP units were to each other the higher the TQY was. Therefore, for ***o*-DPP 1** the highest SF efficiency with a TQY of 40% in benzonitrile was obtained, while for the derivatives ***m*-DPP 3** and ***p*-DPP 2** values of 11% and 0% were gathered respectively, when benzonitrile was used as a solvent. The intraSF was quantitatively suppressed in ***p*-DPP 1**, where the lack of spatial overlap resulted in full charge separation and prevented population of $^{1}(T_1T_1)$ and (T_1+T_1). Therefore, this study has highlighted that the strength of the CT character is decisive whether it mediates intra-SF in DPP-dimers or blocks intra-SF due to trapping. In summary, the intra-SF efficiency follows the trend of ***o*-DPP 1** > ***m*-DPP 3** >>> ***p*-DPP 2**.

1.6. Experimental section

1.6.1. Material and methods

All chemicals and solvents were purchased from Sigma Aldrich (Merck) and TCI and were used without further purification unless otherwise stated.

Column chromatography was performed with SiO_2 (40–63 μm) and the thin-layer chromatography was made using SiO_2 60F254 and were visualized with UV light.

NMR data (^1H and ^{13}C) was recorded at 25 °C with a Bruker AC300 spectrometer with chemical shifts referenced to residual TMS or to the residual solvent signal.

Matrix assisted laser desorption/ionization time-of-flight (MALDI-TOF) mass spectra were obtained on a Bruker Microflex LRF20 intrument using dithranol as a matrix.

UV-vis spectra in CH_2Cl_2 solution were measured with a Helios Gamma spectrophotometer and the extinction coefficients were calculated using the Lambert-Beer law. Steady-state absorption measurements in toluene and benzonitrile were obtained on a PerkinElmer Lambda2 UV/Vis two-beam spectrophotometer with a slit width of 2 nm and a scan rate of 240 $nm.min^{-1}$.

Steady-state fluorescence measurements were gained by using a Horiba Jobin Yvon FluoroMax-3 spectrometer with a slit width of 2 nm for excitation and emission and an integration time of 0.5 s in a wavelength range of 500–1000 nm. Quantum yields were determined from corrected emission spectra using Rhodamine B (EtOH; FQY = 0.70 in EtOH) for **DPP-Ref**, Sulforhodamine 101 (EtOH; FQY = 0.90 in EtOH) for ***o*-DPP 1** and ***m*-DPP 3**, and Oxazine 170 (MeOH; FQY = 0.63 in MeOH) for ***p*-DPP 2** as standards, respectively.

FT-IR spectra were measured with a Nicolet Impact 400D spectrophotometer.

Cyclic voltammetry measurements were performed in 0.1M tetrabutylammonium hexafluorophosphate dichloromethane solution as support electrolyte, a graphite working electrode, a Ag/Ag^+ reference electrode, and carbon counter electrode using a potentiostat/galvanostat μAutolab Type III.

A home-made three-necked spectroelectrochemical cell was used for the spectroelectrochemical measurements. The three-electrode setup consisted of a platinum counter electrode, a silver wire quasi-reference electrode, and a platinum grid as working electrode. All measurements were performed at room temperature in argon saturated toluene/acetonitrile (4/1; v/v) with a 0.1 M $TBAPF_6$ supporting

electrolyte solution. The applied potentials were controlled through a Metrohm PGStat 101 with a 2 min hold time.

A Cary 5000 double beam spectrometer from Varian with the WinUV software was used for recording the spectra. In the femto- and nanosecond transient absorption measurements the excitation was performed using an amplified CPA-2110 titanium:sapphire laser (1kHz; 150 fs pulse width; 400 nJ laser energy) from Clark-MXR Inc. The EOS SYSTEM from Ultrafast Systems operated with a 1 kHz pump laser at 530 nm wavelength. Probing was performed via a 2 kHz continuous white light fiber laser. Data evaluation of the fs- and nsTAS data has been conducted by a combination of multiwavelength and target analysis using the GloTarAn software. Target analysis was performed on the TAS data sets using the proposed kinetic models. The analytic solution to the coupled differential equations that describe the kinetic model is convoluted with a Gaussian instrument response function. After the least-squares fitting has converged, the raw data matrix is deconvoluted using the specific solution to the kinetic model and parameters from the fit to obtain the species-associated spectra and their population as a function of time.

1.6.2. Synthesis

1.6.2.1. Synthesis of 3,6-di(thien-2-yl)-2,5-dihydropyrrolo[3,4-*c*]pyrrol-1,4-dione (4)

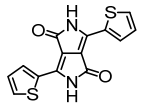

The compound **4** was synthesized by the succinate route. Metallic sodium (2 g, 87 mmol) and $FeCl_3$ (10 mg, 0.062 mmol) were added to 250 mL of *tert*-amyl alcohol then the reaction mixture was heated to 120 ºC. Once Na (s) was completely dissolved, 2- tiophenecarbonitrile (10 g, 92 mmol) and dimethyl succinate (7.3 g, 36 mmol) were added, and the mixture was left stirring 24 hours at 120 ºC. Afterward, the mixture was poured into a solution of 20 mL of HCl 37% in 400 mL of MeOH in order to precipitate the product. Then the suspension was filtered and washed with water and methanol to give a dark red solid (87%). It was used for the next steps without any purification.**^{1}H-NMR:** (300 MHz, DMSO-d_6) δ (ppm) 11.13 (s, 2H), 8.22 (dd, *J*= 3.8 Hz, *J*= 1.1 Hz, 2H), 7.94 (dd, *J*= 5.0 Hz, *J*= 1.1 Hz, 2H), 7.29 (t, *J*= 5.0 Hz, 2H).

1.6.2.2. Synthesis of 2,5-bis(2-ethylhexyl)-3,6-di(thien-2-yl)-2,5-dihydropyrrolo[3,4-*c*]pyrrol-1,4-dione (5)

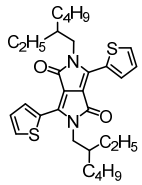

In a two-neck flask under nitrogen that contained **DPP 4** (2.0 g, 6.6 mmol) and Cs_2CO_3 (6.5 mg, 20 mmol) dry *N*,*N*-dimethylformamide (DMF) (20 mL) was added and the mixture

was set at 120 °C. Once this temperature was reached, a solution of 3-(bromomethyl)heptane (6 g, 16 mmol) in dry DMF (10 mL) was added dropwise and left for 24 hours with stirring. The reaction mixture was cooled to rt, a HCl 2M solution was added, and the mixture was extracted with ethyl acetate. Then, the organic layer was dried over anhydrous magnesium sulphate ($MgSO_4$). The solvent was removed off under reduced pressure and the crude product was purified through a silica gel column with toluene to give a red solid with a 49% yield. **^{1}H-NMR:** (300 MHz, $CDCl_3$) δ (ppm) 8.89 (d, *J*= 3.0 Hz, 2H), 7.62 (d, *J*= 3.0 Hz, 2H), 7.28-7.26 (m, 2H), 4.09-3.96 (m, 4H), 1.86-1.84 (m, 2H), 1.38-1.22 (m, 16H), 0.90-0.83 (m, 12H). **UV-vis:** (CH_2Cl_2): λ_{max}/nm (log ε): 292 (4.57), 342 (4.25), 512 (4.51), 548 (4.53).

1.6.2.3. Synthesis of 2,5-bis(2-ethylhexyl)-3,(5-bromotien-2-yl)-6-(thiene-2-yl)-2,5-dihidropyrrolo[3,4-*c*]pyrrol-1,4-dione (6)

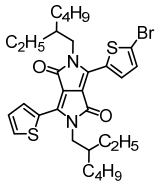

A NBS (100 mg, 0.570 mmol) solution in acetic acid (2 mL) was added dropwise to a solution of **DPP 5** (300 mg, 0.570 mmol) and acetic acid (1 mL) in chloroform (30 mL) at 5 °C. Allowed to reach rt the reaction mixture was stirred for 2h. The mixture was washed with KOH and H_2O, extracted with $CHCl_3$ and dried with Na_2SO_4. The final product was purified in a chromatographic column using toluene as eluent and obtaining the product as a purple powder with 45% yield. **^{1}H-NMR:** (300 MHz, $CDCl_3$) δ= 8.90 (dd, *J*= 3.9 Hz, *J*= 1.2 Hz, 1H), 8.64 (d, *J*= 4.2 Hz, 1H), 7.75 (dd, *J*= 5.0 Hz, *J*= 1.2 Hz, 1H), 7.29-7.26 (m, 2H), 7.23 (d, *J*= 4.2 Hz, 1H), 4.09-3.87 (m, 4H), 1.86-1.84 (m, 2H) 1.38-1.23 (m, 16H), 0.91-0.83 (m, 12H) ppm.

1.6.2.4. Synthesis of 1,4-di(1,3,2-dioxaborinan-2-yl)benzene (8b)

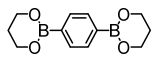

1,4-phenylenediboronic acid (2 g, 12 mmol), propane-1,3-diol and toluene were loaded into a one-neck flask mounted with a Dean-Stark. The reaction mixture was refluxed and stirred overnight. Then, the reaction was cooled to rt and the toluene was removed off under reduced pressure. Recrystallization from ethanol yields a white solid (2.24 g, 76%). **^{1}H NMR** (300 Hz, $CDCl_3$): δ (ppm) 7.74 (s, 4H), 4.16 (t, *J*= 6 Hz, 8H), 2.05 (quint., *J*= 6 Hz, 4H).

1.6.2.5. Synthesis of 6,6'-(1,2-phenylenebis(thiophene-5,2-diyl))bis(2,5-bis(2-ethylhexyl)-3-(thiophen-2-yl)-2,5-dihydropyrrolo[3,4-*c*]pyrrole-1,4-dione) [o-DPP 1]

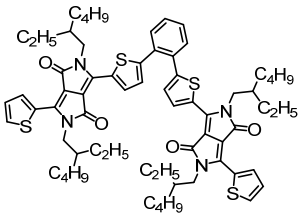

DPP 6 (100 mg, 0.166 mmol), compound **8a** (27.0 mg, 0.0830 mmol), $Pd_2(dba)_3$ (7.6 mg, 0.0083 mmol), PPh_3 (17.0 mg, 0.0664 mmol) and TBAB (2.68 mg, 0.0083 mmol) were dissolved in a degassed mixture of toluene (5 mL) and K_2CO_3 2M solution (0.3 mL). The reaction mixture was heated to reflux for 19.5 h under argon atmosphere. After cooling down to rt, the reaction mixture was filtered using celite, the solvent was removed off under reduced pressure, and the crude product was purified through a silica gel column with CH_2Cl_2/hexane (9:1) to give a dark pink solid (49.2 mg, 53%). **^{1}H NMR** (300 Hz, $CDCl_3$): δ (ppm) 8.99 (d, *J*= 3.0 Hz, 2H), 8.86 (d, *J*= 6.0 Hz, 2H), 7.60 (t, *J*= 6.0 Hz, 4H), 7.50-7.47(m, 2H), 7.25-7.24 (m; with $CHCl_3$), 7.15 (d, *J*= 3.0 Hz, 2H), 4.02-3.92 (m, 8H), 1.85-1.78 (m, 4H), 1.34-1.22 (m, 33H) 0.89-0.79 (m, 24H). **^{13}C NMR** (75 MHz, $CDCl_3$): δ (ppm) 161.8, 161.8, 147.6 140.3, 140.3, 136.3, 135.4, 132.8, 131.4, 130.9, 130.6, 130.0, 129.3, 129.1, 128.6, 108.2, 108.1, 46.2, 46.0, 39.4, 39.2, 30.4, 28.5, 23.7, 23.6, 23.3, 23.2, 14.2, 14.2, 10.6, 10.6, 10.5. **UV-vis (CH_2Cl_2)**: λ_{max}, nm (log ε) 356 (4.48), 528 (4.77), 565 (4.79). **HR-MS (MALDI-TOF)**: 1122.543 *m/z* (calcd. for $[M]^-$ 1122.522). **FT-IR (KBr)** ν_{max} (cm^{-1}):. 2957, 2929, 2856, 1663, 1558-1317, 840-706.

1.6.2.6. Synthesis of 6,6'-(1,4-phenylenebis(thiophene-5,2-diyl))bis(2,5-bis(2-ethylhexyl)-3-(thiophen-2-yl)-2,5-dihydropyrrolo[3,4-*c*]pyrrole-1,4-dione) [*p*-DPP 2]

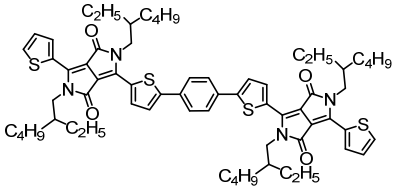

DPP 6 (100 mg, 0.166 mmol), compound **8b** (20.4 mg, 0.0830 mmol), $Pd_2(dba)_3$ (3.8 mg, 0.00415 mmol) and TBAB (2.68 mg, 0.0083 mmol) were dissolved in a degassed mixture of THF (5 mL) and K_2CO_3 2M solution (0.3 mL). The reaction mixture was heated to reflux for 16 h under argon atmosphere. After cooling down to rt, the mixture was poured into brine (100 mL) and extracted with $CHCl_3$ (3 × 50 mL) and the combined organic layers were dried over anhydrous $MgSO_4$. The solvent was removed off under reduced pressure and the crude product was purified through a silica gel column with CH_2Cl_2/hexane (19:1) to give a dark blue solid (34.0 mg, 36%). **^{1}H NMR** (300 Hz, $CDCl_3$): δ (ppm) 8.98 (d, *J*= 3.0 Hz, 2H), 8.91 (d, *J*= 3.0 Hz, 2H), 7.73 (s, 4H), 7.63 (d, *J*= 3.0 Hz, 2H), 7.53 (d, *J*= 6.0 Hz, 2H), 7.29-7.27 (m, with $CHCl_3$), 4.10-4.03 (m, 8H), 1.94-1.86 (m, 4H), 1.43-1.25 (m, 33H), 0.95-0.84 (m, 24H). **UV-vis (CH_2Cl_2):** λ_{max}, nm

(log ε) 377 (4.36), 596 (4.93). **HR-MS (MALDI-TOF):** 1122.553 *m/z* (calcd. for $[M]^-$ 1122.522). **FT-IR (KBr)** ν_{max} (cm^{-1}):. 2958, 2926, 2858, 1665, 1558-1324, 735-609.

1.6.2.7. Synthesis of 6,6'-(1,3-phenylenebis(thiophene-5,2-diyl))bis(2,5-bis(2-ethylhexyl)-3-(thiophen-2-yl)-2,5-dihydropyrrolo[3,4-*c*]pyrrole-1,4-dione) [m-DPP 3]

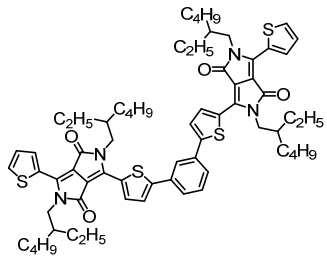

This reaction was carried out using the same procedure mentioned above. **DPP 6** (100 mg, 0.166 mmol), boronic ester **8c** (27.0 mg, 0.0830 mmol), $Pd_2(dba)_3$ (7.6 mg, 0.0083 mmol), PPh_3 (17.0 mg, 0.0664 mmol) and TBAB (2.68 mg, 0.0083 mmol) were dissolved in a degassed mixture of toluene (5 mL) and K_2CO_3 2M solution (0.3 mL). The reaction mixture was heated to reflux for 24 h under argon atmosphere. After cooling down to rt, the reaction mixture was filtered through celite, and the solvent was removed off under reduced pressure and the crude product was purified through a silica gel column with CH_2Cl_2/hexane (4:1) to give a pink solid (40.0 mg, 43%). **^{1}H NMR** (300 Hz, $CDCl_3$): δ (ppm) 8.96 (d, *J*= 6.0 Hz, 2H), 8.92 (d, *J*= 3.0 Hz, 2H), 7.93 (s, 1H), 7.65 (t, *J*= 6.0 Hz, 4H), 7.54-7.47 (m, 3H), 7.30-7.28 (m, with $CHCl_3$), 4.15-3.98 (m, 8H), 1.94-1.88 (m, 4H), 1.37-1.27 (m, 33H), 0.93-0.86 (m, 24H). **^{13}C NMR** (75 MHz, $CDCl_3$): δ (ppm) 161.9, 161.86, 148.6, 140.5, 140.1, 136.8, 135.5, 134.4, 130.7, 130.0, 129.6, 128.6, 126.6, 125.2, 123.8, 108.5, 108.3, 46.1, 39.4, 39.3, 28.7, 28.5, 23.9, 23.7, 23.2, 23.2, 14.2, 14.2, 10.8, 10.7. **UV-vis (CH_2Cl_2):** λ_{max}, nm (log ε) 366 (4.55), 543 (4.86), 580 (4.92). **HR-MS (MALDI-TOF)**: 1122.577 *m/z* (calcd. for $[M]^-$ 1122.522). **FT-IR (KBr)** ν_{max}, (cm^{-1}):. 2957, 2926, 2857, 1666, 1559-1232, 817-735.

Chapter 2

Diketopyrrolopyrroles as active layer in Dye-Sensitized Solar Cells and as acceptors in Bulk Heterojunction Solar Cells

2.1. Introduction

2.1.1. Organic solar cells

Throughout this manuscript, the benefits of using solar energy to combat the environmental issues we face today have been introduced. However, now is the moment to explore the cleanest and simplest solution for converting sunlight into usable energy, the so-called solar cells.

The solar cells can be divided in three generations, the first one, where the silicon solar cells are included, being the most used so far. These solar cells have some inconveniences, namely the high cost and low efficiency (around 25%). The second generation consists of a thin film of CdTe, amorphous silicon, copper, indium and gallium selenide ($CuInGaSe_2$ or CIGS) or copper, zinc and tin sulphide (Cu_2ZnSnS_4 or CZTS). These are more advantageous than the solar cells of first generation because they are cheaper, although the PCE values are not so good. The first and the second generation solar cells are based on single junction devices, therefore the absorption of one photon results in the formation of one single exciton and, as a consequence of that, all the photons with higher energy than the band gap will be lost by thermalization losses. Thus, the third generation of solar cells emerged with the aim of mitigating the disadvantages of the first and second generations. This generation is based on organic solar cells (OSCs) that are considered organic if at least a part of the constituents is composed of organic compounds.

2.1.1.1. Working principle of organic solar cells

Four different types of OSCs are known according to the type of arrangement, structure and nature of the components used, *vide infra*, however the working principle is similar in all types of OSCs, it could be described in four consecutives steps (**Figure 2.1**). This process starts with the (i) *photon absorption* leading to the formation of an excited state, the electron-hole pair (exciton), following (ii) the *exciton diffusion* to a diffusion region, active layer, where occurs the (iii) *charge separation*. The last step is based on the (iv) *charge transport* where the electrons are directed to the cathode and the holes to the anode.[105]

[105] H. Hoppea, N. S. Sariciftci, *J. Mater. Res*., **2004**, *19*, 1924-1945.

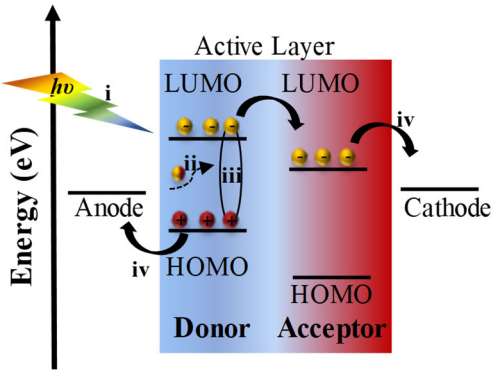

Figure 2.1-*Working principle of OSCs.*

As previously described, depending on the constituents of OSCs they may belong to a family or another, but there are three constituents that are common to all of them (i) the cathode, (ii) the active layer where the chromophores are located, which the function of capturing the photons to generate charge and transfers it respective electrodes, and (iii) the anode.

2.1.1.2. Type of organic solar cells

Over the years, various types of OSCs have been developed in ways that exceed the Shockley-Queisser limit, as explained earlier, due to the increase of the number of energy levels, generation of multiple excitons per each photon absorbed and for the properties modifications of the materials using doping agents. The known OSC architectures are planar heterojunction solar cell (PHJ), bulk heterojunction solar cell (BHJ), dye-sensitized solar cell (DSSC) and perovskite solar cell (PSC).

2.1.1.2.1. Planar heterojunction solar cells (PHJs)

Planar solar cells were first reported in 1986 by Tang.[106] These devices are known to have a sandwich structure where the layers of donor and acceptor materials are stacked on top of each other. In these devices, only excitons generated at a distance of 10-20 nm from the interface can achieved the heterojunction. Under these conditions, the efficiency of these solar cells is limited by the generation of charge. Besides, the photovoltaic properties are strongly dependent on the nature of the electrodes. In this sense BHJs were developed, reducing the distance between the donor and the acceptor as these two parts are blended.

[106] C. W. Tang, *Appl. Phys. Lett.*, **1986**, *48*, 183-185.

2.1.1.2.2. Bulk heterojunction solar cells (BHJs)

As described before, in BHJs the active layer is composed of an intimate mixture of at least two organic semiconductors, forming a blend of a donor (hole transporting) and acceptor (electron transporting) domains. With this blend the recombination of charges is avoided by increasing the probability that the excitons reach the interface creating a greater number of charge carriers.[107] An important step is the selection of the donor:acceptor couple. As donor, conjugated polymers or oligomers are commonly used, although small molecules have also been studied due to the high synthetic versatility, which consequently allows changing the photophysical properties, and the higher purity when compared with polymers.[108] Regarding to the acceptor moiety, fullerene derivatives are the molecules of excellence due to the great properties as large electron affinity, high electron mobility and isotropic charge-transport. Despite these properties, they also present several drawbacks, such as low absorption in the UV-vis spectrum, high cost and limited structural tunability of energy levels. Reasons why polymers and small molecules started to be studied as acceptors of OSCs, relying on their strong absorption and high thermal stability, and in the case of the small molecules, for mentioned above.[109] The new generation of non-fullerene acceptors (NFAs) has played an important role, thus being the way to overcome the photovoltaic performance obtained with fullerenes.

Two different architectures are commonly used in BHJs the standard (**Figure 2.2a**) and the inverted one (**Figure 2.2b**). In the standard architecture the photoactive layer is sandwiched between a hole transporting material (HTM) and an optional electron transporting materials (ETM) which coated a low work function electrode (anode). In turn, the HTM coats a transparent and conductive electrode [indium tin oxide (ITO)] and this coats a cathode (calcium, barium or aluminium) that collect the electrons generated in the photoactive layer.[110] Usually conjugated polymers like PEDOT:PSS or tin oxide layer have been used as HTM and the ETM are often zinc or titanium oxides. The advantage in using an ETM is the improvement of the light absorption in the photoactive layer. However, in the inverted structure the transparent electrode coated on the substrate acts as electron collector and is usually coated with a transparent metal oxide layer (zinc oxide or titanium dioxide). The active layer is deposited on top of the metal layer followed by HTM (PEDOT:PSS), being the last layer a high work- function metal anode like silver or gold.[111] Both structures allow to reach high efficiencies, nevertheless the inverted structure has

[107] J. Chen, Y. Chen, L.-W. Feng, C. Gu, G. Li, N. Su, G. Wang, S. M. Swick, W. Huang, X. Guo, A. Facchetti, T. J. Marks, *EnergyChem.*, **2020**, *2*, 100042.
[108] R. Ilmi, A. Haque, M. S. Khan, *Org. Electron.*, **2018**, *58*, 53-62.
[109] a) J. Hou, O. Inganäs, T. H. Friend, F. Gao, *Nat. Mater.*, **2018**, *17*, 119-128 b) B. C. Thompson, J. M. J. Fréchet, *Angew. Chem., Int. Ed*., **2008**, *47*, 58–77.
[110] M.C. Scharber, N.S. Sariciftci, *Progr. Polym. Sci*., **2013**, *38*, 1929-1940.
[111] H. Gaspar, F. Figueira, L. Pereira, A. Mendes, J. C. Viana, G. Bernardo, *Materials*, **2018**, *11*, 2560.

advantage over the conventional architecture, as it improves the ambient stability, due to the absence of low work function electrodes which can be deposited under normal ambient condition, no vacuum process being required.[111a]

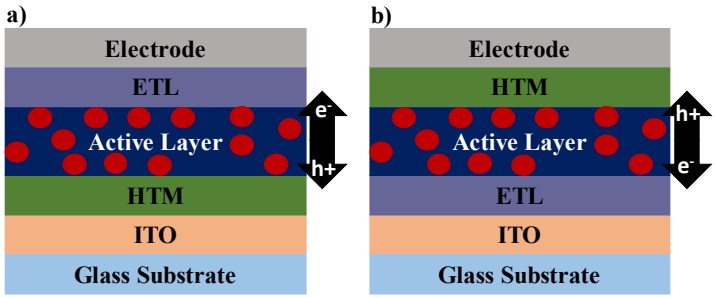

Figure 2.2- a) *Standard BHJs.* ***b)*** *Inverted BHJs.*

2.1.1.2.3. Dye-sensitized solar cells (DSSCs)

Dye-sensitized solar cell technology was developed by O´Regan and Grätzel in 1991[112] differentiating themselves from the conventional semiconductor devices because they separated the function of light absorption from the charge carrier transport. Devices are based on five components, (i) a mechanical support coated in transparent conductive oxide, (ii) the semiconductor film (usually TiO_2), (iii) a sensitizer adsorbed onto the surface of the semiconductor, (iv) an electrolyte containing a redox mediator and (v) a counter electrode capable of regenerating the redox mediator (usually platinum).

DSSCs can be arranged into two different architectures, the n-type DSSC and the p-type DSSC or inverted DSSC (**Figure 2.3a** and **b**). In the case of n-type DSSC the operating principles of DSSCs start with the absorption of a photon by a sensitizer S [$S_{(absorbed)} + h\nu \rightarrow S^*_{(absorbed)}$], following the excited sensitizer S^* which injects an electron into the conduction band of the semiconductor, whereby the dye results oxidized S^+ [$S^*_{(absorbed)} \rightarrow S^+_{(absorbed)} + e^{-+}_{(injected)}$], returning to its fundamental state by a redox reaction with the electrolyte. In turn, the electrons move through an external circuit to reach the counter electrode reducing the electrolite [$I_3^- + 2e^- \rightarrow 3I^-_{(cathode)}$] [$S^+_{(absorbed)} + I^- \rightarrow S_{(absorbed)} + I_3^- \; I^-_3$] and finishing the cycle.[113]
In general, the chromophore has a donor-bridge (π)-acceptor (D_G-π-A_G) structure, where the donor will absorb the light generating an excited state, which transfer an electron to the acceptor, thus generating the charge separated state.[114] As the acceptor part, is connected to the semiconductor by an anchoring group, normally

[112] B. O'Regan, M. Grätzel, *Nature*, **1991**, *353*, 737-740.
[113] M. K. Nazeeruddin, E. Baranoff, M. Grätzel, *Sol. Energy*, **2011**, *85*, 1172-1178.
[114] I. N. Obotowo, I. B. Obot, U. J. Ekpe, *J. Mol. Struct.*, **2016**, *1122*, 80-87.

a carboxylic acid or a cyanoacrylic acid, the electron can be injected into the conduction band of the semiconductor.
In the case of p-type DSSCs the operating principle occurs in an inverse way, it means the light is absorbed by the sensitizer reaching the excited state, this inject a hole in the valence band of the semiconductor (usually NiO or CuO), so the dye is reduced and needs to be regenerated by the subsequent reduction of the electrolyte, which will be regenerated by the electron flow in the external circuit. In p-type DSSCs the charge flow occurs in a similar way as in n-type DSSCs, although what is injected into the semiconductor are holes instead of electrons. In addition to these constituents it is very usual the use of co-adsorbent agents, which have the function of passivate the surface of the semiconductor and decrease the recombination phenomena.[115] So far, the best photosensitizer in n-type DSSCs is based on porphyrin compounds with a PCE above 13% (**Figure 2.3c**).[116]

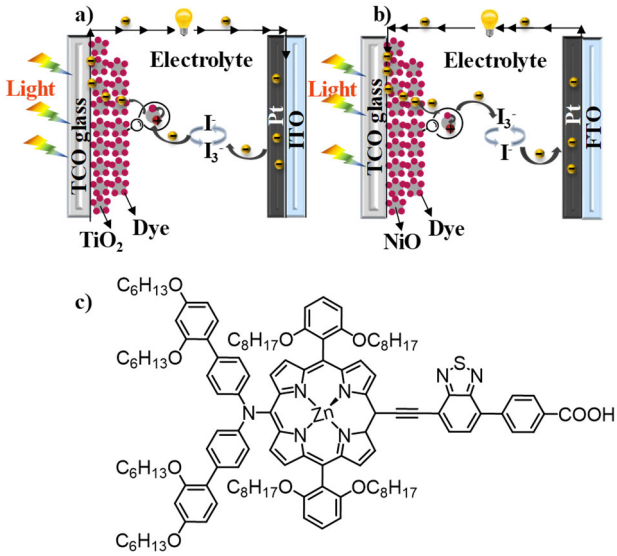

Figure 2.3- a) *Scheme of a n-type DSSC devices using the* I^-/I_3^- *redox couple in the electrolyte and* TiO_2 *as semiconductor and* ***b)*** *Scheme of a p-type DSSC using the same electrolyte and NiO as semiconductor material.* ***c)*** *Best compound for n-type DSSCs.*

2.1.1.2.4. Perovskite solar cells (PSC)

Perovskite solar cells have produced a major revolution in the photovoltaic field reaching PCE values never achieved before with other types of OSCs. It is based on an organic-inorganic light absorbing semiconductor material with an ABX_3 perovskite crystalline structure, where A is an organic cation, such as

[115] A. Hagfeldt, G. Boschloo, L. Sun, L. Kloo, H. Pettersson, *Chem. Rev.*, **2010**, *110*, 6595–6663.
[116] S. Mathew, A. Yella, P. Gao, R. Humphry-Baker, B. F. E. Curchod, N. Ashari-Astani, I. Tavernelli, U. Rothlisberger, M. K. Nazeeruddin, M. Grätzel, *Nat. Chem.*, **2014**, *6*, 242-247.

methylammonium (MA) and/or formamidinium (FA), or an inorganic cation such as cesium or rubidium, B represents a metal generally lead or, to a lesser extent, tin, and X is a halogen such as iodine, bromine or chlorine. Perovskite materials exhibit great properties such as a high absorption coefficient, ambipolar charge mobility meaning that the perovskite can effectively transport hole and electrons, high charge carrier mobility (10 $cm^2V^{-1}s^{-1}$), and long carrier diffusion length.[117] Miyasaka was the pioneer to describe the perovskite as light harvester material in a DSSC variant using a TiO_2 perovskite-sensitized solar cell, obtaining the best PCE of 3.8% using $CH_3NH_3PbI_3$.[118] In recent years, perovskite solar cells have experienced some changes in the morphology improving the device performances. Park and Grätzel replaced the electrolyte ($I^-\backslash I_3^-$) by the 2,2′,7,-7′-tetrakis(*N*,*N*-di-p-methoxyphenylamine)-9,9′-spirobifluorene (spiro-OMeTAD, **Figure 2.4**) obtaining a PCE of 9.5%.[119] However, when the perovskite started to be deposited by layers, the efficiency increased considerably (PCE of 15.4%).[120] Nowadays, according to the National Renewable Energy Laboratory, the efficiency record for perovskite solar cells is 25.5%.[121]

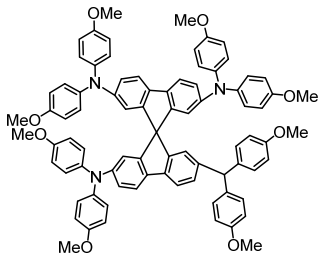

Figure 2.4- *Spiro-OMeTAD structure.*

The PSCs can adopt different configurations depending on the distribution of the layers, the standard (n-i-p) or the inverted (p-i-n) architectures. A transparent glass serves as the substrate where electron-selective (for n-i-p configuration) or hole-selective (for p-i-n configuration) are deposited, followed by the perovskite layer (planar or mesoporous), this being covered with another hole or electron transporting layer, and finally a metal contact for the charges to flow.[122] The function of outermost layer, immediately below the metal electrode, ETM or HTM, is not just to let some charges pass and block others (e.g., the ETM must let electrons pass and prevent the passage of holes to minimize recombination

[117] Yani Chen, Jiajun Peng, Diqing Su, Xiaoqing Chen, Ziqi Liang, A*CS Appl. Mater. Interfaces*, **2015**, *7*, 4471–4475.
[118] A. Kojima, K. Teshima, Y. Shirai, T. Miyasaka, *J. Am Chem. Soc.,* **2009**, *131*, 6050-6051.
[119] H.-S. Kim, C.-R. Lee, J.-H. Im, K.-B. Lee, T. Moehl, A. Marchioro, S.-J. Moon, R. Humphry-Baker, J.-H. Yum, J. E. Moser, M. Grätzel, N.-G. Park, *Sci. Rep*., **2012**, *2*, 591.
[120] M. Liu, M. B. Johnston, H. J. Snaith, *Nature*, **2013**, *501*, 395-398.
[121] National Renewable Energy Laboratory (NREL), https://www.nrel.gov/pv/cell-efficiency.html accessed 15/05/2021.
[122] J.-P. Correa-Baena, M. Saliba, T. Buonassisi, M. Grätzel, A. Abate, W. Tress, A. Hagfeldt, *Sciences*, **2017**, *358*, 739-744.

phenomena) but should protect the device from degradation factors as well, such as moisture.[123]

2.1.1.3. Photovoltaic parameters

The characterization of the performance of photovoltaic cells requires the use of, parameters such as the current density (*J*) and voltage (V), obtained by focusing sunlight on the device. These two parameters allow the construction of a curve which allows to obtain four new parameters, namely open-circuit voltage (V_{OC}), short-circuit current (J_{SC}), fill factor (FF) and power conversion efficiency (PCE) (**Figure 2.5**). V_{OC} is defined as the potential obtained between the two ends of the solar cell when no current flows. The J_{SC} is the current density of the solar cell under illumination at zero potential (short circuit). The short-circuit current is the maximum current that a device can produce. The FF is defined as the ratio between areas A (maximum power output) and B (**Equation 2.1**, **Figure 2.5**). With all these parameters we can define the last parameter denominated PCE, which is defined as the ratio of maximum power output to power input. It can be calculated using **Equation 2.2**. Beyond these parameters, there is another one called external quantum efficiency (EQE) or incident photon to electron conversion efficiency (IPCE) that is defined by the conversion ratio of the incident photons to electrons. This parameter is dependent on the type of dye used and can be described by the **Equation 2.3**.[124]

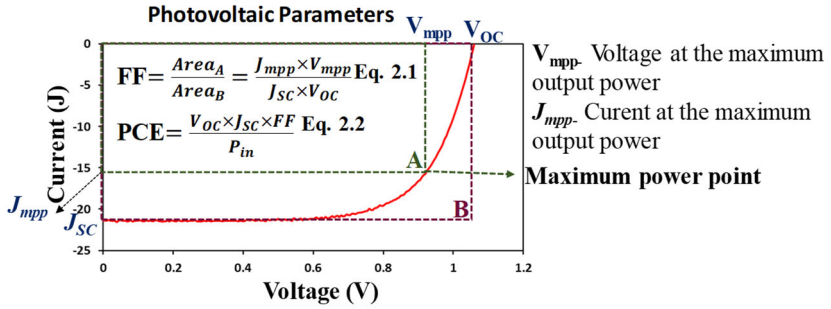

Figure 2.5- *J/V curve and the photovoltaic parameter.*

$$IPCE = \frac{num.of\ generated\ electron}{num.of\ incident\ photons} = \frac{1240(eVnm) \times J_{SC}(mAcm^{-2})}{I_0(mWcm^{-2}) \times \lambda(nm)} \quad \textbf{Eq. 2.3}$$

[123] M. A. Green, A. Ho-Baillie, H. J. Snaith, *Nat. Photonics*, **2014**, *8*, 506-514.
[124] S. Rafiquea, S. M. Abdullaha, K. Sulaimana, M. Iwamoto, *Renew. Sust. Energy Rev.*, **2018**, *84*,43–53.

2.2. Background

2.2.1. DPPs in DSSCs

The history of DPP as a sensitizer in DSSCs began in 2009 when a patent was published. In 2010 appeared the first article where **DPP 2.I** and **2.II** were tested as sensitizers in DSSCs obtaining efficiencies of 4.14% and 0.83% (**Figure 2.6**).[125] From that moment, a series of derivatives were synthesized and device performances have been improved. In this Thesis, the interest was focused on small molecules based on DPPs for n-type DSSCs, reason why we restrict ourselves only to the most efficient DPP small molecules from 2015 that were reported for this type of DSSCs.

It is important to note that in 2013 the record efficiency in DSSCs was achieved stablished with a PCE of 10.1% using **DPP 2.III** and a Co^{2+}/Co^{3+} redox couple (**Figure 2.6**), and up to now it remains the best efficiency achieved with a DPP.[126] Nevertheless, a continuous effort has been made to beat this result and improve the efficiency in DSSCs, which is visible by the huge quantity of articles that can be found in the literature. In 2015, Ganesan published two derivatives based on a D_G-π-A_G system with a strong electron withdrawing cyanoacrylic acid **DPP 2.IV** and another with a weak acceptor carboxylic acid **DPP 2.V** (**Figure 2.6**). While the optoelectrochemical properties are not very different, the photovoltaic properties showed to be different for the two compounds, indicating that the compound **DPP 2.V** presented higher PCE than **DPP 2.IV** under simulated one sun (7.65% *vs* 7.34%).[127]

[125] S. Qu, W. Wu, J. Hua, C. Kong, Y. Long, H. Tian, *J. Phys. Chem. C*, **2010**, *114*, 1343–1349.
[126] J.-H. Yum, T. W. Holcombe, Y. Kim, K. Rakstys, T. Moehl, J. Teuscher, J. H. Delcamp, M. K. Nazeeruddin, M. Grätzel, *Sci. Rep.*, **2013**, *3,* 2446.
[127] P. Ganesan, A. Yella, T. W. Holcombe, P. Gao, R. Rajalingam, S. A. Al-Muhtaseb, M. Grätzel, M. K. Nazeeruddin, *ACS Sustain. Chem. Eng*., **2015**, *3*, 2389−2396.

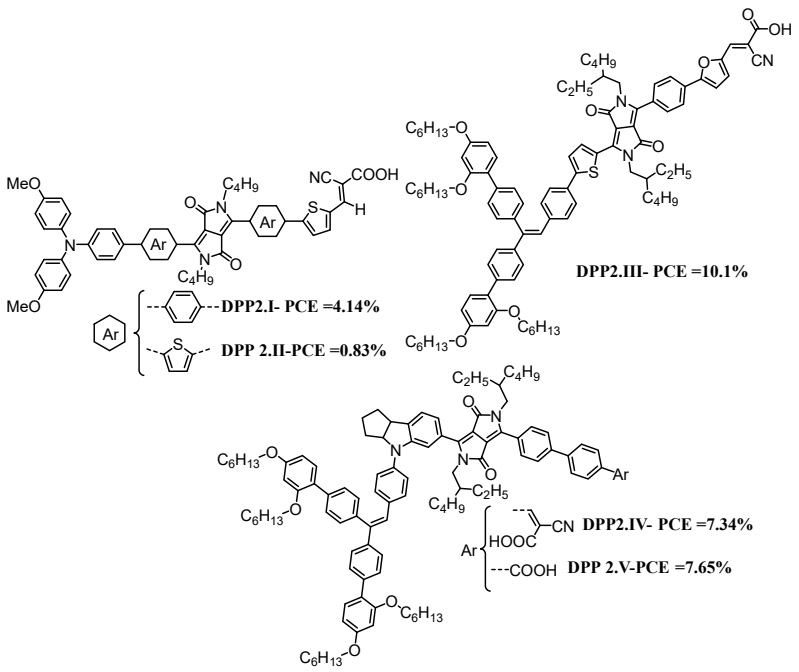

Figure 2.6-*Structures of* ***DPP 2.I- DPP2.V****.*

In the same year, four different derivatives with a D_G-A_G-π -A_G structure were also published, where the donor group were *N*-annulated perylenes, the DPP core was used as acceptor, the thiophene moiety as π-linker and the cyanoacrylic acid as the second acceptor. In the *peri*-position of the *N*-annulated perylenes, different substituents with varying electron-donating abilities were introduced (**Figure 2.7**). The explored modifications leaded to some different photovoltaic properties, leading to the better result when the R position was substituted by a 4-methoxyphenyl group which reduced the charge recombination enhancing the V_{OC} and making the derivative **DPP 2.VII** the most efficient of the four with and without chenodeoxycholic acid (CDCA). **DPP 2.VII** with co-adsorbent showed a PCE of 8.30% with a J_{SC} of 17.14 mA cm^{-2}, a V_{OC} of 698 mV and a FF of 69%.[128] On the other hand, Chiu developed two asymmetric derivatives containing a D_G-π-A_G structure with 4,4′-ditolylaniline as a donor, the DPP unity as a π-conjugated bridge and the cyanoacetic as the acceptor and anchoring moiety. The introduction of the phenyl (**DPP 2.X**) and thienyl (**DPP 2.XI**) groups between the anchoring group and the DPP allowed to study the influence of these two spacers in DSSCs in the presence of CDCA (**Figure 2.7**). Although **DPP 2.XI** had a very high molar extinction coefficient at 530 nm (2.25 x 10^5 M^{-1} cm^{-1}) and a lower band gap, **DPP 2.X** showed better performance (PCE = 7.20% *vs* 6.60% for **DPP 2.XI**) due to a better ability to inject electrons into TiO_2. This phenomenon was explained by the

[128] X. Li, Z. Zheng, W. Jiang, W. Wu, Z. Wang, H. Tian, *Chem. Commun.,* **2015**, *51*, 3590-3592.

linear structure evidenced by DFT calculations and femtosecond time-resolved photoluminescence data.[129]

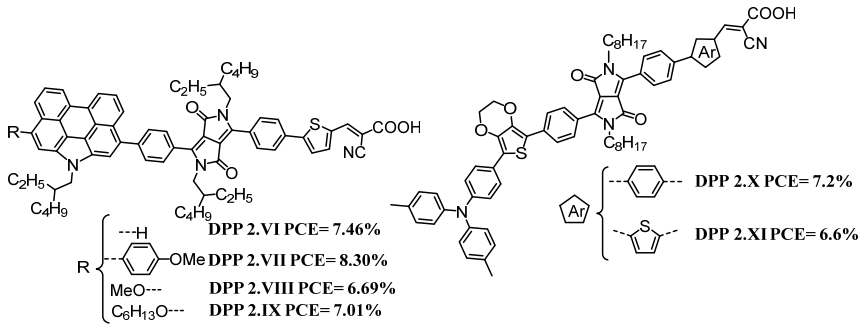

Figure 2.7- *Structures of* ***DPP 2.VI- DPP 2.XI****.*

The study by Hao showed how the co-sensitization between red and blue D_G-π-A_G organic dyes increase photovoltaic performance. In this case, the blue **DPP 2.XII** in contact with red dye **DA** in a 3:4 ratio produced a PCE of 8.70% while when used separately PCEs were 7.30% and 5.50%, respectively, using $[Co(bpy)_3]^{3+/2+}$ under AM1.5 G (**Figure 2.8**).[130]

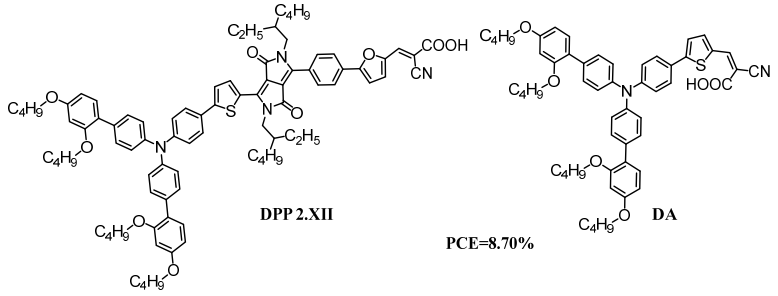

Figure 2.8- *Structures of* ***DPP 2.XII*** *and* ***DA****.*

2.2.2. DPPs in BHJs

The study of polymers and small molecules as NFAs has grown in the past few years in order to overcome the drawbacks of fullerene derivatives, *vide supra*. Moreover, small molecules offer advantages over the polymer materials due to easy synthesis and purification, high charge carrier mobility batch to-batch reproducibility of results. In this context, DPPs have been extensively studied in

[129] K. Y. Chiu, V. Govindan, L.-C. Lin, S.-H. Huang, J-C Hu, K.-M. Lee, H.-H. G. Tsai, S.-H. Chang, C.-G. Wu, *Dyes Pigm.*, **2016**, *125*, 27-35.
[130] Y. Hao, Y. Saygili, J. Cong, A. Eriksson, W. Yang, J. Zhang, E. Polanski, K. Nonomura, S. M. Zakeeruddin, M. Gräzel, A. Hagfeldt, G. Boschloo, *ACS Appl. Mater. Interfaces*, **2016**, *8*, 32797−32804.

this field as summarized in several recent review.[131] In 2013 Lin reported for the first a time DPP-based acceptor with a PCE above 2% with a structure of *5H*-dibenzo[*b,d*]silole (DBS) flanked by two DPP units (**DPP 2.XIII**), presenting a high value of LUMO which leaded to a high V_{OC} (0.97 V) for the P3HT:**DPP 2.XIII** standard device (**Figure 2.9**).[132] However, changing the spacer to dipropylfluorene and adding a phenyl end-group at each side of the dimer, **DPP 2.XIV**, allowed to increase even more the V_{OC} (1.18 V) and obtain a PCE of 3.17% (**Figure 2.9**).[133]

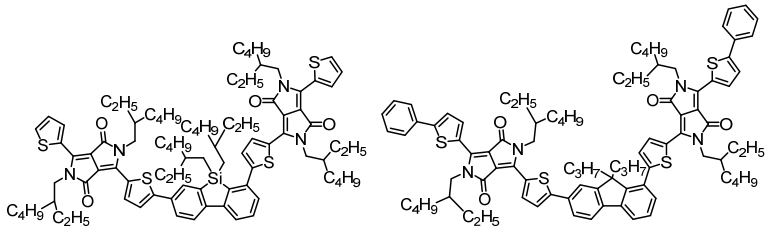

Figure 2.9- *Structures of* ***DPP 2.XIII*** *and* ***DPP 2.XIV****.*

Recently, better approaches have been reported using standard devices which reach PCE higher than 9%. **DPP 2.XV** contains a DPP core linked to a dicyanomethylene-3-ethylrhodanine acceptor via an ethynyl-thiophene bridge (**Figure 2.10**). *p*-DINI-$(FBTTTh_3)_2$ was used as donor because its energy levels matched with those of the DPP-derivative (**DPP 2.XV**). The solvent vapor annealing (SVA) method was implemented obtaining a PCE of 9.14% with a J_{SC} of 13.72 mA/cm^2, a V_{OC} of 980 mV and an FF of 67%, being the current record in single molecules based on DPPs as acceptors in OSCs.[134a] Later the same group reported a derivative that contained a DPP as core linked by selenophene moieties to two terminal rhodanine units. The photovoltaic performance was carried out using a phenothiazine-based small molecule donor obtaining a PCE of 8.96%. However, the best efficiency was obtained using a ternary solar cell with $PC_{70}BM$ as co-acceptor, which showed a remarkable PCE of 10.05%.[134b]

[131] a) Q. Liu, S. E. Bottle, P. Sonar, *Adv. Mater.*, **2019**, 1903882. b) C. Zhao, Y. Guo, Y. Zhang, N. Yan, S. You, W. Li, *J. Mater. Chem. A*, **2019**, *7*, 10174-10199.
[132] Y. Lin, Y. Li, X. Zhan, *Adv. Energy Mater.*, **2013**, *3*, 724−728.
[133] H. Shi, W. Fu, M. Shi, J. Ling, H. Chen, *J. Mater. Chem. A*, **2015**, *3*, 1902-1905.
[134] a) M. Privado, P. d. l. Cruz, S. Biswas, R. Singhal, G. D. Sharma, F. Langa, *J. Mater. Chem. A*, **2018**, *6*, 11714-11724. b) M. Privado, P. Malhotra, P. de la Cruz, R. Singhal, J. Cerdá, J. Aragó, E. Ortí, G. D. Sharma and F. Langa, *Sol. RRL*, **2020**, *4*, 1900471.

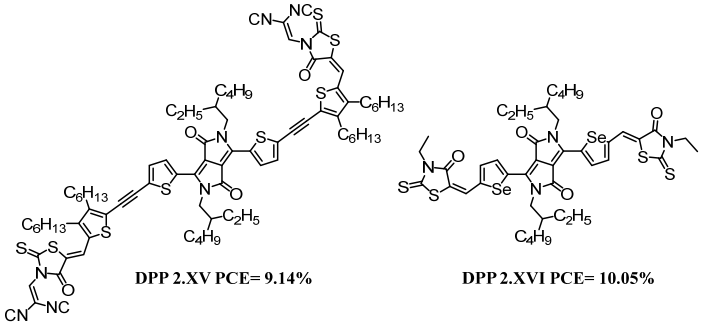

Figure 2.10- *Structures of* ***DPP 2XV*** *and* ***DPP 2.XVI****.*

On the other hand, the inverted structure has been also investigated due to the higher environmental stability in relation with the standard one. In 2016 a derivative with an electron-withdrawing phthalimide group linked by an acetylene bridge to a DPP core was reported (**Figure 2.11**). The best performance for P3HT:**DPP 2.XVII** was obtained using the inverted cell architecture (ITO/ZnO/active layer/MoO_3/Ag), DIO as solvent additive and after thermal annealing treatment. Thus, with these conditions, a PCE of 3.28% was obtained.[135] Later, the same group, studied the effects of the nature (linear or branched alkyl chain) and the position (in the DPP or in the phthalimide) of the side chain on the optical properties and, consequently, in the PV performances. The authors conclude that the branched alkyl chain in the DPP favored the light absorption and promoted a better phase separation with P3HT, while the linear chain in phthalimide improved the charge transport properties (**Figure 2.11**). The efficiencies obtained this time were 0.12%, 0.02% and 1.10% for **DPP 2.XVIII**, **DPP 2.XIX** and **DPP 2.XX**, respectively.[136]

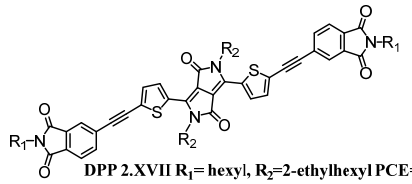

Figure 2.11- *Structures of* ***DPP 2.XVII-DPP 2.XX****.*

A considerable improvement came when McAfee introduced two PDI units flanking at DPP (**DPP 2.XXI**). Two studies were developed to verify which donor (P3HT, PCDTBT, PTB7-Th or PDTT-BOBT) was the most favorable for this

[135] P. Josse, C. Dalinot, Y. Jiang, S. D.-Seignon, J. Roncali, P. Blanchard, C. Cabanetos, *J. Mater. Chem. A*, **2016**, *4*, 250-256.
[136] P. Josse, A. Labrunie, C. Dalinot, S. M. McAfee, S. D.-Seignon, J. Roncali, G. C. Welch, P. Blanchard, C. Cabanetos, *Org. ElectroN.*, **2016**, *37*, 479-484.

acceptor using an inverted architecture ITO/ZnO/Donor: **DPP 2.XXI** /MoOX/Ag (**Figure 2.12**). From these four donors the best performance was obtained when PTB7-Th and SVA method were used (PCE of 4.63% with a *J*sc of 10.84 mA/cm^2, a V_{OC} of 970 mV and a FF of 44%).[137]

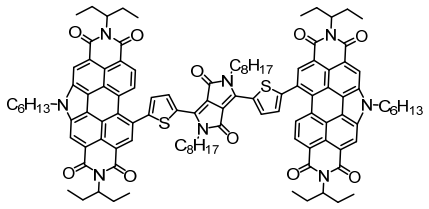

Figure 2.12- *Structure of* ***DPP 2.XXI****.*

The first example of solution-processed NFA-based tandem OSC was described with inverted tandem structure based on ITO/ZnO/PFN/P3HT:**DPP 2.XXII**/MoO_3/Ag/PFN/PTB7-Th:IEIC/MoO_3/Ag, and leaded to a PCE of 8.48% with a V_{OC} 1.97 V (**Figure 2.13)**.

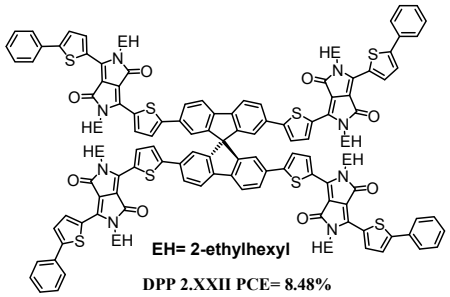

Figure 2.13- *Structure of* ***DPP 2.XXII****.*

2.2.3. SubPc in BHJs

Subphthalocyanines (SubPcs) are a family of organic molecules and, like DPPs, present interesting optical and electronic properties, such as strong optical absorptions in the spectral region of 460–580 nm, and relatively high electron mobilities. The SubPc family has 14 delocalized π-electrons and a boron atom in its central cavity with a cone-shaped structure that prevents aggregation in solution and even in the solid-state (**Figure 2.14 a**).[138] Due to their ambipolar character

[137] a) S. M. McAfee, S. V. Dayneko, P. Josse, P. Blanchard, C. Cabanetos, G. C. Welch, *Chem. Mater.*, **2017**, *29*, 1309−1314. b) S. M. McAfee, A.-J. Payne, S. V. Dayneko, G. P. Kini, C. E. Song, J.-C. Lee, G. C. Welch, *J. Mater. Chem. A*, **2017**, *5*, 16907-16913.

[138] a) T. M. Grant, D. S. Josey, K. L. Sampson, T. Mudigonda, T. P. Bender, B. H. Lessard, *Chem. Rec.* **2019**, *19*, 1093-1112; b) G. de la Torre, G. Bottari, T. Torres, *Adv. Energy Mater*. **2017**, *7*, 1601700; c) C.G. Claessens, D. González-Rodríguez, M.S. Rodríguez-Morgade, A. Medina, T. Torres, *Chem. Rev*. **2014**, *114*, 2192-2277; d) G.E. Morse, T.P. Bender, *ACS Appl. Mater.*

SubPcs can be used as donors[139] or acceptors in the active layer of BHJs, standing out among other chromophores for the preparation of NFA materials due to their high electron mobilities.[140]

The first SubPc used as an acceptor in BHJs appeared published in 2009, when Torres used the **SubPc 2.I** in combination with oligoacenes and other phthalocyanines. An improvement in V_{OC} was achieved but J_{SC} and FF values were much lower when the SubPc was used, resulting in a much lower PCE.[141]

This pioneering work deepened interest in these systems. In 2014 the efficiency record with SubPc-based solar cells was broken, when Cnops fabricated a three-layers vacuum–deposited device with **SubPc 2.I**, **SubNc** and a thiophene oligomer, in a two-step exciton dissociation process, achieving a PCE of 8.4% instead of 4.69% when only **SubPc 2.I** was used in a bilayer solar cell (**Figure 2.14 b**).[142] This record remains until today, but efforts to exceed this value have been notorious.

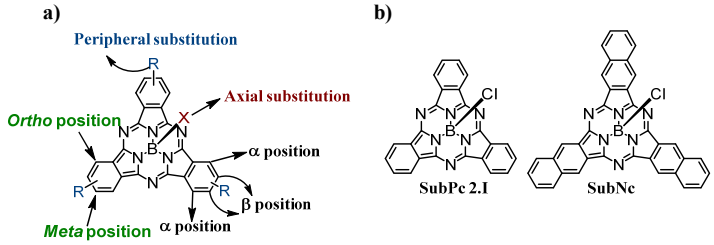

Figure 2.14- a) *General structure of SubPc. R represents substituents at the peripheral positions and X the substituent at the axial position.* ***b)*** *Structure of* ***SubPc 2.I*** *and* ***SubNc****.*

The low solubility of unsubstituted SubPcs makes deposition a tricky step, requiring high vacuum and elevated temperatures. However, Jones published soluble SubPcs by the introduction of F and Cl atoms into peripheral phenyl rings.[143] This change in chemical structure, in addition to the increased the solubility enabling deposition in solution, produced a decrease in LUMO energy

Interfaces, **2012**, *4*, 5055-2068; e) A. Medina, C.G. Claessens, *J. Porphyr. Phthalocyanines* **2009**, *13*, 446-454.

[139] a) Y.-Q. Zheng, J.-L. Yu, W.-G. Li, J. Tang, B. Wei, X.-F. Li, J.-F. Shi, J.-H. Zhang, Y.-F. Wang; *J. Phys. D: Appl. Phys*., **2020**, *53*, 125102; b) M. Xiao, Y. Tian, S. Zheng, *Org. Electron.,* **2018**, *59*, 279-287; c) E. Jouad, E.M. El-Menyawy, G. Louarn, L. Arzel, M. Morsli, M. Addou, J.C. Bernède, L. Cattin, *J. Phys. Chem. Solids*, **2020**, *136*, 109142; d) C.C. Lee, W.C. Su, Y.S. Shu, W.C. Chang, B.Y. Huang, Y.Z. Lee, T.H. Su, K.T. Chen, S.W. Liu, *RSC Adv*., **2015**, *5*, 5617-5626; e) N. Wang, X. Tong, Q. Burlingame, J. Yu, S.R. Forrest, *Sol. Energy Mater. Sol. Cells*, **2014**, *125*, 170-175.

[140] A. Wadsworth, M. Moser, A. Marks, M. S. Little, N. Gasparini, C. J. Brabec, D. Baran, I. McCulloch, *Chem. Soc. Rev.*, **2019**, *48*, 1596-1625.

[141] H. Gommans, T. Aernouts, B. Verreet, P. Heremans, A. Medina, C. G. Claessens, T. Torres, *Adv. Funct. Mater*., **2009**, *19*, 3435-3439.

[142] K. Cnops, B. P. Rand, D. Cheyns, B. Verreet, M. A. Empl, P. Heremans, *Nat. Commun.*, **2014**, *5*, 3406.

[143] P. Sullivan, A. Duraud, I. Hancox, N. Beaumont, G. Mirri, J. H. R. Tucker, R. A. Hatton, M. Shipman, T. S. Jones, *Adv. Energy Mater.*, **2011**, *1*, 352−355.

levels in BHJs and the best performance was obtained when the active layer was constituted by **SubPc 2.I:SubPc 2.VI** with a PCE of 2.68% (**Figure 2.14 b-Figure 2.15 b**).

Years later, Samuel reported two halogenated SubPcs, but with phenoxy groups in the axial position instead of Cl, scrutinizing the photovoltaic performance with three donor polymers (MEH-PPV, P3HT and PTB7) in a standard stack solution BHJ architecture (**Figure 2.15 a**).[144] After optimization with DIO as additive, the authors realized that the best pair PTB7:**SubPc 2.III** achieved a 3.5% PCE, while for PTB7:**SubPc 2.II** a PCE of only 1.9% was reached. This difference was associated to the better morphology, appropriate energy levels and complementary absorption of the former pair compared to the latter.

More recently, a record for halogen SubPc solution-deposited device was reached when four $SubPcCl_6$-X were reported by Torres, where X represents four different substituents, one of them Cl which had previously demonstrated great potential as an n-type material in planar-heterojunction solar cell and others with different phenoxy groups (**Figure 2.15 b**).[145] The modification in axial position leads to a slight difference in electron accepting character. A maximum PCE around 4.0% was obtained for **SubPc 2.IV** with an inverted ITO/ZnO/PTB7-Th:$SubPcCl_6$-X/MoO_x/Ag architecture under stimulated AM 1.5G illumination.

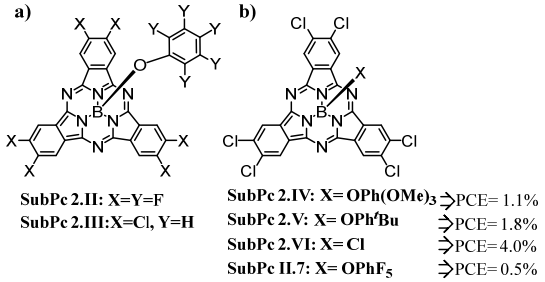

Figure 2.15-a) *Structures of SubPc reported by Samuel.* ***b)*** *Structures of SubPcs studied by Torres.*

However, the relatively narrow absorption window is a handicap of the SubPc core, so they were implemented as building blocks bonded to some other electroactive moieties to build structures with a wider absorption range. Hang developed a new strategy reporting two new star-shaped electron acceptors with a SubPc core and three PDI wing groups (**Figure 2.16a**).[146] The conjugation of these two moieties was advantageous because on the one hand the PDI supplements the absorption

[144] B. Ebenhoch, N. B. A. Prasetya, V. M. Rotello, G. Cooke, I. D. W. Samuel, *J. Mater. Chem. A*, **2015**, *3*, 7345–7352.
[145] C. Duan, G. Zango, M. G. Iglesias, M. F. J. M. Colberts, M. M. Wienk, M. M. Martinez-Diaz, R. A. J. Janssen, T. Torres, *Angew. Chem., Int. Ed*. **2017**, *56*, 148−152.
[146] H. Hao, Z. Zhang, X. Wu, Y. Chen, H. Li, W. Wang, H. Tong, L. Wang, *J. Mater. Chem. C*, **2018**, *6*, 7141−7148.

band of the SubPc, and on the other hand the SubPc reduces the strong aggregation tendency of PDIs which will lead to a better morphology of the blended films. The derivatives differentiation was in the way of binding between PDI and SubPc, **SubPc 2.VIII** was linked by an acetylene bridge while **SubPc 2.IX** had a single bond between both substructures. The devices were constructed with an ITO/ZnO/PBDB-T:acceptor/MoO_3/Al architecture. The single bond increased the LUMO and decreased aggregation regarding with **SubPc 2.VIII**, which contributed to higher V_{OC}, J_{SC} and FF, thus reaching a higher value of PCE 4.53% instead of 1.78%, value obtained for **SubPc 2.VIII**.

Later, the same group published two other SubPc derivatives with a phenoxyl group in axial position and two different electron acceptors as end groups, the 2-(3-oxo 2,3-dihydroinden-1-ylidene)malononitrile (IC, **SubPc 2.X**) and 2-(5,6-difluoro-3-oxo-2,3-dihydro-1H-inden-1-ylidene)malononitrile (2FIC, **SubPc 2.XI**). IC and 2FIC end groups were linked through thiophene bridges to SubPc core (**Figure 2.16b**).[147] These molecules were applied to solution processed NFA solar cells. Both derivatives presented strong absorption spectra between 400-700 nm. The efficient light harvesting abilities and good charge carrier transport properties produced PCEs of 4.69% and 3.80% for PBDB-T:**SubPc 2.X** and PBDB-T:**SubPc 2.XI**, respectively. The higher LUMO level of **SubPc 2.X** leaded to higher V_{OC} and PCE values in OCS compared to PBDB-T:**SubPc 2.XI**.

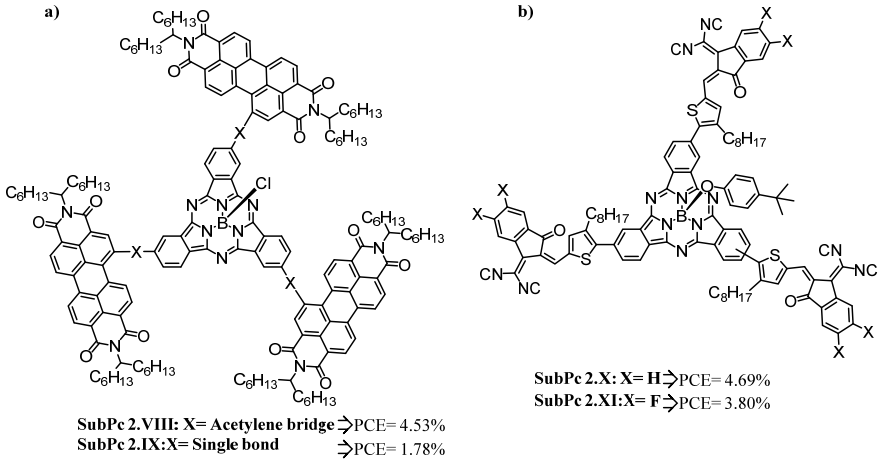

Figure 2.16-*Structures published by Hao.*

In the same year, ten new compounds were described with different alkyl or aryl imide groups fused to SubPcs bearing with F, Cl and phenoxyl groups in the axial position (**Figure 2.17**),[148] demonstrating that the solubility, the mobility and the

[147] H. Hao, X. Wu, Q. Xu, Y. Chen, H. Li, W. Wang, H. Tong, L. Wang, *Dyes Pigm.*, **2019**, *160*, 243−251.
[148] X. Huang, M. Hu, X. Zhao, C. Li, Z. Yuan, X. Liu, C. Cai, Y. Zhang, Y. Hu, Y. Chen, *Org. Lett.*, **2019**, *21*, 3382–3386.

phase separation of the derivatives were directly related to the substitution on these acceptors. An inverted architecture was used with four different donor polymers (PBDB-T-SF, PM6, PM7 and PBDB-T-D) and different solvent additives, obtaining 4.92% as the best performance using PM6:**SubPc 2.XIV**, 1,8-diiodooctane (DIO) as additive and thermal annealing.

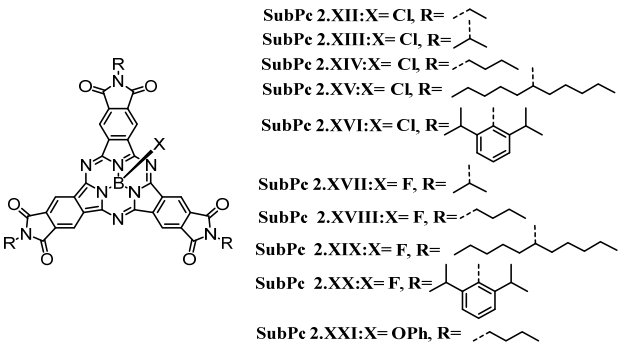

Figure 2.17- *Structures of* ***SubPc 2.XII-XXI****.*

2.3. Goal

The continuous search to improve solar efficiencies has given rise to several studies using a variety of chromophores in different types of solar cells. In this Thesis, it is pretended to build two new DPP families to enhance the DPP library of sensitizers for DSSCs and as acceptors in the active layer of BHJs.

Regarding the compounds for DSSCs, our objective was the synthesis and characterization of DPP units linked to a benzoic acid. The idea behind this work is, on the one hand to study the influence of the position of the anchoring group in the phenyl group used as spacer, thus *para, meta* and *ortho*-DPP acid derivatives were imagined. And on the other hand, with the symmetric derivative [**$(DPP)_2$ acid 11**] is pretended to understand the influence of the introduction of a second DPP moiety, that is, whether the increment of DPP moieties is favourable to the photovoltaic performance due to the existence of intramolecular singlet fission effects (**Figure 2.18**). The photovoltaic studies will be carried out by the Prof. Dirk Guldi´s group at the Friedrich Alexander University in Erlangen-Nürnberg, Germany.

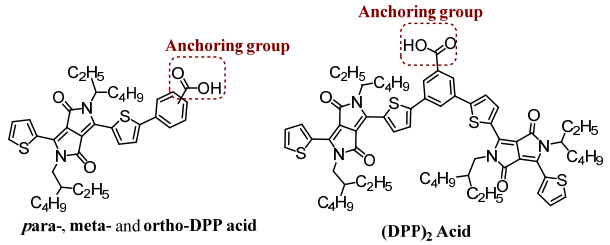

Figure 2.18- *Structures of the proposed compounds.*

On the other hand, it would be interesting to combine the properties of DPP and SubPc in order to have derivatives with a broad absorption in the UV-vis spectrum that contribute to the improvement of photovoltaic performances as non-fullerene acceptors in BHJs devices.

Thus, in this sense, four derivatives will be synthesized and characterized, containing a SubPc core and three DPP as wings linked by acetylene bridges using Cl or *tert*-butylphenoxy group in the axial position which will allow the study of the influence of this modifications on the optical properties and in the photovoltaic performance (**Figure 2.19**). Furthermore, we also pretend to scrutinize whether there is any difference in the photovoltaic response with the different regioisomers (C_1 and C_3). The photovoltaic studies will be carried out in Prof. Lluis Marsal´s group at the Universitat Rovira i Virgili in Tarragona, Spain.

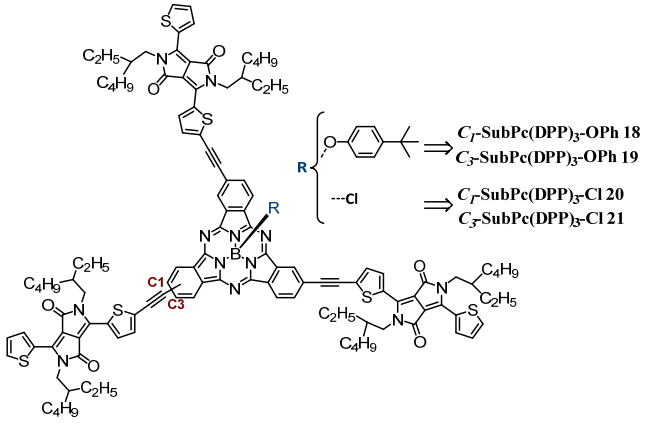

Figure 2.19-*Structures of the acceptors for the study in BHJs.*

2.4. Results and discussion

This section will be divided in two parts, in the first one (Sec. **2.4.1**) the synthesis, characterization and photovoltaic study of DPP acid derivatives will be presented (**DPP 9-11**). In the second part (Sec. **2.4.2**) the synthesis of SubPc(DPP)$_3$ derivatives (**18-21**) will be presented as well as the characterization and photovoltaic study.

2.4.1. DPP derivatives for DSSCs

2.4.1.1. Synthesis and characterization of DPP derivatives

The synthesis of compounds **9**, **10** and **11** was carried out via Suzuki-Miyaura coupling between **DPP 6** and the respective boronic esters **15**, **16** and **17**[149] giving rise to the intermediate compounds **DPP 12** (98%), **DPP 13** (97%) and **DPP 14** (57%) which were purified and characterized (first step in the **Scheme 2.1**). Then, hydrolysis reactions in basic medium led to the respective acids **9**, **10** and **11** with yields of 57%, 68% and 46%, respectively (second step in the **Scheme 2.1**). Regarding to *ortho*-DPP acid derivative, the hydrolysis reaction was unsuccessful, always leading to many degradation products, so, it was not possible to isolate the desired compound in reasonable quantities. In this way the characterization of the intermediate *ortho*-DPP ester will not be described in this manuscript.

Both the ester derivatives and the respective acids showed good solubility in solvents such as CH_2Cl_2, CH_3Cl, THF and toluene, moreover, the acids also happened to be soluble in MeOH.

[149] T. Chatzisideri, S. Thysiadis, S. Katsamakas, P. Dalezis, I. Sigala, T. Lazarides, E. Nikolakaki, D. Trafalis, O. A. Gederaas, M. Lindgren, V. Sarli, *Eur. J. Med. Chem.*, **2017**, *141*, 221- 231.

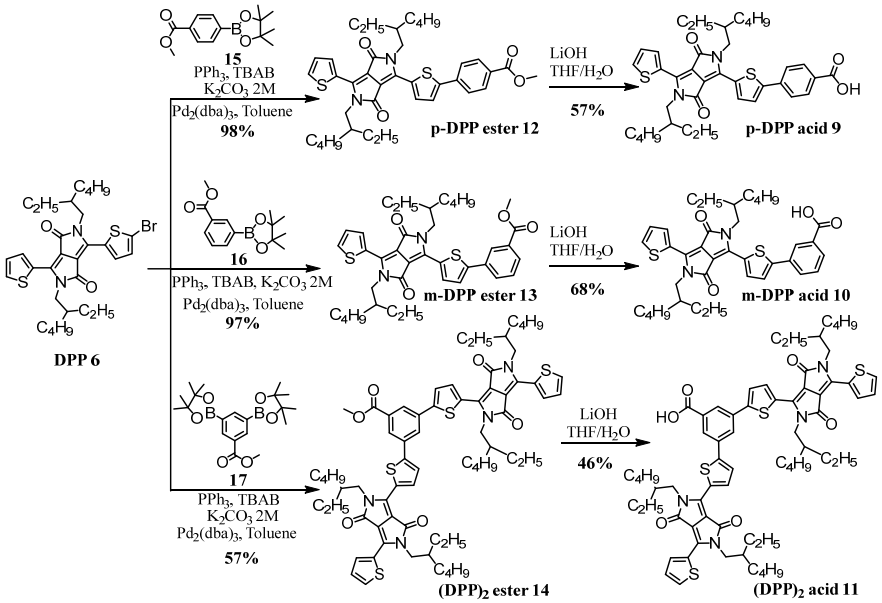

Scheme 2.1-*Synthetic route for compounds **9**, **10** and **11**.*

Regarding the characterization of intermediate compounds **12**, **13** and **14**, the structure could be confirmed by ^{1}H and ^{13}C NMR techniques, as well as by HR-MALDI-TOF mass spectrometry and FT-IR, see **Figures A9-A17**. On the other hand, the optical properties were revealed by the UV-vis and fluorescence spectra.

In relation to the ^{1}H NMR spectra of the compounds, slight differences could be appreciated, with the signals belonging to the benzene rings suffering the greatest shifts, as expected (**Figure 2.20**). In the case of the ***p*-DPP ester 12** two duplets centred at 8.04 ppm (**H7**) and 7.74 ppm (**H6**) could be appreciated, these two signals had the typical shape of two doublets of a *para*-substituted benzene ring. With respect to ***m*-DPP ester 13** four signals were assigned to the benzene ring centred at 8.33, 8.02, 7.87-7.83 and 7.54-7.48 ppm corresponding to the protons **H6**, **H9**, **H7** and **H8**, respectively. Whereas for compound **(DPP)$_2$ ester 14** two signals were observed at 8.29 and 8.07 ppm belonging to the **H6** and **H7**.

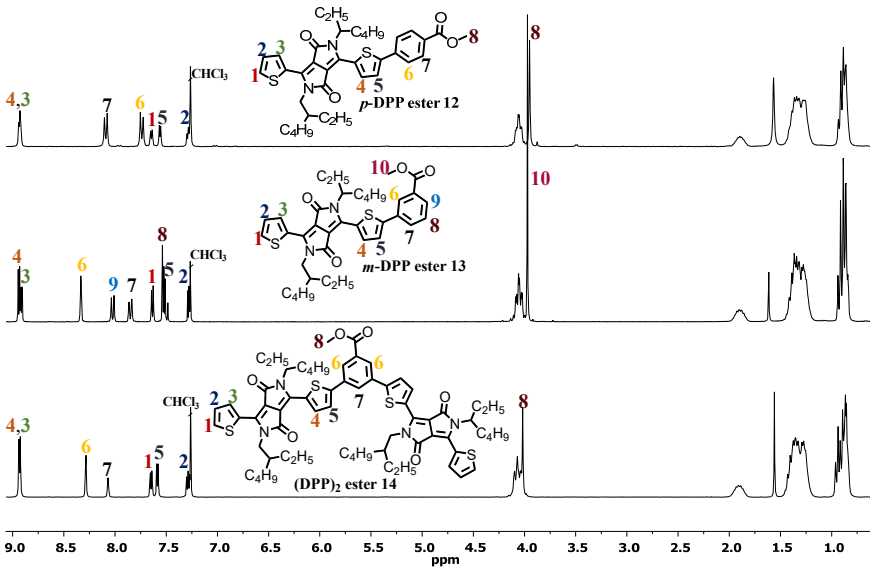

Figure 2.20- *^{1}H NMR spectra of **12**, **13** and **14** in $CDCl_3$ at 25 °C.*

Beyond the NMR spectra, HR-MALDI-TOF spectra also confirmed the presence of the pretended compounds, as the theoretical isotopic pattern of the molecular ion, $[M+H]^+$ for derivatives **12** and **14** and $[M]^-$ for ester **13**, coincided with the experimental isotopic pattern. However, in positive mode, the isotopic pattern obtained for **12** and **14** compounds is a mixture between the isotopes $[M+H]^+$ and $[M]^+$ (**Figures A11**, **A14** and **A17**).

Concerning to the structural characterization by ^{1}H NMR of the desired derivatives **9**, **10** and **11**, what stands out most at first glance was the absence of the singlet around 4.00 ppm that belongs to the CH_3 of the esters (**Figure 2.21**). The lack of this signal confirmed the complete hydrolysis of esters to acids. In addition, performing the spectra in DMSO allowed the observation of OH signals of the acids, which appeared at 13.12 ppm and 13.31 ppm for ***p*-DPP acid 9**, ***m*-DPP acid 10**, see **Figure A18** and **A21**. Unfortunately, **(DPP)$_2$ acid 11** was not soluble in DMSO. However, the disappearance of the carbon signals belonging to the C=O of the ester (at 166.11 ppm) and OCH_3 (around 55 ppm) were further confirmations that the hydrolysis was successful (**Figure A24**).

The FT-IR spectra are also in agreement with the conversion of the ester to the carboxylic acid due to the appearance of a band at 3347, 3446 and 3424 cm^{-1} corresponding to the O-H stretch of **9**, **10** and **11** carboxylic acids, respectively. On the other hand, the band corresponding to C=O of esters generally appears at a higher rangers (1730-1715 cm^{-1}) than acids that it appear between 1700-1680 cm^{-}

[1],[150] which is in agreement with the obtained values for the ester derivatives (1721 cm^{-1}, 1723 cm^{-1} and 1730 cm^{-1} were obtained for **12**, **13** and **14**, respectively), and for the acid derivatives (1699 cm^{-1} for **9**, 1695 cm^{-1} for **10** and 1721 cm^{-1} for **11**) (**Figures A20**, **A23** and **A25**).

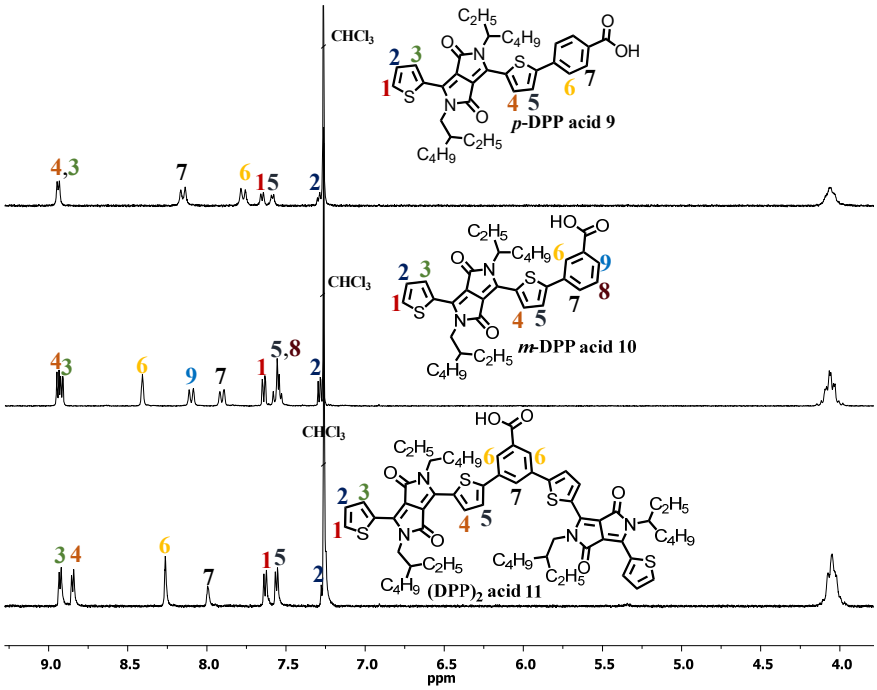

Figure 2.21- *Expansion of [1]H NMR between 9.25-4.0 ppm of the three acids,* **p-*DPP acid 9***, **m-*DPP acid 10*** *and* ***(DPP)$_2$ acid 11*** ($CDCl_3$ at 25 °C).

As in the case of ester derivatives, in the HR-MALDI-TOF spectra of the DPP acids **9-11** in positive mode, there are also a mixture of the $[M+H]^+$ and $[M]^+$ molecular ions (**Figure 2.22**).

[150] E. Pretsch, P. Bühlmann, C. Affolter, A. Herrera, R. Martínez, Structure Determination of Organic Compounds, Elsevier España S.L. **2002**, pag 290-293.

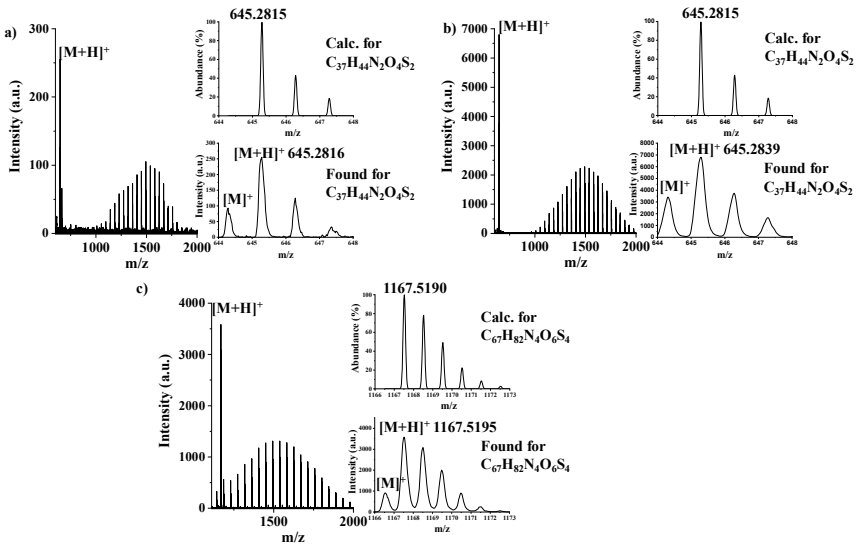

Figure 2.22- *HR-MALDI-TOF spectra of* ***9****,* ***10*** *and* ***11****.*

The optical properties of all intermediate and final products were properly characterized by UV-vis and fluorescence spectroscopies in CH_2Cl_2 (**Figure 2.23**, **Table 2.1)**. Analysing the ground state of the ester and acid derivatives, **Figure 2.23a** and **Figure 2.23b**, respectively, all the derivatives presented a band in the ultraviolet (320-420 nm) that was assigned as the π-π* transitions of the conjugated backbone, and the intramolecular charge transfer interactions between the thiophene donor and the DPP core was ascribed to the band that appeared between the 420-720 nm.[151] The resemblance in the shape of the spectra of the ester derivatives in relation with those of the corresponding acid derivatives was observed in all cases. Only the molar extinction coefficients changed, and in the case of ester derivatives higher values were obtained. Thus, for *para* derivatives values of 29000 $M^{-1}cm^{-1}$ and 36575 $M^{-1}cm^{-1}$ were obtained for ester and acid derivatives, respectively, and values of 82840 $M^{-1}cm^{-1}$ and 60819 $M^{-1}cm^{-1}$ for **(DPP)$_2$ ester 14** and **(DPP)$_2$ acid 11**, respectively. An exception ocurred for the *meta* derivatives, where the acid had a higher value (39881 $M^{-1}cm^{-1}$ *vs* 36043 $M^{-1}cm^{-1}$), see **Table 2.1**. In general, all derivatives showed red-shifted absorptions compared to **DPP 5**, which was used as reference. In the case of ester derivatives, ***m*-DPP ester 13** was the compound that suffered the smallest shift in relation with **DPP 5**, 21 nm (considering the maximum peak of the two compounds), while ***p*-DPP ester 12** and **(DPP)$_2$ ester 14** presented an identical shift of 32 and 31 nm, respectively. A closer look in the UV-vis spectra of the acid derivatives show the same results, meaning that between the three acids, the ***m*-DPP acid 10** suffered the smaller shift when compared with **DPP 5**.

[151] Y. Kim, C. E. Song, E.-J. Ko, D. Kim, S.-J. Moon, E. Lim, *RSC Adv.*, **2015**, *5*, 4811-4821.

To provide a first insight at the differences in the excited state, steady-state fluorescence measurements were performed (**Figure 2.23c** and **d**). The maximum between the esters and the corresponding acids did not change significantly, and the *para*-derivatives showed greater quenching in relation to the other derivatives.

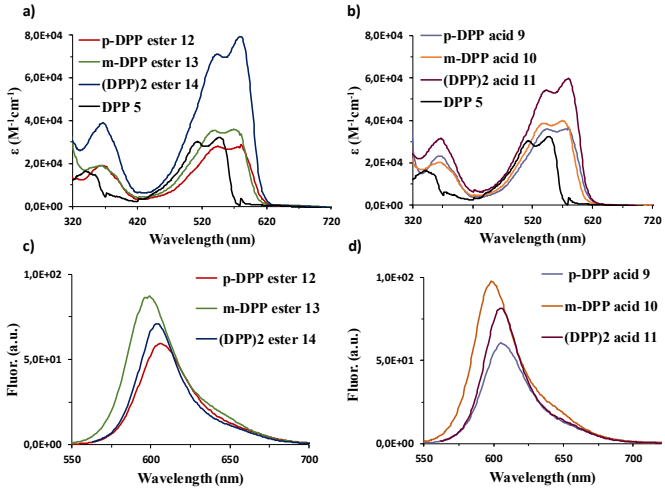

Figure 2.23- *Absorption spectra of* ***a)*** *ester derivatives* ***12***, ***13*** *and* ***14***. ***b)*** *acid derivatives* ***9***, ***10*** *and* ***11***. *Fluorescence spectra of* ***c)*** *ester derivatives* ***12***, ***13*** *and* ***14***. ***d)*** *acid derivatives* ***9***, ***10*** *and* ***11***.

Table 2.1- *Optical and electrochemical parameters of ester derivatives* ***12-14*** *and the respective acid derivatives* ***9-10.***

Compound	λ_{abs}(nm)/ ε($M^{-1}cm^{-1}$)	λ_{em} (nm)	Stoke Shift	E_{red1}/ E_{oxi1} (eV)	$-E_{g,opt}$/ $-E_{g,EC}$[a] (eV)	LUMO[b]	HOMO[c]
p-DPP 12	580/29000	604	24	-	2.09/ -	-	-
p-DPP 9	580/36575	605	25	-1.61/ 0.47	2.09/ 2.08	-3.19	-5.27
m-DPP 13	569/36043	599	30	-	2.12/ -	-	-
m-DPP 10	570/39881	599	29	-1.69/ 0.46	2.11/ 2.15	-3.11	-5.26
$(DPP)_2$ 14	579/82840	604	25	-	1.83/ -	-	-
$(DPP)_2$ 11	580/60819	606	26	-1.66 / 0.46	2.08/ 2.12	-3.14	-5.26

The energy positions of the HOMOs were estimated from the onset values for the oxidation potentials through: **a)** $E_{g,opt}$ was determined from the intersection of absorption and normalized emission spectra registered in CH_2Cl_2 ($E_{g,opt}$= 1240/λ [eV]) and $E_{g,EV}$ =E_{red1} – E_{oxi1}. **b)** LUMO was calculated by LUMO= **-** $\left|E_{red1}\right.$ (vs. Fc/Fc^+) + 4.8$\left.\right|$. **c)** HOMO was calculated by HOMO= LUMO - $E_{g,opt}$ (eV).

2.4.1.2. Photovoltaic performance-DSSCs

In order to study the possibility of electron transfer from excited DPP dyes to the TiO_2 conduction band, CV experiments of the three acid derivatives were performed using CH_2Cl_2 as solvent containing 0.1 M of $TBAPF_6$ as supporting electrolyte (**Figure 2.24a** and **Table 2.1**), potential values were obtained by oxidation and reduction DPVs. One quasi-reversible reduction wave was observed for the three products complementing the two quasi-reversible oxidations for **9** and **10** derivatives and three irreversible for **(DPP)$_2$ acid 11**. Both derivatives have similar oxidation values, however in the reduction waves slight differences were noticed due to different acceptor character of carboxylic acid, with ***p*-DPP acid 9** being a better electron-acceptor it means that is easier to be reduced.

The diagram presented at **Figure 2.24b** shows the energy levels of some components of n-type devices, where it is possible to observe that LUMOs of the acid derivatives are well aligned with the conduction band of TiO_2. In addiction HOMOs of the acid derivatives **9**, **10** and **11** are suitable to ensure that there is enough driving force to efficiently regenerate the dye by recapturing the injected electrons of I^- by the dye radical cation.

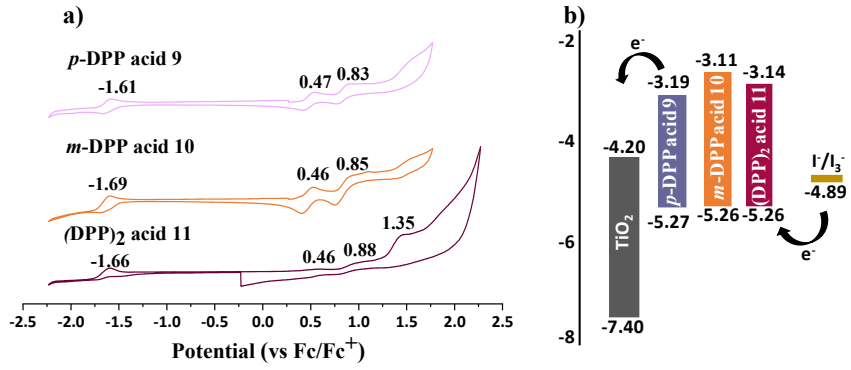

***Figure 2.24- a)** Cyclic voltammograms of **p-DPP acid 9**, **m-DPP acid 10** and **(DPP)$_2$ acid 11** in CH_2Cl_2 containing 0.1 M $TBAPF_6$ as supporting electrolyte and measured against Fc/Fc^+. **b)** Level diagram of DPP acid derivatives **9**, **10** and **11** with respect to the TiO_2 and the redox potential of the electrolyte.*

For a preliminary study of the new DPPs as dyes in solar cells, n-type cells were assembled with TiO_2 as n-type electrode material and **DPP 9-11** as photosensitizers. The slides of TiO_2 were immersed into an anhydrous THF solution of DPP dyes (5×10^{-5} M) for 30 min (***m*-DPP acid 10**), 90 min (***p*-DPP acid 9**) and 25 min [**(DPP)$_2$ acid 11**] in order to achieve optimal coverage of the semiconducting surface, realizing that the absorption increased with the time of exposure to the dyes until reaching a maximum and from then on the absorption

began to decrease, meaning that this maximum it is the ideal time for the optimal coverage (**Figure 2.25**).

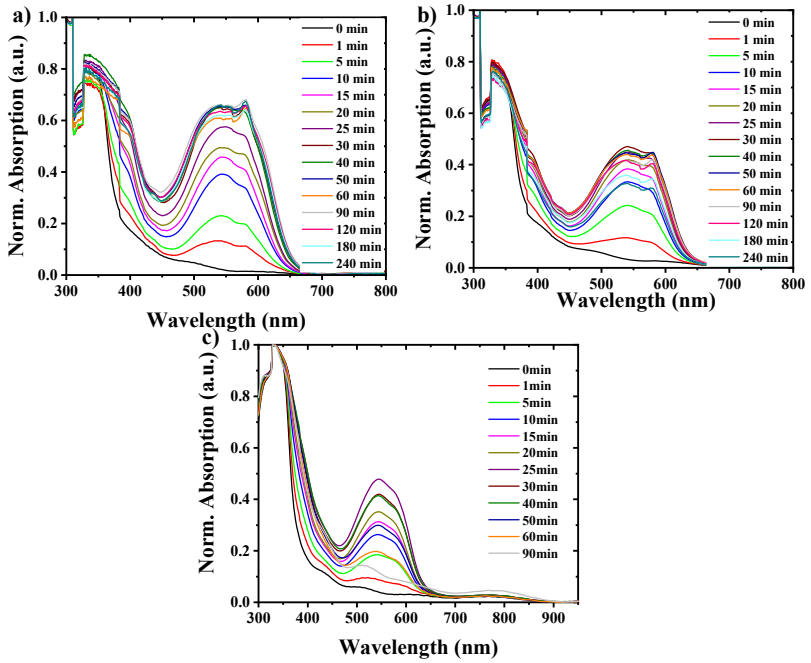

Figure 2.25- *Absorption kinetics of* ***a) p-DPP acid 9****,* ***b) m-DPP acid 10*** *and* ***c)(DPP)$_2$ acid 11****.*

The concentrations of iodine and lithium in the electrolyte were parameters to optimize, in order to increase the *Jsc* and facilitate dye regeneration and charge-injection. So, we started by finding the most favourable iodine concentration and knowing that we looked for the best lithium concentration. Then, the influence of the layer thickness was also studied.

At starting point, the devices were measured under 1 sun illumination and AM 1.5 conditions. The electrolyte used was an 85:15 v/v mixture of acetonitrile and valeronitrile with 0.6 M 1,2-dimethyl-3-propylimidazolium iodide, 0.5 M 4-*tert*-butylpyridine, 0.1 M iodine and 0.1 M lithium iodide. The photovoltaic response achieved for ***p*-DPP acid 9** was the best compared to the responses of the dyes **10** and **11**, with a J_{SC} of 5.54 mA/cm^2, a V_{OC} of 600 mV, FF of 68% and a PCE of 2.4%, perhaps due to a better electronic transport to the TiO_2 than the other DPPs. For ***m*-DPP acid 10** and **(DPP)$_2$ acid 11** PCE values of 1.02% (J_{SC} of 2.64 mA/cm^2, V_{OC} of 570 mV and FF of 68%) and 0.19% (J_{SC} of 0.54 mA/cm^2, V_{OC} of 570 mV and FF of 61%) were obtained, respectively. Although derivative **(DPP)$_2$ acid 11** has a much lower efficiency than ***p*-DPP acid 9**, the value of V_{OC} is not that different, perhaps derivative **11** prevents the electron recombination increasing the

V_{OC} value.[152] The lower values of J_{SC} for DPPs **10** and **11** were related to the lower IPCEs (**Figure 2.26**).

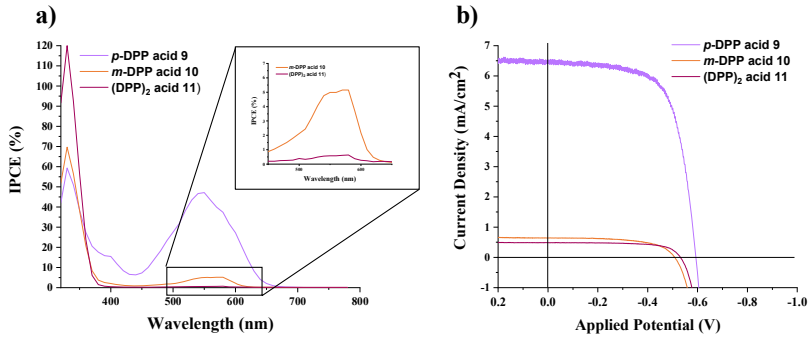

Figure 2.26- a) *IPCE spectra, and amplification, of the three dimers.* ***b)*** *J-V curves for* ***p-DPP acid 9****,* ***m-DPP acid 10*** *and* ***(DPP)₂ acid 11*** *devices.*

Regarding to iodine optimization, different concentrations of iodine were added (0.1-1.0 M) to the electrolyte maintaining constant the concentration of LiI (0.1 M). The figures-of-merit are summarized in **Figure 2.27**, where it is possible to observe that when iodine content exceed 0.1 M the photovoltaic parameters harmed. The PCE value of ***p*-DPP acid 9** at high iodine content was about 1.1%, while 0.2% and 0.08% values were obtained for ***m*-DPP acid 10** and **(DPP)₂ acid 11**, respectively. In the case of **(DPP)₂ acid 11**, there was a slight increase in J_{SC} value at a concentration of 0.3 M and the FF value slowly decreased and almost remained more or less constant at 39% from this concentration on (**Figure 2.27c**).

[152] W. Ying, J. Yang, M. Wielopolski, T. Moehl, J. Moser, P. Comte, J. Hua, S. M. Zakeeruddin, H.Tian, M. Grätzel, *Chem. Sci.*, **2014**, *5*, 206-214.

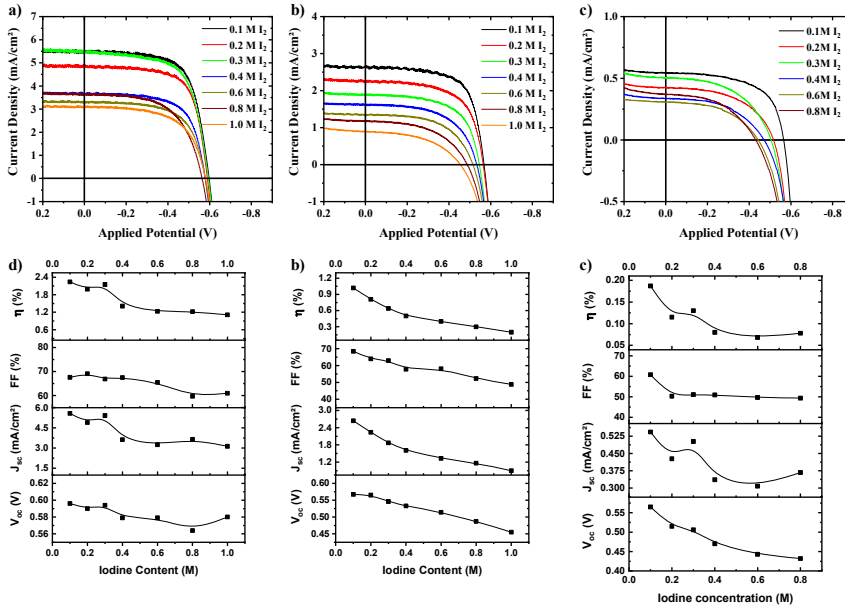

Figure 2.27- *J-V curves of* ***a) p-DPP acid 9****,* ***b) m-DPP acid 10*** *and* ***c) (DPP)$_2$ acid 11.*** *And figure-of-merit of the photovoltaic performance of* ***d) p-DPP acid 9****,* ***e) m-DPP acid 10*** *and* ***f) (DPP)$_2$ acid 11*** *featuring different contents of iodine.*

After studying the best concentration of iodine, lithium optimization for all dyes was explored in order to stablish the influence of this ion in the photovoltaic devices. Thus, the study started by establishing photovoltaic values without LiI. It was found that the presence of LiI is essential for the devices since photovoltaic parameters decreased compared to the values obtained with 0.1M LiI. ***p*-DDP acid 9** in absence of Li^+ achieved a PCE of 1.5%, whereas **DPP 10** and **DPP 11** achieved 0.13 and 0.07%, respectively.

Once addressed the importance of the LiI for the devices, $LiClO_4$ was added little by little in order to increase the lithium concentration, maintaining constant the amount of I_2/LiI (0.1:0.1 M). Analyzing the figures-of-merit, summarized in **Figure 2.28a-c**, the addition of $LiClO_4$ was harmful for ***p*-DPP acid 9** and ***m*-DPP acid 10**, because the PCE decreased with the increase in the amount of $LiClO_4$. Nevertheless, it was advantageous in the case of **(DPP)$_2$ acid 11** at least up to 0.5 M of $LiClO_4$, reaching a maximum PCE of 0.28% with a V_{OC} of 570 mV, a J_{SC} of 0.68 mA/cm^2 and a FF of 61%.

Regarding layer thickness optimization, several devices were made with different layer. In the case of derivatives **9** and **10** the best performance was obtained when the device was built with the thinnest layer. Generally, photovoltaic parameters decreased with increasing layer thickness, except for the V_{OC} of derivative **10** which increased with increasing layer thickness. FF values remained almost

constant with increasing of the layer thickness in the devices. On the other hand, best results for **11** were obtained the thickest layer (**Figure 2.28d-f**).

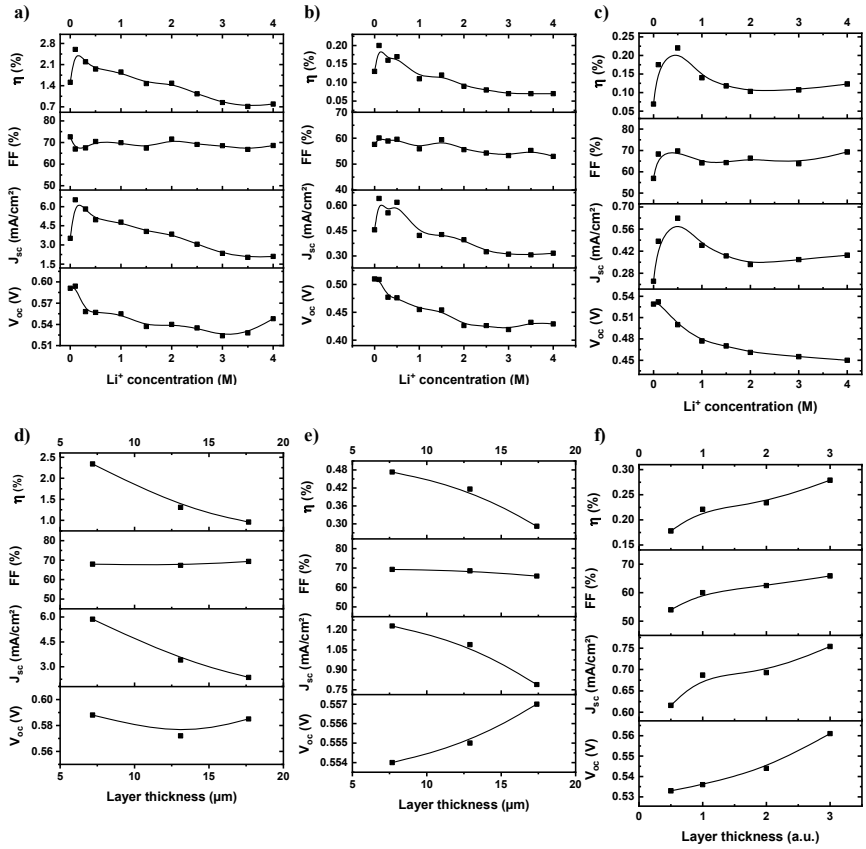

Figure 2.28- *Figure-of-merit of the photovoltaic performance of: lithium optimization* ***a) p-DPP acid 9***, ***b) m-DPP acid 10*** *and* ***c) (DPP)₂ acid 11***, *and layer thickness* ***d) p-DPP acid 9***, ***e) m-DPP acid 10*** *and* ***f) (DPP)₂ acid 11***.

2.4.2. SubPc-DPP derivatives for BHJs

2.4.2.1. Synthesis and characterization of SubPc-DPP acceptors

- **Intermediate compounds**

DPP 23 was obtained in two steps, the first one consisted of a Sonogashira coupling between **DPP 6** and ethynyltrimethylsilane giving rise to **DPP 22** with 92% yield, followed by a deprotection reaction of the etynyl group with K_2CO_3 in $CHCl_3$/MeOH in order to obtain **DPP 23** with 88% yield, as described in the literature (**Scheme 2.2**).[153]

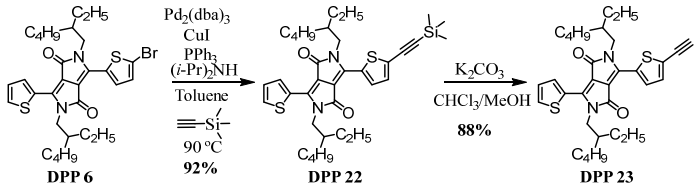

Scheme 2.2- *Synthetic route of* ***DPP 23****.*

To confirm the structure of the synthesized compounds, ^{1}H NMR spectra were acquiered and analysed as shown in the **Figure 2.29**. Confirmation that the reaction was successful was mainly due to the appearance of the singlet at 3.58 ppm (**H7** of **DPP 23**) instead of the singlet of the methyl group at 0.28 ppm (**H7** of **DPP 22**).

[153] C. Yu, Z. Liu, Y. Yang, J. Yao, Z. Cai, H. Luo, G. Zhang, D. Zhang, *J. Mater. Chem. C*, **2014**, 2, 10101-10109.

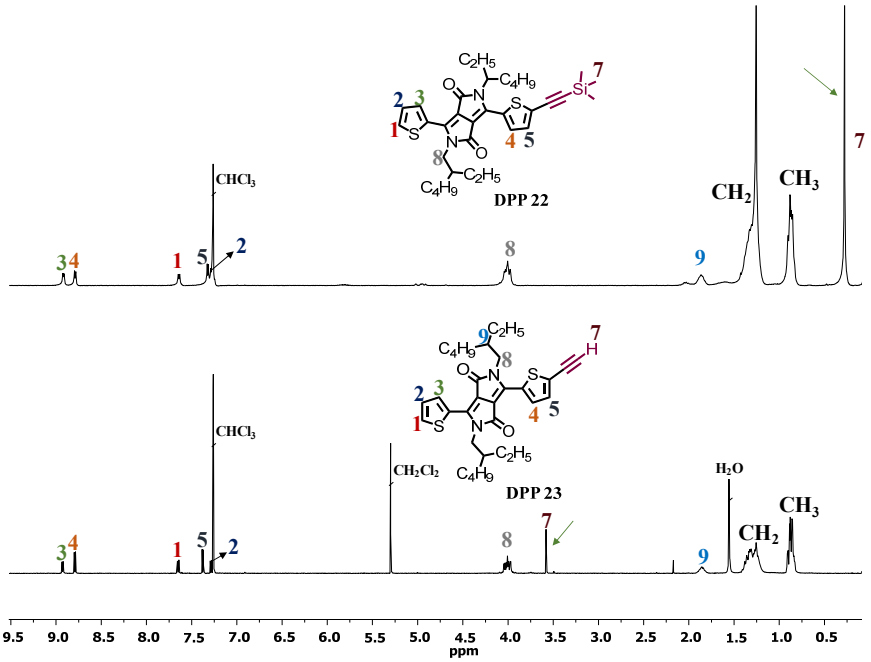

Figure 2.29- *^{1}H NMR of* ***DPP 22*** *and* ***DPP 23*** (CDCl$_3$ at 25 °C).

- **Synthesis of SubPc-(DPP)$_3$ derivatives**

The four SubPc(DPP)$_3$ acceptors (***C$_1$*-SubPc(DPP)$_3$-OPh 18**, ***C$_3$*-SubPc(DPP)$_3$-OPh 19**, ***C$_1$*-SubPc(DPP)$_3$-Cl 20** and ***C$_3$*-SubPc(DPP)$_3$-OPh 21**)[154] were synthesized by a Sonogashira coupling between **DPP 23** and the corresponding triiodo **SubPc I$_3$** (**Scheme 2.3**). **SubPc I$_3$**[155] was kindly provided by the research group of Prof. Torres. ***C$_3$*-SubPc(DPP)$_3$-OPh 19** was obtained with the best yield (i.e. 73%), whereas only a 17% yield was reached for regioisomer ***C$_1$*-SubPc(DPP)$_3$-OPh 18** due to problems in the purification process by chromatographic column. On the other hand, the SubPc(DPP)$_3$ derivatives ***C$_1$*-SubPc(DPP)$_3$-Cl 20** and ***C$_3$*-SubPc(DPP)$_3$-Cl 21**, with chloride on the axial position, proved to be quite unstable in silica gel, due to the replacement of the apical halogen by a hydroxyl group, yielding around 15% and 8%, respectively.

[154] To facilitate captions in figures or tables, compound names were sometimes abbreviated. For ***C$_1$*-SubPc(DPP)$_3$-OPh 18** was used ***C$_1$*-OPh 18**, for ***C$_3$*-SubPc(DPP)$_3$-OPh 19** was used ***C$_3$*-OPh 19**, for ***C$_1$*-SubPc(DPP)$_3$-Cl 20** was used ***C$_1$*-Cl 20** and for ***C$_3$*-SubPc(DPP)$_3$-OPh 21** was used ***C$_3$*-Cl 21**.

[155] a) C. G. Claessens, M. J. Vicente-Arana, T. Torres, *Chem. Commun.*, **2008**, 6378–6380. b) I. Sánchez-Molina, B. Grimm, R. M. Krick Calderon, C. G. Claessens, D. M. Guldi, T. Torres, *J. Am. Chem. Soc.,* **2013**, *135*, 10503−10511. c) C. G. Claessens, D. González-Rodríguez, B. del Rey, T. Torres, G. Mark, H.-P. Schuchmann, C. von Sonntag, J. G. MacDonald, R. S. Nohr, *Eur. J. Org. Chem.* **2003**, 2547-2551. d) C. G. Claessens, T. Torres, *Tetrahedron Lett.* **2000**, *41*, 6361-6365.

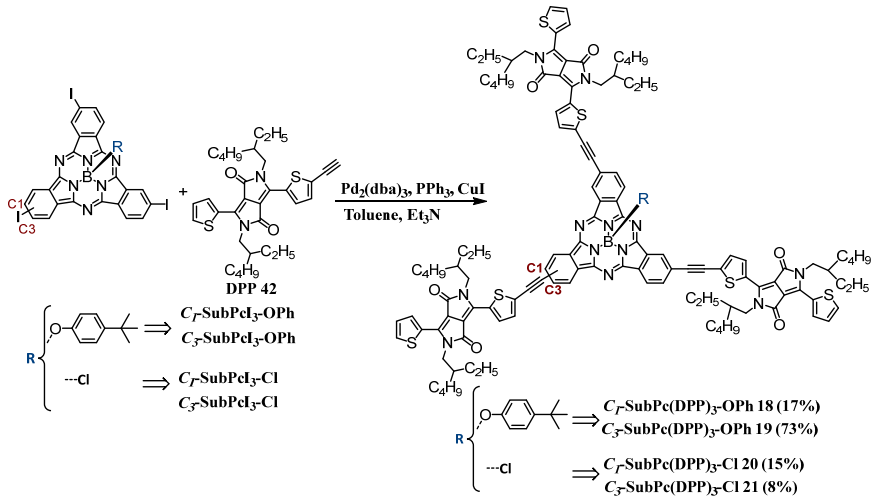

Scheme 2.3- *Synthetic route to SubPc(DPP)₃ derivatives* ***18-21****.*

The four derivatives were characterized by techniques that allow to confirm the chemical structures such as ^{1}H NMR, ^{11}B NMR (**Figure A26**, **A29** and **A32**), FT-IR (**Figure A27**, **A30** and **A33**) and MALDI-TOF (**Figure A28**, **A31** and **A34**). Optical (UV-VIS and fluorescence) and electrochemical properties (CV) were also carried out.

The ^{1}H NMR spectra of the same regioisomer have the same profile between them, it means that the shape of the spectra of C_1-symmetric derivatives, *i.e.* **C₁-SubPc(DPP)₃-OPh 18** and **C₁-SubPc(DPP)₃-Cl 20** have the same profile, and the same is valid for C_3-symmetric derivatives ***C₃*-SubPc(DPP)₃-OPh 19** and ***C₃*-SubPc(DPP)₃-Cl 21**. The great difference between the spectra of the OPh- and Cl-substitued derivatives were the presence of two doublets at 6.80 ppm and 5.35 ppm in the OPh-spectra belonging to **H2´** and **H1´**, respectively, signals attributed to the protons of the phenoxy group. Comparing the spectra of OPh-derivatives (i.e. ***C₁*-SubPc(DPP)₃-OPh 18** and ***C₃*-SubPc(DPP)₃-OPh 19**) it was possible to see a rupture of the symmetry environment in the ***C₁*-SubPc(DPP)₃-OPh 18** spectrum due to the presence of a more complex pattern.[156] This character was mainly observed in the signals between 8.84-8.80 ppm belonging to the DPP units (**HH** and **HC**), which appear for ***C₁*-SubPc(DPP)₃-OPh 18** in the form of two overlapping doublets centered at 8.83 ppm and 8.82 ppm and for ***C₃*-SubPc(DPP)₃-OPh 19** as doublet centered at 8.81 ppm (**HC**) (**Figure 2.30**). In the case of the ***C₁*-SubPc(DPP)₃-Cl 20** and ***C₃*- SubPc(DPP)₃-Cl 21** spectra, the same behavior was observed (**Figure 2.31**). Regarding to ^{11}B NMR spectra, a single singlet signal was

[156] C. Yu, Z. Liu, Y. Yang, J. Yao, Z. Cai, H. Luo, G. Zhang, D. Zhang, *J. Mater. Chem. C*, **2014**, 2, 10101-10109.

observed in all spectra, appearing at -14.60 ppm for OPh derivatives and -12.9 ppm and -13.9 ppm for **20** and **21** derivatives, respectively (**Figure A26**, **A29** and **A32**).

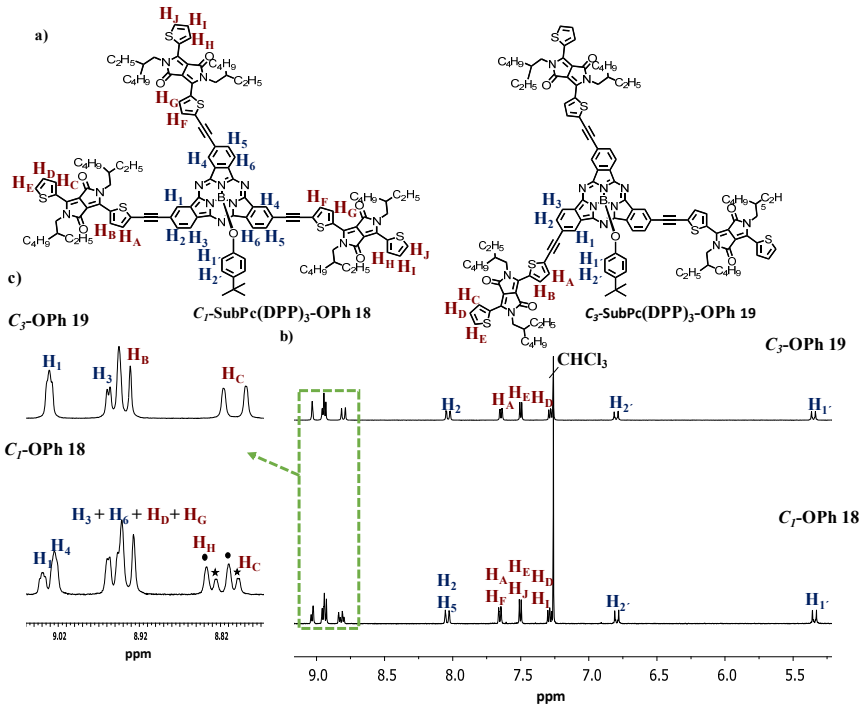

Figure 2.30- a) *Chemical structures of* ***C_1-SubPc(DPP)$_3$-OPh 18*** *and* ***C_3-SubPc(DPP)$_3$-OPh 19***. ***b)*** *Aromatic region of the ^{1}H NMR spectra of* ***C_1-SubPc(DPP)$_3$-OPh 18*** *and* ***C_3-SubPc(DPP)$_3$-OPh 19*** *($CDCl_3$, 25 °C).* ***c)*** *Aromatic regions zoom between 8.75 and 9.15-ppm, overlapping doublets between 8.79 and 8.82 ppm marked with circles and stars.*

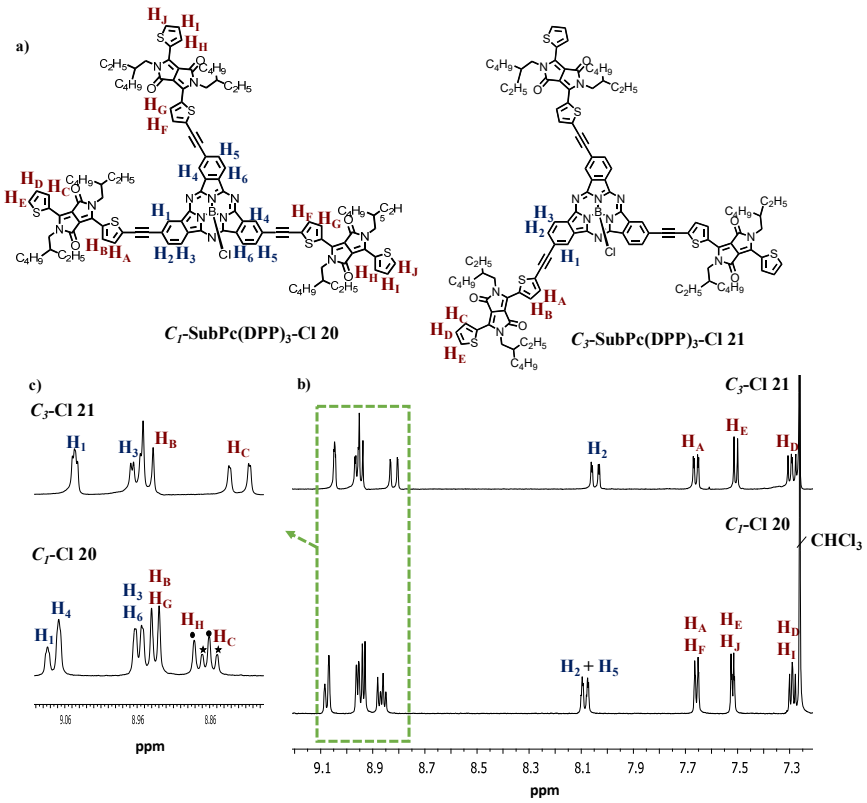

Figure 2.31- a) *Chemical structures of* ***C_1-SubPc(DPP)$_3$-Cl 20*** *and* ***C_3-SubPc(DPP)$_3$-Cl 21****. **b)** Aromatic region of the ^{1}H NMR spectra of* ***C_1-SubPc(DPP)$_3$-Cl 20*** *and* ***C_3-SubPc(DPP)$_3$-Cl 21*** *($CDCl_3$, 25 °C). c) Aromatic regions zoom between 7.79 and 9.10 ppm, overlapping doublets between 8.85 and 8.88 ppm marked with circles and stars.*

The MALDI-TOF MS technique also allowed confirming the structure of the compounds, showing *m/z* peaks at 2184.162 and 2184.191 for ***C_1*-SubPc(DPP)$_3$-OPh 18** and ***C_3*-SubPc(DPP)$_3$-OPh 19**, respectively, corresponding to $[M]^+$. Moreover, for Cl-derivatives **20** and **21** a *m/z* peak of 2068.906 ($[M+H]^+$) was obtained (**Figure A28**, **A31** and **A34**).

To gain insight into the ground-state interactions UV-vis measurements were made in $CHCl_3$ solution and in film (**Figure 2.32** and **Table 2.2**). In the spectra of the four acceptors two different bands were observed, one in the ultraviolet (250-450 nm) and other in the visible/ near IR (450-700 nm) regions (**Figure 2.32a** and **b**). The spectrum of ***C_1*-SubPc(DPP)$_3$-Cl 20** did not present the characteristic shape typically observed for SubPc chromophores, showing a broader Q-band at 592 nm with a molar extinction coefficient lower than the other derivatives (**Figure 2.32c**). This difference was connected with the existence of orbital overlap among the chromophoric units in ***C_1*-SubPc(DPP)$_3$-Cl 20** leading to a strong interaction in the

ground state. In contrast, the other derivatives ***C*$_1$-SubPc(DPP)$_3$-OPh 18**, ***C*$_3$-SubPc(DPP)$_3$-OPh 19** and ***C*$_3$-SubPc(DPP)$_3$-Cl 21** presented the typical shape of SubPc with a maximum peak at 654, 623 and 624 nm, respectively. Besides, all three spectra exhibit a shoulder attributable to the DPP units at 553, 550, and 554 nm, respectively.

Comparing the SubPc(DPP)$_3$ derivatives with the reference compounds (**DPP 5** and **SubPcI$_3$**), the Q-band of the four acceptors suffered a red-shift. ***C*$_3$-SubPc(DPP)$_3$-OPh 19** suffered the largest displacement (*i.e.* 54 nm) and ***C*$_1$-SubPc(DPP)$_3$-Cl 20** the smallest red-shift (*i.e.* 19 nm). The bathochromic shift of the Soret and Q-bands of the acceptors, compared to the corresponding SubPc reference compounds, was attributed to an increase in the π-conjugation of the ring by the substitution of the peripheral positions of the SubPc core with three DPP units (**Figure 2.32 a** and **b**).[138c]

Regarding to the spectra in the films, the absorbance peaks of the four acceptors showed a broader shape due to higher aggregation of the compounds in solid-state. A closer look at the absorption bands in film spectra allowed us to realize a red-shift of 21, 23, 10 and 18 nm in relation to the absorption peaks in solution of ***C*$_1$-SubPc(DPP)$_3$-OPh 18** (637 nm), ***C*$_3$-SubPc(DPP)$_3$-OPh 19** (646 nm), ***C*$_1$-SubPc(DPP)$_3$-Cl 20** (602 nm) and ***C*$_3$-SubPc(DPP)$_3$-Cl 21** (642 nm), respectively. OPh derivatives suffered higher shifts, which could be associated with a stronger intermolecular aggregation in the solid state (**Figure 2.32 d** and **Table 2.2**).

The excited states of the four new acceptors were studied by steady-state photoluminescence spectra carried out in $CHCl_3$ (**Figure 2.32 e** and **Table 2.2**). In close resemblance to the absorption spectra, compound ***C*$_1$-SubPc(DPP)$_3$-Cl 20** had a broader emission spectrum, suggesting a higher tendency toward aggregation in solution than the other compounds. Stokes shifts of all compounds vary from 17 to 29 nm, being ***C*$_3$-SubPc(DPP)$_3$-Cl 21** the compound with the lowest Stokes shift and ***C*$_1$-SubPc(DPP)$_3$-OPh 18** the one with the highest.

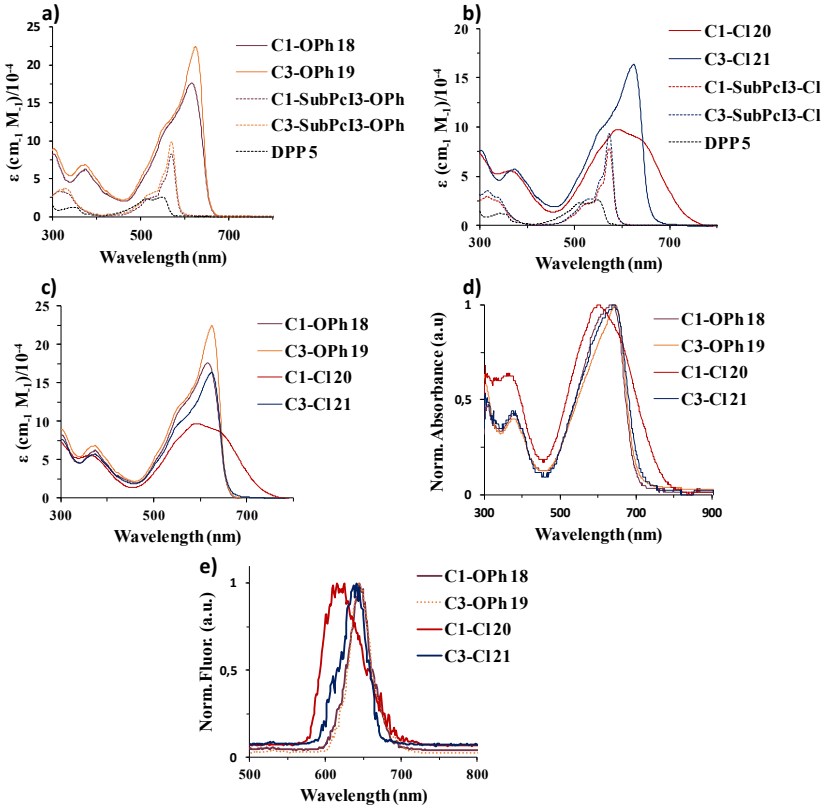

Figure 2.32- *Absorption spectra of* ***a) C_1-SubPc(DPP)$_3$-OPh 18***, ***C_3-SubPc(DPP)$_3$-OPh 19*** *(solid lines) and the corresponding precursors* ***C_1-SubPcI$_3$-OPh*** *and* ***C_3-SubPcI$_3$-OPh*** *(dashed lines) in $CHCl_3$ solution,* ***b) C_1-SubPc(DPP)$_3$-Cl 20***, ***C_3-SubPc(DPP)$_3$-Cl 21*** *(solid lines) and the corresponding precursors* ***C_1-SubPcI$_3$-Cl*** *and* ***C_3-SubPcI$_3$-Cl*** *(dashed lines) in $CHCl_3$ solution,* ***c)*** *compounds* ***18-21*** *in $CHCl_3$ solution and* ***d)*** *compounds* ***18-21*** *in film.* ***e)*** Normalized fluorescence spectra of the four acceptors in $CHCl_3$.

2.4.2.2. Photovoltaic performance-BHJs

In order to establish the HOMO and LUMO levels of the acceptors under study, the cyclic voltammetry was made in CH_2Cl_2 as solvent containing 0.1 M $TBAPF_6$ as supporting electrolyte (**Figure 2.33 a**). HOMO and LUMO values do not vary significantly between enantiomers of the same family, as can be observed in the scheme of energetic levels in **Figure 2.33 b**. However, the variation is significant when phenoxy is changed by a Cl since the phenoxy derivatives were more easily reduced and as a consequence, lower LUMO values were determined for this family (**Figure 2.33 a** and **Table 2.2**). For ***C_1*-SubPc(DPP)$_3$-OPh 18** and ***C_3*-SubPc(DPP)$_3$-OPh 19** values of LUMO of -3.79 eV and -3.74 eV and HOMO of -5.74 eV, and -5.69 eV were estimated, respectively. On the other hand, LUMO values of -3.37 eV and -3.40 eV and HOMO values of -5.41 eV and -5.36 eV were

estimated for ***C*1-SubPc(DPP)3-Cl 20** and ***C*3-SubPc(DPP)3-Cl 21**, respectively (**Table 2.2**).

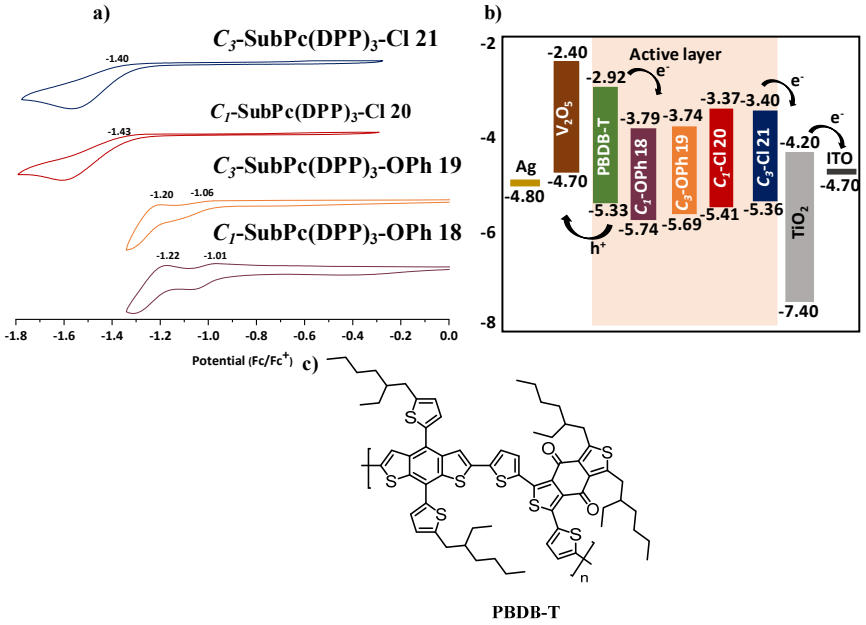

Figure 2.33- a) *Reduction waves of cyclic voltammograms vs Fc/Fc^+ of acceptors containing 0.1 M Bu_4NPF_6 as supporting electrolyte. b) Energy levels diagram for the device layers. c) Chemical structure of donor polymer PBDB-T.*

Table 2.2-*Optical and electrochemical parameters of compounds under study.*

CX-R	λ_{max}(nm)^{sol}/ $\varepsilon(M^{-1}cm^{-1})$[a]	λ_{max}^{film} (nm)	λ_{em} (nm) [a]	$E_{g,opt}$ [b]	E_{red1} (eV)	LUMO/ HOMO (eV)[c]
***C*1-OPh 18**	616/ 173780	637	645	1.95	-1.01	-3.79/ -5.74
***C*3-OPh 19**	623/ 223872	646	645	1.95	-1.06	-3.74/ -5.69
***C*1-Cl 20**	592/ 97724	602	615	2.04	-1.43	-3.37/ -5.41
***C*3-Cl 21**	625/ 162181	642	641	1.96	-1.40	-3.40/ -5.36

a) Absorption and emission spectra were measured in $CHCl_3$.**b)** $E_{g,opt}$ was determined from the intersection of absorption and normalized emission spectra registered in $CHCl_3$ ($E_{g,opt}$ = 1240/λ [eV]). c) LUMO was calculated by LUMO= - | $Ered_1$ (vs. Fc/Fc^+) + 4.8 |. And HOMO was calculated by HOMO= LUMO - $E_{g,opt}$ (eV).

The photovoltaic devices were fabricated with the inverted structure ITO/TiO_2/PBDB-T/SubPc(DPP)$_3$/V_2O_5/Ag. The energy levels of the four acceptors, compiled in **Figure 2.33b**, are well aligned with the respective LUMO and HOMO of the polymer PBDB-T (**Figure 2.33c**) allowing the movement of electrons and holes in the material, thus leading to a transfer of energy cascade. The device optimization was made in order to improve the photovoltaic performance and it was discovering that using an annealing temperature at 100 ºC, a chlorobenzene/DIO concentration of 99.5:0.5 (for SubPc(DPP)$_3$ **18**, **19** and **21**) and 99:1 (for SubPc(DPP)$_3$ **20**) and a donor/acceptor ratio of 1:1 with a final concentration of 20 mg mL^{-1} lead to the better results.

J-V curves of the best-performing optimized devices are presented in **Figure 2.34a**, whereas the best and average (of eight devices) values of performance characteristics are summarized in **Table 2.3**. Analyzing the photovoltaic values, what stand out most is the high V_{OC} values, around 1V, being a merit to what has been published in the literature.[157] A deeper look reveals that the OPh derivatives presented higher performance parameters than those constituted by SubPc(DPP)$_3$-Cl, having obtained the best efficiency with the ***C*$_1$-SubPc(DPP)$_3$-OPh 18**, 3.17%, and the worst with the ***C*$_1$-SubPc(DPP)$_3$-Cl 20** which presented an efficiency of 1.01%. In the case of OPh-derivatives both enantiomers presented similar performance, however in the case of Cl-derivatives, ***C*$_3$-SubPc(DPP)$_3$-Cl 21** regioisomer achieved an efficiency twice greater than ***C*$_1$-SubPc(DPP)$_3$-Cl 20**. This result indicates that symmetry of the peripheral substitution pattern influences the performance of OSCs when a chloride group is used in the axial position.

The external quantum efficiency (EQE) was also determined, and in all OSCs broad spectra from 300 to 800 nm were observed due to the absorption of PBDB-T and SubPc(DPP)$_3$ derivatives. Apart, of that from 450-500 nm the EQE spectra suffered a slight decrease since the acceptor derivatives presented low absorption over this range. By integrating the EQE spectra, *J*sc values were determined and proved to be similar to those calculated from the *J-V* curves (**Figure 2.34b** and **Table 2.3)**.

[157] a) Y. Cui, H. Yao, J. Zhang, K. Xian, T. Zhang, L. Hong, Y. Wang, Y. Xu, K. Ma, C. An, C. He, Z. Wei, F. Gao, J. Hou*, Adv. Mater.* **2020**, *32*, 1908205. b) Y. Lin, Y. Firdaus, F. H. Isikgor, M. I. Nugraha, E. Yengel, G. T. Harrison, R. Hallani, A. E.-Labban, H. Faber, C. Ma, X. Zheng, A. Subbiah, C. T. Howells, O. M. Bakr, I. McCulloch, S. D. Wolf, L. Tsetseris, T. D. Anthopoulos, *ACS Energy Lett.,* **2020**, *5*, 2935−2944

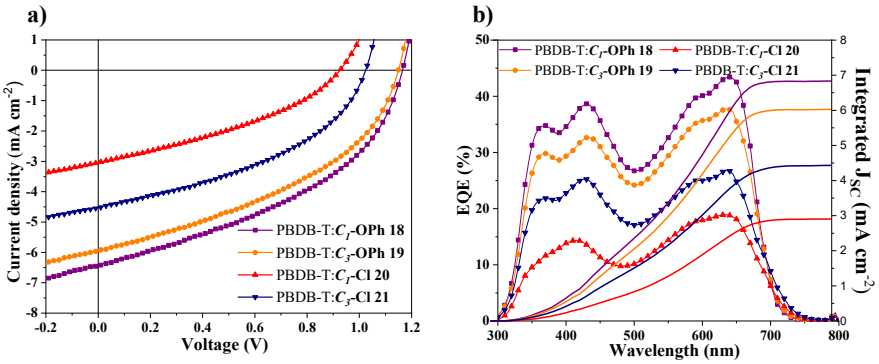

Figure 2.34- a) *J-V curves and* ***b)*** *EQE spectra of the best-performing OSCs based on the optimized blends of PBDB-T: SubPc(DPP)$_3$ acceptors.*

Table 2.3- *Photovoltaic parameter of the optimized OSCs based on PBDB-T:SubPc(DPP)$_3$ derivatives.*

PBDB-CX-R	V_{OC} (V)	J_{SC} (mAcm^{-2})	FF (%)	PCE (%)
***C$_1$*-OPh 18**	1.17 (1.16)	6.42 (6.39)	42.16 (41.63)	3.17 (3.08)
***C$_3$*-OPh 19**	1.15 (1.14)	5.95 (5.91)	41.35 (39.98)	2.83 (2.62)
***C$_1$*-Cl 20**	0.93 (0.89)	3.04 (2.89)	35.72 (36.07)	1.01 (0.91)
***C$_3$*-Cl 21**	1.02 (0.99)	4.50 (4.23)	42.02 (39.58)	1.93 (1.68)
PC$_{60}$BM	0.80 (0.70)	12.99 (12.44)	48.70 (46.78)	5.09 (4.64)

* Maximum value (average of eight devices)

By way of comparison, the PBDB-T:PC$_{60}$BM device was also fabricated in the same conditions as SubPc(DPP)$_3$-based devices. Although the devices based on PBDB-T:PC$_{60}$BM presented better photovoltaic performance (J_{SC} of 12.99 mA/cm^2, FF of 48.70%, and PCE of 5.09%.), the SubPc(DPP)$_3$ devices presented higher V_{OC} due to their lower LUMO values.

In order to evaluate the exciton dissociation and charge carrier transport performance of OSCs, the morphology of the active layer was studied by atomic force spectroscopy (AFM). To mimic the devices conditions, these films of active layer were deposited on TiO_2-covered ITO substrates. **Figure 2.35a-h** show the AFM images of the different acceptors, in all cases the blended thin films had a similar smooth surface. The thin films presented a root-mean-square roughness (RMS) range between 1.16 and 1.68 nm. Cl-derivatives exhibited less roughness (1.16 and 1.21 nm for ***C$_1$*-Cl 20** and ***C$_3$*-Cl 21**, respectively) than the OPh-derivatives (1.55 nm for ***C$_1$*-OPh 18** and 1.68 nm for ***C$_3$*-OPh 19**). In addition, thin films made with SubPc(DPP)$_3$-OPh derivatives presented higher peak-to peak values (17.57 nm and 15.34 nm for ***C$_1$*-SubPc(DPP)$_3$-OPh 18** and ***C$_3$*-SubPc(DPP)$_3$-OPh 19**, respectively) than those of thin films made with ***C$_1$*-**

SubPc(DPP)$_3$-Cl 20 and ***C*$_3$-SubPc(DPP)$_3$-Cl 21** (12.21 nm and 12.11 nm, respectively). Complementarily, the AFM 3D-images (**Figure 2.35i-l**) revealed that all PBDB-T: SubPc(DPP)$_3$ thin films have the similar "mountain and valley"-like aspect without significant differences in the morphology. Therefore, we assume that the reason for the limited efficiency of devices made with ***C*$_1$-SubPc(DPP)$_3$-Cl 20** and ***C*$_3$-SubPc(DPP)$_3$-Cl 21** could lie on the degree of recombination dynamics and exciton dissociation.[158]

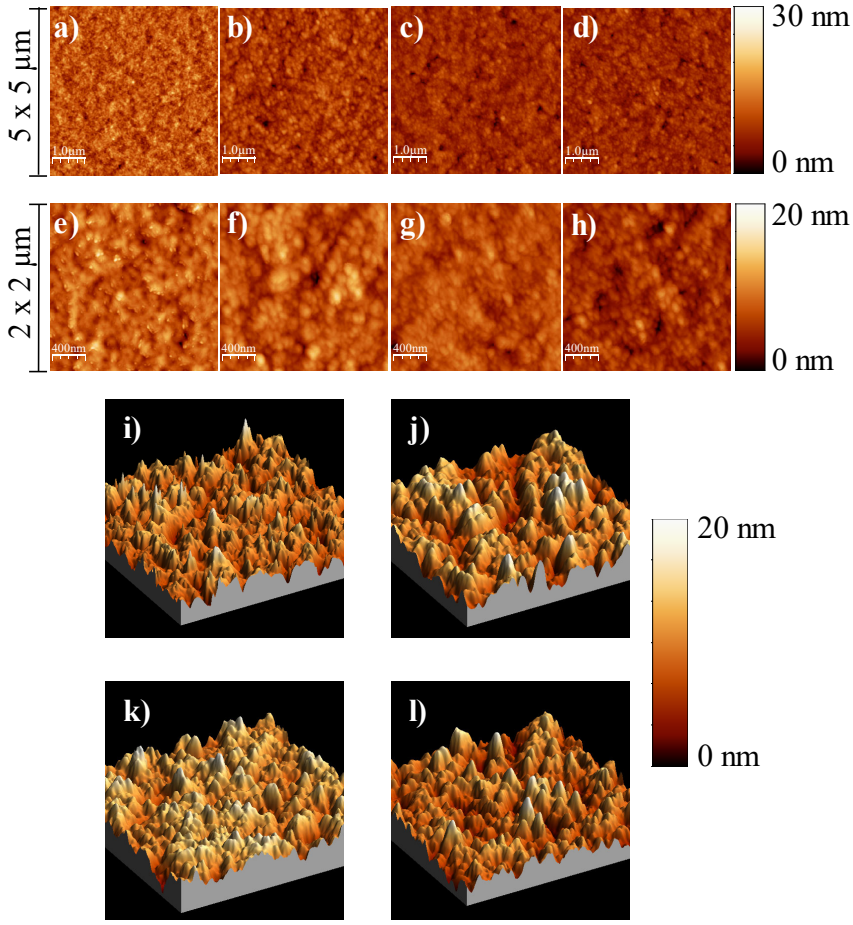

Figure 2.35- *AFM images of PBTB-T:**C*$_1$***-OPh 18** (**a**, **e**), PBTB-T:**C*$_3$***-OPh 19** (**b**, **f**), PBTB-T:**C*$_1$***-Cl 20** (**c**, **g**) and PBTB-T:**C*$_3$***-Cl 21** (**d**,**h**). The scan size is 5×5 (**a-d**) and 2×2 µm (**e-h**). AFM 3D-images for PBTB-T:**C*$_1$***-OPh 18** (**i**), PBTB-T:**C*$_3$***-OPh 19** (**j**), PBTB-T:**C*$_1$***-Cl 20** (**k**) and PBTB-T:**C*$_3$***-Cl 21** (**l**). The scan is 2×2 µm for all AFM images.*

[158] H. Cha, S. Wheeler, S. Holliday, S. D. Dimitrov, A. Wadsworth, H. H. Lee, D. Baran, I. McCulloch, J. R. Durran, *Adv. Funct. Mater.*, **2018**, *28*, 1704389.

2.5. Conclusions

In summary, two new families of DPP derivatives were described for their application in photovoltaic technology. On the one hand three different dyes were studied as photosensitizers in DSSCs, and on the other hand, four SubPc-DPPs were developed as acceptors of the active layer of BHJs.

Regarding DPP-sensitized solar cells, the three new derivatives were synthesized by a Suzuki-Miyaura coupling reaction on **DPP 6** to yield and the DPP ester derivatives **12**, **13** and **14**, which after hydrolysis in basic medium gave rise ***p*-DPP acid 9**, ***m*-DPP acid 10** and **(DPP)$_2$ acid 11** with 57%, 68% and 46% yield, respectively.

These dyes have been used as photosensitizers in n-type DSSCs. After the electrolyte optimization, the best PCEs were 2.61%, 1.02% and 0.22% for ***p*-DPP acid 9**, ***m*-DPP acid 10** and **(DPP)$_2$ acid 11**, respectively. Regarding the layer thickness optimization, it was verified that bigger layer thickness increases the PCE value for **(DPP)$_2$ acid 11** which contradicts the observed tendency for the other derivatives. ***p*-DPP acid 9** achieved higher PV performance maybe due to a better electronic transport to the TiO_2 than the other DPPs.

In relation to the BHJ derivatives, four new star-shaped electron acceptors based on a SubPc core decorated with three DPP wings linked through an acetylene bridge were synthesized by a Suzuki-Miyaura reaction between **DPP 23** and the $SubPcI_3$.

The four compounds present a broad absorption in the 450-700 nm range. Unexpectedly, the absorption spectrum of ***C*$_1$-SubPc(DPP)$_3$-Cl 20** was found to slightly differ from those of the other derivatives, as it exhibits a broader Q-band with a lower molar extinction coefficient.

All these materials were probed as acceptors in BHJ-inverted polymer solar cells, with the polymer PBDB-T as the donor counterpart. After optimizing several experimental parameters, the best photovoltaic performance was obtained for ***C*$_1$-SubPc(DPP)$_3$-OPh 18**, with a V_{OC} as high as 1.17 V, a PCE of 3.17%, a J_{SC} of 6.42 mA/cm^2 and a FF of 42.16%. These results can be attributed to the good electron mobility and low electron trap density. On the other hand, ***C*$_1$-SubPc(DPP)$_3$-Cl 20** gave rise to the lowest photovoltaic parameters (PCE of 1.01%). ***C*$_3$- SubPc(DPP)$_3$-OPh 19** afforded better PCE than the other C_3-regioisomer, perhaps due to higher V_{OC} and J_{SC} values because the latter achieved a higher FF (42.16% *vs.* 41.35%).

Briefly, the OPh derivatives gave the best results as acceptors in the studied conditions. Whereas for the axially chlorinated derivatives it was found that the C_1

regioisomer present better photovoltaic parameters than the C_3 species, for the OPh-substituted species the two regioisomers afforded similar values.

Although the PCE values were not as high as those already described in the literature, these compounds exhibited exceptionally high V_{OC} values and for this reason, they are high promising NFAs for application in ternary OSCs in which a high V_{OC} is desired.

2.6. Experimental section

2.6.1. Material and methods

All chemicals and solvents were purchased from Sigma Aldrich (Merck) and TCI and were used without further purification unless otherwise stated.

Column chromatography was performed with SiO_2 (40–63 μm) and the thin-layer chromatography was made using SiO_2 60F254 and were visualized with UV light.

NMR data (^1H and ^{13}C) was recorded at 25 °C with a Bruker AC300 spectrometer with chemical shifts referenced to residual TMS or to the residual signal solvent.

Matrix assisted laser desorption/ionization time-of-flight (MALDI-TOF) mass spectra were obtained on a Bruker Microflex LRF20 instrument using dithranol as a matrix.

UV-vis spectra in CH_2Cl_2, $CHCl_3$ and toluene solution were measured with a Helios Gamma spectrophotometer and the extinction coefficients were calculated using the Lambert-Beer Law.

FT-IR spectra were measured with a Nicolet Impact 400D spectrophotometer.

Cyclic voltammetry measurements were performed in 0.1M tetrabutylammonium hexafluorophosphate dichloromethane solution as support electrolyte, a graphite working electrode, a Ag/Ag^+ reference electrode, and carbon counter electrode using a potentiostat/galvanostat μAutolab Type III.

2.6.2. Synthesis of the derivatives for DSSC

2.6.2.1. Synthesis of methyl 3,5-bis(4,4,5,5-tetramethyl-1,3,2-dioxaborolan-2-yl) benzoate (17)

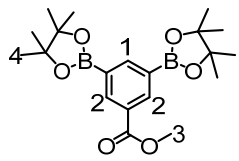

Methyl 3,5-dibromobenzoate (150 mg, 0.51 mmol) and $Pd(dppf)Cl_2$ (22 mg, 0.027 mmol) were added to a round-bottom flask under inert atmosphere. Then, 2.6 mL of dry toluene were added, and the mixture was degassed with argon. Dry trimethylamine (0.6 mL) and 4,4,5,5-

tetramethyl-1,2,3-dioxaboralane (0.25 mL, 1.53 mmol) were successively added. The reaction was ultrasonicated and then it was stirred overnight at 120 ºC. After cooling, the reaction was filtered through celite, the filtrate was concentrated, and the mixture was purified by column chromatography using hexane/ethyl acetate 10:1 obtaining the compound as white solid in 40% yield. **^{1}H NMR** (300 MHz, $CDCl_3$): δ (ppm) 8.56 (s, 2H, H_1), 8.43 (s, 2H, H_2), 3.91 (s, 3H, H_3), 1.35 (s, 24H, H_4).

2.6.2.2. Synthesis of ester derivatives

DPP 6 (150 mg, 0.249 mmol), the corresponding methyl benzoate derivative (196 mg, 0.75 mmol), TBAB (3.2 mg, 0.01 mmol) and PPh_3 (52 mg, 0.025 mmol) were added under nitrogen to a 25 mL round-bottom flask. Then, 5 mL of degassed toluene were added to the flask and the solution was degassed again. Afterwards, a degassed K_2CO_3 2 M solution (1 mL), and $Pd_2(dba)_3$ (23 mg, 0.025 mmol) solution in toluene (3 mL) were added to the reaction flask. The reaction was stirred overnight at 100 °C. After that, the crude was filtered through a celite head. The compounds were purified by silica gel column chromatography obtaining dark pink solids.

- **Methyl 4-(5-(5-(2-ethylhexyl)-2-(heptan-3-yl)-3,6-dioxo-4-(thiophen-2-yl)-2,3,5,6-tetrahydropyrrolo[3,4-*c*]pyrrol-1-yl)thiophen-2-yl)benzoate (*p*-DPP ester 12):** Eluent $CHCl_3$. Yield 98%.

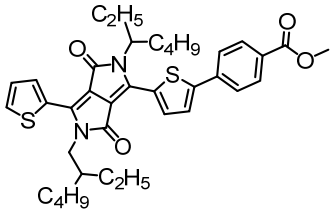

^{1}H NMR (300 MHz, $CDCl_3$): δ (ppm) 8.94-8.92 (m, 2H), 8.09 (d, *J*= 8.0 Hz, 2H), 7.74 (d, *J*= 8.4 Hz, 2H) 7.65 (d, *J*= 4.8 Hz, 2H), 7.56 (d, *J*= 4.2 Hz, 1H), 7.30-7.26 (m, 1H), 4.14-4.00 (m, 4H), 3.95 (s, 3H), 1.92-1.86 (m, 2H), 1.39-1.28 (m, 16H), 0.93-0.86 (m, 12H). **^{13}C-NMR:** ($CDCl_3$): δ (ppm) 166.6, 161.9, 161.86, 147.9, 137.4, 136.7, 135.6, 130.9, 130.6, 130.3, 130.1, 130.0, 128.6, 126.0, 125.8, 108.7, 108.2, 52.4, 46.1, 39.4, 39.2, 28.7, 28.5, 23.7, 23.2, 23.2, 14.2, 14.2, 10.7, 10.7. **FT-IR (KBr)** ν (cm^{-1}): 2958, 2931, 2857, 1721, 1668, 1603, 1559, 1448, 1403, 1278, 1233, 1183, 1107, 853-694. **UV-vis** (CH_2Cl_2), λmax (log ε): 365 (4.28), 544 (4.44), 580 (4.46). **HR-MS (MALDI-TOF):** 659.2972 m/z cal. for $C_{38}H_{46}N_2O_4S_2$ (found for $[M+H]^+$ 659.2972).

- **Methyl 3-(5-(5-(2-ethylhexyl)-2-(heptan-3-yl)-3,6-dioxo-4-(thiophen-2-yl)-2,3,5,6-tetrahydropyrrolo[3,4-*c*]pyrrol-1-yl)thiophen-2-yl)benzoate (*m*-DPP ester 13):** Eluent $CHCl_3$. Yield 97%.

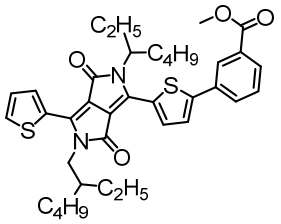

^{1}H NMR (300 MHz, $CDCl_3$): δ (ppm) 8.94 (d, *J*= 4.2 Hz, 1H), 8.92 (d, *J*= 3.9 Hz, 1H), 8.34-8.33 (m, 1H), 8.02 (d, *J*= 7.8 Hz, 1H), 7.86-7.83 (m, 1H), 7.64 (d, *J*= 2.8 Hz, 1H) 7.54-7.48 (m, 2H), 7.29-7.26 (m, 1H), 4.14-3.99 (m, 4H), 3.97 (s, 3H), 1.92-1.88 (m, 2H), 1.41-1.25 (m, 16H), 0.94-0.84 (m, 12H). **^{13}C-NMR:** (75 MHz, $CDCl_3$): δ (ppm) 166.6, 161.89, 161.85, 148.3, 136.7, 135.5, 131.4, 130.7, 130.4, 130.0, 129.8, 129.4, 128.6, 127.2, 125.2, 108.5, 108.3, 52.5, 46.1, 39.4, 39.3, 30.5, 28.7, 28.5, 23.9, 23.7, 23.2, 14.2, 10.72, 10.66. **FT-IR (KBr)** *ν* (cm^{-1}): 2990, 2956, 2858, 1723, 1666, 1560, 1447, 1403, 1263, 1288, 1263, 1112, 1088, 1030, 855-717. **UV-vis** (CH_2Cl_2), λmax (log ε): 364 (4.28), 539 (4.55), 569 (4.56). **HR-MS (MALDI-TOF):** 658.2904 m/z cal. for $C_{38}H_{46}N_2O_4S_2$ (found for $[M]^-$ 658.2906).

- **Methyl 3-(5-(5-(2-ethylhexyl)-2-(heptan-3-yl)-3,6-dioxo-4-(thiophen-2-yl)-2,3,5,6-tetrahydropyrrolo[3,4-*c*]pyrrol-1-yl)thiophen-2-yl)-5-(5-(2-(2-ethylhexyl)-5-(heptan-3-yl)-3,6-dioxo-4-(thiophen-2-yl)-2,3,5,6-tetrahydropyrrolo[3,4-c]pyrrol- 1-yl) thiophen-2-yl) benzoate [(DPP)$_2$ ester 14]:**

It is important to note that 2 equivalents of **DPP 6** (140 mg, 0.233 mmol) were used in relation to ester **36** (46 mg, 0.116 mmol). Eluent CH_2Cl_2. Yield 57%.

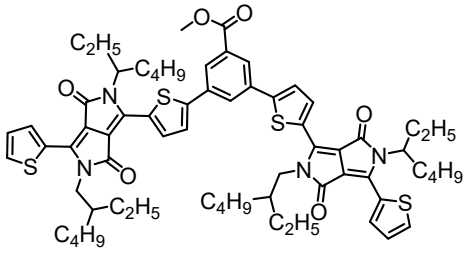

^{1}H NMR (300 MHz, $CDCl_3$): δ (ppm) 8.94-8.92 (m, 4H), 8.29 (d, *J*= 1.8 Hz, 2H), 8.07 (t, *J*= 1.8 Hz, 1H), 7.65 (dd, *J*= 5.1 Hz, *J*= 1.2Hz, 2H), 7.59 (d, *J*= 4.2 Hz, 2H), 7.30-7.27 (m, 2H), 4.10-4.02 (m, 11H), 1.95-1.84 (m, 2H), 1.43-1.25 (m, 32H), 0.96-0.83 (m, 24H). **^{13}C-NMR:** (75 MHz, $CDCl_3$): δ (ppm) 166.1, 161.9, 161.8, 147.2, 140.9, 139.8, 136.6, 135.7, 134.8, 130.9, 130.1, 130.0, 128.7, 127.1, 125.8, 108.8, 108.2, 52.8, 46.1, 39.4, 39.3, 30.4, 28.7, 28.5, 23.9, 23.7, 23.2, 14.2, 10.8, 10.7. **FT-IR (KBr)** *ν* (cm^{-1}): 2957, 2928, 2857, 1730, 1672, 1557, 1446, 1408, 1265, 1232, 1091, 875-712. **UV-vis** (CH_2Cl_2), λmax (log ε): 366 (4.61), 543 (4.87), 579 (4.92). **HR-MS (MALDI-TOF):** 1181.5346 m/z cal. for $C_{68}H_{84}N_4O_6S_4$ (found for $[M+H]^+$ 1181.5322).

2.6.2.3. Synthesis of acid derivatives

DPP ester derivatives (100 mg, 0.151 mmol) were dissolved in 12 mL of THF. Later, $LiOH.H_2O$ (57 mg, 1.13 mmol) and H_2O (4 mL) were added to the previous solution. The mixture was allowed to stir for 30 minutes in an ice bath, and then the reaction was heated to 60 ºC, until there is total hydrolysis. After that, the crude was washed with 2M HCl and H_2O and extracted with $CHCl_3$. The compounds were purified by silica gel column chromatography using THF/toluene 8:3 as eluent obtaining dark pink solids.

- **4-(5-(5-(2-ethylhexyl)-2-(heptan-3-yl)-3,6-dioxo-4-(thiophen-2-yl)-2,3,5,6-tetrahydropyrrolo[3,4-*c*]pyrrol-1-yl)thiophen-2-yl)benzoic acid (*p*-DPP acid 9):** Yield 57%

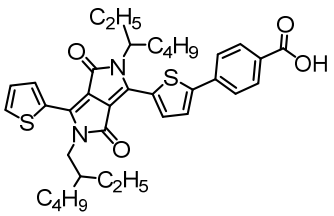

^{1}H NMR (300 MHz, $CDCl_3$): δ (ppm) 8.93 (d, *J*= 3.9 Hz, 2H), 8.15 (d, *J*= 8.1 Hz, 2H), 7.79 (d, *J*= 8.7 Hz, 2H), 7.65 (d, *J*= 5.1 Hz, 1H), 7.59 (d, *J*= 4.2 Hz, 1H), 7.30-7.26 (m, 1H), 4.11-4.07 (m, 4H), 1.94-1.86 (m, 2H), 1.43-1.24 (m, 16H), 0.94-0.86 (m, 12H). **^{13}C-NMR:** (75 MHz, $CDCl_3$): δ (ppm) 169.9, 161.9, 161.9, 147.7, 140.9, 139.8, 138.2, 136.6, 135.7, 131.2, 131.0, 130.5, 130.0, 128.7, 126.0, 108.9, 108.3, 46.1, 39.5, 39.3, 30.5, 30.4, 28.8, 28.5, 23.9, 23.7, 23.3, 14.2, 14.2, 10.7, 10.7. **FT-IR (KBr)** *ν* (cm^{-1}): 2959, 2928, 2858, 1662, 1603, 1553, 1452, 1419, 1319, 1283, 1231, 856-704. **UV-vis** (CH_2Cl_2), λmax (log ε): 363 (4.36), 543 (4.55), 580 (4.56). **HR-MS (MALDI-TOF):** 645.2815 m/z cal. for $C_{37}H_{44}N_2O_4S_2$ (found for $[M+H]^+$ 645.2816).

- **3-(5-(2-(heptan-3-yl)-5-(2-methylbutyl)-3,6-dioxo-4-(thiophen-2-yl)-2,3,5,6-tetrahydropyrrolo[3,4-*c*]pyrrol-1-yl)thiophen-2-yl)benzoic acid (*m*-DPP acid 10):** Yield 68%

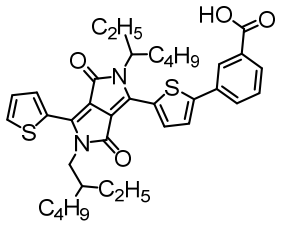

^{1}H NMR (300 MHz, $CDCl_3$): δ (ppm) 8.94 (d, *J*= 4.2 Hz, 1H), 8.92 (dd, *J*= 3.9 Hz, *J*= 1.2 Hz, 1H), 8.41 (s, 1H), 8.10 (d, *J*= 8.1 Hz, 1H), 7.90 (d, *J*= 8.1 Hz, 1H), 7.64 (dd, *J*= 5.1 Hz, *J*= 1.2 Hz, 1H), 7.58-7.53 (m, 2H), 7.30-7.28 (m, 1H), 4.12-4.03 (m, 4H), 1.95-1.84 (m, 2H), 1.39-1.25 (m, 16H), 0.94-0.86 (12H). **^{13}C NMR:** (75 MHz, $CDCl_3$): δ (ppm) 161.9, 148.1, 140.6, 140.1, 135.5, 133.9, 130.8, 130.0, 129.7, 128.6, 125.4, 108.6, 108.3, 46.1, 39.5, 39.3, 30.5, 29.8, 28.5, 23.9, 23.8, 23.3, 23.2, 14.2, 10.7, 10.7. **FT-IR (KBr)** *ν* (cm^{-1}): 2960, 2929, 2871, 1695, 1657, 1557, 1458, 1401, 1298,1232, 858-708. **UV-vis** (CH_2Cl_2), λmax (log ε): 365 (4.31), 539 (4.59), 570 (4.60). **HR-MS**

(MALDI-TOF): 645.2815 m/z cal. for $C_{37}H_{44}N_2O_4S_2$ (found for $[M+H]^+$ 645.2839).

- **3-(5-(5-(2-ethylhexyl)-2-(heptan-3-yl)-3,6-dioxo-4-(thiophen-2-yl)-2,3,5,6-tetrahydropyrrolo[3,4-c]pyrrol-1-yl)thiophen-2-yl)-5-(5-(2-(2-ethylhexyl)-5-(heptan-3-yl)-3,6-dioxo-4-(thiophen-2-yl)-2,3,5,6-tetrahydropyrrolo[3,4-*c*]pyrrol-1-yl)thiophen-2-yl)benzoic acid [(DPP)$_2$ acid 11]:** Yield 46%

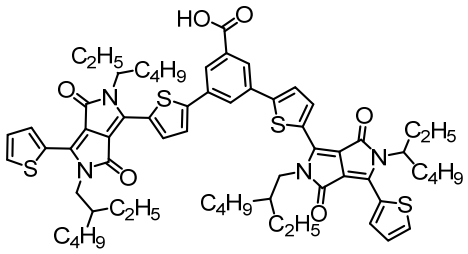

^{1}H NMR (300 MHz, $CDCl_3$): δ (ppm) 8.93 (d, *J*= 3.9 Hz, 2H), 8.85 (d, *J*= 3.9 Hz, 2H), 8.26 (s, 2H), 8.00-7.99 (m, 1H), 7.63 (d, *J*= 4.8 Hz, 2H), 7.56 (d, *J*= 3.9 Hz, 2H), 7.28-7.25 (m, 2H), 4.08-4.03 (m, 8H), 1.90-1.87 (m, 4H), 1.42-1.25 (m, 32H), 0.95-0.85 (m, 24H). **^{13}C NMR:** (75 MHz, $CDCl_3$): δ (ppm) 162.0, 161.8, 147.0, 140.9, 139.9, 136.5, 135.7, 134.8, 131.0, 130.2, 130.0, 128.7, 125.8, 108.9, 108.2, 46.1, 39.4, 30.4, 28.7, 28.5, 23.9, 23.7, 23.2, 14.2, 10.8, 10.7. **FT-IR (KBr)** ν (cm^{-1}): 2959, 2929, 2859, 1695, 1670, 1557, 1454, 1233, 1092, 856-734. **UV-vis** (CH_2Cl_2), λmax (log ε): 366 (4.50), 543 (4.74), 580 (4.78). **HR-MS (MALDI-TOF):** 1167.5190 m/z cal. for $C_{67}H_{82}N_4O_6S_4$ (found for $[M+H]^+$ 1167.5195).

2.6.3. Synthesis of the derivatives for BHJ

2.6.3.1. Synthesis of 2-(2-ethylhexyl)-5-(heptan-3-yl)-3-(thiophen-2-yl)-6-(5-((trimethylsilyl)ethynyl)thiophen-2-yl)-2,5-dihydropyrrolo[3,4-*c*]pyrrole-1,4-dione (DPP 22)

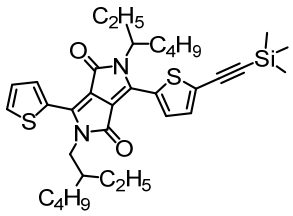

DPP 6 (600 mg, 0.997 mmol), $Pd_2(dba)_3$ (18.3 mg, 0.020 mmol), CuI (11.3 mg, 0.0060 mmol) and PPh_3 (42 mg, 0.159 mmol) were introduces into a 50 mL round-bottom flask under inert atmosphere. Then, 20 mL of degassed/anhydrous toluene and 5 mL of dry diisopropylamine [(*i*-Pr)$_2$NH] were added, finally, ethynyltrimethylsilane (196 mg, 19.9 mmol) was added. The reaction was heated overnight to 90 °C. After cooling to rt the crude solution was poured into H_2O and extracted several times with ethyl acetate. The combine organic extracts were dried over $MgSO_4$ and concentrated in vacuum. The compound was purified by silica gel column chromatography using $CHCl_3$: hexane 1.5:1 yielding a purple solid in 92%. **^{1}H NMR** (300 MHz, $CDCl_3$): δ (ppm) 8.92 (d, *J* =3.9 Hz, 1H), 8.79 (d, *J* =3.9 Hz, 1H), 7.64 (d, *J* =4.8 Hz, 1H), 7.33-7.29 (m,

2H), 4.04-3.98 (m, 4H), 1.89-1.82 (m, 2H), 1.23-1.31 (m, 16H), 0.90- 0.85 (m, 12H), 0.28 (s, 9H).

2.6.3.2. Synthesis of 2-(2-ethylhexyl)-6-(5-ethynylthiophen-2-yl)-5-(heptan-3-yl)-3-(thiophen-2-yl)-2,5-dihydropyrrolo[3,4-*c*]pyrrole-1,4-dione (DPP 23)

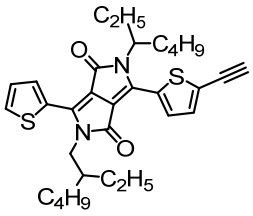

K_2CO_3 (542 mg, 3.93 mmol) was then 10 mL of MeOH were added to a solution of **DPP 22** (348 mg, 56 mmol) in CH_2Cl_2, the reaction was stirred during 3h. After this time, 1 mL of 2M HCl was added and the crude solution was then poured into H_2O and extracted several times with CH_2Cl_2. The organic extracts were dried over $MgSO_4$ and concentrated in vacuum. The compound was purified by silica gel column chromatography using CH_2Cl_2/hexane 2:1 affording a purple solid in 88% yield. **^{1}H NMR** (300 MHz, $CDCl_3$): δ (ppm) 8.93 (dd, *J* =3.9 Hz, *J* =0.9 Hz, 1H), 8.79 (d, *J* =4.2 Hz, 1H), 7.65 (dd, *J* =5.4 Hz, , *J* =1.2 Hz, 1H), 7.38 (d, *J* =4.2Hz, 1H), 7.29-7.27 (m, 1H), 4.09-3.92 (m, 4H), 3.58 (s, 1H), 1.88-1.82 (m, 2H), 1.41-1.26 (m, 16H), 0.91-0.85 (m, 12H).

2.6.3.3. Synthesis of SubPc-(DPP)$_3$ derivatives.

The corresponding $SubPcI_3$ (49 mg, 0.054 mmol), $Pd_2(dba)_3$ (31 mg, 0.035 mmol), CuI (6.8 mg, 0.035 mmol), PPh_3 (75 mg, 0.288 mmol) and 1 mL of anhydrous toluene were added under nitrogen to a 25 mL round-bottom flask. Then, 2 mL of triethylamine were added, and the solution was deoxygenated. Finally, a degassed solution containing **DPP 23** with 4 mL of toluene was added. The reaction was stirring overnight at rt After that, the crude was washed with 2M HCl and water and extracted with chloroform. The combined organic extracts were dried over $MgSO_4$ and concentrated in vacuum. The compounds were obtained in the form of dark blue solids.

- ***C1*-SubPc(DPP)3-OPh 18.** The compound was purified by silica gel column chromatography using 1:100 $CHCl_3$/ethyl acetate as eluent. Yield: 17%.

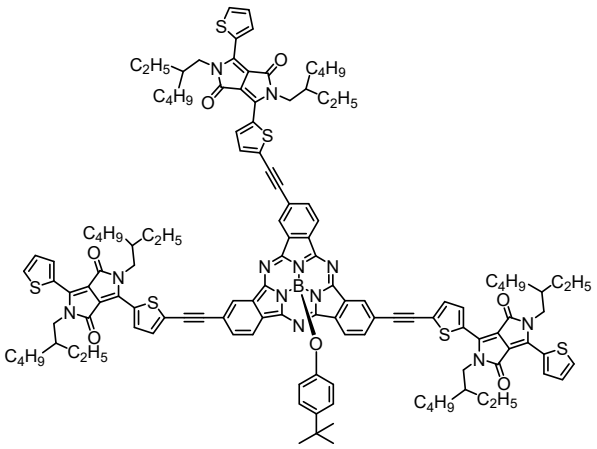

^{1}H NMR (300 MHz, $CDCl_3$): δ (ppm) 9.04- 9.02 (m, 3H), 8.96-8.93 (m, 6H), overlapping doublets centered at 8.03 and 8.02 (d, *J* =9.0 Hz, 3H), 8.04 (d, *J* =6.0 Hz, 3H), 7.65 (d, *J* =6.0 Hz, 3H), 7.51 (d, *J* =3.0 Hz, 3H), 7.30-7.27 (m, 3H), 6.80 (d, *J* =9.0 Hz, 2H), 5.35 (d, *J* =9.0 Hz, 2H), 4.12-3.99 (m, 12H), 1.94-1.89 (m, 6H), 1.45-1.25 (m, 48H), 1.10 (s, 9H), 0.96-0.85 (m, 36H). **^{11}B NMR** (96 MHz, $CDCl_3$): δ (ppm) -14.6. **FT-IR (KBr)** ν (cm^{-1}): 2959, 2924, 2856, 2186, 1665, 1640, 1552, 1509, 1455, 1399, 1324, 1289, 1257, 1230, 1175, 1090, 1060, 1020, 856, 825, 760, 733, 706. **UV/Vis** ($CHCl_3$), λmax (log ε):303 (4.91), 372 (4.80), 616 (5.24). **MS (MALDI-TOF):** m/z=2184.2 $[M+H]^+$.

- ***C3*-SubPc(DPP)3-OPh 19.** The compound was purified by silica gel column chromatography using 1:100 $CHCl_3$/ethyl acetate as eluent. Yield: 73%.

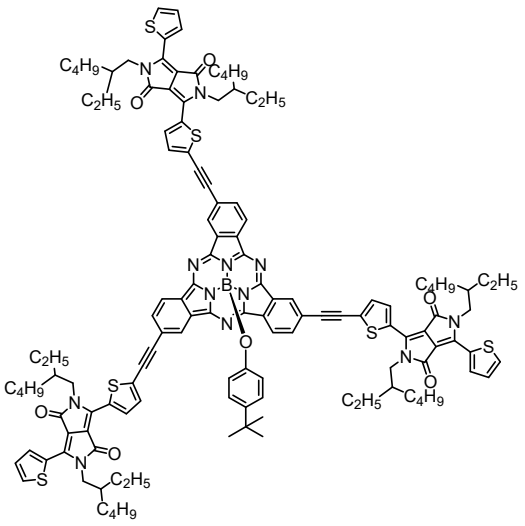

^{1}H NMR (300 MHz, $CDCl_3$): δ (ppm) 9.031-9.028 (m, 3H), 8.96-8.93 (m, 6H), 8.81 (d, *J* =9.0 Hz, 3H), 8.03 (dd, *J* =8.4 Hz, *J* =1.2 Hz, 3H), 7.65 (dd, *J* =5.0 Hz, *J* =1.1 Hz, 3H), 7.50 (d, *J* =6.0 Hz, 3H), 7.29-7.28 (m, 3H), 6.80 (d, *J* =6.0 Hz, 2H), 5.35 (d, *J* =6.0 Hz, 2H), 4.12-3.99 (m, 12H), 1.94-1.89 (m, 6H), 1.48-1.26 (m, 48H), 1.10 (s, 9H), 0.96-0.85 (m, 36H). **^{11}B NMR** (96 MHz, $CDCl_3$): δ (ppm) -14.6. **FT-IR (KBr)** ν (cm^{-1}): 2924, 1665, 1553, 1453, 1399, 1230, 1175, 1061, 827, 760, 734,

705. **UV/Vis** ($CHCl_3$), λmax (log ε):302 (5.00), 369 (4.90), 553 (5.15), 623 (5.41). **MS (MALDI-TOF):** m/z=2184.2 $[M+H]^+$.

- ***C$_1$*-SubPc(DPP)$_3$-Cl 20.** The compound was purified by preparative TLC plate using 2:1 $CHCl_3$/ethyl acetate as eluent. Yield: 15%.

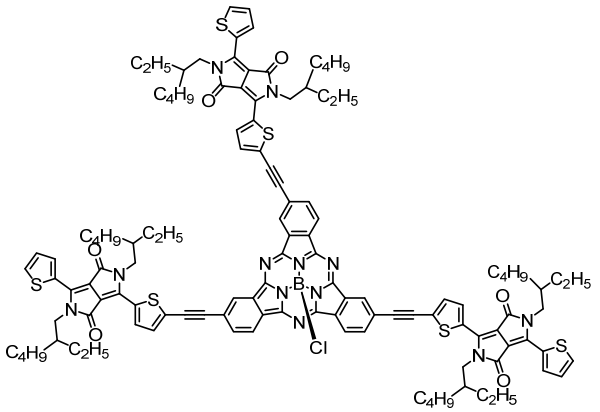

^{1}H NMR (400 MHz, $CDCl_3$): δ (ppm) 9.08-9.07 (m, 3H), 8.96 (d, *J*= 8.0 Hz, 3H), 8.94 (d, *J*= 4.0 Hz, 3H), overlapping doublets centered at 8.87 and 8.86 (d, *J*=8.0 Hz, 3H), 8.09 (d, *J*=8.0 Hz, 3H), 7.66 (d, *J*= 4.0 Hz, 3H), 7.52 (d, *J*=8.0 Hz, 3H), 7.29 (t, *J*= 4.0 Hz, 3H), 4.11-4.00 (m, 12H), 1.94-1.89 (m, 6H), 1.45-1.25 (m, 57H), 0.96-0.85 (m, 38H). **^{11}B NMR** (96 MHz, $CDCl_3$): δ (ppm) -12.9. **FT-IR (KBr)** ν (cm^{-1}): 2955, 2927, 2857, 2187, 1730, 1666, 1613, 1555, 1509, 1454, 1401, 1326, 1291, 1263, 1230, 1178, 1095, 1021, 977, 890, 857, 827, 788, 765, 734, 708. **UV/Vis** (toluene), λmax (log ε):373 (4.65), 595 (4.90). **MS (MALDI-TOF):** m/z=2068.9 $[M]^+$.

- ***C$_3$*-SubPc(DPP)$_3$-Cl 21.** The compound was purified by preparative TLC plate using CH_2Cl_2 as eluent. Yield: 8%.

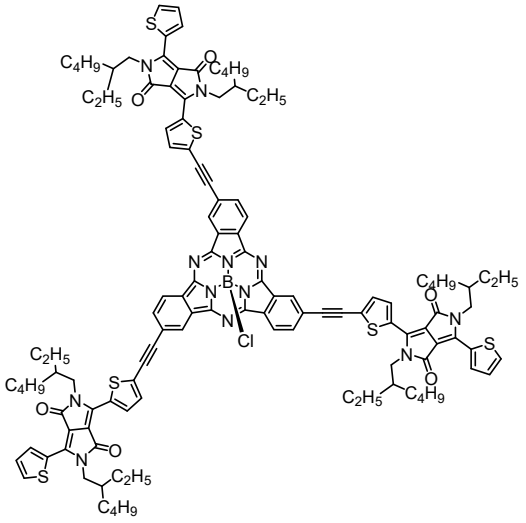

^{1}H NMR (400 MHz, $CDCl_3$): δ (ppm) 9.05-9.04 (m, 3H), 8.97-8.94 (m, 6H), 8.82 (d, *J*= 8.0 Hz, 3H), 8.05 (dd, *J*=8.0 Hz, *J*=1.6 Hz, 3H), 7.66 (dd, *J*=6.8 Hz, *J*=1.6 Hz, 3H), 7.51 (d, *J*= 8.0 Hz, 3H), 7.31-7.28 (m, 3H), 4.08-4.05 (m, 12H), 1.94-1.85 (m, 6H), 1.45-1.25 (m, 60H), 0.96-0.85 (m, 36H). **^{11}B NMR** (96 MHz, $CDCl_3$): δ (ppm) -13.9. **FT-IR (KBr)** ν (cm^{-1}): 2954, 2954, 2856, 2189, 1730, 1665, 1612, 1554, 1509, 1453, 1400, 1381,1304, 1263, 1229, 1178, 1095,

1065, 1020, 976, 891, 856, 826, 790, 734, 706, 663. **UV/Vis** (toluene), λmax (log ε):373 (4.73), 628 (5.19). **MS (MALDI-TOF):** m/z=2068.9 $[M]^+$.

2.6.4. OSC devices fabrication and characterization

DSSC- FTO substrates were cleaned by a standard procedure immersing the slides into solutions of acetone, soap solution (deconex FPD 120, 1% vol. solution in 150 mL deionized water), pure deionized water and isopropanol. The solutions were sonicated for 15 min each (Elma, Elmasonic P), and finally dried under a nitrogen flow. To cleanse the electrode surface of remaining organic waste the slides were treated with a UV-ozone cleaner (model 42-220, Jelight Company). For preparation of the TiO_2-based electrodes a standard Ti-Nanoxide T/SP paste was purchased from Solaronix. Utilizing a circular scotch tape with a diameter of 5 mm and thickness of 50 µm, the TiO_2 pastes were doctor bladed onto the conducting side of FTO substrates. For multilayer essays, the doctor bladed slides were heated at 80 ºC for 8 min, after which another layer was applied until the desired thickness was reached. FTOs were then heated from room temperature up to 150 ºC with a ramp of 10 ºC/min, holding the temperature for 10 min. Then, utilizing a ramp of 15 ºC/min, the temperature was increased to 325 ºC and kept constant for 5 min. Next the slides were heated up to 375 ºC with a ramp of 5 ºC/min, holding the temperature for 5 min. Afterwards the temperature was increased up to 450 ºC at 7 ºC/min and kept for 30 min. Finally, a temperature of 500 °C was obtained by a ramp of 5 ºC/min. The samples were kept at this temperature for 15 min, after which they were slowly cooled to 80 ºC. The slides were immersed into an anhydrous THF solution of ***p*-DPP acid 9** and ***m*-DPP acid 10** dyes (5 x 10^{-5} M) for 30 min (***m*-DPP acid 10**) and 90 min (***p*-DPP acid 9**) in order to achieve optimal coverage of the semiconducting surface. For the counter electrodes, FTO slides with two 1 mm diameter holes at the edge of the semiconductor layer were prepared. The slides were cleaned with the afore mentioned procedure. Next, a thin film of 26 µL H_2PtCl_6 (0.5 mmol in isopropanol), prepared from chloroplatinic acid hydrate (38wt% Pt concentration, Sigma Aldrich) was drop casted onto the counter electrode slides. The FTO substrates were dried in air prior to baking at 400 ºC for 20 min with a ramp of 40 ºC/min. For the final step, both electrodes were sealed together, utilizing a transparent film of Surlyn (DuPont Ltd., UK), featuring a 6 mm hole for the active layer. An electrolyte solution, in an 85:15 v/v mixture of acetonitrile and valeronitrile, consisting of 0.6 M 1,2-dimethyl-3-propylimidazolium iodide 99%, 0.5 M 4-*tert*-butylpyridine 96%, 0.1-1.0 M iodine and 0-1.0 M lithium iodine 98%, was added into the cells by capillary force using the drilled holes. The final cell was sealed immediately after, using Surlyn and a piece of microscope glass.

BHJ- The devices were fabricated using the inverted architecture ITO/TiO_2/PBDB-T: SubPc$(DPP)_3$/V_2O_5/Ag. Patterned ITO-coated glass substrates were cleaned with a surface-active detergent and then sequentially sonicated in acetone, methanol, and isopropanol solvents bath. Then, ITO substrates were dried at 120 °C in an oven during 20 min followed by a UV-ozone treatment. Then, a TiO_2 film was deposited on the ITO by spin coating at 6000 rpm from a TiO_2 solution and then heated up to 400 °C for 10 min. The TiO_2 solution was prepared by mixing 2-methoxyethanol, ethanolamine, and titanium (IV) isopropoxide (10:2:1 v/v). Thereafter, the TiO_2 solution was diluted in methanol (6:1 v/v). The active layer solutions with a concentration of 20 mg mL^{-1} were prepared by dissolving PBDB-T and the SubPc$(DPP)_3$ derivatives in chlorobenzene/1,8-diiodooctane (99.5:0.5 v/v for **18**, **19** and **21** and 99:1 v/v for **20**). The active layer solutions were deposited on top of the TiO_2 layer by spin coating at 5000 rpm for 45 seconds and then they were thermally annealed at 100 °C during 10 min. Finally, the samples were transferred to a vacuum chamber where 5 nm of V_2O_5 and 100 nm of Ag were thermally evaporated onto the active layer. The effective area for all devices was 0.09 cm^2. The overall fabrication process was carried out under nitrogen atmosphere. The *J-V* curves of the OSCs devices were recorded using a Keithley 2400 source-measure unit under 100 mW cm^2 AM 1.5G light illumination provided by a solar simulator (Abet Technologies model 11 000 class type A, Xenon arc). The EQE measurements were taken under forward wavelength sweep direction from 300 nm to 800 nm using Lasing IPCE-DC system with a serial number of LS1109-232.The AFM images of the samples were recorded in tapping mode on a Molecular Imaging model Pico SPM II (pico +). Images were collected in the air using silicon probes with a typical spring constant of 1–5 nN/m, and at a resonant frequency of 75 kHz.

Chapter 3

Supramolecular chirality induction from silica nanostructures to achiral diketopyrrolopyrrole derivatives

3.1. Introduction

The property based on the symmetry of one elemental particle, molecule or even a macroscopic element is called as chirality. An element is considered chiral if has two mirror-image forms which are not superimposable in the three dimensions. These mirror images are denominated as enantiomers, the "left-handed" and "right-handed". According to the Cahn-Ingold-Prelong system, the chiral center can be described as R (right) or S (left) and this is defined by the substituents surrounding the stereocenter, it means the denomination of R or S depending on the molecular weight (the priority is assigned to the higher molecular weight over the lower) of the substituents bonded to the chiral carbon. The enantiomer is R if the order of the substituents goes in the clockwise direction when facing the stereocenter from the opposite side to least priority group, and S when is counter clockwise direction. Moreover, the stereocenters can be called as d (dextrorotatory) or l (levorotatory) if the compound rotates the plane of the polarized light in the clockwise or counter clockwise direction, respectively.

Over the years, chiral molecules have been intensely sought after by the scientific community, since the first chiral molecule reported by Louis Pasteur in 1848 when he discovered the racemic mixture of the sodium ammonium tartrate.[159] In nature there are a huge number of examples of chiral molecules, such as amino acids that make up proteins, sugars, nucleotides, among others.[160] In this sense this property can be applied in several areas like chemistry, biology, medicine, among other.

Usually both enantiomers present identical physical and chemical properties unless they get in contact with polarized light or another chiral molecule.[161] The enantiomer specificity is crucial namely in medicine, pharmacy or biology areas because there are several examples in the literature where only one of the enantiomers is active and it often happens that the other is not active or can lead to harmful changes in the functioning of a certain organism, as is the well-known example of thalidomide. In this example the S-enantiomer is responsible for the abnormalities during embryonic development and the R-enantiomer is the responsible for sedation.[162]

Chiral properties are not only observed in molecules with chiral centers, as well can be detected in different dimensions; this means that a chiral molecule can build different levels of chiral structures carrying transmissible chiral information. The most common example is DNA that is made up of nucleotides with a specific

[159] M. L. Pasteur, *C. R. T. Acad. Sci.*, **1848**, *26*, 535-539.
[160] a) N. M. Maier, P. Franco, W. Lindner, *Journal Chromatogr. A,* **2001**, *906*, 3–33. b) M. D. Ward, *Nature*, **2003**, *426*, 615-616.
[161] J. Mu, M Kim, Y. Yang, T. Badloe, J. Ni, Y. Chen, C.-W. Qiu, J. Rho, *Light: Sci. Appl.*, **2020**, *9,* 139.
[162] J. B. Bartlett, K. Dredge, A. G. Dalgleish, Nat. Rev. Cancer, **2004**, *4*, 314-322.

arrangement that occurs only in the right helical form.[163] The knowledge of the transmissibility properties of chirality allows to build new materials and can be applied in new applications. [164] In chemistry the chiral properties have been used in several areas such as in asymmetric catalysis, [165] chiral recognition,[166] sensors[167] and light manipulation.[168]

There are some ways to measure the chiroptical properties of one sample, namely the circular dichroism.[161] Circular dichroism (CD) is related to the way the sample influences the light beams. Before trying to understand how it is possible to study the properties of chirality with circular dichroism spectroscopy, it is essential to be aware of the definition of light polarization. The polarization is a property of electromagnetic waves with a specific geometry orientation. Two types of polarization can be obtained. The linear polarization is when the polarization plane does not change along the direction of the propagation, and the circular polarization is when there is a rotation of the polarization plane, meaning that light can rotate in a right- or left-handed way.

3.1.1. Circular dichroism spectroscopy

Circular dichroism spectroscopy is a technique that measure the difference in the absorption of the left (A_L)- and right-(A_D) circularly polarized light through an optically active substance. Circular dichroism signal may be determined according to the following equation:[169]

$$\Delta A_{CD} = A_L - A_D \qquad \textbf{Eq. 3.1}$$

In a CD spectrum, positive ($A_L > A_D$) or negative ($A_L < A_D$) bands can appear only when the compounds absorb in the UV-vis. The CD spectrometer presents similarities with a UV-vis spectrophotometer, the higher difference is the presence of a photoelastic modulator (PEM) before the sample (**Figure 3.1a**). The PEM acts as a quarter-wave plate changing the linearly polarized light to circularly polarized light.

[163] A. Aggeli, I. A. Nyrkova, M. Bell, R. Harding, L. Carrick, T. C. B. McLeish, A. N. Semenov, N. Boden, *PNAS*, **2001**, *98*, 11857-11862.
[164] Y. Yang, Y. Zhang, Z. Wei*, Adv. Mater.* **2013**, *25*, 6039–6049.
[165] a) D. Liu, B. Li, J. Chen, I. D. Gridnev, D. Yan, W. Zhang, *Nat. Commun*, **2020**, *11*, 5935. b) W. Wen, M.-J. Luo, Y. Yuan, J.-H. Liu, Z.-L. Wu, T. Cai, Z.-W. Wu, Q. Ouyang, Q.-X. Guo, *Nat. Commun.*, **2020**, *11*, 5372. c) J. Wang, S. Zheng, S. Rajkumar, J. Xie, N. Yu, Q. Peng, X. Yang, *Nat. Commun.*, **2020**, *11*, 5527.
[166] a) L. Pu, *Chem. Rev*., **2004**, *104*, 1687-1716. b) Y. Kubo, S. Maeda, S. Tokika, M. Kubo, *Nature*, **1996**, *382*, 522-524.
[167] Z. Chen, Q. Wang, X. Wu, Z. Liu, Y. Jiang, *Chem. Soc. Rev.*, **2015**, *44*, 4249-4263.
[168] Y. Xia, *Nanoscale*, **2011**, *3*, 1374-1382.
[169] F. Zsila, *in Pharmaceutical Sciences Encyclopedia: Drug Discovery, Development, and Manufacturing,* John Wiley & Sons, Inc., **2010**, pag.1-5.

Depending on the potential applied, PEM can be generating right or left handed CP light. The results are commonly recorded as an ellipticity function (Θ) that refers to the extent of distortion of the circularly polarized light to an elliptical shape as the sample absorbs either left or right-handed light more and is measured in millidegrees (mdeg), which are defined as tangent of the ratio of the minor to major elliptical axis (**Figure 3.1b**).

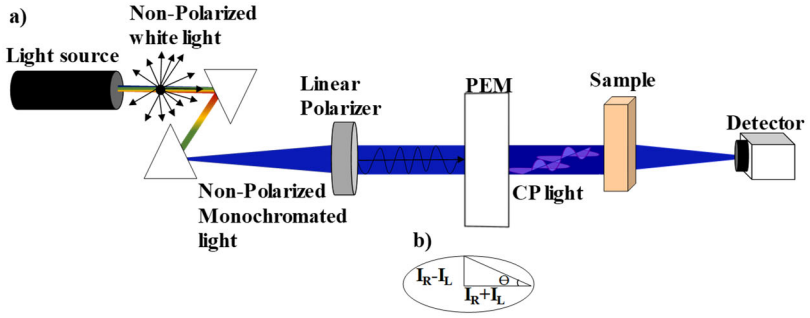

Figure 3.1- a) *Schematic representation of a CD spectrometer.* ***b)*** *Illustration of elliptical measurement.*

Thus the variation in absorption can be defined using **Eq. 3.2**:

$$\Delta A_{CD} = A_L - A_D \cong \frac{\theta_{abs}}{32982} \qquad \textbf{Eq. 3.2}$$

CD values depend on absorbance, so they are dependent on sample concentration, thus making necessary to be very careful when preparing the samples, as different concentrations lead to different results. CD results can be converted in a unitless factor denominated dissymmetry factor, that can be determinate dividing the CD values by the absorbance, as it can be observing in the **Eq. 3.3**.[169]

$$g_{abs} = \frac{\Delta A_{CD}}{A} \approx \frac{\theta_{abs}}{32982 \times A} \qquad \textbf{Eq.3.3}$$

3.1.2. Chirality transmission

As mentioned earlier, chirality can be transmitted in several ways, namely from one atom to the whole molecule, from a molecule to several molecules or even in a higher scale from several molecules to a supramolecular assembly and from a nanostructure to a particle. This affirmation can be justified with several reports present in the literature. For example, when the chirality is transmitted from a reactant to the final product mediating a chemical reaction the transmission occurs between species of the same size.[170] Another example is the use of a chiral catalyst to introduce chirality through asymmetric catalysis, it means from nano-objects to

[170] B. List, *Acc. Chem. Res.*, **2004**, *37*, 548-557.

small molecules.[171] Also it is possible to introduce chirality from a nano-object (10-100 nm) to small molecules (using a chiral enzyme).[172] However, in all examples, there is a common disadvantage, which is the requirement for a pure enantiomer and it is sometimes difficult to reach this point of purity, either due to synthetic difficulties or problems at the time of purification.

These reasons were enough to start looking for new ways to induce chirality, and the idea that came up consisted in the introduction of in achiral molecules using only a chiral environment, thus overturning the present difficulty in the synthesis of pure enantiomers. Matsubara works came to justify this possibility reporting a co-crystallization of one achiral chromophore (2-anthracenecarboxylic acid) with a chiral molecule (1,2-diphenylethylenediamine) observing the chirality with CD and CPL (circularly polarized luminescence spectroscopy).[173] Other example was reported by Tang that constructed a novel helical fibre by assembling a tetraphenylethylene derivative containing a L-leucine methyl ester moiety. After the non-covalent aggregation, these helical fibres presented chiral properties when examined by CD and CPL.[174] However, these processes have limitation, like the necessity to control the experimental conditions (solvent, the temperature) and not to mention that laterality is not always switchable (as it may not be possible to synthesize the two enantiomers of the model).

After exposing these difficulties, we can already understand the idea that brought the group of Dr Oda, who was the pioneer in the induction of chirality in achiral systems from chiral silica morphologies. The synthetic method for the synthesis of the silica nanostructure has been developed over the last twenty years.[175] Over the years, different type of achiral components has been studied in order to understand the behaviour of these components in the chiral nanospaces in sol–gel matrices, but also provide a new strategy for the design of chiral organic–inorganic or inorganic-inorganic composite materials. Several reports have been published using hybrid nanostructures (structures consisting of an inorganic part, the outer walls consisting of silica, and an organic part, the interior of the structures constituted by the tartrate counterion) or inorganic nanostructures (consisting only of silica walls). In some

[171] W. S. Knowles, *Acc. Chem. Res*., **1983**, *16*, 106-112.
[172] H. Beinert, M. C. Kennedy, C. D. Stout, *Chem. Rev.*, **1996**, *96*, 2335−2373.
[173] Y. Imai, K Kawano, Y. Nakano, K. Kawaguchi, T. Harada, T. Sato, M. Fujiki, R. Kurodacd, Y. Matsubara, *New J. Chem*., **2008**, *32*, 1110–1112.
[174] H. Li, J. Cheng, H. Deng, E. Zhao, B. Shen, J. W. Y. Lam, K. S. Wong, H. Wu, B. S. Li, B. Z. Tang, *J. Mater. Chem. C*, **2015**, *3*, 2399-2404.
[175] R. Oda, Huc, M. Schmutz, S. J. Candau, F. C. MacKintosh, *Nature,* **1999**, *399*, 566-569.

studies, they proposed inducing chirality in monoatomic anions[176], gold nanoparticles, [177] perovskites nanocrystals,[178] among others.

In addition to using inorganic achiral species, they also developed methodologies using organic compounds. On the one hand inducing chirality through ionic exchange between the tartrate counterion (present inside the nanostructures) and the compound under study, as also using totally inorganic morphologies with the interaction between the nanostructure and the organic compound taking place on the surface of these nanostructures. The first report focused in the first point was reported by Oda that used methyl-orange which was confined in the chiral space of the hybrid helices. The chirality appearance was verified by the appearance of CD signal.[179] Years later another work was published where biphenyl-linked polysilesquoxane through a sol-gel transcription of self-assembling nanohelices from dication in gemini surfactants was used.[180]

For the progress of the present work, the methodology of covalent bonding of organic compounds to totally inorganic surfaces was used, in this way the works developed until the moment that are described in the literature will be presented in detail.

3.2. Background

The first report that can be found in the literature about the chirality induction of achiral compounds through bonding at the surface of an inorganic silica nanostructure was based on polyoxometalates (POM). In this work the authors studied the effect of electrostatic and covalent bond of the POM on the chiral silica nanostructures. These structures were formed due to the surface modification with APTES, making the surface positively charged while POM is negatively charged. The direct adsorption approach proved to be the best way to induce chirality in this type of systems, a fact justified by the closer proximity and better arrangement of the POM clusters onto the chiral source, obtaining a g_{abs} around 1.12×10^{-4} while for the electrostatic approach a value of 3.3×10^{-5} was obtained.[181] Later, Oda studied the chirality induction on phosphotungstic acid, $H_3PW_{12}O_{40}$, with excess of H_2O_2 in helices and ribbons nanostructures, leading to the decomposition of this

[176] Y. Okazaki, N. Ryu, T. Buffeteau, S. Pathan, S. Nagaoka, E. Pouget, S. Nlate, H. Ihara, R. Oda, *Chem. Commun*., **2018**, *54*, 10244-10247.
[177] J. Gao, W. Wu, V. Lemaire, A. Carvalho, S. Nlate, T. Buffeteau, R. Oda, Y. Battie, M. Pauly, E. Pouget, *ACS Nano*, **2020**, *14*, 4111−4121.
[178] P. Liu, W. Chen, Y. Okazaki, Y. Battie, L. Brocard, M. Decossas, E. Pouget, P. Müller-Buschbaum, B. Kauffmann, S. Pathan, T. Sagawa, R. Oda, *Nano. Lett*., **2020**, *20*, 8453-8640.
[179] N. Ryu, Y. Okazaki, K. Hirai, M. Takafuji, S. Nagaoka, E. Pouget, H. Ihara, R. Oda, *Chem. Commun.,* **2016**, *52*, 5800-5803.
[180] N. Ryu, T. Kawaguchi, H. Yanagita, Y. Okazaki, T. Buffeteau, K. Yoshida, T. Shirosaki, S. Nagaoka, M. Takafuji, H. Ihara, R. Oda, *Chem. Commun.*, **2020**, *56*, 7241-7244.
[181] M. Attoui, E. Pouget, R. Oda, D. Talaga, G. Le Bourdon, T. Buffeteau, S. Nlate, *Chem. Eur. J*., **2018**, *24*, 11344–11353.

POM forming the trianionicperoxophosphotungstate $[PO_4(WO(O_2)_2)_4]^{3-}$ and the dinuclear peroxotungstate $[\{WO(O_2)_2(H2O)\}_2O]^{2-}$.[182] Besides, to chiroptic properties, catalytic properties have also been successfully studied in these two articles, demonstrating the importance of this type of work.

These discoveries promoted the opening of a door to new ways to induce chirality. In fact, one year later the same group reported other work using organic chromophores, instead of POM, covalently linked to a chiral inorganic helix. In this work, Oda studied the chirality induction in two pyrenes (**PCA** and **PAA**) and two perylene derivatives (**DPBIPh** and **DPBICl**). The authors attributed this chirality appearance to supramolecular chiral organization on the helical surface as evidenced by the variation of the induced circular dichroism signal with the increment of achiral chromophore density on the surface (**Figure 3.2**).[183]

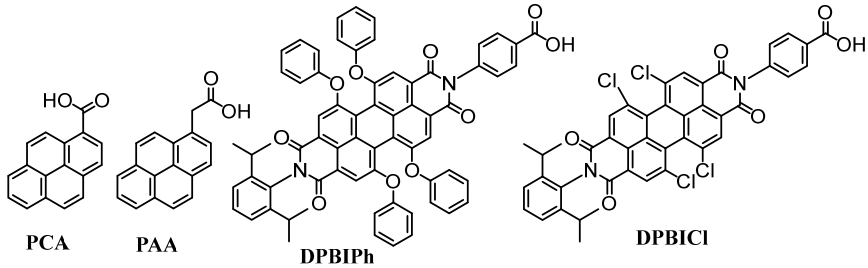

Figure 3.2- *Chemical structures of pyrenes and perylesnes under study on the work of Oda.*

The dissymmetry factor values obtained in this work were not so high comparatively with the values obtained in other works using chiral systems. Nonetheless, some differences were observed with the different systems, obtaining the higher g_{abs} for the **PAA**-helices system, with values of 4.9×10^{-5} and -1.6×10^{-5} for right-and left-handed helices, respectively. This difference in g_{abs} values was attributed to the discrepancy in the molecule density on the surfaces.

3.3. Goal

Chirality is a property that can be found in all environments, in nature, in biological systems, among others and that is why it becomes one of the properties that arouses so much interest in the scientific community. However, mimicking nature in a synthesis laboratory is a difficult task and obtaining chiral chromophores it is not

[182] M. Attoui, E. Pouget, R. Oda, D. Talaga, T. Buffeteau, S. Nlate, *Inorg. Chim. Acta*, **2019**, *498*, 119127.
[183] A. Scalabre, A. M. G. Vílchez, Á. Sastre-Santos, F. Fernández-Lázaro, D. M. Bassani, R. Oda, *J. Phys. Chem. C*, **2020**, *124*, 23839−23843.

so easy, as it can take a long time and at the end, it may not be possible to have a pure enantiomer.

For that reason, we inspired in these reports presented before and proposed the synthesis and the characterization of three molecules where a DPP is linked to the *ortho*-, *para*- and *meta*- position of a benzoic acid, in order to study the influence of the position of the DPP in relation to the silica template in the chirality induction. Moreover, we intended to study this effect in two different nanostructures, one more chiral (helices) than the other (ribbons), in order to understand the importance of the curvature of the nanostructures in the chirality induction and the influence of DPP aggregation when linked to the nanostructures. The activation of the carboxylic acid allows to covalently bond the achiral chromophores to the NH_2 present on the surface of the inorganic template (**Figure 3.3**). The choice for totally inorganic nanostructures is based on the opportunity to work at room temperature, and with different solvents, which is not the case with hybrid nanostructures, as it is necessary to work with low temperatures and the use of solvents such as methanol is not recommended because dissolves the organic matrix that is inside the nanostructures.

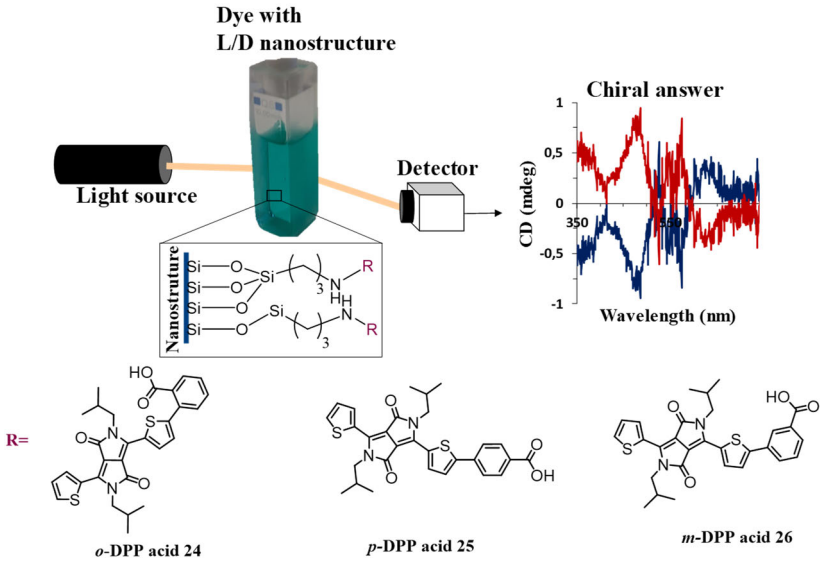

Figure 3.3- *Scheme of the goal work and the structures of the DPP derivatives. Notice that the scheme is not a real representation of the CD spectrometer, it is just a summary of the work steps.*

The synthesis and the characterization of the chromophores based on DPP acid will be made in the DYSMOL group of the Universidad Miguel Hernández de Elche. The synthesis of silica templates and the grafting of the dyes on the surface of the silica will be carried out in the NEO and CMA groups in the Bordeaux University,

where I realized an internship for three months. Besides that, the circular dichroism spectroscopy is the tool that will be used to determine chiral induction.

3.4. Results and discussion

In this chapter a series of sections are presented in order to sequence the necessary steps to achieve the final objective of this work.

3.4.1. Synthesis and characterization of achiral dyes

- **Synthesis of intermediate compounds**

To achieve the goal of this work the racemic aliphatic chain 3-(bromomethyl)heptane, used in the previous works, had to be replaced by a non-racemic and achiral chain, the 1-bromo-2-methylpropane chain, due to the need for derivatives without any chiral part. The synthesis of **DPP 28** was carried out under the same conditions as **DPP 6** presented in **Chapter 1** (pag 38). The fact that the alkyl chain was changed did not alter the yield of the *N*-alkylation reaction, obtaining 49% of a bright red crystalline solid (**DPP 27**). As expected, the undesirable *O*-alkylation reaction also occurred.

The compound exhibited less solubility in volatile organic solvents than **DPP 5**, however it proved to be quite soluble in CH_2Cl_2 and $CHCl_3$. Then, **DPP 28** was obtained by bromination reaction of **DPP 27** in the presence of NBS and AcOH in $CHCl_3$. In this case, the reaction yield was much better than the yield of the reaction of **DPP 6**, 72% yield was obtained instead of 45% (**Scheme 3.1**). These DPP intermediates were not described in the literature so, all the intermediate compounds were isolated and characterized by ^{1}H-NMR, ^{13}C NMR, UV-vis and FT-IR spectroscopies and by HR-MALDI-TOF mass spectrometry (**Figures A38-A43**).

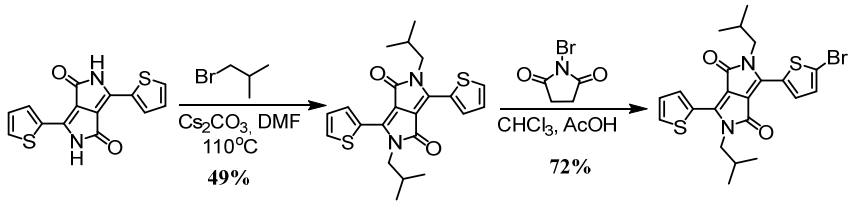

Scheme 3.1- *Synthetic route to* ***DPP 28****.*

The ^{1}H NMR spectra of **DPP 27** and **DPP 28** were made in $CDCl_3$. **Figure 3.4** shows the ^{1}H NMR of **DPP 27** as well as a comparative spectrum between **DPP 27** and **DPP 5**. As expected, due to the symmetry of the compound three signals in the aromatic zone belonging to the thiophene protons and three more signals that

belongs to the alkyl chain were obtained. Slight differences in the aromatic zone between **DPP 27** and **DPP 5** were noted. Namely in the dd signal at 8.98 ppm, represented by the orange stars in **Figure 3.4c**, which undergoes a shift to higher ppm in **DPP 27**. Nevertheless, in the aliphatic zone the differences are more visible due to the disappearance of the multiplet signal at 1.38-1.22 ppm in the **DPP 27** spectrum, represented in **Figure 3.4c** in the form of blue points. Also, the appearance of a doublet at 3.95 ppm instead of a multiplet (4.09-3.96 ppm) and a multiplet at 2.22-2.03 ppm instead of a multiplet (1.38-1.22 ppm). The ^{13}C NMR is presented in **Figure A38** where it is possible to observe the expected peaks, three CH (135.6, 130.7, and 128.8 ppm) and four Cq (161.8, 140.4, 130.0 and 107.9 ppm) in the aromatic zone corresponding to the DPP core and three signals belonging to the alkyl chain in the aliphatic zone .

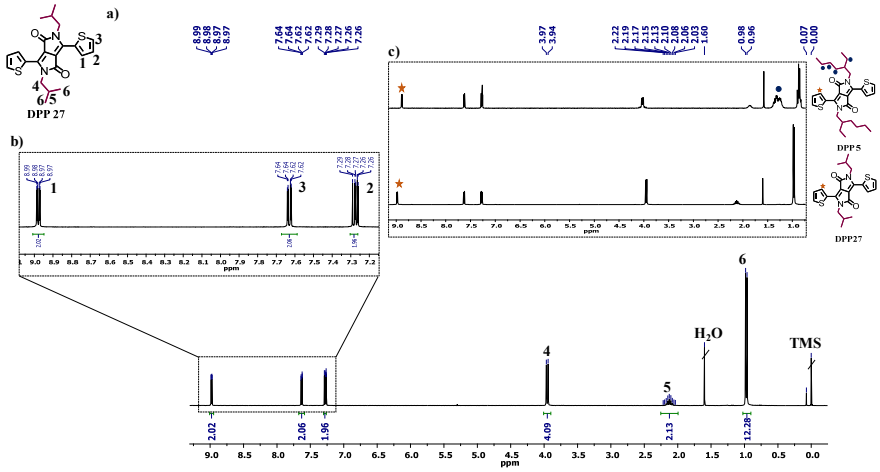

Figure 3.4- a) *^1H NMR of **DPP 27** in $CDCl_3$, at 25 °C and the chemical structure.* ***b)*** *^1H NMR zoom in the aromatic zone.* ***c)*** *Comparison of ^1H NMR between the **DPP 27** and **DPP 5** in $CDCl_3$ at 25 °C.*

Figure 3.5a shows the ^1H NMR spectrum of **DPP 28** in $CDCl_3$. A comparison between the spectrum of **DPP 27** and **DPP 28** was made and as expected the symmetry of **DPP 28** was broken by the presence of the Br atom, thus appearing more signals in this spectrum (**Figure 3.5b**), namely two new doublets appearing at 8.72 and 7.22 ppm corresponding to **H4** and **H5** of the disubstituted thiophene, respectively. The symmetry break was also visible in the ^{13}C NMR with an increase in the number of carbon signals, as expected, **Figure A41**.

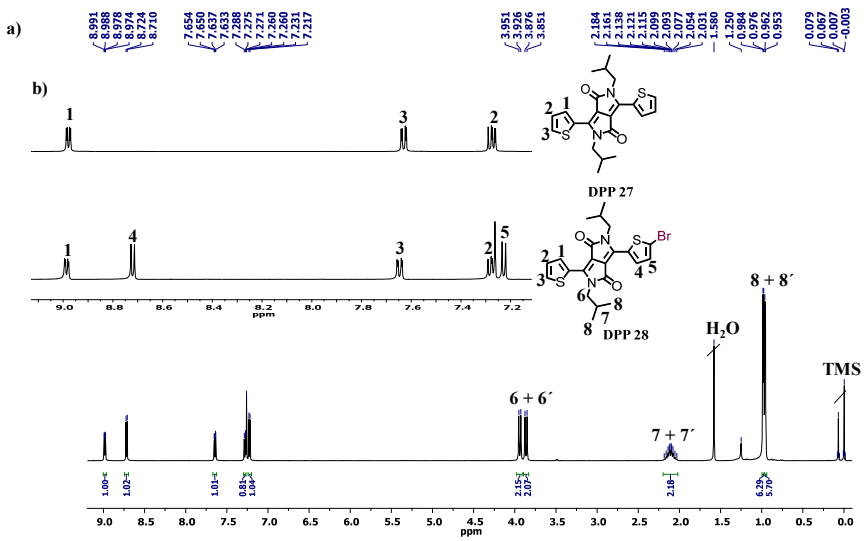

Figure 3.5- a) *^{1}H NMR of **DPP 28** in $CDCl_3$, at 25 °C.* ***b)*** *Comparison of ^{1}H NMR between the **DPP 27** and **DPP 28** zoom in the aromatic zone and the chemical structures.*

The optical properties in the ground-state and in the excited state of **DPP 27** and **DPP 28** were studied by UV-vis and fluorescence measurements in MeOH (**Figure 3.6**). The UV-vis spectra of both compounds display a set of well-resolved maxima between 500 and 550 nm, which represent the transitions to the lowest singlet excited state, showing a slight red-shit of the **DPP 28** relative to **DPP 27**. But the most visible difference was the molar extinction coefficient values, which was higher for **DPP 28** (24457 $M^{-1}cm^{-1}$) than for **DPP 27** (13112 $M^{-1}cm^{-1}$). For **DPP 27** the fluorescence maximum lies at 557 nm and for the **DPP 28** at 567 nm with a Stokes shift of 18 nm for both compounds.

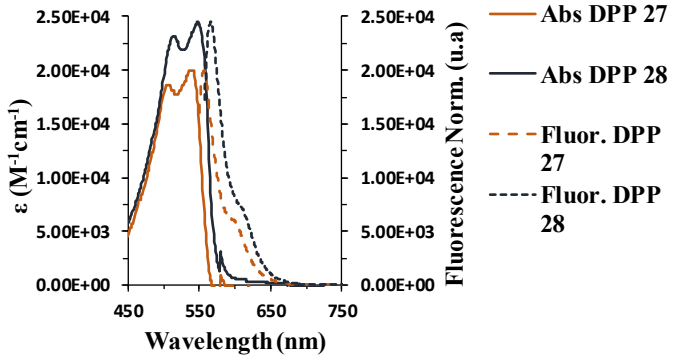

Figure 3.6- *Continuous lines: Room-temperature absorption spectra of **DPP 27** (orange) and **DPP 28** (grey) in MeOH. Dashed lines: Fluorescence spectra in MeOH following photoexcitation at 550 nm for **DPP 27** and at 557 nm for **DPP 28**.*

Besides that, boronic ester derivatives have also been synthesized namely the 2-(4,4,5,5-tetramethyl-1,3,2-dioxaborolan-2-yl)benzoic acid (**29**) and 4-(4,4,5,5-tetramethyl-1,3,2-dioxaborolan-2-yl) benzoic acid (**30**). These compounds were obtained by a hydrolysis reaction of the respective *ortho*- and *para*- phenylboronic acid pinacol esters in the presence of KOH in a 3:1 solution of THF/methanol (**Scheme 3.2**). The compounds were isolated and washed with hexane.

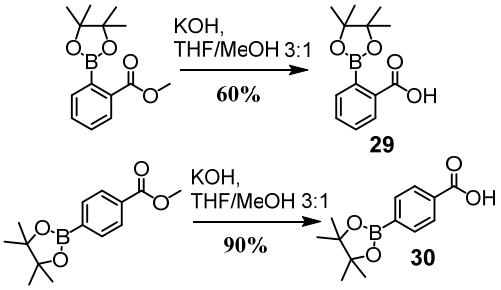

Scheme 3.2- *Synthetic route to **29** and **30**.*

The compounds were characterized by ^{1}H NMR in $CDCl_3$ (**Figure 3.7**), and the chemical shifts were confirmed with the literature results.[184]

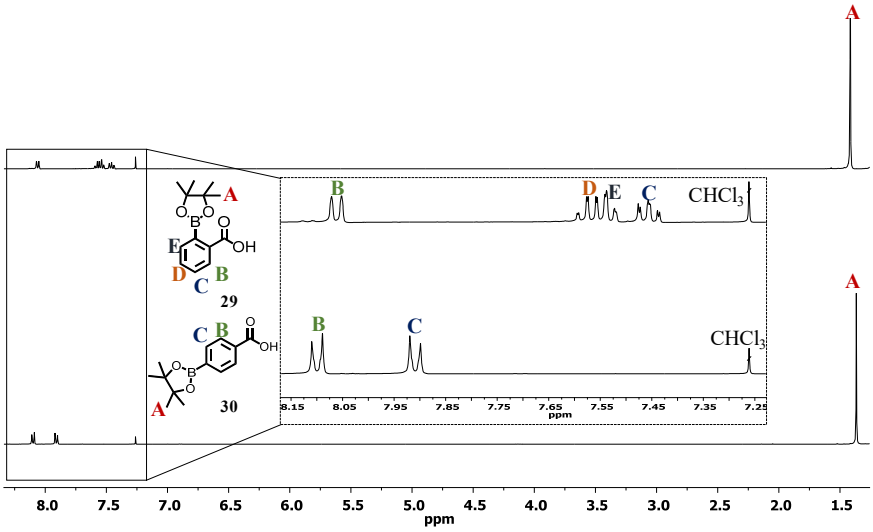

Figure 3.7- *^{1}H NMR of **29** and **30** in $CDCl_3$* at 25 °C.

[184] a) T. J. Auvil, A. E. Mattson, *Synthesis*, **2012**, *44*, 2173-2180. b) A. Zernickel, W. Du, S. A. Ghorpade, D. N. Sawant, A. A. Makki, N. Sekar, J. Eppinger, *J. Org. Chem*., **2018**, *83*, 1842−1851.

- **Synthesis of achiral DPP dyes**

To achieve the desired final compounds, different synthetic routes were tried. The first one consisted of a Suzuki-Miyaura coupling reaction between **DPP 28** and the *ortho*- (**31**) and *para*- boronic ester (**15**), obtaining the ***o*-DPP ester 32** and the ***p*-DPP ester 33** with 64% and 94% yield, respectively, in the form of dark purple solids. The compounds were characterized by ^{1}H NMR (**Figure A44-A45**). Then, a hydrolysis reaction was tried, however, in this step several adversities were felt, like degradation of DPP core or low reaction yield, leading to a change in the synthetic plans (**Scheme 3.3**).

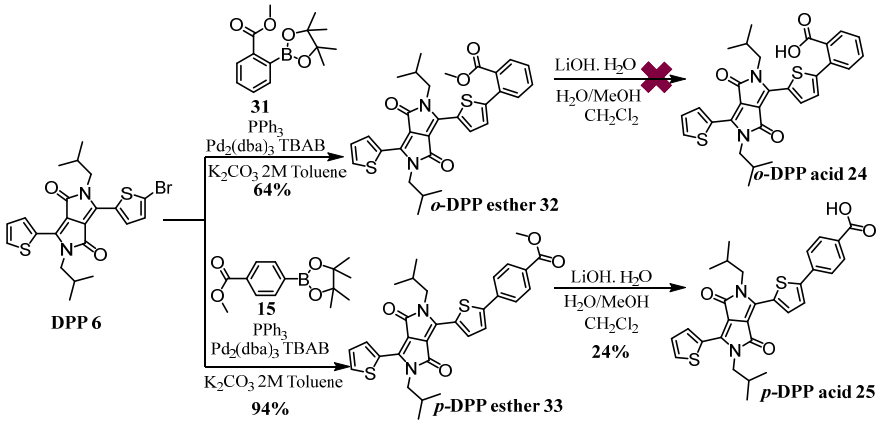

***Scheme 3.3-** First synthetic route of **o-DPP acid 24** and **p-DPP acid 25**.*

The solution found for the synthesis of these compounds was to react **DPP 28** directly with the respective benzoic acid derivatives via Suzuki-Miyaura coupling reactions (**Scheme 3.4**). The first attempts were made in toluene; however, this was not the best reaction solvent, due to its inability to properly solubilize the benzoic acids. So, after changing to dioxane it was possible to obtain the intended compounds with yields of 3, 46 and 55% for ***o*-DPP acid 24**, ***p*-DPP acid 25** and ***m*-DPP acid 26**, respectively. With this alternative, better yields were gathered, for example in the case of ***p*-DPP acid 25** the yield improved from 24% to 46%. And in the case of ***o*-DPP acid 24**, it was possible to obtain this compound, which had not been seen with the previous route, although the yield was still not as good as desired.

Contrary to the DPP derivatives with a 3-(bromomethyl)heptane chain (**Chapter 1**), these derivatives did not show good solubility in the usual organic solvents, being partially soluble in CH_2Cl_2, $CHCl_3$ and MeOH.

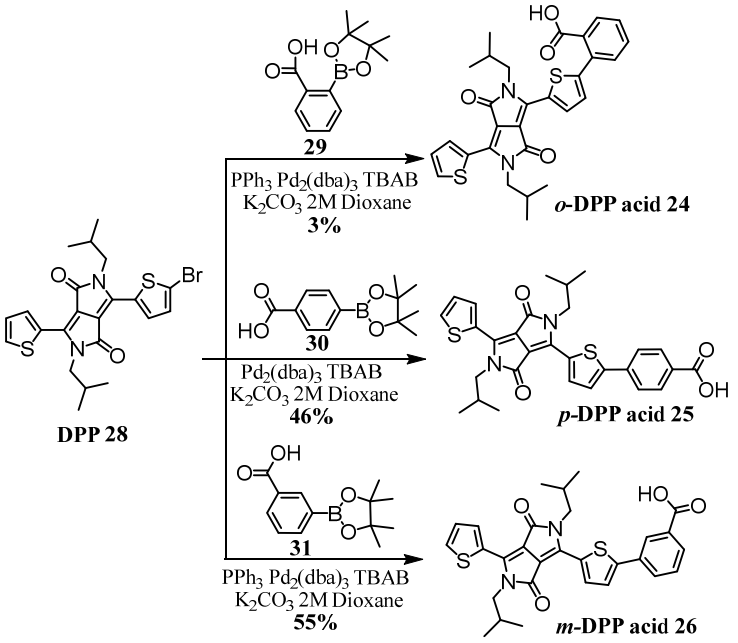

***Scheme 3.4**- Synthetic route to **o-DPP acid 24**, **p-DPP acid 25** and **m-DPP acid 26**.*

The three acid derivatives were characterized by ^{1}H-NMR (**Figure 3.8**), UV-vis (**Figure 3.10**) and FT-IR (**Figure A47**, **A49** and **A51**) spectroscopies and by MALDI-TOF mass spectrometry (**Figure 3.9**). Due to the low solubility, it was not possible to obtain ^{13}C NMR spectra. By analyzing the ^{1}H NMR spectra of the three derivatives it was possible to observe a dependence of the signals with the distance between the DPP and the carboxylic acid, as it was expected (**Figure 3.8)**. In the case of ***p*-DPP acid 25** just two doublets at 8.04 ppm (**HA**) and 7.80 ppm (**HB**) belonging to the phenylene group were observed. For ***o*-DPP acid 24**, two signals were also observed, which was not expected, however, it was confirmed by the signal integrations that the protons **HB**, **HC** and **HD** were superimposed in a multiplet at 7.50-7.45 ppm and the **HA** appeared in another multiplet at 7.62-7.57 ppm. Finally, in the ***m*-DPP acid 26** spectrum appeared a singlet at 8.39 ppm that belongs to **HA**, one multiplet at 8.06-7.99 ppm pertain to **HB** and **HD** and another at 7.61-7.54 ppm that belong to **HC**.

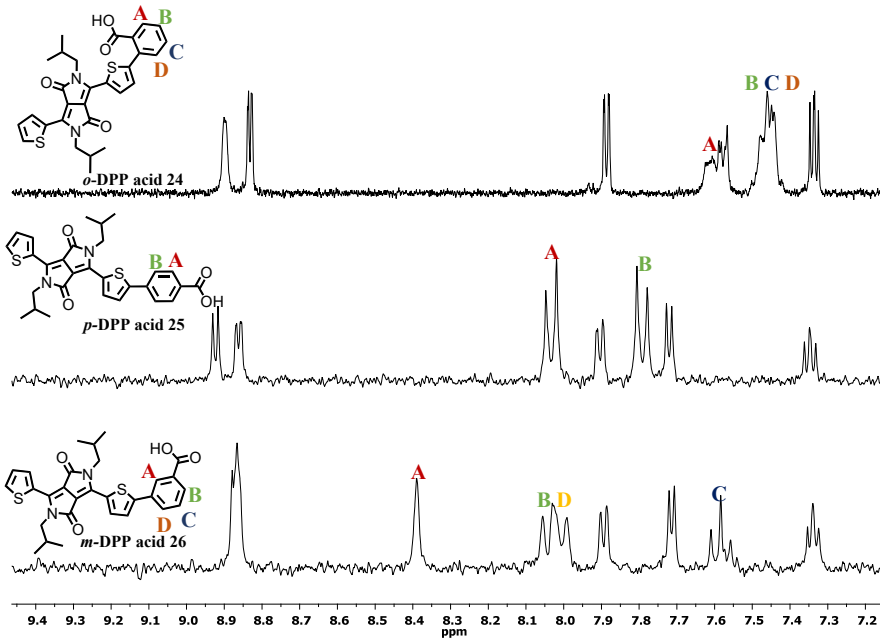

Figure 3.8- *Expansion of ^{1}H NMR in the aromatic zone of the three acids,* ***o-DPP acid 24****,* **p-*DPP acid 25*** *and* **m-*DPP acid 26*** (MeOD-d_4 at 25 °C).

Beyond the NMR spectra, the HR-MALDI-TOF spectra confirmed the presence of the pretended compounds showing the m/z peaks at 533.156, 533.154 and 533.157 for ***o*-DPP acid 24**, ***p*-DPP acid 25** and ***m*-DPP acid 26** corresponding with the theoretical isotopic distribution of $[M+H]^+$ (533.156). However, a peak appeared in all the compounds around 532.1 indicating that the isotopic pattern obtained for the three compounds is a mix between the $[M+H]^+$ and $[M]^+$ ions.

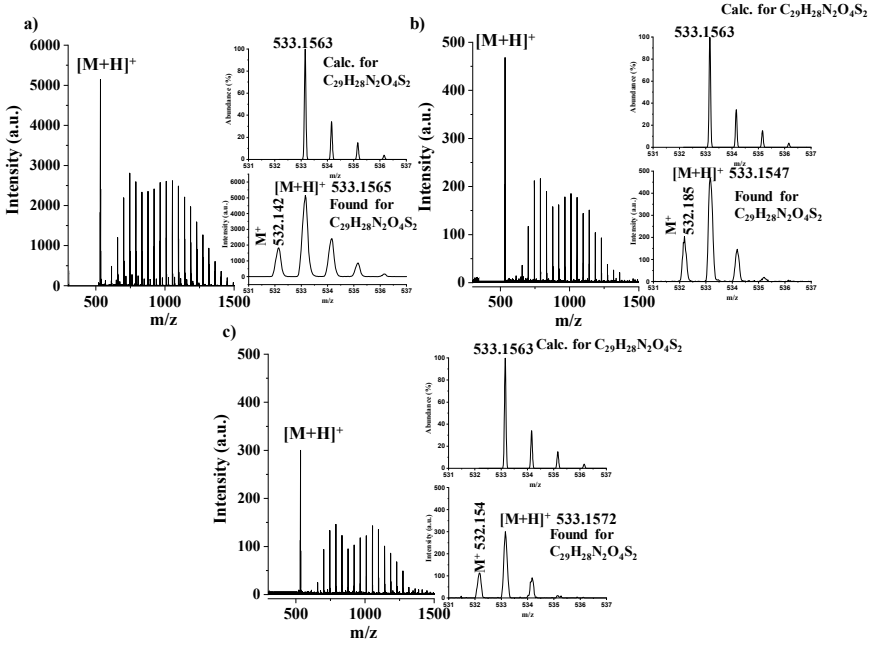

Figure 3.9. *HR-MALDI-TOF of* ***a) o-DPP acid 24****,* ***b) p-DPP acid 25*** *and* ***c) m-DPP acid 26.*** *The peaks that appear in the range between 600-1500 correspond to PEG1000 used for the calibration.*

To gain insight into the ground-state interactions, the UV-vis measurements in MeOH were made (**Figure 3.10a**). At first glance, similar shapes for the absorption spectra were found for the three DPP-acid derivatives. Absorptions in the zone of high-energy (325-425 nm) corresponding to the transition to higher singlet excited state, and in the zone of low range (425-705 nm), which are attributed to the transitions for the lowest singlet excited state, were detected. In relation to DPP-acids, what stands out most is the red shift compared to **DPP 27**, due to the extended conjugation with the introduction of the benzoic acid. ***p*-DPP acid 25** suffered the largest shift, 25 nm, followed by ***m*-DPP acid 26**, suffering a displacement of 23 nm, and finally the ***o*-DPP acid 24** moved 16 nm. In addition, the position of the carboxylic acid in relation to the DPP unit causes a variation in the molar extinction coefficient values. The farther away the two subunits are, the greater the molar extinction coefficient is, thus for the ***p*-DPP acid 25** a value of 31150 $M^{-1}cm^{-1}$ was reached, and 27590 $M^{-1}cm^{-1}$ and 14396 $M^{-1}cm^{-1}$ for ***m*-DPP acid 26** and ***o*-DPP acid 24**, respectively.

The indications of differences in the excited states were provided by the steady-state fluorescence measurements (**Figure 3.10b**). Comparing the fluorescence peaks with the same absorption peaks in all compounds, there was a red shift between 32 and 38 nm, with the ***m*-DPP acid 26** having the shorstest deviation and the ***p*-DPP acid 25** suffering the largest one. The FQY for ***o*-DPP acid 24** was 7.1%

while for ***p*-DPP acid 25** and ***m*-DPP acid 26**, lower values were obtained, 5.3% and 4.6%, respectively, due to greater fluorescence quenching in the last two compounds.

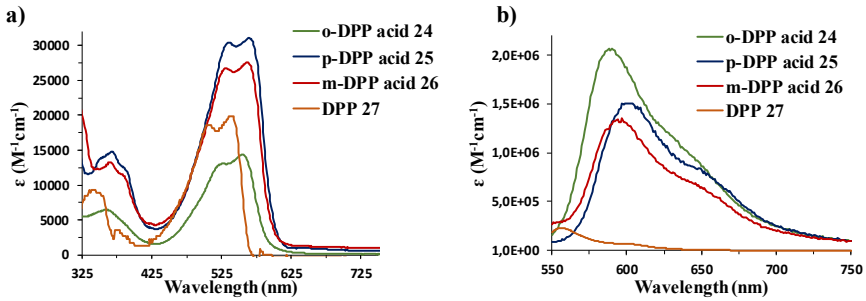

Figure 3.10- a) *Room-temperature absorption spectra of* ***o-DPP acid 24*** *(green),* ***p-DPP acid 25*** *(blue),* ***m-DPP acid 26*** *(red) and* ***DPP 27*** *(orange) in MeOH.* ***b)*** *Fluorescence spectra in MeOH following photoexcitation at 550 nm for the same compounds.*

Excited-state emission decays, measured with the time-resolved fluorescence measurements with 610 nm excitation wavelength, revealed for the DPP-acid derivatives two fluorescent components. In detail, the lifetime in MeOH were 3.3 and 2.1 ns for ***o*-DPP acid 24**, 1.9 and 3.6 ns ***p*-DPP acid 25** and 2.1 and 4.1 ns ***m*-DPP acid 26** (**Figure 3.11**).

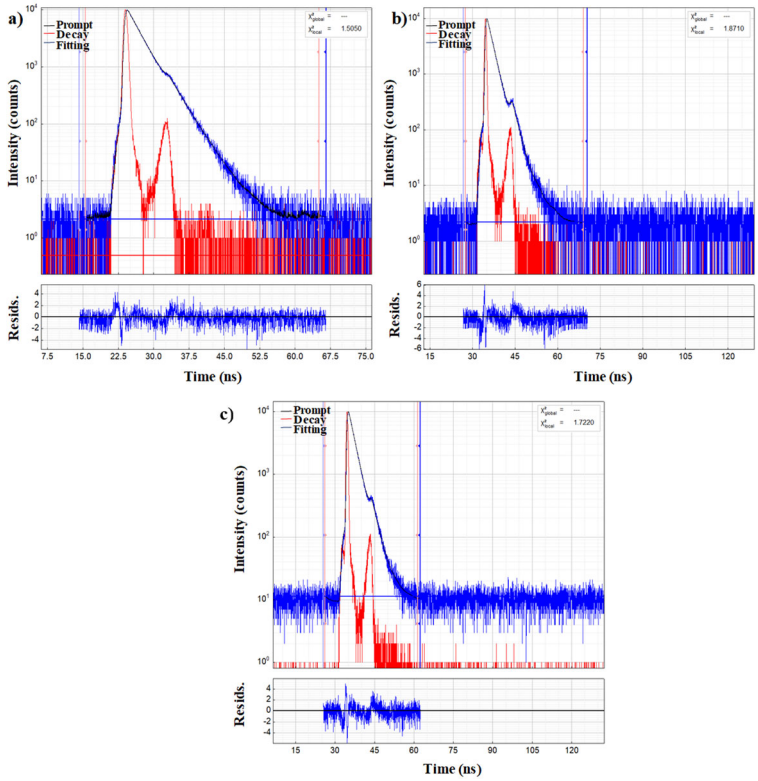

Figure 3.11- *Fluorescence time profiles (excitation at 610 nm) of* ***a) o-DPP acid 24****,* ***b) p-DPP acid 25*** *and* ***c) m-DPP acid 26****, in MeOH at rt. The response of the instrument was defined by the black line, the emission decay by the red line and the blue line is the fitting with a biexponential decay. The blue line in the residual graphic is the residual data from fitting.*

3.4.2. Synthesis and characterization of chiral template

The followed procedure for the synthesis of the silica nanostructures has been developed in the CMA group over the years.[175] It can be divided into three major steps, where in the first step the synthesis of the organic reactants was carried out, following the self-assembly process and the silica transcription (**Figure 3.12**). In this work, two different types of silica nanostructures have been addressed, nano-helices and the twisted ribbons, in order to compare the chirality induction in both. Whenever the type of nanostructures or the enantiomer is not relevant, it will be referenced in this manuscript with L-Helix (right handed helix), for easy reading. **Figure 3.12** represents the simplified scheme carried out for the synthesis of the nanostructures. It should be noted that for visual reasons only the L enantiomer nanostructures were presented, however, the conditions used for the D enantiomer were the same, as previously mentioned.

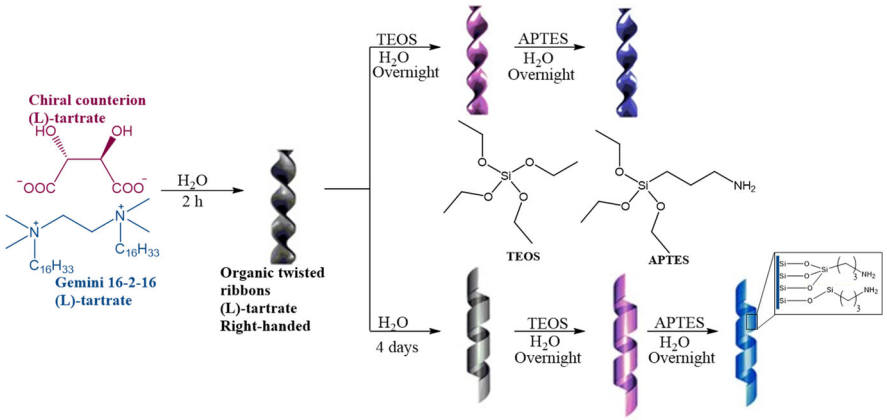

Figure 3.12- *Scheme of the synthesis pathway for the helices or ribbons used in this study, adapted from* [182].

The first step consists on the synthesis of the **16-2-16 tartrate** which is divided into three sub-steps, as can be seen in the **Scheme 3.5**. The first one was the synthesis of the amphiphilic moiety, the **16-2-16 bromide** [or 1,2-ethane bis(dimethylhexadecylammonium), 16-2-16 gemini with bromide counterions], that occurs in the presence of *N*,*N*,*N*',*N*'-tetramethylethylenediamine (TMEDA) with 1-bromohexadecane, and is obtained in 66% yield as a white solid.[185] Once **16-2-16 bromide** was isolated, the ion exchange between the bromide and the acetate in presence of silver acetate in methanol was carried out with a 33% yield causing a precipitate of silver bromide salt. The **16-2-16 acetate** in presence of the appropriate enantiomer of tartaric acid in methanol/acetone 1:9 allow to obtain the **16-2-16 tartrate** in a 66% yield. The intermediary reaction between **16-2-16 bromide** and the **16-2-16 tartrate** was a fundamental step because, it is not possible to obtain the **16-2-16 tartrate** directly from the ion exchange with the bromide. The structure of these three compounds were confirmed by ^{1}H NMR (**Figure 3.13**).

[185] R. Oda, S. J. Candau, R. Oda, I. Huc, *Chem. Commun*., **1997**, 2105–2106.

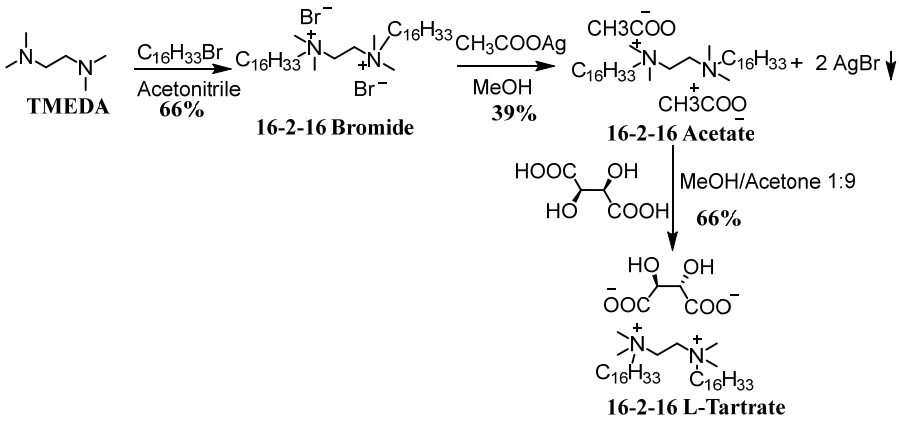

Scheme 3.5- *Synthetic route for the synthesis of* ***16-2-16 L-tartrate.***

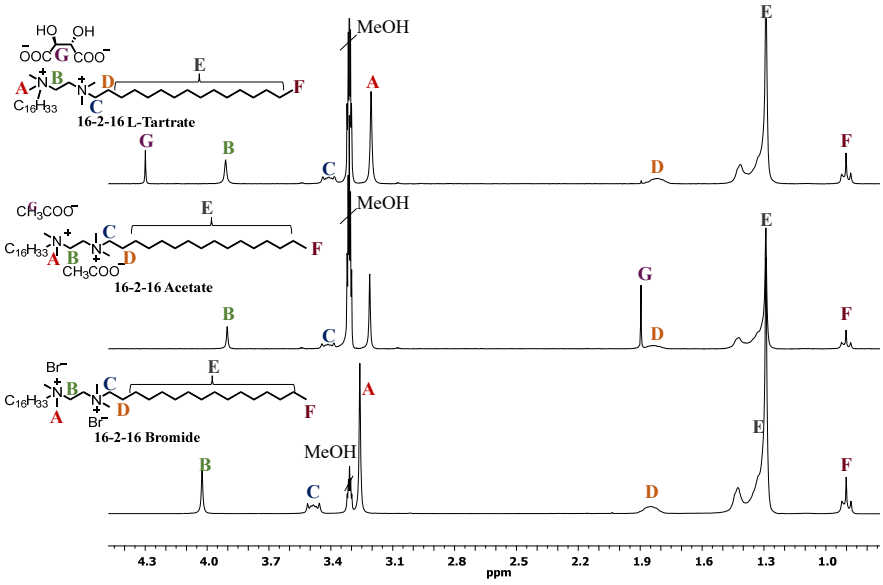

Figure 3.13- *^{1}H NMR of the* ***16-2-16 bromide****,* ***16-2-16 acetate*** *and* ***16-2-16-L-Tartrate*** *in MeOD-d_4 at 25 °C.*

The second step for the formation of the silica nanostructure was made by coating the self-assembly of **16-2-16 tartrate** with silica shell by sol-gel polycondensation.[186] The self-assembly of organic part (**16-2-16 tartrate**) was triggered by the suspension of **16-2-16 tartrate** in ultrapure water and raising its temperature above the Krafft temperature in order to dissolve all the white powder. And then, the temperature of the solution was lowered to 20 °C and depending on the type of nanostructure the solutions were aged for 2 hours (twisted nano-ribbons)

[186] a) K. Sugiyasu, S Tamaru, M. Takeuchi, D. Berthier, I. Huc, R. Oda, S. Shinka, *Chem. Commun*., **2002**, 1212–1213. b) Y. Ono, K. Nakashima, M. Sano, Y. Kanekiyo, K. Inoue, J. Hojo, S. Shinka, *Chem. Commun.,* **1998***,* 1477–1478.

or for 4 days for nano-helices. After obtaining the desired morphologies, the organic parts were coated with the silica shell. This process allowed to maintain the shape of the self-assembled structure through a polycondensation of tetraethylorthosilicate (TEOS).[187] This consists in the hydrolysis of the TEOS in a 100 µM solution of tartaric acid for 7 hours, and then adding it to a tube containing the self-assembled organic structure and left the reaction overnight at 20 °C. The reaction happened just around the nanostructures because the quaternary ammonium of the template catalyses silica condensation, thereby, accelerating the reaction only at the surface.
After the reaction time, the TEOS excess was eliminated by several washes and centrifugation with methanol. Between the washes the solutions were heated at 70 °C. Furthermore, with this method it was possible to dissolve the organic part, allowing in the end the nanostructures to be completely inorganic, as intended. After all washes, the morphology was controlled using TEM and to ensure good dispersion the nanostructures were tip-sonicating (**Figure 3.14**).

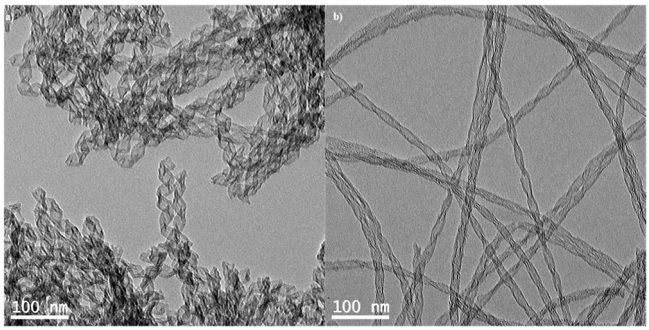

***Figure 3.14**- TEM pictures of **a)** L-nano-helices. **b)** L-twisted nano-ribbons.*

Finally, the last step consisted in functionalization of the surface in order to make the template surfaces reactive to allow reaction with the chromophores, and for this several methods can be found. The most common, and the one used in this work, was functionalization with terminal amine groups using (3-aminopropyl)triethoxysilane (APTES) in methanol overnight at 80 °C. This procedure leads to a good coverage of the surface.[188] Between the first and the second APTES reaction the nanostructures were calcinated to improve the chirality, as explained in the literature.[189]

[187] Y. Okazaki, J. Cheng, D. Dedovets, G. Kemper, M.-H. Delville, M.-C. Durrieu, H. Ihara, M. Takafuji, E. Pouget, R. Oda, *ACS Nano,* **2014**, *8*, , 6863–6872.
[188] a) S. Flink, F. C. J. M. van Veggel, D. N. Renhoudt, *J. Phys. Org. Chem.,* **2001**, *14*, 407–415. b) E. A. Smith, W. Chen, *Langmuir*, **2008**, *24*, 12405-12409.
[189] Y. Okazaki, T. Buffeteau, E. Siurdyban, D. Talaga, N. Ryu, R. Yagi, E. Pouget, M. Takafuji, H. Ihara, R. Oda, *Nano Lett.*, **2016**, *16*, 6411−6415.

3.4.3. Grafting of the dyes to the silica templates

The grafting of the compounds onto silica templates was performed through covalent bonding, therefore, it was necessary to activate the carboxylic acid group of DPP acid derivatives to allow the reaction with the NH_2 groups of the templates. This activation was made with ethyl chloroformate containing trimethylamine, synthesizing the anhydrides corresponding to the derivatives **24**, **25** and **26** (**Figure 3.15**). Then, the activated dyes were placed in contact with the templates without any purification step, so the linked systems were obtained.

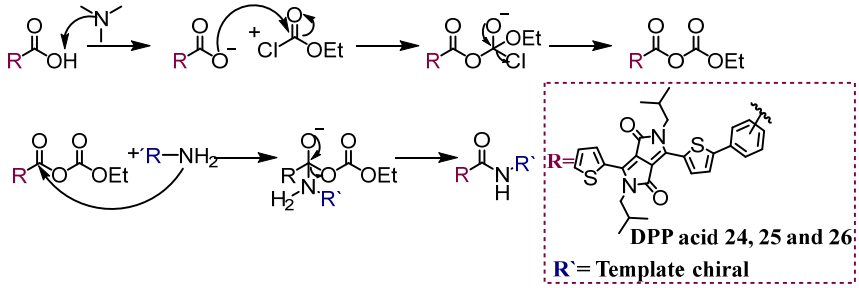

***Figure 3.15**- Mechanism of dye activation and the subsequent reaction with the silica templates.*

As explained before this is a method with several steps, however the experimental process of grafting in the helices or in the ribbons is similar.

- **<u>Grafting in helices nanostructures</u>**

The first evidence of the grafting was the change in the colour of the helices from white to the respective colour of the DPP acid derivatives after several washes to remove all free dye. With the UV-vis spectra it was possible to realize the interactions in the ground state between the DPP derivatives and the DPP-helices in MeOH (**Figure 3.16 down**). In the three cases, broad spectra were observed that were slightly shifted from the corresponding free dyes, which can be attributed to electronic coupling and enhanced π-π interactions when grafted onto the surface of the nanostructure. These differences allow to prove that the grafting was effective allowing to study the chirality induction by CD. In a first observation, it was possible to notice that the compound ***o*-DPP acid 24** was the one that induced the least chirality, due to the a shapeless and noisy spectrum, and for this reason it was not possible to calculate the dissymmetry factor (**Figure 3.16 top a**). In addition, low molecular density values were also obtained, which can also be observed in the UV-Vis spectrum due to the low absorption (**Figure 3.16 a down** and **Table 3.1**). On the other hand, the appearance of peaks in the CD spectra of ***p*-DPP acid 25** and ***m*-DPP acid 26** reveal an induction of chirality in these two compounds (**Figure 3.16 top b** and **c**).

A closer look reveals that the grafting of the ***p*-DPP acid 25** into the helices showed an opposite Cotton effect[190] at around 483 nm, a dissymmetry factor of -7.52×10^{-5} and 4.99×10^{-5} for right (LH) and left (DH) handed helices, respectively. This difference in the dissymmetry values could be explained by a difference in the density of the chromophore on the surface between the samples. And in fact a higher coverage on the right handed helices was obtained (0.62 molecule/nm^2 *vs* 0.46 molecule/nm^2). For the ***m*-DPP acid 26** a perfect mirror-image spectrum was obtained. However, a lower dissymmetry value was calculated (around $\pm5.5\times10^{-5}$ calculated for 480 nm) comparing with the values obtained for ***p*-DPP acid 25**, explained by a lower density of molecules on the surface (around 0.30 molecules/nm^2). The ***m*-DPP acid 26** spectra were less noisy compared to the spectra of the other compounds, being able to observe the other signal with low intensity at 559 nm. In all cases, the CD signal came from the supramolecular chirality induction in chromophores since the CD signal of the APTES functionalized silica nanostructure is close to zero.[181]
Therefore, the greater the distance between the DPP and the nanostructure, the greater the chirality induction is, as can be seen from the data compiled **Table 3.1**.

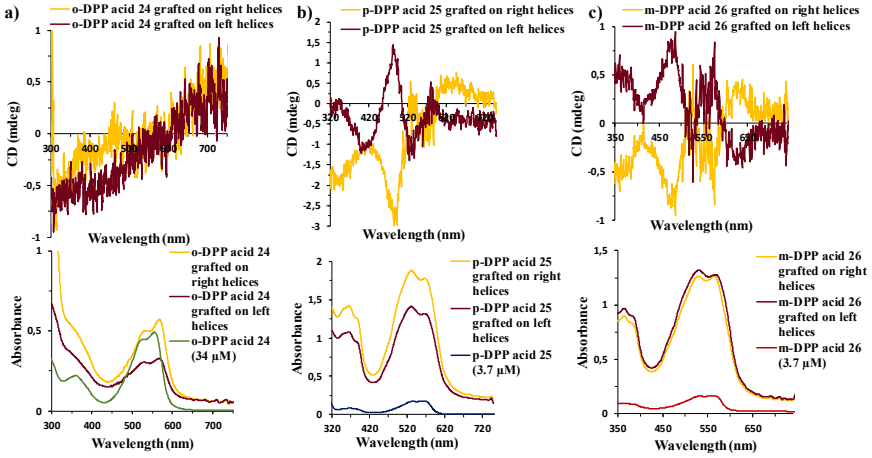

Figure 3.16- *Top correspond to CD spectra and down to UV-vis spectra of* ***a) o-DPP acid 24*** *and after the grafting on the surface of the helices,* ***b) p-DPP acid 25*** *and after the grafting on the surface of the helices and* ***c) m-DPP acid 26*** *and after the grafting on the surface of the helices.*

In addition, to the studies carried out in the fundamental state, the excited state was also studied through fluorescence measurements in MeOH (**Figure 3.17**). Common to ***o*-DPP acid 24**, ***p*-DPP acid 25** and ***m*-DPP acid 26**, hypsochromic shifts were visible in the dye-helix systems when compared with the free dye spectra, however, this displacement was not as noticeable for ***m*-DPP acid 26**-helix systems.

[190] The Cotton effect is the characteristic change in optical rotational dispersion and/or circular dichroism in the vicinity of a substance absorption band.

Furthermore, the increment of the shoulder in the spectra of systems with helices can be explained by the existence of an excimer. This excimer was formed due to the close contact between the chromophores, it means that there was a close packing of the chromophores in the silica surface. These discrepancies with the free chromophore spectra allow us to confirm new intermolecular interactions between DPP units that are an additional guarantee that allows us to conclude the effectiveness of the grafting (**Table 3.1**).

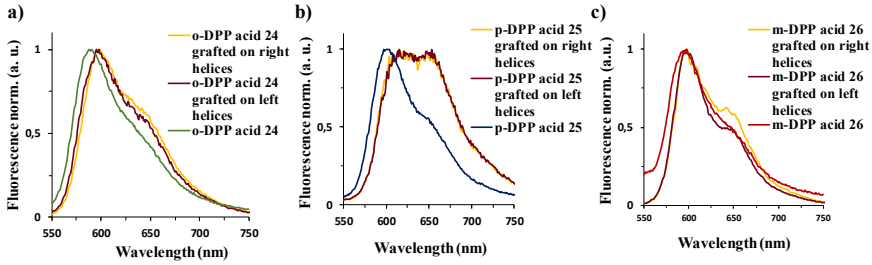

***Figure 3.17**- Emission spectra of **a) o-DPP acid 24**, **b) p-DPP acid 25** and **c) m-DPP acid 26** as free dyes and the dyes grafted on the surface of right (yellow) and left (brown) handed helices in MeOH.*

The lifetime of the fluorescence in MeOH was also measured for the DPP-helix systems and gave rise to two fluorescence components. In detail, comparing with free dye, with the dye-helix systems there was an increase in the lifetime (around 2 ns for 4 ns) but, as with the free dyes, the lifetimes did not vary much between the different compounds (**Table 3.1** and **Figure A52-A54**). This increment on the fluorescence lifetime could be explained by the appearance of an excimer in the excited state.[191]

The morphology of the nanostructures was studied by TEM images (**Figure 3.18**). Comparing the TEM images of grafting helices and the APTES functionalized silica (**Figure 3.14 a**), no discernible change was observed in the preservation of the morphology just some deformities appeared, indicating a stability of the silica helices during the grafting process.

[191] J. Gorman, R. Pandya, J. R. Allardice, M. B. Price, T. W. Schmidt, R. H. Friend, A. Rao, N. J. L. K. Davis, *J. Phys. Chem. C*, **2019**, *123*, 3433−3440.

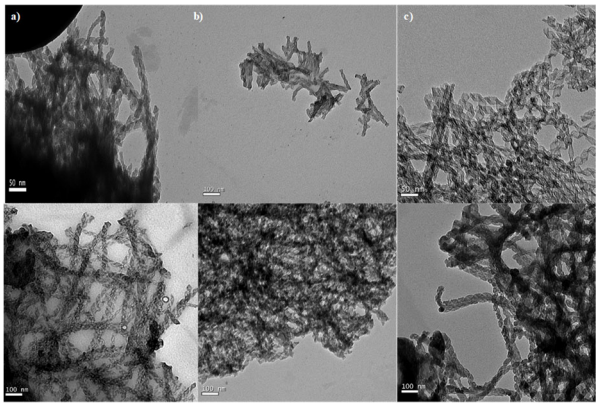

***Figure 3.18**- TEM picture of right (top) and left (down) handed helices after grafting of **a) o-DPP acid 24**, **b) p-DPP acid 25** and **c) m-DPP acid 26**.*

- **<u>Grafting in ribbons nanostructures</u>**

As it was studied for the previous supramolecular systems, the grafting of DPP derivatives in the ribbon nanostructures was studied by the UV-vis and fluorescence spectra and the chirality induction by CD graphics. Once again, changes were observed in the UV-vis spectra in relation to the free dyes spectra, in addition to getting broader spectra, a red shift of the maximum was also noticed in all cases (**Figure 3.19 down** and **Table 3.1**). These changes were attributed to intermolecular interactions between DPP units due to their proximity after grafting. Besides the UV-vis spectra, the emission spectra also demonstrated alterations between the supramolecular systems and the free dyes (**Figure 3.20**). As observed in supramolecular templates using helices, large changes in the emission spectra were noted. Namely, the increment of a shoulder that appears at 630-675 nm giving us an indication of the existence of an excimer, which was increased by those intermolecular interactions when DPPs were linked to the nanostructure, that form a dimer in the excited state.

The chirality induction was ascertained by the CD spectra (**Figure 3.19 top**). And again, the greater the distance between the nanostructure and the DPP unit the greater the value of dissymmetry, so the order was ***p*-DPP acid 25>*m*-DPP acid 26>*o*-DPP acid 24** (**Table 3.1**). However, a better grafting was obtained for ***m*-DPP acid 26** in the sense that the grafting density for both enantiomers was similar, which was not obtained for the case of ***p*-DPP acid 25**. For the right handed ribbons system was obtained a 0.36 molecules/cm^2 coverage was obtained, while for the system with the other enantiomer a 0.58 molecules/cm^2 value was obtained. Nevertheless, the most surprising fact was that the g_{abs} for the right handed system around 488 nm was -7.33×10^{-5} while for the left handed system was $+3.81\times10^{-5}$ nm and the expected would be that the higher the density of molecules on the surface of the nanostructure the larger the g_{abs} would be. And, in addition to these

inequalities in values, a spectrum that is mirror image of each other has not been observed, with a slight shift between them. In the case of ***o*-DPP acid 24**, a shapeless and noisy spectrum was also obtained making it hard to calculate the value of g_{abs}.

Although, it is not possible to directly compare the results of helices and ribbons due to their difference in curvature, in literature the helices are described as more chiral than ribbons due to their higher shrinkage.[189] However, within this study the difference between both nanostructures it is not significant.

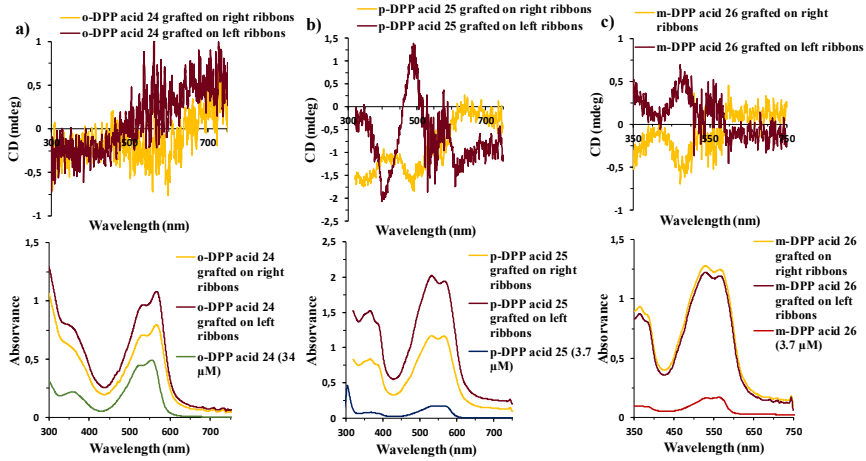

Figure 3.19- *Top correspond to UV-vis spectra and down to CD spectra of* ***a) o-DPP acid 24*** *and after the grafting on the surface of the ribbons,* ***b) p-DPP acid 25*** *and after the grafting on the surface of the ribbons and* ***c) m-DPP acid 26*** *and after the grafting on the surface of the ribbons.*

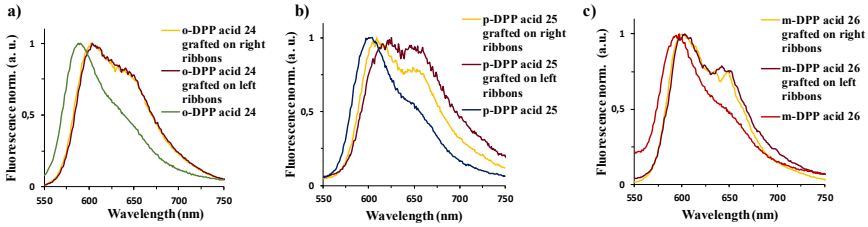

Figure 3.20*- Emission spectra of a)* ***o-DPP acid 24****, b)* ***p-DPP acid 25*** *and* ***c) m-DPP acid 26*** *as free dyes and the dyes grafted on the surface of right (yellow) and left (brown) handed ribbons.*

The fluorescence lifetimes of the systems were measured and by the shape of the fluorescence spectra and the results obtained with the helices, two components were observed as expected. In detail, the higher lifetime for all systems was around 4 ns and the other one was around 1 ns (**Table 3.1** and **Figure A55-A56**).

TEM images (**Figure 3.21**) showed the same morphology than the APTES functionalized silica-ribbons (**Figure 3.14b**) convincing that the introduction of chromophores did not destroy these structures.

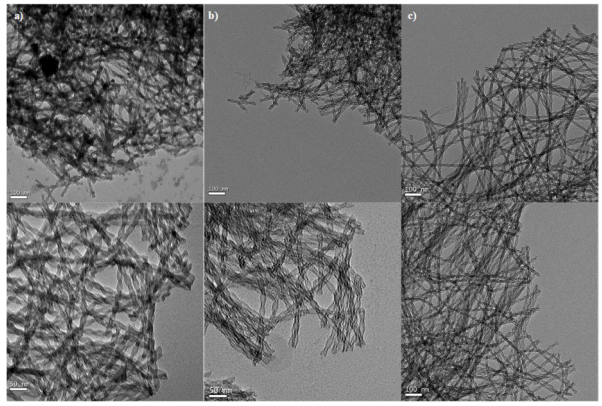

Figure 3.21**- TEM picture of right (top) and left (down) handed ribbons after grafting of **a) o-DPP acid 24**, **b) p-DPP acid 25** and **c) m-DPP acid 26.

***Table 3.1-** Chiroptical parameters of **o-DPP acid 24**, **p-DPP acid 25** and **m-DPP acid 26**.*

System		Absorption (nm)	g_{abs}/λ (nm)	Emission (nm)	Density of chromophores (molecules/ nm^2)[b]
***o*-DPP acid 24**	**a**	527/ 555	-	590	-
	LH	563/ 567	-	599/641	0.071
	DH	530/ 566	-	598/640	0.040
	LR	533/ 567	-	602/641	0.091
	DR	533/ 567	-	604/641	0.124
***p*-DPP acid 25**	**a**	535/ 564	-	600	-
	LH	532/ 568	-7.52×10^{-5}/484	615/654	0.618
	DH	531/ 567	-4.99×10^{-5}/482	616/653	0.457
	LR	531/ 565	-7.33×10^{-5} /488	609/649	0.357
	DR	533/ 567	$+3.05\times10^{-5}$ /487	625/647	0.580
***m*-DPP acid 26**	**a**	534/ 563	-	597	-
	LH	528/ 564	-5.54×10^{-5}/480 -2.31×10^{-5}/559	598/642	0.301
	DH	528/ 567	$+5.54\times10^{-5}$/480 $+2.31\times10^{-5}$/559	597/643	0.295
	LR	529/ 565	-4.34×10^{-5}/474 -2.65×10^{-5}/559	600/648	0.275
	DR	530/ 565	$+4.34\times10^{-5}$/474 $+2.65\times10^{-5}$/559	603/649	0.265

a) Results for the free dyes. **–** no value (for the free dyes) and small value difficult to determinate with precision (***o*-DPP acid 24**). **b)** to determine the density of chromophores the scattering of the UV-VIS spectra was removed with the Voigt´s functions.

3.5. Conclusions

In summary, a novel family of DPP derivatives was synthesized and characterized, ***o*-DPP acid 24**, ***p*-DPP acid 25** and ***m*-DPP acid 26**. The 1-bromo-2-methylpropane chain being smaller than 3-(bromomethyl)heptane chain led to a decrease of the solubility.

The best synthetic route for the three compounds was obtained when a Suzuki-Miyaura coupling was made between the **DPP 28** and the benzoic acids **29**, **30** and **31**. The structures of the acid derivatives were confirmed with the usual characterization techniques namely with ^{1}H NMR. The biggest difference that stands out when the three compounds were compared, was the shift of the signals from the benzene rings.

The ground and the excited states of the compounds were studied by the UV-vis and fluorescence spectra. In UV-vis spectra of all compounds, two ranges were observed, one in the high-energy (325-425 nm) and other in the low- energy zone (425-705 nm). DPP acids appeared red shifted relative to **DPP 27** due to an increment in the conjugation. A smaller distance between the DPP and the acid unit led to a decrease in the molar extinction coefficient. For the ***p*-DPP acid 25** a value of 31150 $M^{-1}cm^{-1}$ was reached and 27590 $M^{-1}cm^{-1}$ and 14396 $M^{-1}cm^{-1}$ for ***m*-DPP acid 26** and ***o*-DPP acid 24**, respectively.

A red shift was also observed in the DPP acids emission spectra. FQY values of 7.1% for ***o*-DPP acid 24**, of 5.3% for ***p*-DPP acid 25** and 4.6% for ***m*-DPP acid 26** were obtained. Besides that, the fluorescence lifetimes were also measured, demonstrating that there is not a big difference between the three compounds.

The synthesis of the chiral templates was made with a sol-gel methodology already described in the literature. The success in grafting the dyes onto the surface of the nanostructures was analysed by UV-vis and fluorescence spectra that appeared shifted in relation to the spectra of the respective free chromophores.

In the fluorescence spectra, besides the shifted spectra a more intense shoulder appeared in all cases that can be explained by the intermolecular interaction between the DPP units due to the higher proximity when the compounds were grafted.

In both systems, it was concluded that the greater the distance between the nanostructure and the DPP unit, the greater the value of dissymmetry and the greater the induction of chirality. And interestingly, also for both types of systems, with ***m*-DPP acid 26** a perfect Cotton effect was obtained.

One of the objectives of this work was to verify whether ribbon systems, which are described as systems that induce less chirality due to their curvature, could also

induce chirality in systems such as DPP, and in fact it was possible to induce chirality in these systems, however the results were not significantly different from those obtained with the helix nanostructures.

The g_{abs} values were not so high as pretended and that weakness might be due to low chirality induction for the molecules which are too far from each other to interact through electron transfer, or the distance to the chiral source because of the APTES chain. Due to this weak chiroptical signals, we were not able to detect CPL.

3.6. Experimental section

3.6.1. Material and methods

DySMol laboratory

All chemicals and solvents were purchased from Sigma Aldrich (Merck) and TCI and were used without further purification unless otherwise stated.

Column chromatography was performed with SiO_2 (40–63 μm) and the thin-layer chromatography was made using SiO_2 60F254 and was visualized with UV light.

NMR data (^1H and ^{13}C) was recorded at 25 °C with a Bruker AC300 and Bruker A400 spectrometer.

Matrix assisted laser desorption/ionization time-of-flight (MALDI-TOF) mass spectra were obtained on a Bruker Microflex LRF20 instrument using PEG as a matrix.

UV-vis spectra in MeOH solution were measured with a Helios Gamma spectrophotometer and the extinction coefficients were calculated using the Lambert-Beer Law.

FT-IR spectra were measured with a Nicolet Impact 400D spectrophotometer

NEO and CMA laboratories

All chemicals and solvents were obtained in Sigma Aldrich (Merck) and were used without further purification.

For supramolecular characterization, the TEM microscopes with LVEM5 from Delong Instruments (Brno, Czech Republic) were used. The instrument is working with a Schottky field emission gun operating at a nominal acceleration voltage of 5kV, and a crystal of yttrium aluminium garnetis (YAG) used to convert the electronic image into a visible image, which is observed using a camera (Zyla 5.5 Scientific CMOS) through a microscope objective (Objectives Olympus M 4x or 40x).

Circular dichroism spectra were measured on a Jasco J-815 (190-800nm) equipped with a xenon-mercury lamp and running under nitrogen atmosphere. The sample temperature was maintained to 20°C using a Peltier device (PFD-425S/15). All samples were stirred at 1000 rpm during measurements, and every spectrum was taken as the average of 4-10 scans.

Absorption spectra were collected on a PekinElmer UV/VIS/NIR Lamba 750 spectrometer.

Fluorescence spectra were measured on a Fluormax-4 spectrophotometer. Quantum yields were determined from corrected emission spectra using Rhodamine G (MeOH; FQY = 0.95 in MeOH: EtOH) for ***o*-DPP acid 24**, ***p*-DPP acid 25** and ***m*-DPP 26**.

Lifetime spectra were performed on a PicoQuant PDL 800-D. The excitation originated from a diode laser at 453 nm operated in pulsed mode.

3.6.2. Synthesis of achiral dyes

3.6.2.1. Synthesis of 2,5-bis(2-methyl-propane)-3,6-di(tyien-2-yl)-2,5-dihydropyrrolo[3,4-*c*]pyrrol-1,4-dione (27)

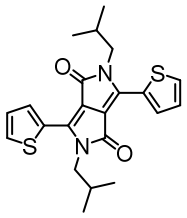

Dry DMF (20 mL) was added to a two-neck flask under nitrogen that contained **DPP 4** (2.0 g, 6.6 mmol) and Cs_2CO_3 (6.5 g, 20 mmol), and the mixture was warmed up to 120 °C. Once this temperature was reached, a solution of 1-bromo-2-methylpropane (2.7 g, 20 mmol) in dry DMF (10 mL) was added dropwise and the reaction was left for 24 hours. The reaction mixture was cooled to rt, a HCl 2M solution was added and it was extracted with ethyl acetate. Then the organic layer was dried over anhydrous $MgSO_4$, and the solvent was removed off under reduced pressure. The crude product was purified through a silica gel column with toluene as eluent to give a red solid with a 49% yield. **^{1}H-NMR** (300 MHz, $CDCl_3$): δ (ppm) 8.98 (dd, *J*= 3.9 Hz, *J*= 1.2 Hz, 2H), 7.63 (dd, *J*= 5.1 Hz, *J*= 1.2 Hz, 2H), 7.29-7.26 (m, 2H), 3.96 (d, *J*= 7.5 Hz, 4H), 2.22-2.03 (m, 2H), 0.97 (d, *J*= 6.6 Hz, 12H). **^{13}C-NMR** (75 MHz, $CDCl_3$): δ (ppm) 161.8, 140.4, 135.6, 130.7, 130.0, 128.6, 107.9, 48.8, 29.4, 20.1. **UV-vis** (MeOH): λ_{max}, nm (log ε) 340 (3.79), 506 (4.09), 539 (4.12). **FT-IR (KBr)** ν (cm^{-1}): 3097, 3084, 2957, 2984, 2864, 1671, 1569, 1506, 1454, 1420-1402, 1305, 1095, 1068, 815-734. **HR-MS (MALDI-TOF)**: 413.1368 m/z cal. for $C_{29}H_{28}N_2O_4S_2$ (found for $[M+H]^+$ 413.1352).

3.6.2.2. Synthesis of 2,5-bis(2-methyl-propane)-3,(5-bromotien-2-il)-6-di(thien-2-yl)-2,5-dihidropyrrolo[3,4-*c*]pyrrol-1,4-dione (28)

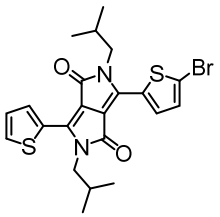

1 mL of acetic acid was added to a solution of **DPP 27** (300 mg, 0.730 mmol) in $CHCl_3$ (20 mL) at 5 °C. Then, a NBS (129 mg, 0.730 mmol) solution in acid acetic (2 mL) was added dropwise. Allowed to reach the rt the mixture was stirred for 2h. Then, the product was washed with NaOH and H_2O, extracted with $CHCl_3$ and dried with Na_2SO_4. The final product was purified in a chromatographic column using toluene as eluent obtaining 257 mg (72%) of a purple powder. **^{1}H-NMR** (400 MHz, $CDCl_3$) δ (ppm) 8.89 (dd, *J*= 4.0 Hz, *J*= 1.2 Hz, 1H), 8.72 (d, *J*= 5.6 Hz, 1H), 7.64 (dd, *J*= 5.2 Hz, *J*= 1.6 Hz, 1H), 7.29-7.26 (m, 1H), 7.23 (d, *J*= 5.6 Hz, 1H), 3.94 (d, *J*=10 Hz, 2H), 3.87 (d, *J*=10 Hz, 2H), 2.19-2.03 (m, 2H), 0.99-0.95 (m, 12H). **^{13}C-NMR** (75 MHz, $CDCl_3$): δ (ppm) 161.7, 161.5, 140.8, 138.9, 135.9, 135.5, 131.6, 131.4, 131.0, 130.0, 130.0, 128.7, 118.9, 108.1, 107.8, 48.9, 29.5, 29.4, 20.1. **UV-vis** (MeOH): λ_{max}, nm (log ε) 346 (4.10), 513 (4.37), 547 (4.39). **FT-IR (KBr)** *v* (cm^{-1}): 3076, 2956, 2928, 2867, 1654, 1558, 1504, 1449, 1067, 817-731. **HR-MS (MALDI-TOF)**: 491.0487 m/z cal. for $C_{29}H_{28}N_2O_4S_2$ (found for $[M+H]^+$ 491.0457).

3.6.2.3. Synthesis of benzoic acid derivatives

Methyl 2- or 4-(4,4,5,5-tetramethyl-1,3,2-dioxaborolan-2-yl)benzoate, KOH and THF/H_2O (3:1) were added to a reaction flask. Subsequently the reaction was refluxed for 2h. After that, the reaction was allowed to reach rt and 2 mL of HCl (2M) and H_2O were added and the mixture was extracted with ethyl acetate, dried over anhydrous $MgSO_4$ and the solvent was removed off under reduced pressure. The crude product, a white solid, was washed several times with hexane and used in the next step without any other type of purification.

- **Synthesis of 2-(4,4,5,5-tetramethyl-1,3,2-dioxaborolan-2-yl)benzoic acid (29):** Yield 60%.

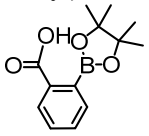

^{1}H NMR (300 MHz, $CDCl_3$): δ (ppm) 8.06 (d, *J*= 6.0 Hz, 1H), 7.59-7.52 (m, 2H), 7.48-7.45 (m, 1H), 1.42 (s, 12H).

- **Synthesis of 4-(4,4,5,5-tetramethyl-1,3,2-dioxaborolan-2-yl)benzoic acid (30)**: Yield 90%

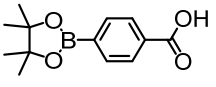

^{1}H NMR (300 MHz, $CDCl_3$): δ (ppm) 8.10 (d, *J*= 6.0 Hz, 2H), 7.91 (d, *J*= 6.0 Hz, 2H), 1.37 (s, 12H).

3.6.2.4. Synthesis of ester derivatives

DPP 28 (100 mg, 0.204 mmol), the corresponding methyl benzoate derivative (80 mg, 0.31 mmol) and TBAB (3.2 mg, 0.01 mmol) were added under nitrogen to a 25 mL round-bottom flask. Then, 5 mL of degassed toluene were added to the flask and the solution was degassed again. Afterwards, a degassed K_2CO_3 2 M solution (1 mL), and $Pd_2(dba)_3$ (18 mg, 0.02 mmol) solution in toluene (6 mL) were added to the reaction flask. The reaction was stared overnight at 100 °C. After that, the crude was washed with HCl (2M) and water and extracted with $CHCl_3$. The compounds were purified by silica gel column chromatography using CH_2Cl_2 as eluent obtaining them in the form of dark pink solids.

- **Methyl 2-(5-(2,5-diisobutyl-3,6-dioxo-4-(thiophen-2-yl)-2,3,5,6-tetrahydropyrrolo[3,4-*c*]pyrrol-1-yl)thiophen-2-yl)benzoate (*o*-DPP ester 32):** Yield 64%

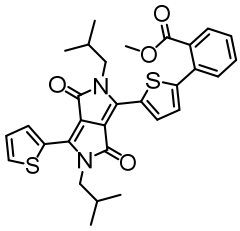

^{1}H NMR (300 Hz, $CDCl_3$): δ (ppm) 9.05 (d, *J*= 4.0 Hz, 1H), 8.99 (dd, *J*= 4.0 Hz, *J*= 1.2 Hz, 1H), 7.83 (dd, *J*= 8.0 Hz, *J*= 1.0 Hz, 1H), 7.63 (dd, *J*= 4.8 Hz, *J*= 1.0 Hz, 1H), 7.59-7.52 (m, 2H), 7.50-7.46 (m, 1H), 7.29-7.27 (m, 1H), 7.19 (d, *J*= 4.0 Hz, Hz, 1H), 3.97 (dd., *J*= 5.2 Hz, *J*= 2.4 Hz, 4H), 3.78 (s, 3H), 2.25- 2.09 (m, 2H), 0.99 (dd, *J*= 4.4 Hz, *J*= 2.4 Hz, 1H).

- **Methyl 4-(5-(2,5-diisobutyl-3,6-dioxo-4-(thiophen-2-yl)-2,3,5,6-tetrahydropyrrolo[3,4-*c*]pyrrol-1-yl)thiophen-2-yl)benzoate (*p*-DPP ester 33):** Yield 94%

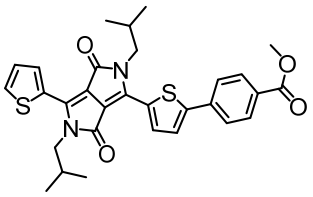

^{1}H NMR (300 Hz, $CDCl_3$): δ (ppm) 9.01 (dd, *J*= 4.0 Hz, *J*= 1.2 Hz, 1H), 8.98 (d, *J*= 4.4 Hz, 1H), 8.09 (d, *J*= 8.4 Hz, 2H), 7.74 (d, *J*= 8.8 Hz, 2H), 7.643 (dd, *J*= 5.2 Hz, *J*= 4.0 Hz, 1H), 7.56 (d, *J*= 4.4 Hz, 1H), 7.29 (dd, *J*= 4.0 Hz, *J*= 1.2 Hz, 1H), 4.00-3.95 (m, 7H), 2.24-2.09 (m, 2H), 1.00 (dd, *J*= 6.8 Hz, *J*= 3.2 Hz).

3.6.2.5. Synthesis of acid derivatives

DPP 28 (100 mg, 0.20 mmol), the corresponding benzoic acid (75.9 mg, 0.31 mmol) and TBAB (3.2 mg, 0.01 mmol) were added under nitrogen to a 25 mL round-bottom flask. Then 5 mL of degassed dioxane were added to the flask and the solution was degassed again. After that, a degassed K_2CO_3 2 M solution (1 mL), and $Pd_2(dba)_3$ (18 mg, 0.02 mmol) solution in dioxane (6 mL) were added to the reaction flask. The reaction was stirred overnight at 90 °C. After that, the crude

was washed with HCl (2M) and water and extracted with chloroform. The compounds were purified by silica gel column chromatography using different ratio of chloroform/methanol as eluent and were obtained in the form of dark pink solids.

- **2-(5-(2,5-diisobutyl-3,6-dioxo-4-(thiophen-2-yl)-2,3,5,6-tetrahydropyrrolo[3,4-*c*]pyrrol-1-yl)thiophen-2-yl)benzoic acid *(o*-DPP acid 24).** Yield: 3%.

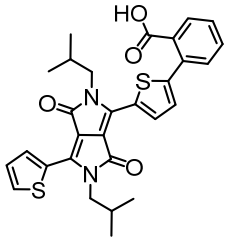

^{1}H NMR (400 MHz, CD_3OD-d_4): δ (ppm) 8.90-8.89 (m, 1H), 8.84 (d, *J*= 4.0 Hz, 1H), 7.98 (d, *J*= 4.0 Hz, 2H), 7.61-7.57 (m, 2H), 7.50-7.45 (m, 3H), 7.35-7.32 (q, *J*= 4.0 Hz,1H), 3.99-3.96 (m, 4H), 2.17-2.04 (m, 2H), 0.98-0.94 (m, 12H). **FT-IR (KBr)** *v* (cm^{-1}): 3511, 3107, 2962, 2870, 1700, 1644, 1555, 1433-1403, 816-735. **UV-vis** (MeOH), λ_{max} (log ε): 295 (3.99), 362 (3.81), 527 (4.12), 555 (4.16). **HR-MS (MALDI-TOF)**: 533.1563 m/z cal. for $C_{29}H_{28}N_2O_4S_2$ (found for $[M+H]^+$ 533.1563).

- **4-(5-(2,5-diisobutyl-3,6-dioxo-4-(thiophen-2-yl)-2,3,5,6-tetrahydropyrrolo[3,4-*c*]pyrrol-1-yl)thiophen-2-yl)benzoic acid (*p*-DPP acid 25).** Yield: 46%.

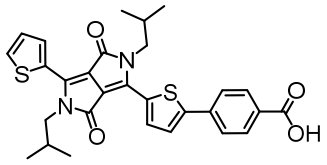

^{1}H NMR (400 MHz, CD_3OD-d_4): δ (ppm) 8.93 (d, *J*= 4.0 Hz, 1H), 8.87 (d, *J*= 4.0 Hz, 1H), 8.04 (d, *J*= 12.0 Hz, 2H), 7.91(d, *J*= 4.0 Hz, 2H) 7.80 (d, *J*= 12.0 Hz, 2H), 7.72 (d, *J*= 8.0 Hz, 1H), 7.35 (t, *J*= 8.0 Hz, 1H), 4.01(dd, *J*= 12.0 Hz, 4H), 2.22-2.11 (m, 2H), 1.01-0.95 (m, 12H). **FT-IR (KBr)** *v* (cm^{-1}): 3450,3076, 2959, 2927, 1686, 1656, 1606, 1554, 1425-1401, 818-733. **UV-vis** (MeOH), λ_{max} (log ε): 306 (3.98), 366 (3.98), 536 (4.25), 564 (4.26). **HR-MS (MALDI-TOF)**: 533.1547 m/z cal. for $C_{29}H_{28}N_2O_4S_2$ (found for $[M+H]^+$ 533.1563).

- **3-(5-(2,5-diisobutyl-3,6-dioxo-4-(thiophen-2-yl)-2,3,5,6-tetrahydropyrrolo[3,4-*c*]pyrrol-1-yl)thiophen-2-yl)benzoic acid (*m*-DPP acid 26).** Yield: 55%.

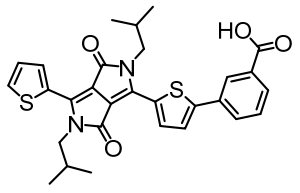

^{1}H NMR (400 MHz, CD_3OD-d_4+ 2 drops TFA-d_1): δ (ppm) 8.88-8.87 (m, 2H), 8.39 (s, 1H), 8.03 (t, *J*=12.0 Hz, 2H), 7.91 (d, *J*= 4.0 Hz, 2H), 7.72 (d, *J*= 4.0 Hz, 1H), 7.61-7.54 (m, 1H), 7.34 (t, *J*= 8.0 Hz, 1H) 4.02-3.94 (m, 4H), 2.06-1.99 (m, 2H), 1.05-0.95 (m, 12H). **FT-IR (KBr)** *v* (cm^{-1}): 3448, 3078, 2961, 2930, 2869, 1725, 1689, 1664, 1555, 1420-1389, 815-734. **UV-vis** (MeOH), λ_{max}

(log ε): 305 (4.22), 365 (4.12), 531 (4.48), 561 (4.49). **HR-MS (MALDI-TOF)**: 533.1563 m/z cal. for $C_{29}H_{28}N_2O_4S_2$ (found for $[M+H]^+$ 533.1563).

3.6.3. Synthesis of chiral template

3.6.3.1. Synthesis of 1,2 ethane bis(dimethylhexadecylammonium) (16-2-16-gemini) bromide (16-2-16 Bromide)

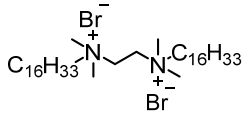

A solution of *N,N,N′,N′*-tetramethylethylenediamine (770 mg, 6.6 mmol) and 1-bromohexadecane (6.0 g, 19.9 mmol) in 50 mL of acetonitrile was stirred during 48h at reflux temperature. Then, the solution was centrifuged (5 min/3893 G/20 °C), washed with acetone and centrifuged again this step was repeated five times. The final product was obtained as a solid with a 66% yield. **^{1}H-NMR** (300 MHz, CD_3OD-d_4): δ (ppm)= 4.02 (s, 4H), 3.51-3.46 (m, 4H), 3.26 (s, 4H), 1.43-1.29 (m, 56H), 0.90 (t, *J*= 6.0 Hz, 6H).

3.6.3.2. Ion exchange to acetate (16-2-16 Acetate)

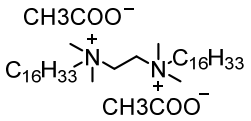

16-2-16 bromide (4.6 g, 6.3 mmol) was dissolved in 50 mL of methanol at 50 °C, then silver acetate (3.17 g, 19.0 mmol) was added into the solution and allowed to react for 24 h. The product was washed 4 times with acetone, centrifuged (12 min, 3983 G, 4 °C) and dried under vacuum, obtaining a white powder with 39% of yield. **^{1}H-NMR** (300 MHz, CD_3OD-d_4): δ (ppm)= 3.90 (s, 4H), 3.44-3.39 (m, 4H), 3.21 (s, 12H), 1.90 (s. 6H), 1.83-1.81 (m, 4H) 1.42-1.29 (m, 52H), 0.90 (t, *J*= 6.4 Hz, 6H).

3.6.3.3. Ion exchange to tartrate (16-2-16 L/D- Tartrate)

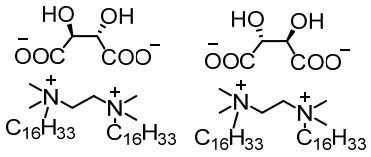

16-2-16 L-Tartrate **16-2-16 D-Tartrate**

A solution of 16-2-16 acetate (1 g, 1.46 mmol) in 50 mL methanol/acetone 1:9 was added dropwise to a solution containing the tartaric acid enantiomer in methanol/acetone 1:9 stirring during 2h at rt. The purification was carried out through several washes with cold water (5-8 times until the pH of the supernant was around 5), with MeOH/acetone (2 times) and the last 2 washed with acetone. The final product was dried under vacuum obtaining a white powder with 66% yield. **^{1}H-NMR** (300 MHz, CD_3OD- d_4): δ (ppm)= 4.30 (s, 2H), 3.91 (s, 4H), 3.44-3.38 (m, 4H), 3.20 (s, 12H), 1.85-1.79 (m, 4H) 1.41-1.29 (m, 56H), 0.90 (t, *J*= 6.5 Hz, 6H).

3.6.4. Formation of silica coated chiral nano-structures

The silica coated chiral nanostructures were synthesized in two steps, the preparation of organic gels and the polycondensation of silica shell. It is important to note that the procedure that was carried out was based on the best conditions used in the work of Oda, using the best conditions and the best grafting density on the surface of the nanostructures obtained in this work.[183]

a) Preparation of organic gel nanostructures

The organic gel was prepared at a concentration of 1mM by adding 20 mg of L / or D 16-2-16 tartrate in 25 mg of ultra-pure water in a 50 mL tube. The solution was heated up to 60 °C (above the Kraft temperature) for 5 min and sonicated 5 minutes. This process was repeated as many times as necessary to dissolve all the solid. The solution was divided into equal amounts by 5 tubes of 10 mL and incubated at 20 °C. Twisted ribbons were observed after 2h, whereas the helices were observed after 4 days.

b) Polycondensation of silica shell in the organic templates

The silica shell formation in the organic templates was made through the polycondensation of TEOS, where 2 mL of TEOS were aggregated to 37.6 mg of water, followed by the addiction of 0.4 mL of L or D tartaric acid solution. The reaction was kept at 20 °C during 7h stirred in a roller-mixer. After the prehydrolysis, 5 mL of TEOS solution were added into the tubes containing the organic template in an equal volume (matching the enantiomers of tartaric acid of both solutions). Letting the reaction overnight stirring on the roller mixer at 20 °C. Once the reaction time was passed, the solutions were washed with methanol at rt, and were heated to 70 °C for 5 min and centrifuged, this process was repeated at least five times.

After removing all the organic part, the silica surfaces were functionalized using APTES for the covalent grafting of the acid derivatives with 20 μmol of APTES per 1 mg of silica nanostructures in methanol at 80 °C overnight. Then, the samples were washed three times with ethanol, between each wash it was centrifuged to remove the supernatant (30 min/10000 G/20 °C). This process was repeated two times more in order to make sure the walls were well functionalized, however between the first and second functionalization of the surface, the nanostructures were lyophilized and calcined (2h at 900 °C). After the calcination, the inorganic templates were washed once with a NaOH solution with pH 9 and then 3 times with water and 3 times more with ethanol, between each wash the solvent was removed by centrifugation (10 min, 3893 G, 20 °C).

3.6.5. Grafting of dye in nanostructures

The covalent grafting of dyes on the surface of the nanostructures takes place in two steps, the first one consists in the carboxylic acid activation and the second one was the grafting itself. The activation reaction was carried out in a reaction flask where the acid derivatives were dissolved in an aprotic solvent [dry acetone (for ***o*-DPP acid 24**) or DMF (for ***p*-DPP acid 25** and ***m*-DPP acid 26**)], then 2 equivalents of ethyl chloroformate and 2.5 equivalents of triethylamine were added under nitrogen atmosphere. The reaction was left at rt for 3h. Meanwhile, the APTES-nanostructures were washed five times with the solvent used in the acid activation. Once the activation reaction ended, and without any purification, the solution of activated dye was introduced in the nanostructures (1 μmol of chromophores per mg of nanostructure). This reaction was stirred overnight at rt. Then, the samples were washed several times with acetone or DMF using the centrifuge (10 min, 9800 G, rt) until all free dye was removed, that is, when no colour was observed in the supernatant. To gather the maximum dye on the surface this process was repeated once more.

Final Conclusion

The present Thesis describes the synthesis and characterization of several DPP derivatives with the purpose of increasing the library of this family of organic compounds and to take advantage of their optical and electronic properties to study /apply them in SF, photovoltaic technology, and chirality induction.

Although this Thesis includes three chapters, the first two are in harmony regarding to the overall objective, which is, the attempt was made to study ways to improve clean energies. The first chapter addresses the physical properties of the compounds, that is, it is based on the study of a property called singlet fission, which when understood and applied can abruptly improve the Shockley-Queisser limit and, in turn, increase the photovoltaic yield. For this objective, three DPP dimers linked via different phenylene spacers, ***o*-DPP 1**, ***p*-DPP 2** and ***m*-DPP 3**, were reported in order to study the influence of the position of one DPP in relation to the other.

The obtained results depend directly on the nature of the solvent. It was verified that when toluene was used as a non-polar solvent, no triplet states were detected in any of the dimers. On the other hand, in benzonitrile, triplet states were populated from the CT intermixed singlet excited state intermediate in derivatives **1** and **3**. The strong electronic communication in ***o*-DPP 1** resulted in a better intra-SF performance. In the case of ***p*-DPP 2** the spatial separation of the DPP and the directing nature of para-position leaded to the symmetry-breaking charge separation (SBCS) state replaced by the $(S_1S_0)_{CT}$, working as a trap-state impeding the transition to the triplet state.

In the second chapter, an application of DPP in photovoltaics is shown. In this chapter two approaches are considered. The first one studies the DPP acid derivatives as sensitizers in dye sensitized solar cells (DSSCs), and the second one investigates the use of SubPc-DPP conjugates as acceptors in the active layer of bulk heterojunction (BHJ) devices.

The photosensitizers used in n-type DSSC devices are distinguished between them by the relative position of the anchoring group in the phenylene group spacer with respect to the DPP moiety: *para*- and *meta*-DPP acid derivatives. Beyond that, a dimer derivative was studied in order to understand the influence of the introduction of two DPP moieties in the photovoltaic properties, due to the existence of an intramolecular singlet fission effect. The results obtained are not as good as expected, with the best efficiency of 2.61% for ***p*-DPP acid 9**.

On the other hand, four new star-shaped electron acceptors based on a SubPc core decorated with three DPP wings linked through an acetylene bridge were applied as non-fullerene acceptors (NFAs) in BHJ inverted-devices. These compounds probed not to have high photovoltaic efficiencies, but exhibited exceptionally high

V_{OC} values, leading us to think they might be promising in ternary OSCs in which a high V_{OC} is desired.

The third chapter deviates from the main objective of the first two chapters, but it has equal importance, because it is an approach to combat another problem that is the preparation of pure enantiomers or the induction of chirality without having to synthesize chiral compounds. In general, the induction of chirality from the silica nanostructure to the DPP derivatives was not the best alternative to erase this problematic, however, it was verified that the greater the distance between the nanostructure and the DPP unit, the greater the value of dissymmetry and the greater the induction of chirality.

As a general conclusion of this Thesis, it was verified once again the great chemical versatility of DPP and how important it is to study and understand the phenomena that occur after the absorption of photons by the synthetized derivatives. Since light/sun is our greatest source of energy, it is essential to know how to make the best use of this inexhaustible source.

Conclusión Final

La presente Tesis describe la síntesis y caracterización de varios derivados de DPP con el propósito de incrementar la biblioteca de esta familia de compuestos orgánicos y aprovechar sus propiedades ópticas y electrónicas para estudiarlos /aplicarlos en fisión singlete, tecnología fotovoltaica e inducción de quiralidad.

Aunque esta Tesis consta de tres capítulos, los dos primeros están en sintonía con respecto al objetivo general, es decir, se ha llevado a cabo un estudio con el fin de mejorar las energías limpias. Así, el primer capítulo aborda las propiedades físicas de los compuestos, es decir, se basa en el estudio de una propiedad denominada fisión singlete, que al ser comprendida y aplicada puede mejorar fuertemente el límite Shockley-Queisser y, a su vez, incrementar el rendimiento fotovoltaico. Para este objetivo, se han descrito tres dímeros de DPP unidos a través de diferentes espaciadores de fenileno, ***o*-DPP 1**, ***p*-DPP 2** y ***m*-DPP 3**, con el fin de estudiar la influencia de la posición de una unidad de DPP en relación con la otra unidad.

Los resultados obtenidos dependen directamente de la naturaleza del disolvente. Se verificó que cuando se utilizó tolueno como disolvente no polar, no se detectaron estados de triplete en ninguno de los dímeros. Por otro lado, en benzonitrilo, los estados de triplete se poblaron a partir del $(S_0S_1)_{CT}$ en las derivadas **1** y **3**. La fuerte de comunicación electrónica en ***o*-DPP 1** llevó a un mejor rendimiento intra-SF. En el caso de ***p*-DPP 2**, la separación espacial del DPP y la naturaleza directriz de la posición *para* condujeron al estado de separación de carga rompiendo la simetría (SBCS) reemplazando el $(S_1S_0)_{CT}$, funcionando como un estado trampa impidiendo la transición al estado triplete.

En el segundo capítulo se muestra la aplicación de DPPs en tecnología fotovoltaica. En este capítulo se consideran dos enfoques. En el primero se estudió derivados ácidos de DPP como sensibilizadores en células solares basadas en colorante (DSSC), y el segundo se investigó el uso de compuestos conjugados del tipo SubPc-DPP como aceptores de electrones en la capa activa de dispositivos de heterounión masiva (BHJ).

Los fotosensibilizadores utilizados en los dispositivos DSSC de tipo n se distinguen entre ellos por la posición relativa del grupo de anclaje en el espaciador del grupo fenileno con respecto al DPP: derivados de ácido *para*- y *meta*-DPP. Más allá de eso, se estudió un dímero para comprender la influencia de la introducción de dos unidades de DPP en las propiedades fotovoltaicas, debido a la existencia de un efecto de fisión singlete intramolecular. Los resultados obtenidos no son tan buenos como se esperaba, siendo la mejor eficiencia del 2,61% para ***p*-DPP acido 9**.

Por otro lado, cuatro nuevos aceptores de electrones basados en un núcleo de SubPc decorado con tres moléculas de DPP unidas a través de un puente de acetileno se

aplicaron como aceptores de electrones no-fulerénicos (NFA) en dispositivos invertidos de BHJ. Se comprobó que estos compuestos no presentan eficiencias muy altas, pero exhiben valores de V_{OC} bastante altos, lo que nos indica que podrían ser compuestos prometedores en las células solares orgánicas ternarias, en las que se desea un V_{OC} alto.

El tercer capítulo se desvía del objetivo principal de los dos primeros, pero tiene igual importancia, porque se trata de una aproximación para combatir otro problema que es la preparación de enantiómeros puros o la inducción de quiralidad sin tener que sintetizar compuestos quirales. En general, la inducción de quiralidad de la nanoestructura de sílice a los derivados de DPP no fue la mejor alternativa para combatir esta problemática, sin embargo, se verificó que a mayor distancia entre la nanoestructura y la unidad de DPP, mayor valor de disimetría y consecuentemente mayor es la inducción de quiralidad.

Como conclusión general de esta Tesis, se comprobó una vez más la gran versatilidad química de los DPP y lo importante que es estudiar y comprender los fenómenos que ocurren tras la absorción de fotones en los derivados sintetizados. Dado que la luz/sol es nuestra mayor fuente de energía, es fundamental saber aprovechar al máximo esta fuente inagotable.

Attachments

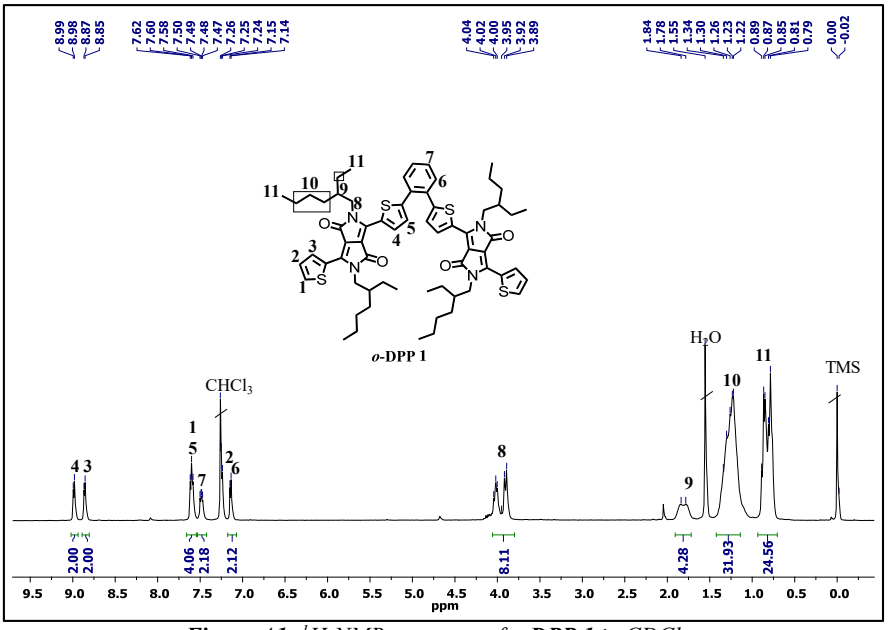

Figure A1- *^{1}H-NMR spectrum of* ***o-DPP 1*** *in $CDCl_3$.*

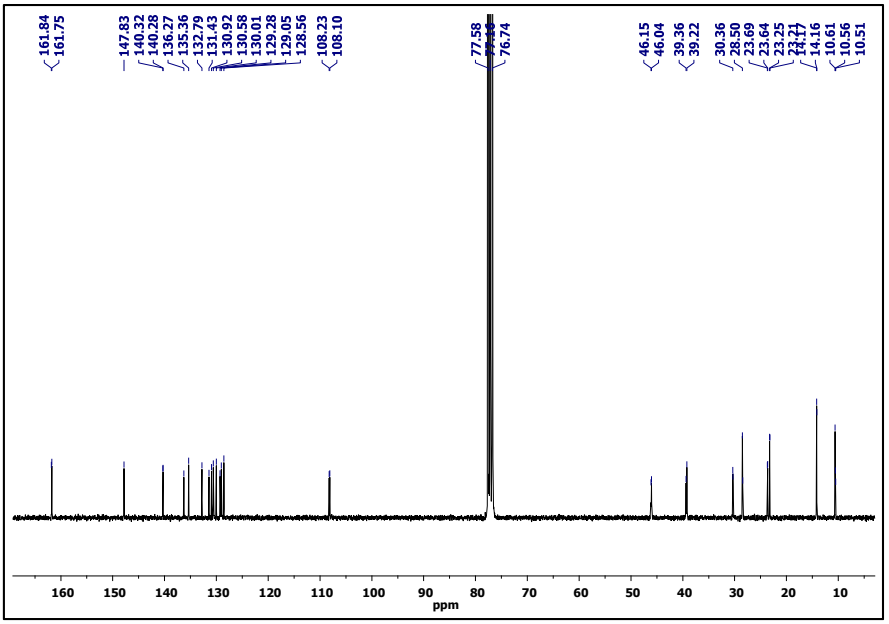

Figure A2- *^{13}C NMR spectrum of* ***o-DPP 1*** *in $CDCl_3$.*

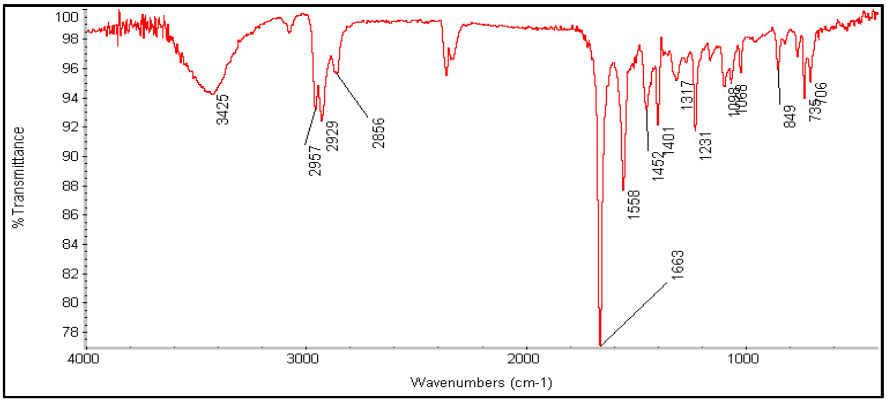

Figure A3- *FT-IR of* ***o-DPP 1****.*

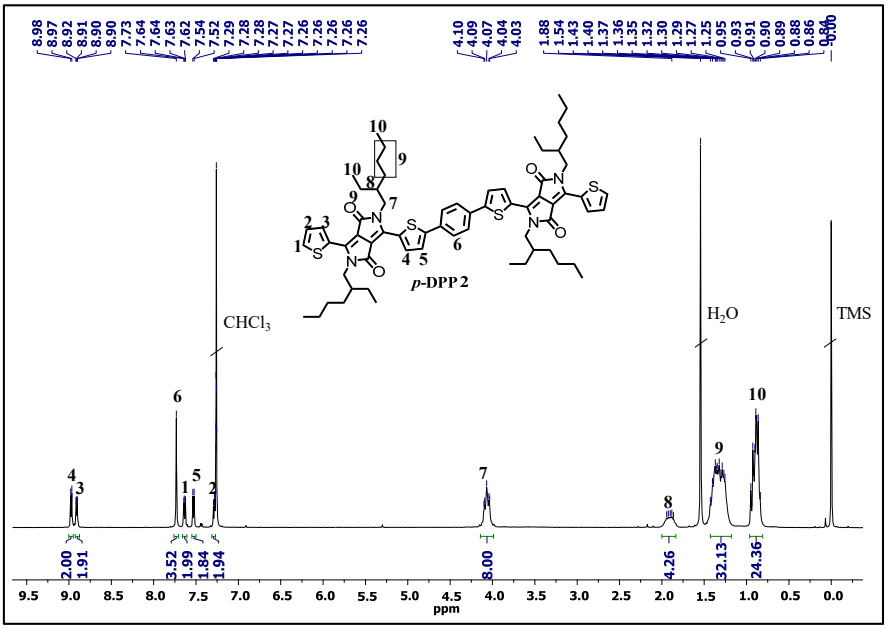

Figure A4- *^{1}H NMR spectrum of* ***p-DPP 2*** *in $CDCl_3$.*

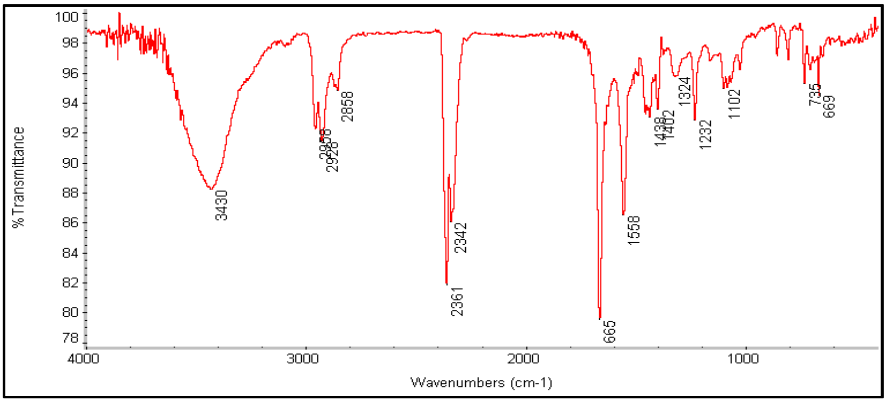

Figure A5- *FT-IR of* ***p-DPP 2****.*

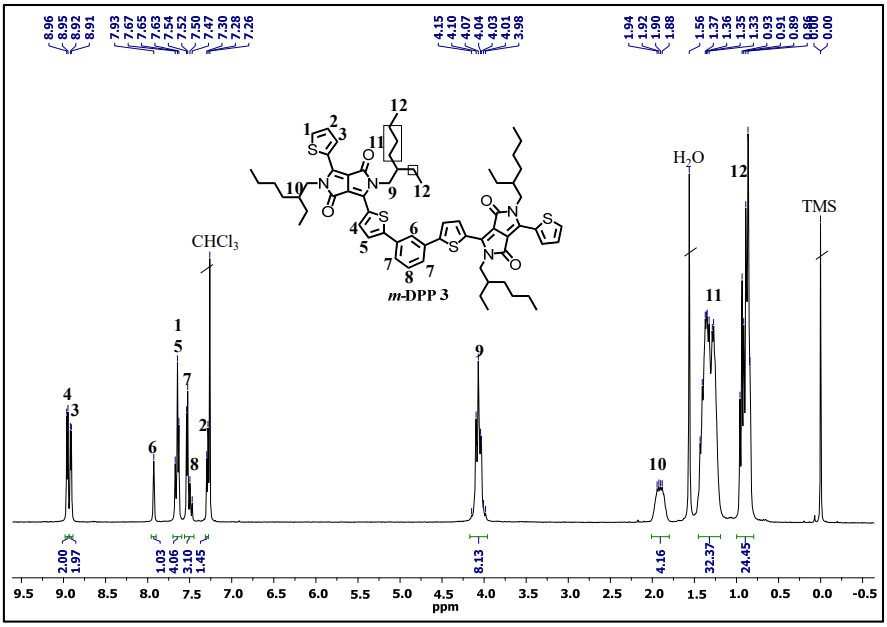

Figure A6- *^{1}H NMR spectrum of* ***m-DPP 3*** *in $CDCl_3$.*

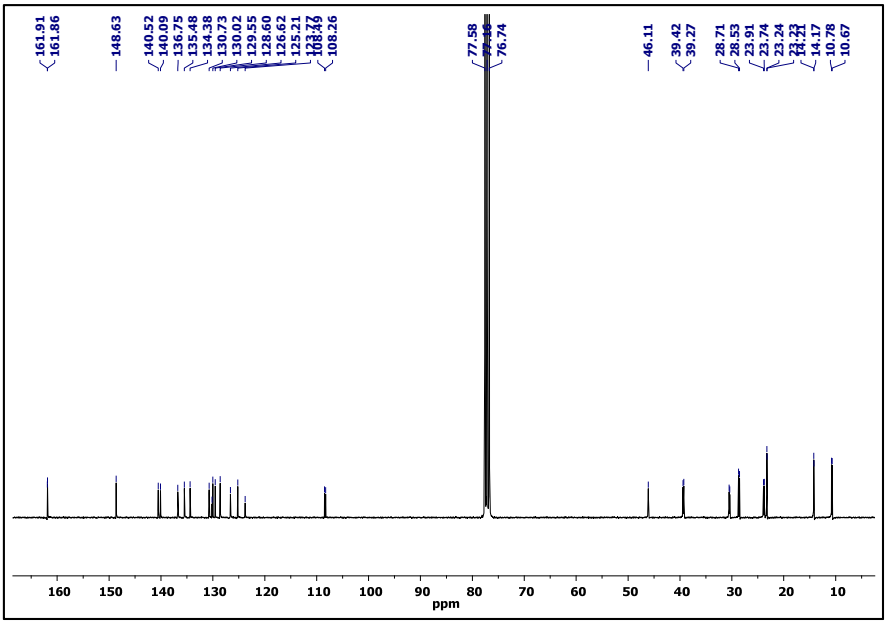

Figure A7- *^{13}C NMR spectrum of* ***m-DPP 3*** *in $CDCl_3$.*

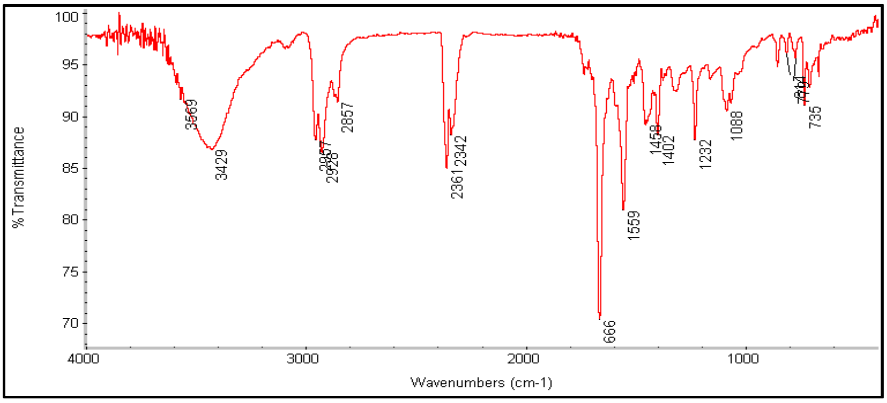

Figure A8- *FTIR of* ***m-DPP 3****.*

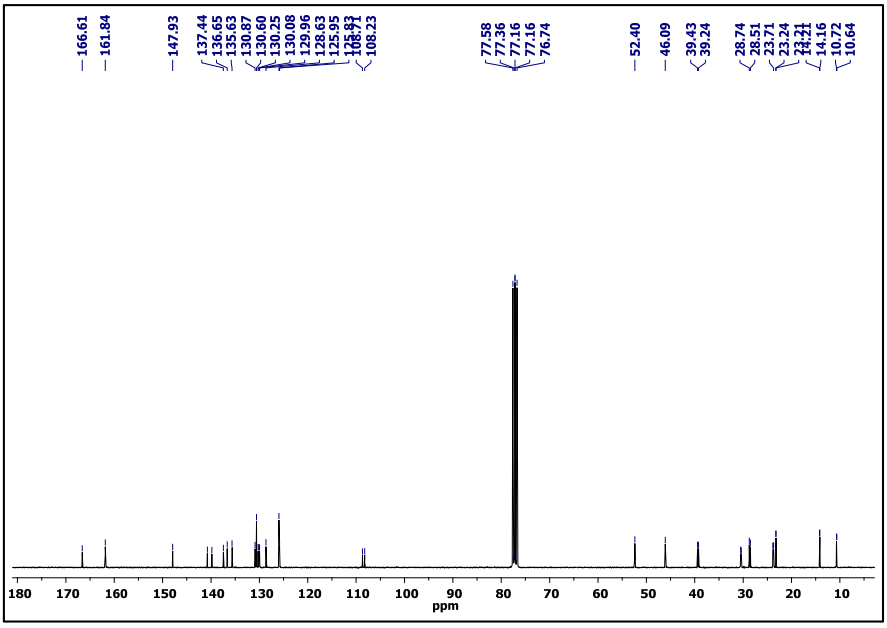

Figure A9- *^{13}C NMR spectrum of* ***p-DPP ester 12*** *in $CDCl_3$.*

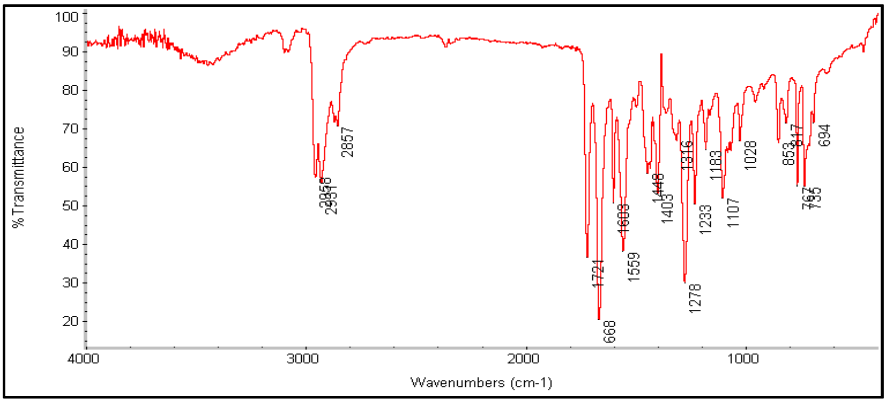

Figure A10- *FT-IR of* ***p-DPP ester 12****.*

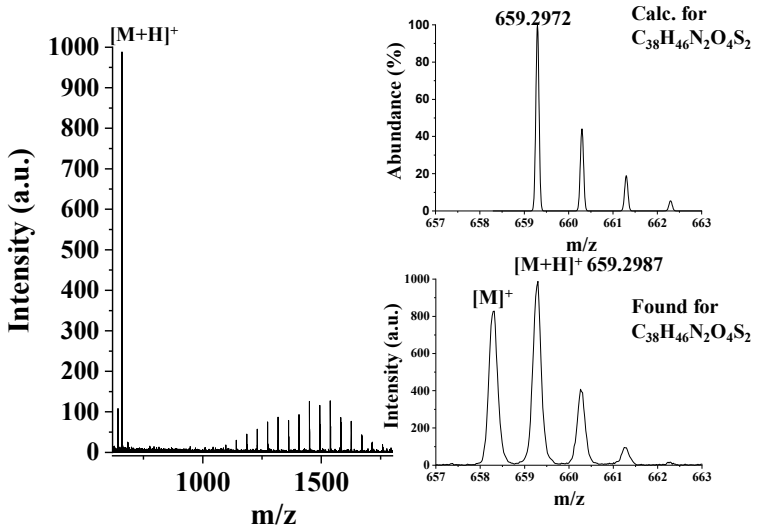

Figure A11- *HR-MALDI-TOF spectrum (dithranol) of* ***p-DPP ester 12****.*

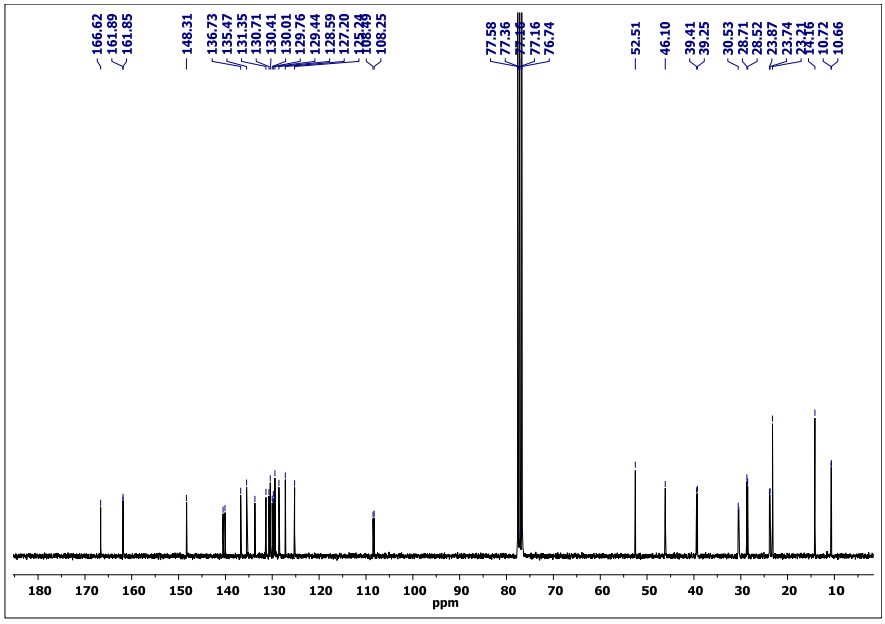

Figure A12- *^{13}C NMR spectrum of* ***m-DPP ester 13*** *in $CDCl_3$.*

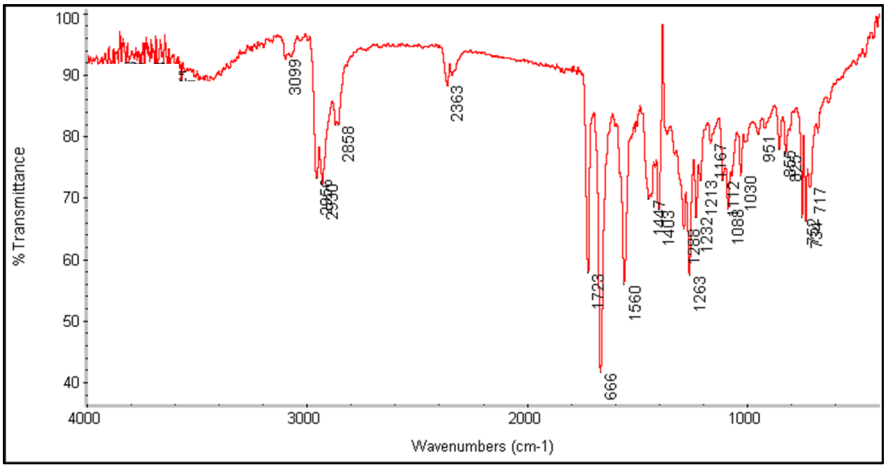

Figure A13- *FT-IR of* ***m-DPP ester 13****.*

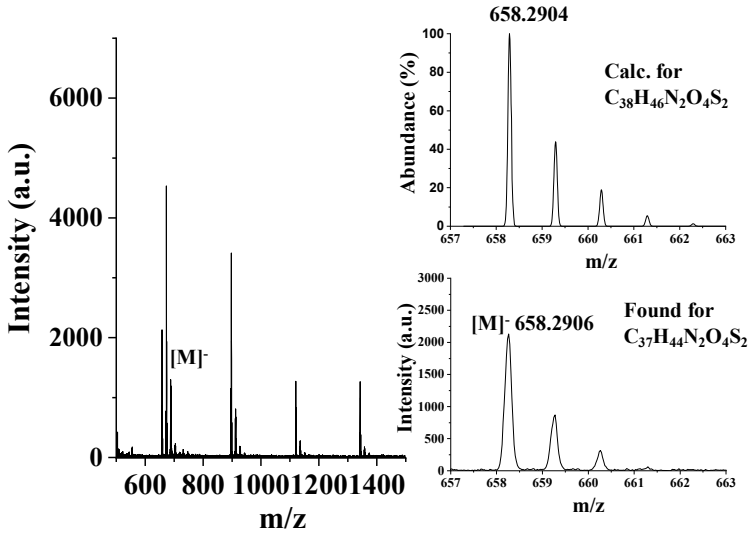

Figure A14- *HR-MALDI-TOF spectrum (dithranol) of* ***m-DPP ester 13****.*

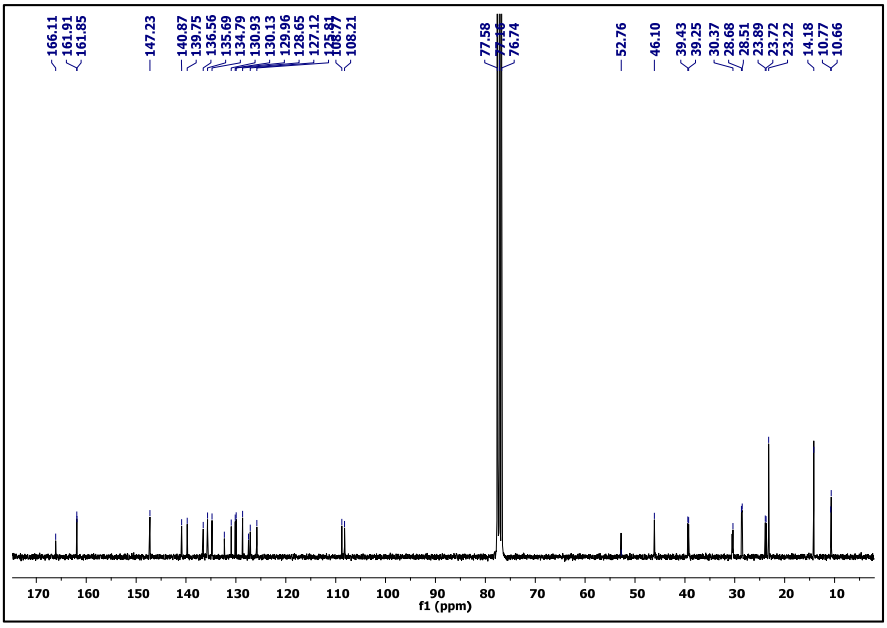

Figure A15- *^{13}C NMR spectrum of.* ***(DPP)$_2$ ester 14*** *in $CDCl_3$.*

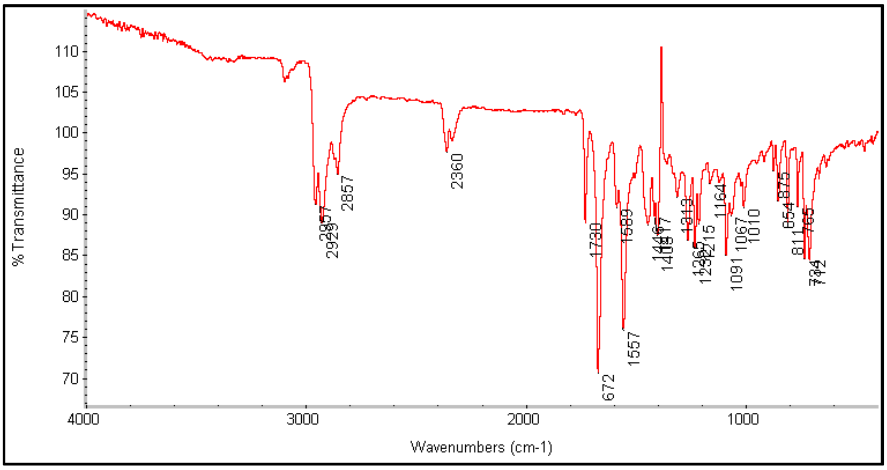

Figure A16- *FT-IR of* ***(DPP)$_2$ ester 14****.*

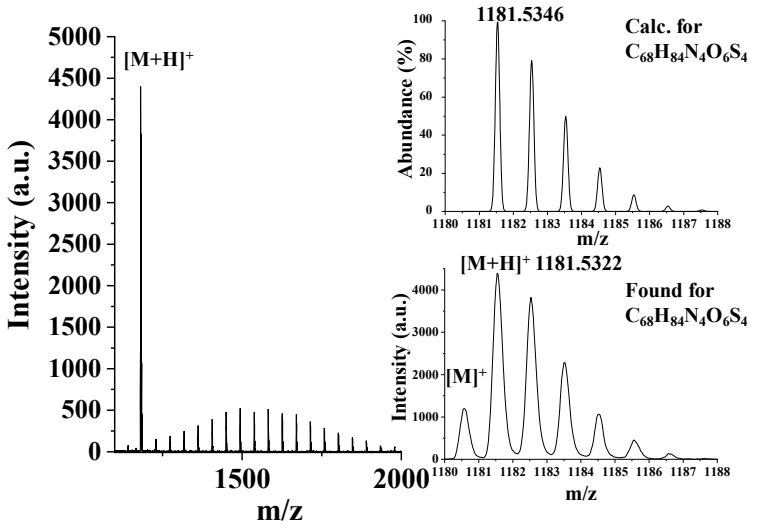

Figure A17- *HR-MALDI-TOF spectrum (dithranol) of* ***(DPP)₂ ester 14****.*

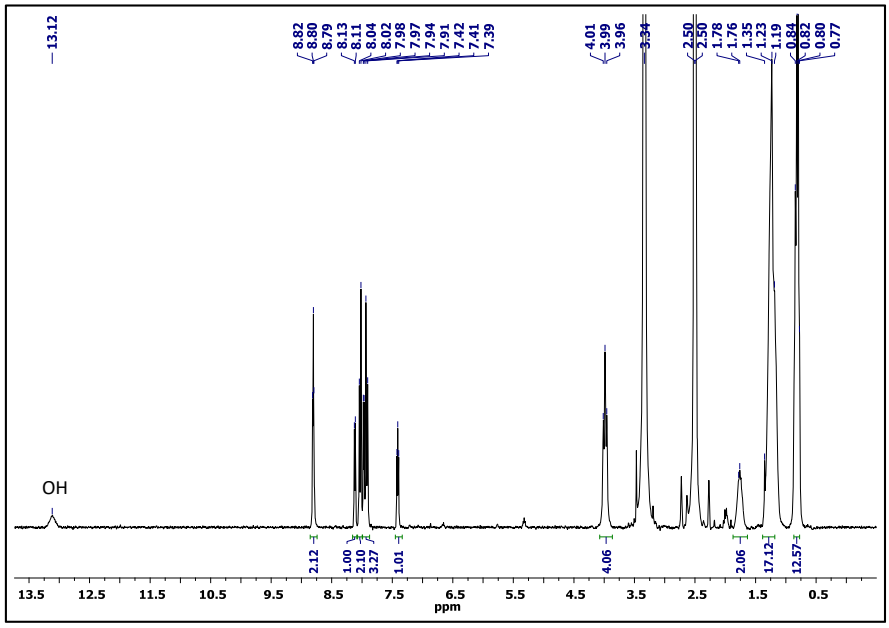

Figure A18- *^{1}H NMR spectrum of* ***p-DPP acid 9*** *in DMSO-d_6.*

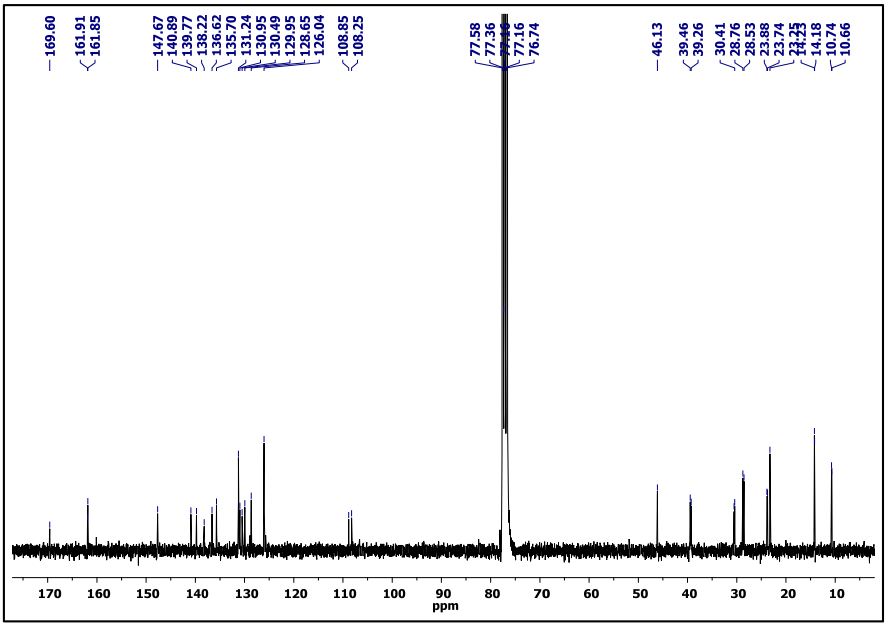

Figure A19- *^{13}C NMR spectrum of* ***p-DPP acid 9*** *in $CDCl_3$.*

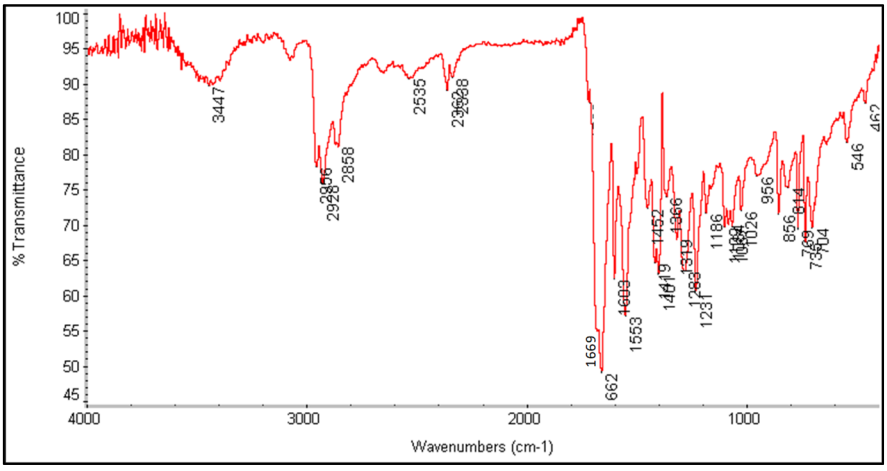

Figure A20- *FT-IR of* ***p-DPP acid 9****.*

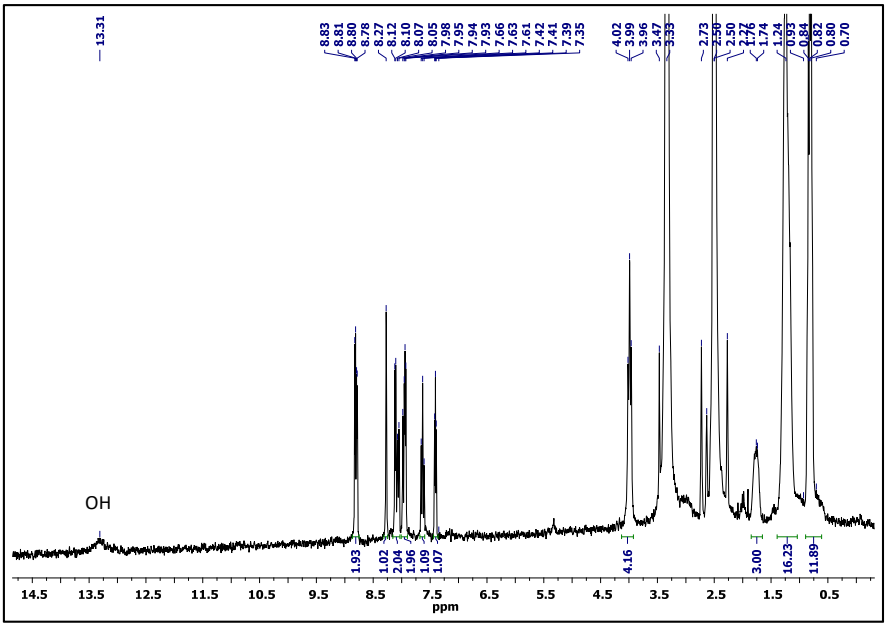

Figure A21- *^{1}H NMR spectrum of* ***m-DPP acid 10*** *in DMSO-d_6.*

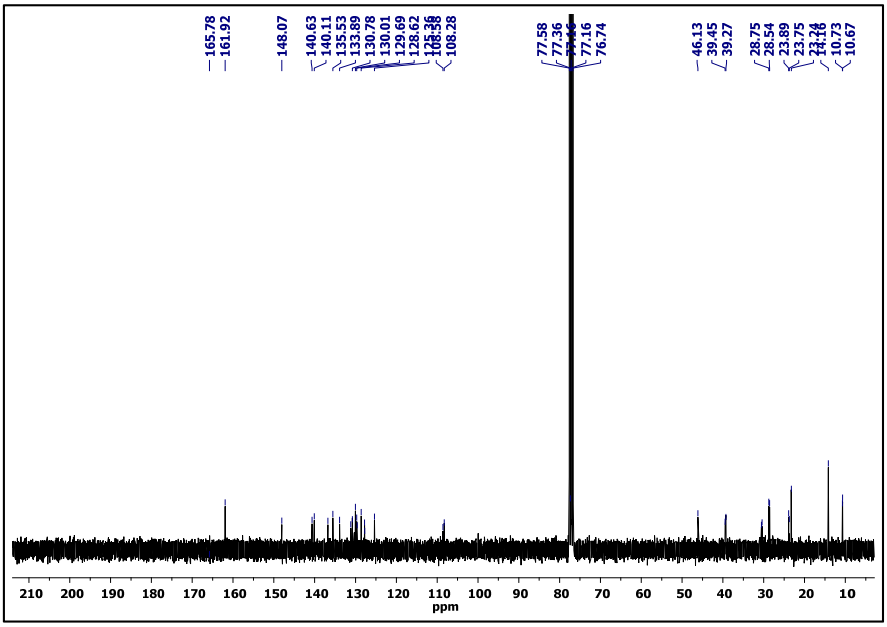

Figure A22- *^{13}C NMR spectrum of* ***m-DPP acid 10*** *in $CDCl_3$*

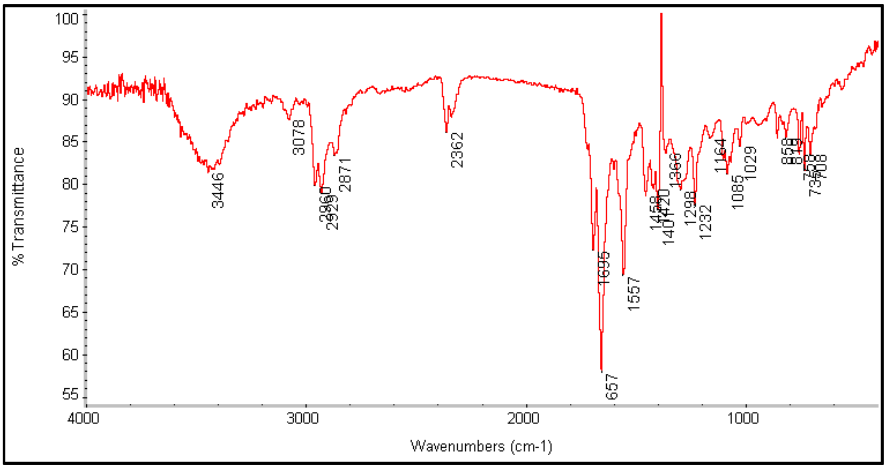

Figure A23- *FT-IR of* ***m-DPP acid 10****.*

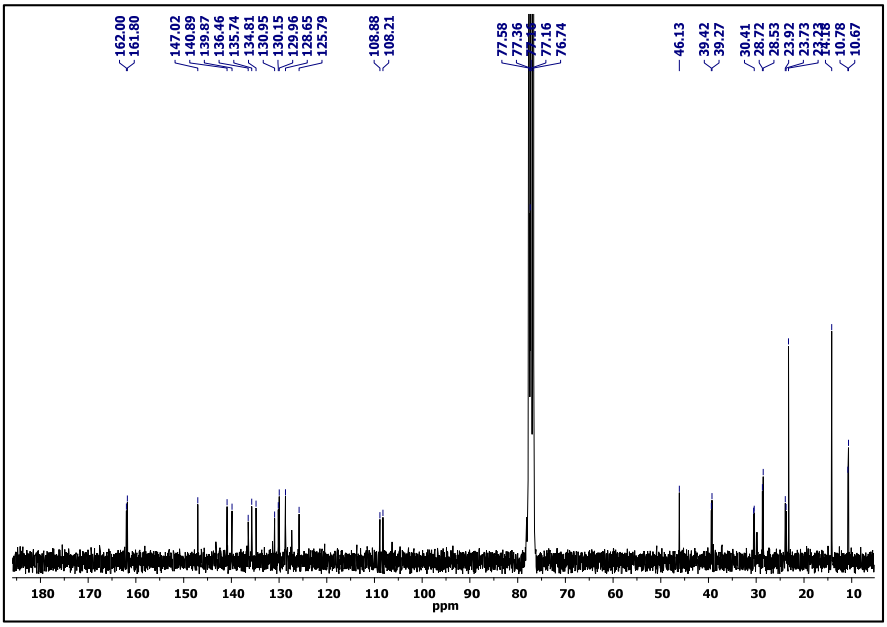

Figure A24- *^{13}C NMR spectrum of* ***$(DPP)_2$ acid 11*** *in $CDCl_3$*

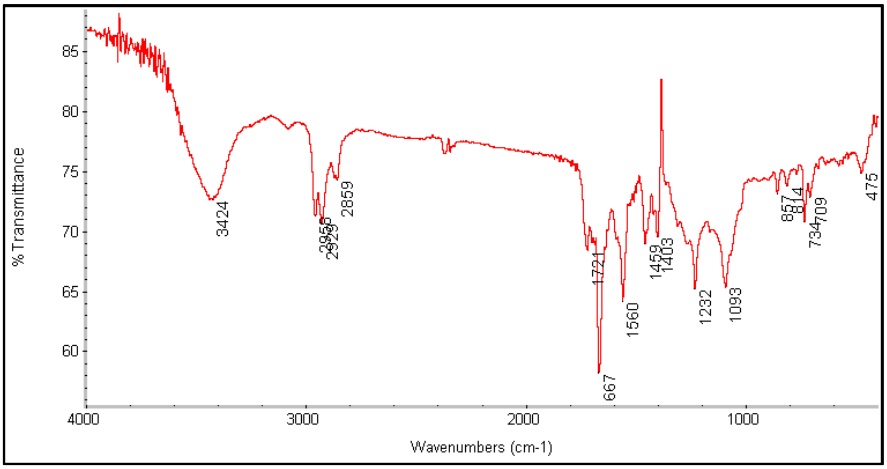

Figure A25- *FT-IR of* ***(DPP)$_2$ acid 11****.*

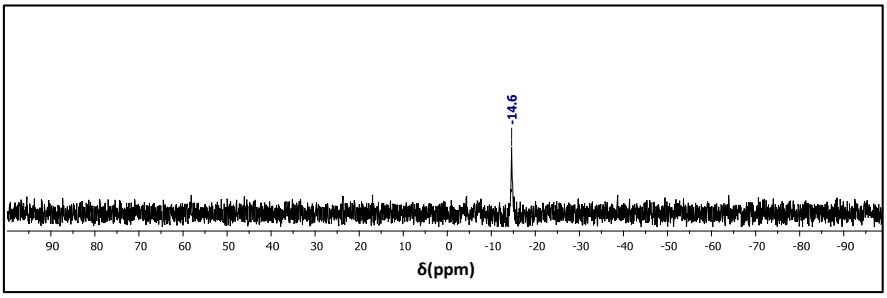

Figure A26- *^{11}B NMR spectrum of* ***C$_1$-SubPc(DPP)$_3$-OPh 18*** *in $CDCl_3$.*

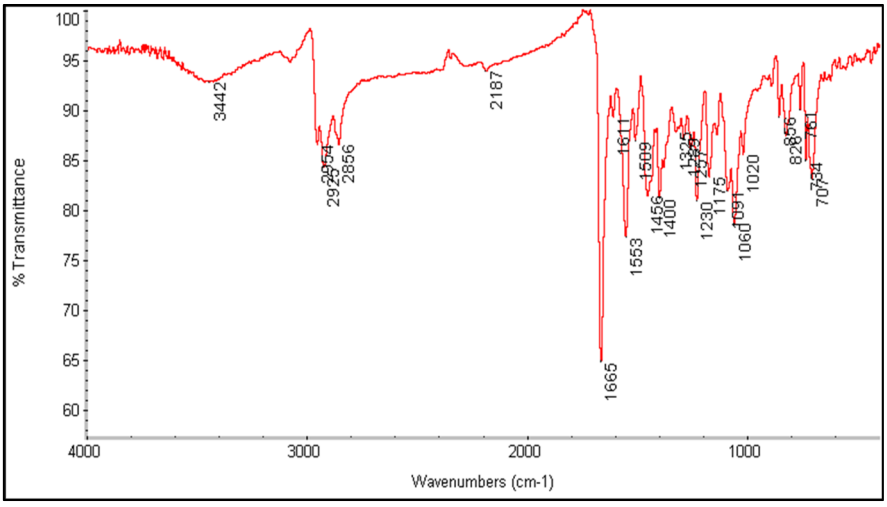

Figure A27- *FT-IR of* ***C$_1$-SubPc(DPP)$_3$-OPh 18****.*

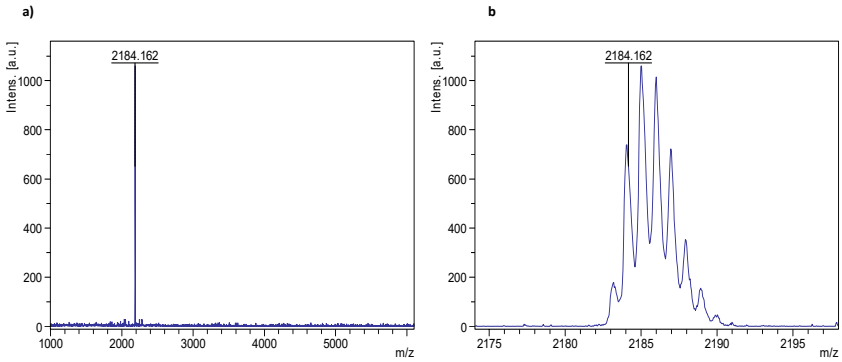

Figure A28- *a) MS spectrum (MALDI-TOF, dithranol) of* ***C_1-SubPc(DPP)$_3$-OPh 18****. b) MS spectrum zoom.*

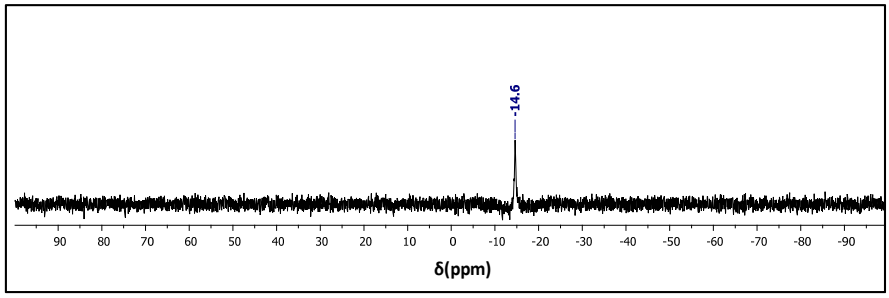

Figure A29- *^{11}B NMR spectrum of* ***C_3-SubPc(DPP)$_3$-OPh 19*** *in $CDCl_3$.*

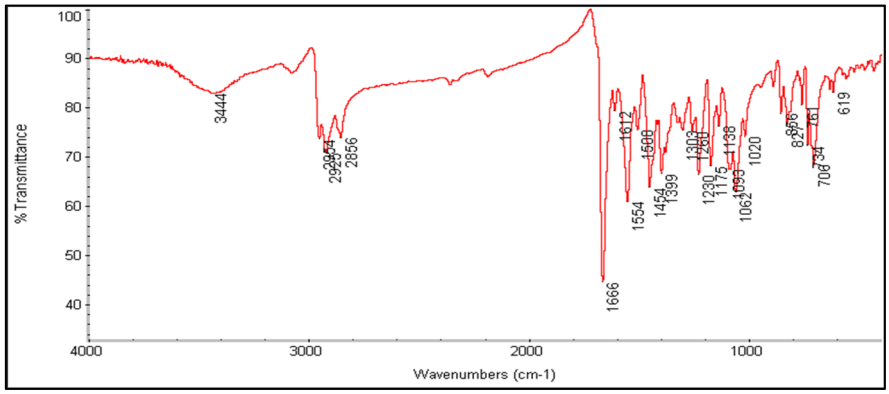

Figure A30- *FT-IR of* ***C_3-SubPc(DPP)$_3$-OPh 19****.*

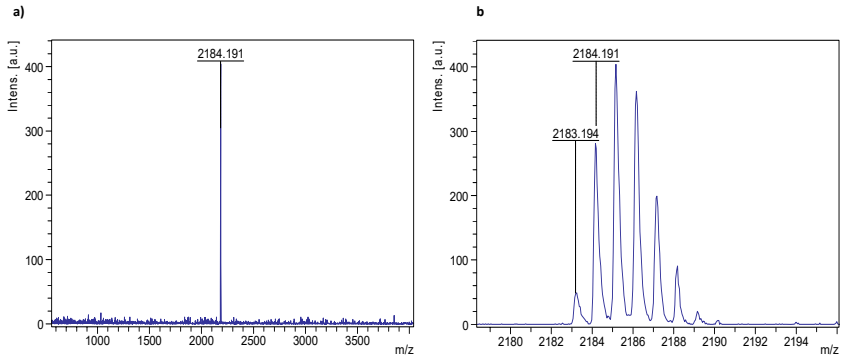

Figure A31- a) *MS spectrum (MALDI-TOF, dithranol) of* ***C_3-SubPc(DPP)$_3$-OPh 19****. **b)** MS spectrum zoom.*

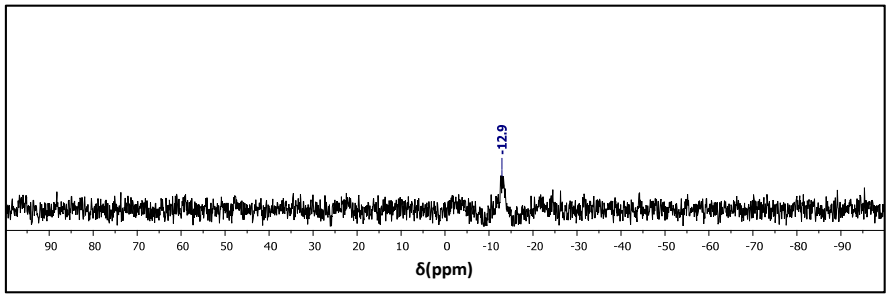

Figure A32- *^{11}B NMR spectrum of* ***C_1-SubPc(DPP)$_3$-Cl 20*** *in $CDCl_3$.*

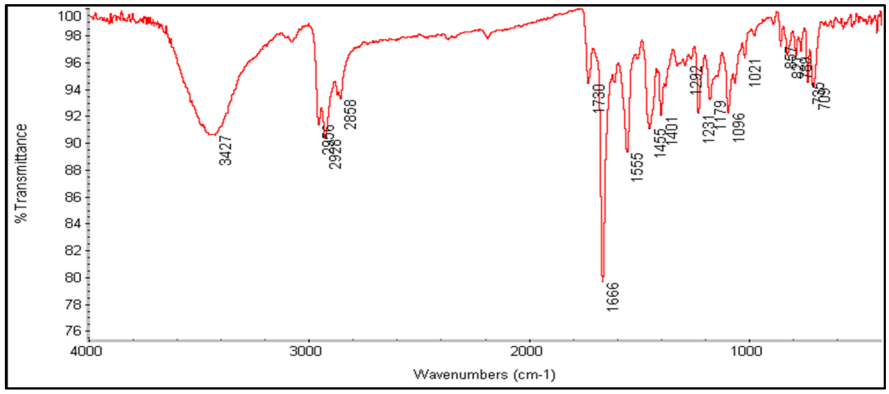

Figure A33- *FT-IR of* ***C_1-SubPc(DPP)$_3$-Cl 20****.*

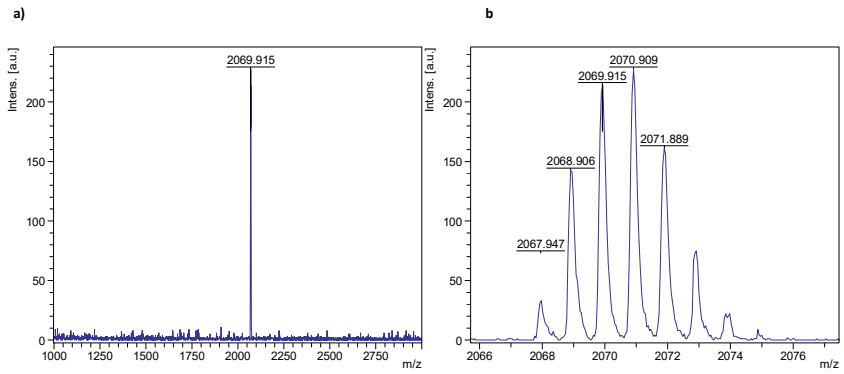

Figure A34- a) *MS spectrum (MALDI-TOF, dithranol) of* ***C_1-SubPc(DPP)$_3$-Cl 20. b)*** *MS spectrum zoom.*

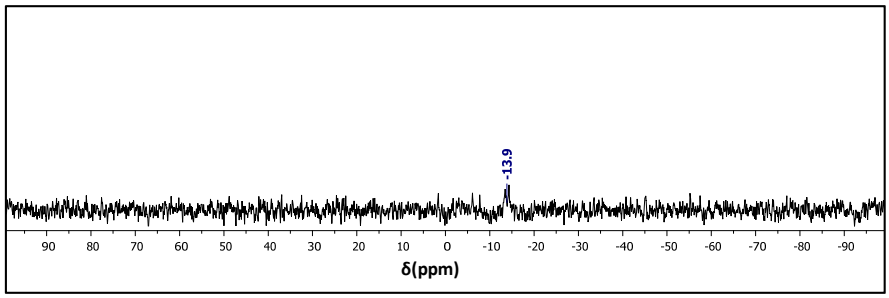

Figure A35- *^{11}B NMR spectrum of* ***C_3-SubPc(DPP)$_3$-Cl 21*** *in $CDCl_3$.*

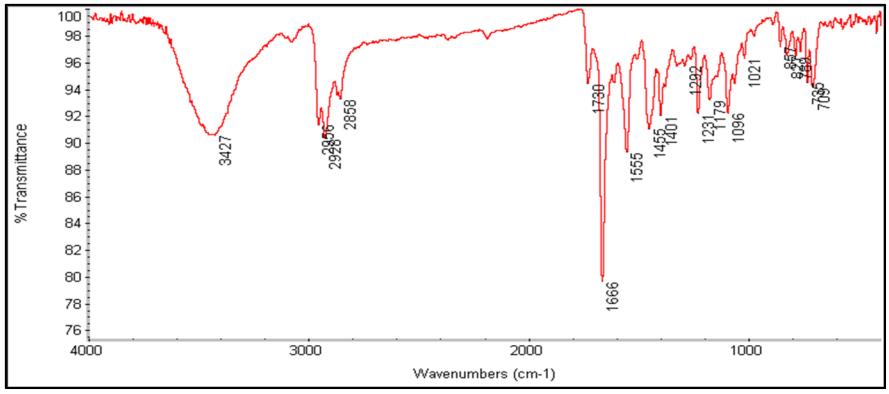

Figure A36- *FT-IR of* ***C_3-SubPc(DPP)$_3$-Cl 21****.*

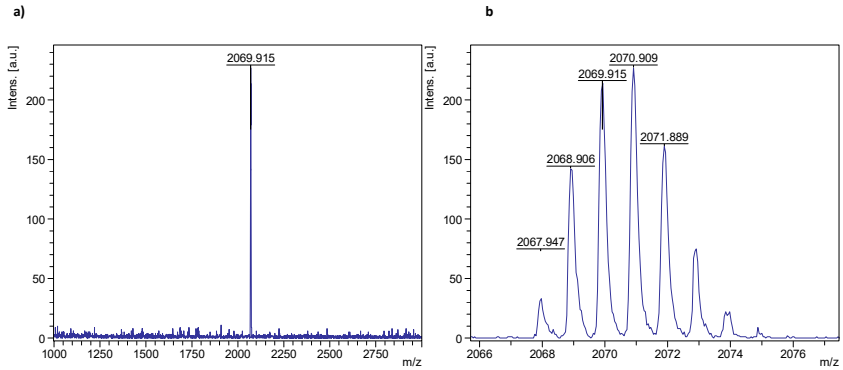

Figure A37- *a) MS spectrum (MALDI-TOF, dithranol) of* ***C_3-SubPc(DPP)$_3$-Cl 21****. **b)** MS spectrum zoom.*

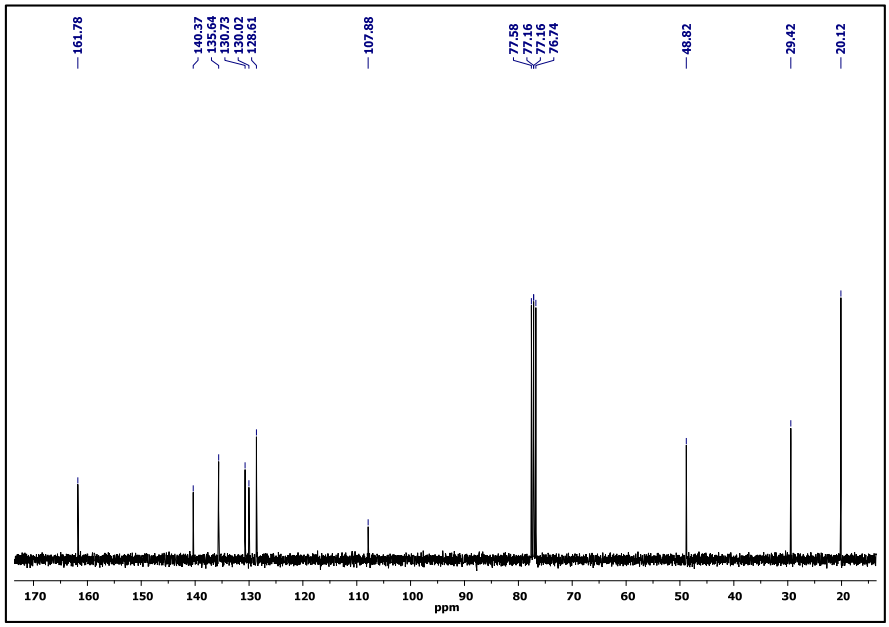

Figure A38- *^{13}C NMR spectrum of* ***DPP 27*** *in $CDCl_3$.*

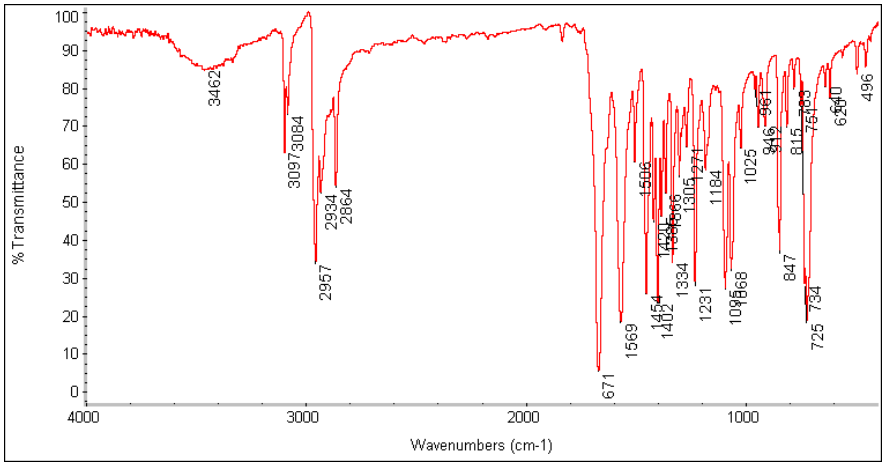

Figure A39- *FT-IR spectrum of* ***DPP 27****.*

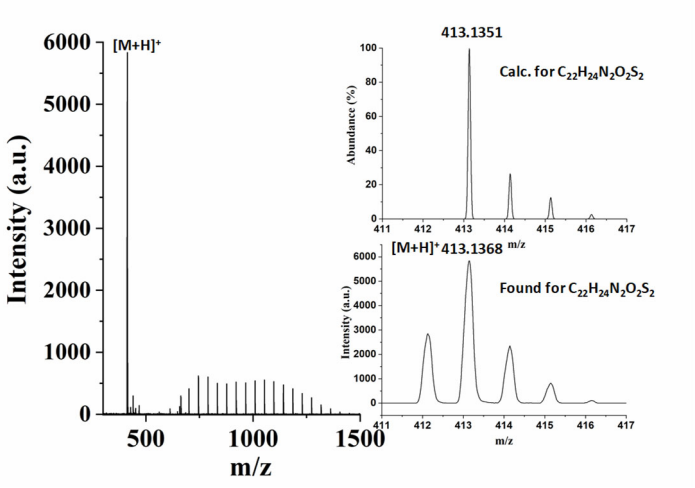

Figure A40- *HR-MALDI-TOF of* ***DPP 27****.*

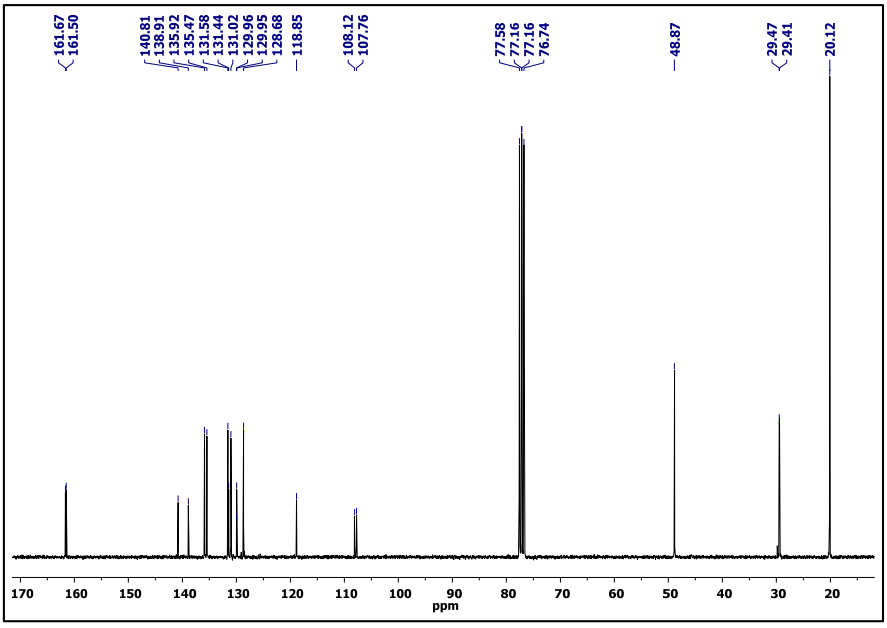

Figure A41- *^{13}C NMR spectrum of* ***DPP 28*** *in $CDCl_3$.*

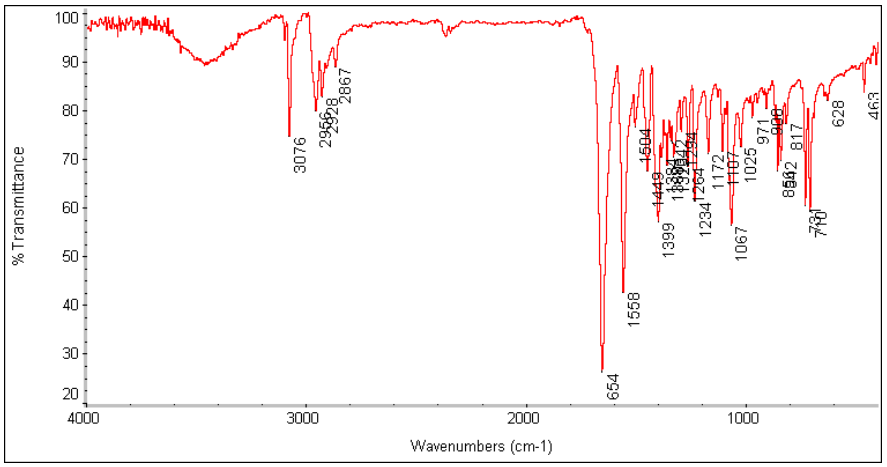

Figure A42- *FT-IR spectrum of* ***DPP 28****.*

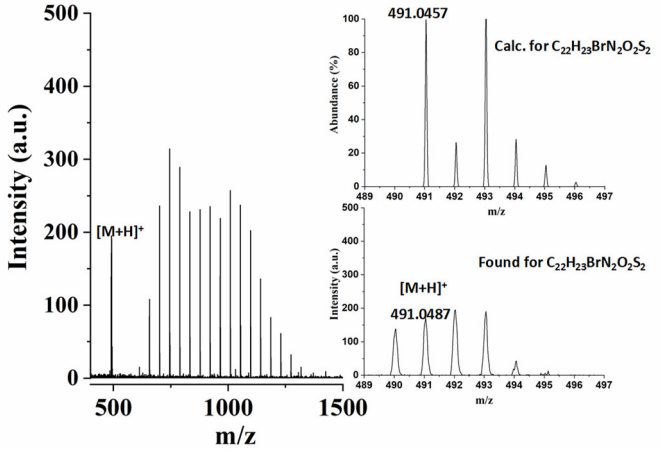

Figure A43- *HR-MALDI-TOF of* ***DPP 28****.*

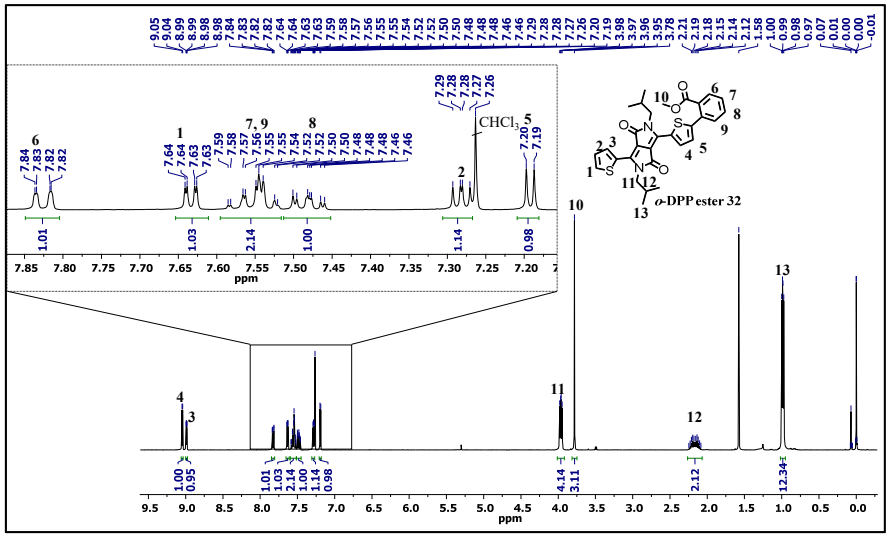

Figure A44- *^{1}H NMR of* ***o-DPP ester 32*** *in $CDCl_3$.*

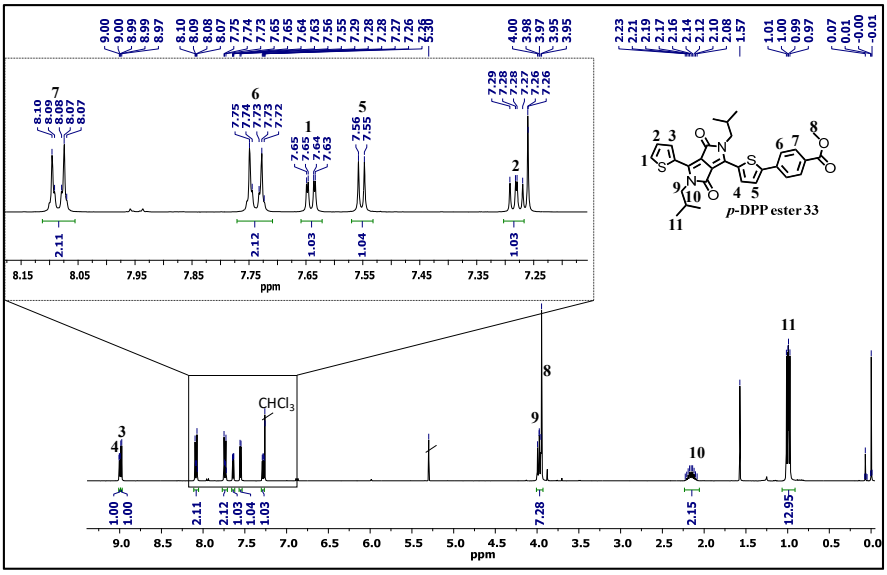

Figure A45- *^{1}H NMR of* ***p-DPP ester 33*** *in $CDCl_3$.*

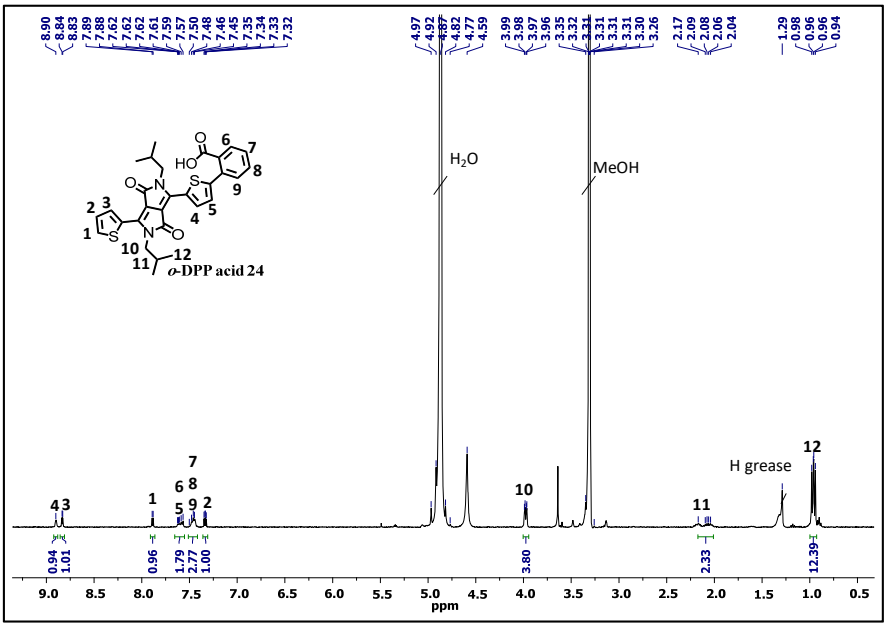

Figure A46- *^{1}H NMR of* ***o-DPP acid 24*** *in MeOH-d_4.*

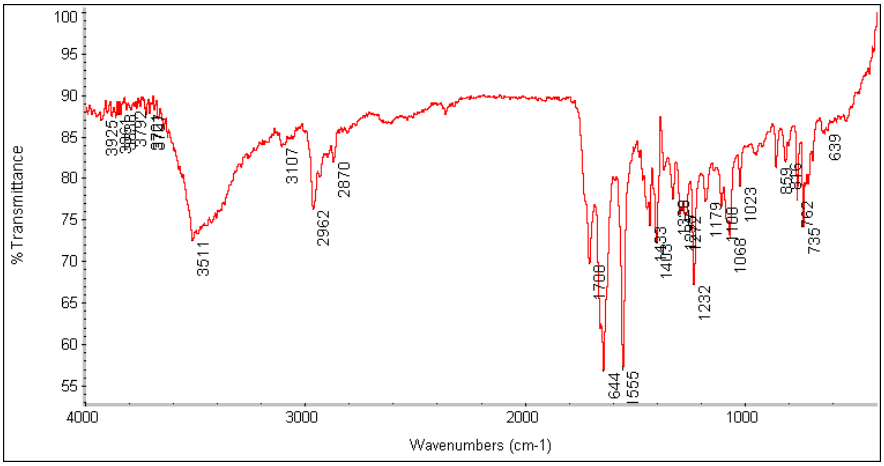

Figure A47- *FT-IR of* ***o-DPP acid 24****.*

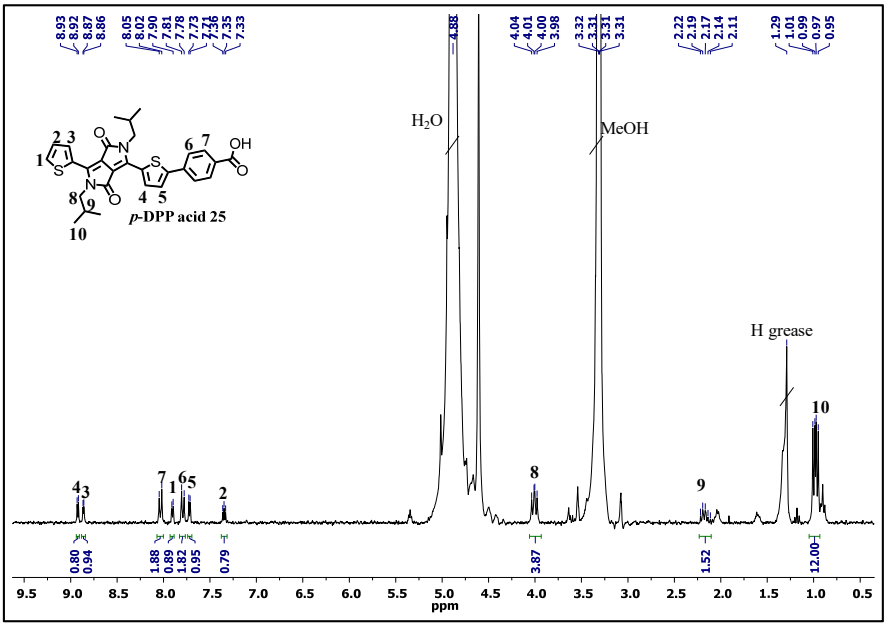

Figure A48- *^{1}H NMR of* ***p-DPP acid 25*** *in MeOH-d$_4$.*

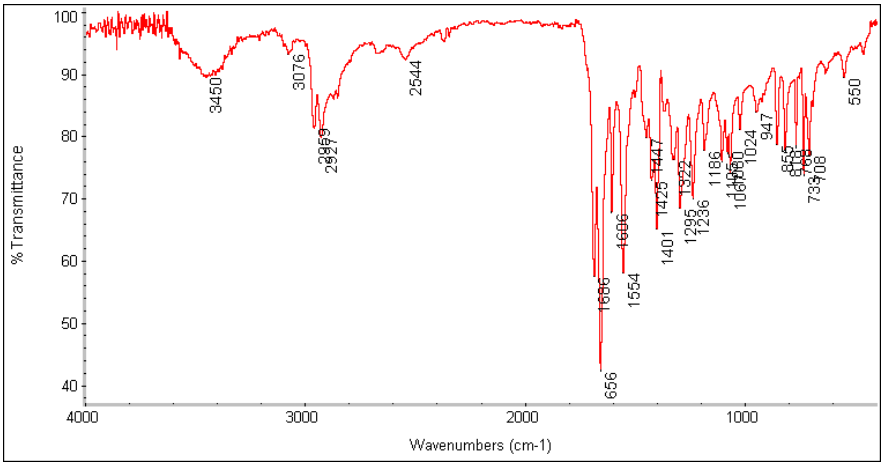

Figure A49- *FT-IR of* ***p-DPP acid 25****.*

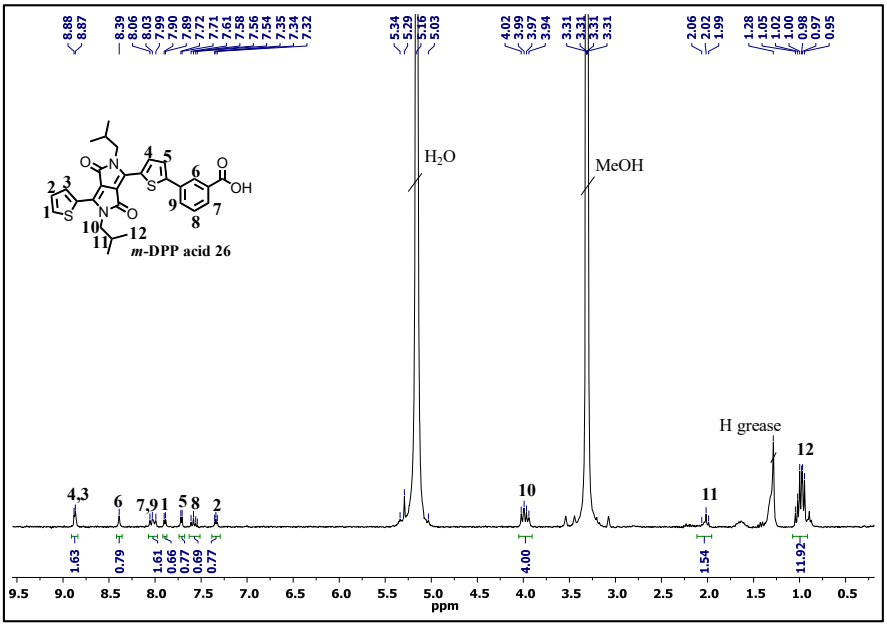

Figure A50- *^{1}H NMR of* ***m-DPP acid 26*** *in MeOH-d_4 + 2 drops of TFA-d.*

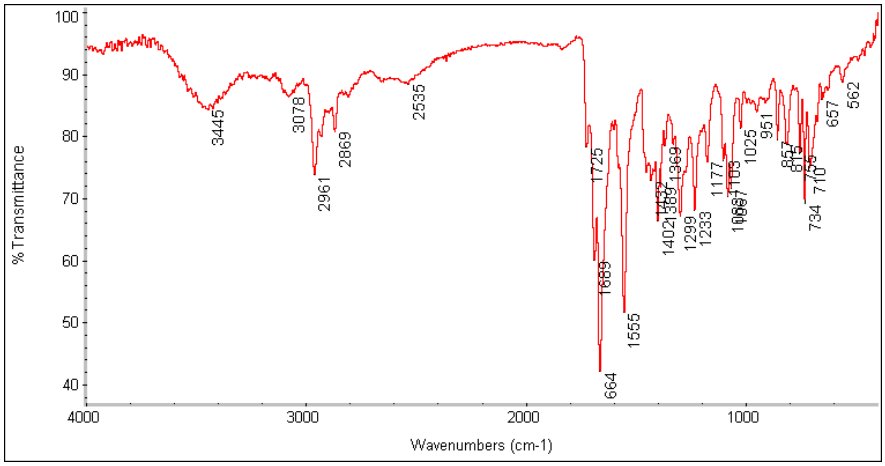

Figure A51- *FT-IR of* ***m-DPP acid 26.***

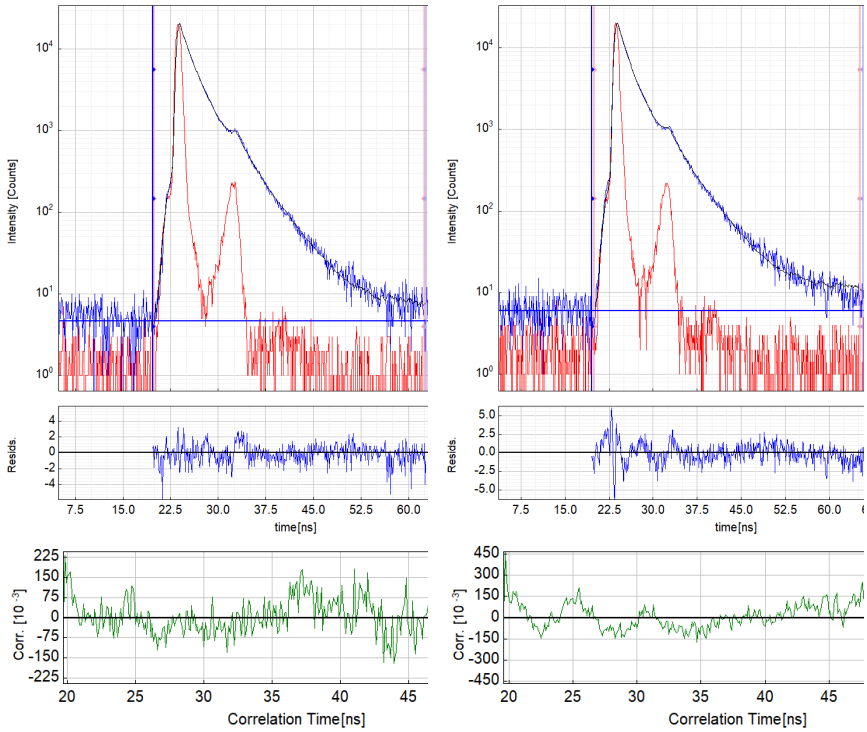

Parameter	Value	Δ	δ
A_1[kCnts/Chnl]	6.51	±0.22	3.3%
τ_1[ns]	3.785	±0.038	1.0%
I_1[kCnts]	246.1	±6.9	2.8%
A_{Rel1}[%]	27.4	±1.0	3.6%
I_{Rel1}[%]	48.7	±1.5	3.0%

Parameter	Value	Δ	δ
A_1[kCnts/Chnl]	6.08	±0.12	1.8%
τ_1[ns]	4.116	±0.033	0.8%
I_1[kCnts]	250.3	±3.2	1.2%
A_{Rel1}[%]	24.0	±0.5	2.1%
I_{Rel1}[%]	48.8	±0.8	1.6%

A_2[kCnts/Chnl]	17.32	±0.22	1.3%
τ_2[ns]	1.501	±0.027	1.8%
I_2[kCnts]	259.8	±8.3	3.2%
A_{Rel2}[%]	72.7	±1.0	1.4%
I_{Rel2}[%]	51.4	±1.5	2.9%
$Bkgr_{Dec}$[kCnts]	0.0047	±0.0006	11%
$Bkgr_{IRF}$[Cnts/Chnl]	0.14	±0.16	122%
$Shift_{IRF}$[ps]	238.8	±2.6	1.0%
A_{Scatt}[kCnts]	72.4	±1.5	2.0%
τ_{AvInt}[ns]	2.6113	±0.0094	0.4%
τ_{AvAmp}[ns]	2.124	±0.011	0.5%

A_2[kCnts/Chnl]	19.32	±0.29	1.5%
τ_2[ns]	1.365	±0.030	2.2%
I_2[kCnts]	263.5	±5.5	2.1%
A_{Rel2}[%]	76.1	±0.5	0.7%
I_{Rel2}[%]	51.3	±0.8	1.5%
$Bkgr_{Dec}$[kCnts]	0.0060	±0.0009	14%
$Bkgr_{IRF}$[Cnts/Chnl]	-0.33	±0.22	65%
$Shift_{IRF}$[ps]	243	±12	4.7%
A_{Scatt}[kCnts]	64.3	±4.8	7.3%
τ_{AvInt}[ns]	2.705	±0.014	0.5%
τ_{AvAmp}[ns]	2.023	±0.028	1.4%

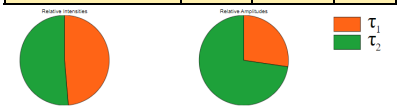

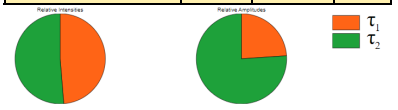

Figure A52- *Lifetime of* ***o-DPP acid 24*** *grafted on right helices (first) and left helices (second).*

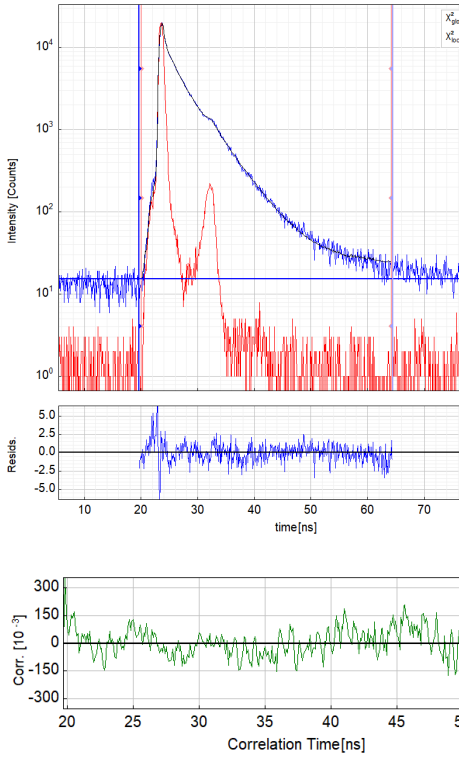

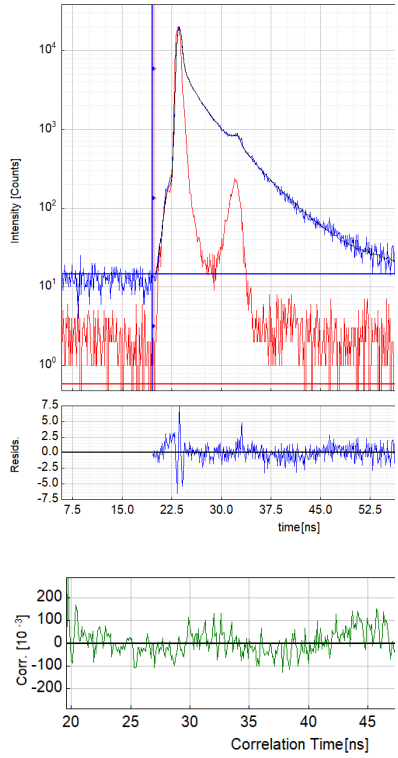

Parameter	Value	Δ	δ
A_1[kCnts/Chnl]	7.82	±0.46	5.9%
τ_1[ns]	4.350	±0.066	1.5%
I_1[kCnts]	341	±16	4.4%
A_{Rel1}[%]	50.9	±1.0	2.0%
I_{Rel1}[%]	73.5	±2.4	3.2%
-			
A_2[kCnts/Chnl]	7.55	±0.25	3.2%
τ_2[ns]	1.63	±0.15	9.0%
I_2[kCnts]	122.9	±9.3	7.6%
A_{Rel2}[%]	49.2	±1.0	2.0%
I_{Rel2}[%]	26.6	±2.4	8.9%
-			
$Bkgr_{Dec}$[kCnts]	0.0154	±0.0030	19%
-			
$Bkgr_{IRF}$[Cnts/Chnl]	-2.0	±1.1	51%
$Shift_{IRF}$[ps]	116.6	±9.9	8.5%
A_{Scatt}[kCnts]	104.0	±2.1	2.0%
-			
τ_{AvInt}[ns]	3.628	±0.032	0.9%
τ_{AvAmp}[ns]	3.014	±0.052	1.7%

Parameter	Value	Δ	δ
A_1[kCnts/Chnl]	3.36	±0.31	9.2%
τ_1[ns]	4.80	±0.13	2.6%
I_1[kCnts]	162	±12	6.8%
A_{Rel1}[%]	0.4	±0.2	42%
I_{Rel1}[%]	16.4	±4.2	25%
-			
A_2[kCnts/Chnl]	3.91	±0.22	5.5%
τ_2[ns]	1.98	±0.18	9.0%
I_2[kCnts]	77	±11	14%
A_{Rel2}[%]	0.5	±0.2	37%
I_{Rel2}[%]	7.9	±1.8	23%
-			
A_3[kCnts/Chnl]	910	±630	69%
τ_3[ns]	0.083	±0.013	16%
I_3[kCnts]	750	±320	43%
A_{Rel3}[%]	99.3	±0.4	0.3%
I_{Rel3}[%]	75.9	±5.9	7.7%
-			
$Bkgr_{Dec}$[kCnts]	0.0146	±0.0020	14%
-			
$Bkgr_{IRF}$[Cnts/Chnl]	0.59	±0.86	148 %
$Shift_{IRF}$[ps]	63.6	±5.0	7.8%
A_{Scatt}[kCnts]	- 234	±96	41%
-			
τ_{AvInt}[ns]	1.01	±0.24	24%
τ_{AvAmp}[ns]	0.109	±0.024	21%

Figure A53- *Lifetime of* ***p-DPP acid 25*** *grafted on right helices (first) and left helices (second).*

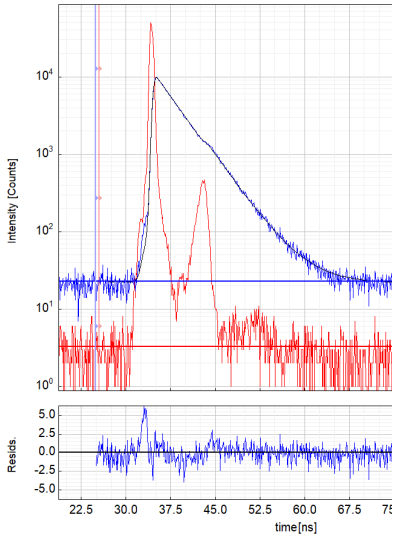

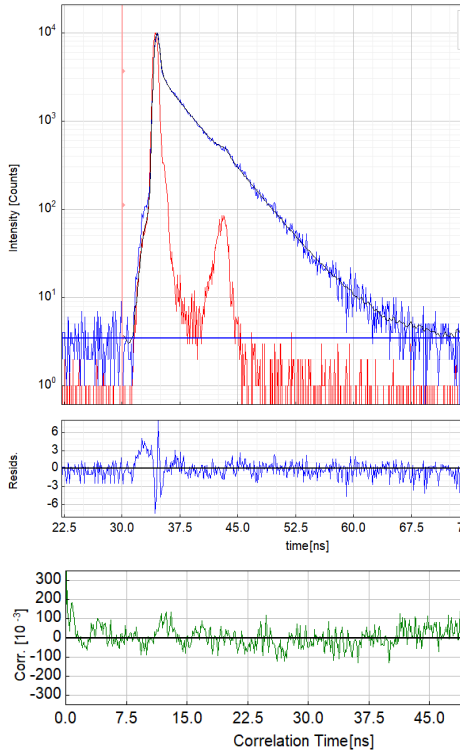

Parameter	Value	Δ	δ
A_1[kCnts/Chnl]	13.240	±0.076	0.6 %
τ_1[ns]	3.931	±0.011	0.3 %
I_1[kCnts]	520.4	±3.7	0.7 %
A_{Rel1}[%]	100.0	---	---
I_{Rel1}[%]	100.0	---	---
-			
A_2[kCnts/Chnl]	- 670	±120	17%
τ_2[ns]	0.0570	±0.0034	5.9 %
I_2[kCnts]	- 384	±61	16%
A_{Rel2}[%]	0.0	---	---
I_{Rel2}[%]	0.0	---	---
-			
$Bkgr_{Dec}$[kCnts]	0.0229	±0.0011	4.5 %
-			
$Bkgr_{IRF}$[Cnts/Chnl]	3.27	±0.84	25%

Parameter	Value	Δ	δ
A_1[kCnts/Chnl]	3.749	±0.028	0.7%
τ_1[ns]	3.996	±0.011	0.3%
I_1[kCnts]	149.79	±0.44	0.3%
A_{Rel1}[%]	3.9	±0.9	22%
I_{Rel1}[%]	50.9	±3.6	6.9%
-			
A_2[kCnts/Chnl]	93	±18	19%
τ_2[ns]	0.156	±0.017	11%
I_2[kCnts]	145	±19	13%
A_{Rel2}[%]	96.2	±0.9	0.9%
I_{Rel2}[%]	49.2	±3.6	7.2%
-			
$Bkgr_{Dec}$[kCnts]	0.0035	±0.0001	2.7%
-			
$Bkgr_{IRF}$[Cnts/Chnl]	0.461	±0.050	11%
$Shift_{IRF}$[ps]	-42.0	±5.3	13%
A_{Scatt}[kCnts]	-37.8	±8.4	22%
-			
τ_{AvInt}[ns]	2.11	±0.14	6.4%

$Shift_{IRF}$[ps]	- 116	±32	27%
A_{Scatt}[kCnts]	110	±19	17%
-			
τ_{AvInt}[ns]	3.931	±0.011	0.3 %
τ_{AvAmp}[ns]	3.931	±0.011	0.3 %

τ_{AvAmp}[ns]	0.305	±0.048	16%

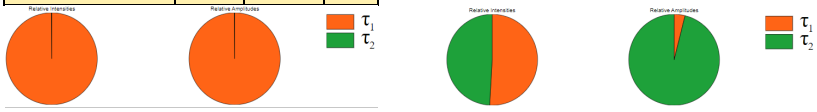

Figure A54- *Lifetime of* ***m-DPP acid 26*** *grafted on right helices (first) and left helices (second).*

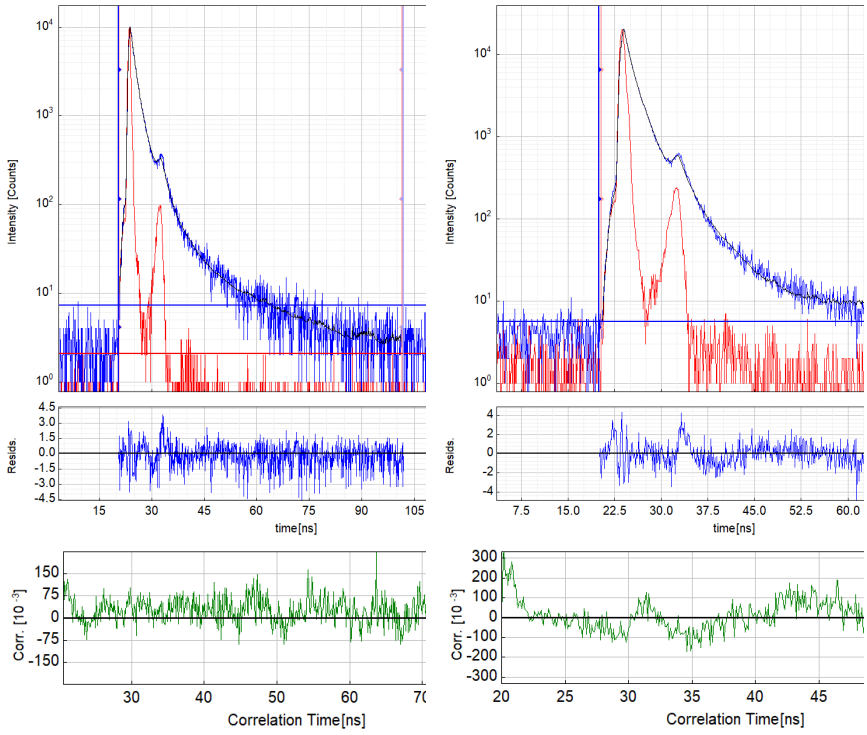

Parameter	Value	Δ	δ
A_1[kCnts/Chnl]	11.46	±0.13	1.1%
τ_1[ns]	1.176	±0.039	3.3%
I_1[kCnts]	134.7	±3.9	2.9%
A_{Rel1}[%]	85.2	±1.7	2.0%
I_{Rel1}[%]	64.0	±2.5	3.8%
-			
A_2[kCnts/Chnl]	0.0490	±0.0082	17%
τ_2[ns]	18.1	±1.8	9.7%

Parameter	Value	Δ	δ
A_1[kCnts/Chnl]	17.88	±0.47	2.6%
τ_1[ns]	1.432	±0.026	1.8%
I_1[kCnts]	255.9	±6.4	2.5%
A_{Rel1}[%]	31	±15	48%
I_{Rel1}[%]	61.4	±6.7	11%
-			
A_2[kCnts/Chnl]	1.94	±0.17	8.5%
τ_2[ns]	4.15	±0.11	2.7%

I_2[kCnts]	8.84	±0.55	6.1%
A_{Rel2}[%]	0.4	±0.1	17%
I_{Rel2}[%]	4.2	±0.3	5.9%
-			
A_3[kCnts/Chnl]	1.95	±0.27	14%
τ_3[ns]	3.46	±0.23	6.4%
I_3[kCnts]	67.3	±5.6	8.3%
A_{Rel3}[%]	14.5	±1.8	12%
I_{Rel3}[%]	32.0	±2.4	7.4%
-			
$Bkgr_{Dec}$[kCnts]	0.0074	±0.0024	33%
-			
$Bkgr_{IRF}$[Cnts/Chnl]	2.08	±0.67	32%
$Shift_{IRF}$[ps]	74.0	±7.6	10%
A_{Scatt}[kCnts]	27.7	±2.1	7.3%
-			
τ_{AvInt}[ns]	2.609	±0.048	1.8%
τ_{AvAmp}[ns]	1.567	±0.022	1.4%

I_2[kCnts]	80.2	±5.1	6.3%
A_{Rel2}[%]	3.4	±1.9	57%
I_{Rel2}[%]	19.3	±3.0	15%
-			
A_3[kCnts/Chnl]	39	±55	142%
τ_3[ns]	0.212	±0.073	34%
I_3[kCnts]	81	±48	59%
A_{Rel3}[%]	66	±17	25%
I_{Rel3}[%]	19.4	±8.0	41%
-			
$Bkgr_{Dec}$[kCnts]	0.0057	±0.0008	14%
-			
$Bkgr_{IRF}$[Cnts/Chnl]	-0.43	±0.39	93%
$Shift_{IRF}$[ps]	185	±11	5.8%
A_{Scatt}[kCnts]	44	±35	78%
-			
τ_{AvInt}[ns]	1.72	±0.18	10%
τ_{AvAmp}[ns]	0.72	±0.31	42%

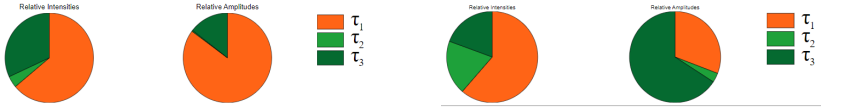

Figure A55- *Lifetime of* ***o-DPP acid 24*** *grafted on right ribbons (first) and left ribbons (second).*

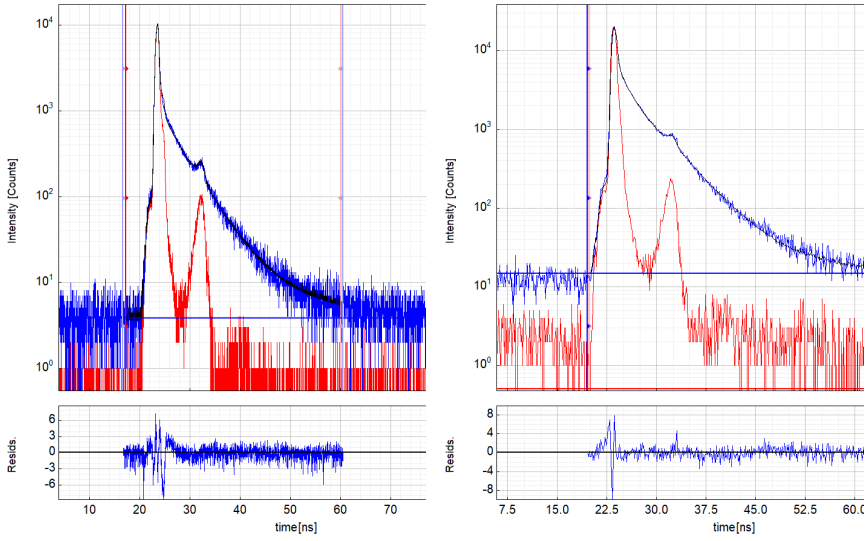

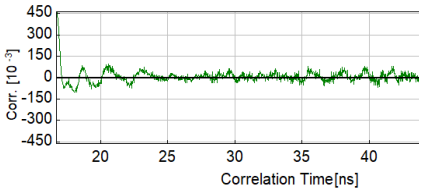

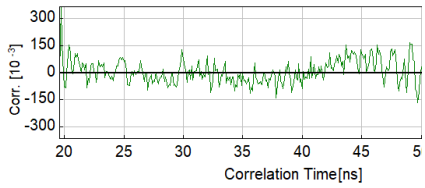

Parameter	Value	Δ	δ
A_1[kCnts/Chnl]	1.113	±0.015	1.3%
τ_1[ns]	4.028	±0.076	1.9%
I_1[kCnts]	179.3	±3.1	1.7%
A_{Rel1}[%]	97.3	±1.1	1.1%
I_{Rel1}[%]	92.1	±1.9	2.0%
-			
A_2[kCnts/Chnl]	0.032	±0.013	40%
τ_2[ns]	12.2	±2.0	16%
I_2[kCnts]	15.5	±3.8	24%
A_{Rel2}[%]	2.8	±1.1	38%
I_{Rel2}[%]	8.0	±1.9	24%
-			
$Bkgr_{Dec}$[kCnts]	0.0039	±0.0003	6.3%
-			
$Bkgr_{IRF}$[Cnts/Chnl]	0.20	±0.20	99%
$Shift_{IRF}$[ps]	-56.0	±1.5	2.5%
A_{Scatt}[kCnts]	332.1	±1.2	0.4%
-			
τ_{AvInt}[ns]	4.673	±0.087	1.8%
τ_{AvAmp}[ns]	4.253	±0.052	1.2%

Parameter	Value	Δ	δ
A_1[kCnts/Chnl]	3.81	±0.30	7.8%
τ_1[ns]	4.60	±0.11	2.4%
I_1[kCnts]	175.2	±9.3	5.3%
A_{Rel1}[%]	49.0	±2.1	4.3%
I_{Rel1}[%]	74.1	±3.1	4.2%
-			
A_2[kCnts/Chnl]	3.97	±0.19	4.8%
τ_2[ns]	1.55	±0.23	14%
I_2[kCnts]	61.5	±6.8	11%
A_{Rel2}[%]	51.1	±2.1	4.1%
I_{Rel2}[%]	26.0	±3.1	12%
-			
$Bkgr_{Dec}$[kCnts]	0.0149	±0.0009	5.6%
-			
$Bkgr_{IRF}$[Cnts/Chnl]	0.50	±0.68	135%
$Shift_{IRF}$[ps]	155.5	±6.3	4.0%
A_{Scatt}[kCnts]	150.5	±7.2	4.8%
-			
τ_{AvInt}[ns]	3.808	±0.057	1.5%
τ_{AvAmp}[ns]	3.05	±0.17	5.4%

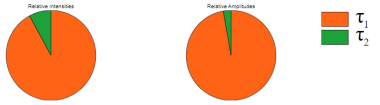

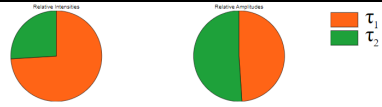

Figure A56- *Lifetime of* ***p-DPP acid 25*** *grafted on right ribbons (first) and left ribbons (second).*

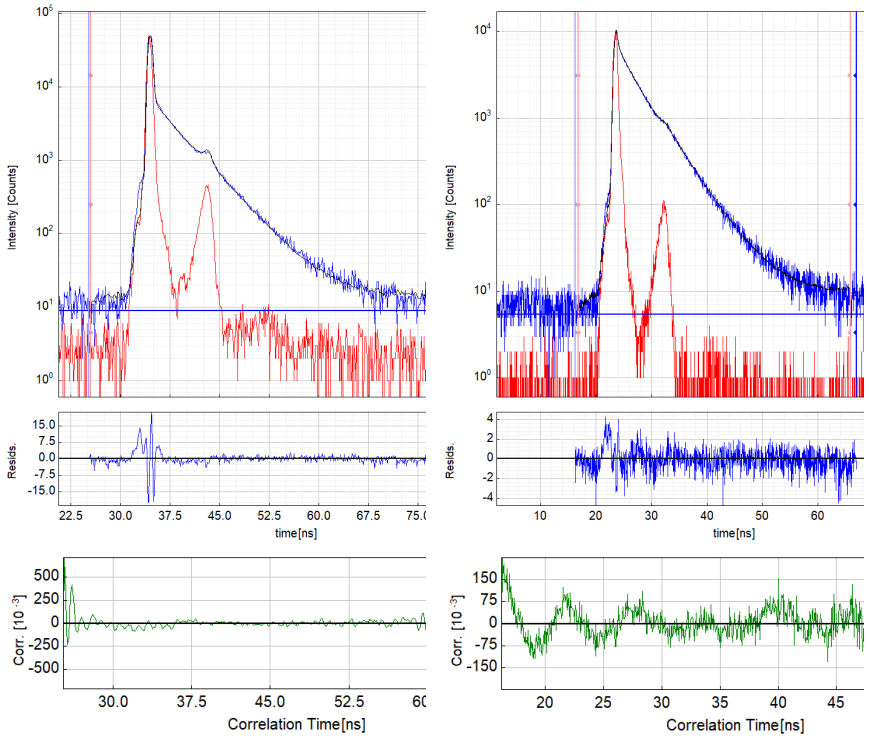

Parameter	Value	Δ	δ
A_1[kCnts/Chnl]	1 280	±260	20%
τ_1[ns]	0.146	±0.017	11%
I_1[kCnts]	1 870	±400	21%
A_{Rel1}[%]	99.5	±0.2	0.1%
I_{Rel1}[%]	85.9	±2.2	2.5%
-			
A_2[kCnts/Chnl]	7.396	±0.088	1.2%
τ_2[ns]	4.151	±0.026	0.6%
I_2[kCnts]	307.0	±1.6	0.5%
A_{Rel2}[%]	0.6	±0.2	17%
I_{Rel2}[%]	14.2	±2.2	15%
-			
A_3[kCnts/Chnl]	- 450	±130	27%
τ_3[ns]	0.186	±0.016	8.5%
I_3[kCnts]	- 850	±280	33%
A_{Rel3}[%]	0.0	---	---
I_{Rel3}[%]	0.0	---	---
-			
$Bkgr_{Dec}$[kCnts]	0.0091	±0.0027	29%
-			

Parameter	Value	Δ	δ
A_1[kCnts/Chnl]	2.159	±0.091	4.2%
τ_1[ns]	1.48	±0.12	8.1%
I_1[kCnts]	63.7	±8.3	13%
A_{Rel1}[%]	26.7	±1.2	4.2%
I_{Rel1}[%]	11.2	±1.5	13%
-			
A_2[kCnts/Chnl]	5.93	±0.17	2.8%
τ_2[ns]	4.292	±0.038	0.9%
I_2[kCnts]	508.7	±9.6	1.9%
A_{Rel2}[%]	73.4	±1.2	1.5%
I_{Rel2}[%]	88.9	±1.5	1.7%
-			
$Bkgr_{Dec}$[kCnts]	0.0055	±0.0003	4.5%
-			
$Bkgr_{IRF}$[Cnts/Chnl]	-0.791	±0.072	9.1%
$Shift_{IRF}$[ps]	-44.2	±4.4	9.8%
A_{Scatt}[kCnts]	96.8	±2.0	2.0%
-			
τ_{AvInt}[ns]	3.978	±0.011	0.3%
τ_{AvAmp}[ns]	3.540	±0.035	1.0%

$Bkgr_{IRF}$[Cnts/Chnl]	-0.7	±1.8	284%
$Shift_{IRF}$[ps]	-46.5	±3.4	7.3%
A_{Scatt}[kCnts]	- 278	±69	25%
-			
τ_{AvInt}[ns]	0.72	±0.11	15%
τ_{AvAmp}[ns]	0.169	±0.021	12%

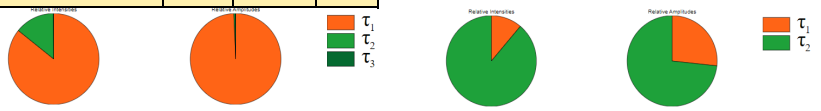

Figure A57- *Lifetime of* ***m-DPP acid 26*** *grafted on right ribbons (first) and left ribbons (second).*

Attachments 2

Solvent-dependent singlet fission in diketopyrrolopyrrole dimers – a mediating charge transfer versus a trapping symmetry-breaking charge separation

Ilias Papadopoulos,[‡] Maria João Álvaro-Martins,[‡] Desire Molina, Patrick M. McCosker, Paul A. Keller, Timothy Clark, Ángela Sastre-Santos, Dirk M. Guldi**

Ilias Papadopoulos, Prof. Dr. Dirk M. Guldi

Department of Chemistry & Pharmacy, Interdisciplinary Center for Molecular Materials (ICMM), Friedrich-Alexander-Universität Erlangen-Nürnberg (FAU), Egerlandstr. 3, 91058 Erlangen, Germany.
E-mail: dirk.guldi@fau.de

Maria João Álvaro-Martins, Desire Molina, Prof. Dr. Ángela Sastre-Santos

Área de Química Orgánica, Instituto de Bioingeniería, Universidad Miguel Hernández, Avda. de la Universidad s/n, 03203 Elche, Spain
E-mail: asastre@umh.es

Patrick M. McCosker, Prof. Dr. Timothy Clark

Department of Chemistry & Pharmacy, Computer-Chemie-Center (CCC), Friedrich-Alexander-Universität Erlangen-Nürnberg, Nägelsbachstr. 25, 91052 Erlangen, Germany

Patrick M. McCosker, Prof. Dr. Paul A. Keller

School of Chemistry & Molecular Bioscience, Molecular Horizons, Illawarra Health & Medical Research Institute, University of Wollongong, NSW 2522, Australia

Keywords: intramolecular singlet fission, diketopyrrolopyrrole dimers, charge transfer states

A novel set of three diketopyrrolopyrrole (DPP) dimers, linked via different dithienylphenylene spacers, *ortho*-DPP (***o*-DPP**), *meta*-DPP (***m*-DPP**), and *para*-DPP (***p*-DPP**), were synthesized, characterized, and probed in light of intramolecular singlet fission (*i*-SF). Importantly, in the corresponding DPP reference (**DPP-ref**) singlet and triplet excited state energies of 2.22 and 1.04 eV, respectively, suggested that *i*-SF is thermodynamically feasible. The investigations focused on the impact of the relative positioning of the DPPs, and gave compelling evidence that solvent polarity and/or spatial overlap govern *i*-SF dynamics and efficiencies. For example, polar solvents made the involvement of an intermediate charge transfer (CT) state possible, which was followed

by the population of $^1(T_1T_1)$ and subsequently ($T_1 + T_1$), while spatial overlap drove the mutual interactions between the DPPs. In ***o*-DPP** the correct balance between polar solvents and spatial overlap lead to the highest total quantum yield (TQY) of 40%. Notable was the superimposition of CT characteristics with those of triplet excited states, so that an accurate TQY determination was impossible. For ***m*-DPP**, poorer spatial overlap correlated with a weaker CT character and manifested itself through a TQY of 11%. If the CT character was strong, the intermediate state acts as a trap and prevents *i*-SF, as found with ***p*-DPP**. The DPP separation is decisive, enabling a symmetry-breaking charge separated (SBCS) state rather than CT formation, shutting down the pathway to $^1(T_1T_1)$ formation

1. Introduction

The down-conversion of singlet excited states by means of singlet fission (SF) is currently at the forefront of advanced photon management. SF enables multiple excitons to be generated after the absorption of just a single photon.[1–9] By integrating SF-materials into solar-cell architectures, it is feasible to overall increase the efficiency of solar cells by pushing the Shockley-Queisser limit from 32% to approximately 45%. Several requirements must, however, be met to allow for efficient SF well beyond 100%.[10,11]

Thermodynamically, the energy level of the singlet excited state must be equal to or higher than twice that of the triplet excited state; $(S_1) \geq 2(T_1)$.[2,3,12] In addition, the energy levels of higher-lying triplet excited states should exceed twice the energy of the lowest-lying triplet excited state; $(T_2) \geq 2\ (T_1)$.[2,3,12] The latter avoids (T_2) population as a product of triplet-triplet annihilation up-conversion (TTA-UC).[2,3,12] Sufficient electronic interaction between two or more chromophores is essential, and is usually realized for monomers by overlaps in the crystal packing or high concentrations in the solid state or solution, respectively.[12–16] Dimers, in which different spacers are employed to link the chromophores, rather than monomers represent yet another strategy to adjust and fine tune, for instance, electronic coupling, spatial overlap, and to probe the SF-mechanisms, kinetics, and efficiencies.[5,8]

Currently, not all mechanistic aspects of SF are completely understood.[17,18] Although SF has seemingly many mechanistic facets, two main pathways have emerged. The first one is a one-step, direct mechanism, by which the initial (S_1S_0) transforms into the final $^1(T_1T_1)$ without populating any transient intermediate. The second is the indirect, two-step mechanism, in which the population of the final $^1(T_1T_1)$ is mediated by a transient state, either virtual or a real.[12,19–27]

Acenes, in general, and pentacenes in particular, fulfill all SF-requirements and, consequently have attracted a great deal of attention.[16,24,28–35] Other promising SF-materials include rylene-diimides[26,36–44] and diketopyrrolopyrroles (DPPs).[45–51] Incentives for this study were to improve our understanding of intramolecular SF (*i*-SF) in DPP dimers. In general, DPPs are strongly fluorescent, feature high stability, are widely accessible due to their relatively simple synthesis, and exhibit good carrier mobility.[52–58] DPPs are found in a broad range of

applications including field-effect transistors, solar-cell devices, fluorescence imaging and importantly, SF.[52,53,66,58–65] Some SF-reports are known from the literature, but most focus on intermolecular SF (inter-SF) in monomers,[45,46,49] rather than intra-SF in dimers.[48,50] As far as the triplet excited state (T_1) energies of DPPs are concerned they range from 1.02 to 1.21 eV.[45,46,67]

In this study, we have synthesized, characterized, and probed a versatile set of three different DPP dimers, in which the DPPs are linked by dithienylphenylene spacers substituted in the *ortho*-, *meta*-, and *para*-positions; ***o*-DPP**, ***m*-DPP** and ***p*-DPP**, respectively. Different DPP positions allow the influence of spatial overlap on the SF-dynamics and efficiencies to be explored. In addition, the use of different solvents, from non-polar toluene to polar benzonitrile, make analysis of the participation of a transient CT state and its impact on SF possible.

2. Results and Discussion

2.1. Synthesis

***o*-DPP**, ***m*-DPP** and ***p*-DPP** were obtained by Suzuki-Miyaura coupling between **BrDPP**[68] and the boronic esters **2**, **3**[69] and **4** respectively, in 53%, 43% and 36% yield, respectively (**Scheme 1**). BrDPP was prepared as previously described from **DPP-Ref**.[70,71] ***p*-DPP** was previously synthesized by direct heteroarylation, but not completely characterized.[72] All three dimers are soluble in common organic solvents, such as toluene, dichloromethane (DCM) and chlorobenzene (**Figures S31-S53).**

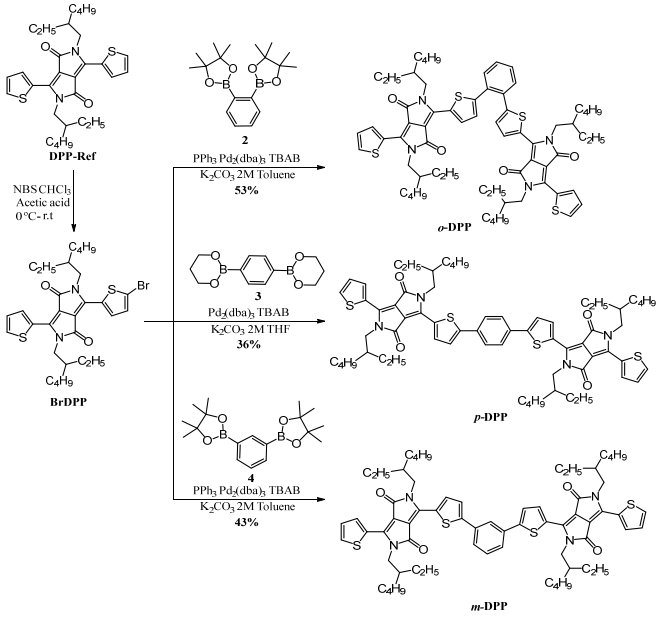

Scheme 1. Synthesis of ***o*-DPP, *m*-DPP, and *p*-DPP** by Suzuki-Miyaura coupling and chemical structure of **DPP-Ref** and **BrDPP**.

2.2 Theory

Density functional theory (DFT) and its time-dependent (TD-DFT) counterpart were used to investigate the ground- (S_0) and excited-state (S_1, T_1, T_2) properties of **DPP-Ref**, ***o*-DPP**, ***m*-DPP**, and ***p*-DPP**. The S_0 geometries were found using the B3LYP hybrid functional with Grimme's dispersion correction (D3) and Becke-Johnson dampening (BJ),[73–76] combined with the 6-311G(d) basis set for the **DPP-Ref** structure, or the split valence 6-31G(d) for the dimers.[77,78] It was found that substitution of the nitrogen atoms with at least *iso*-butyl groups was necessary to reproduce the geometry and vertical excitations (VE) of **DPP-Ref**. The dimers were therefore optimized with *iso*-butyl substituents (**Figure S29**, **Table S3**).

Comparison of different conformations of **DPP-Ref** indicated the thiophene-*trans* configuration to be lowest in energy, as also found for the dimer conformers (**Figure S30**). Subsequent analysis of the ***o*-DPP** conformers revealed that stacking of the DPP monomers resulted in the lowest energy structure, whereas ***m*-DPP** and ***p*-DPP** preferred monomer separation (**Figure**). The separation of monomer planes in ***o*-DPP** was found to be 5.7 Å and in contrast the ***m*-DPP** and ***p*-DPP** dimers are significantly separated such that spatial overlap is minimized or completely eliminated respectively.

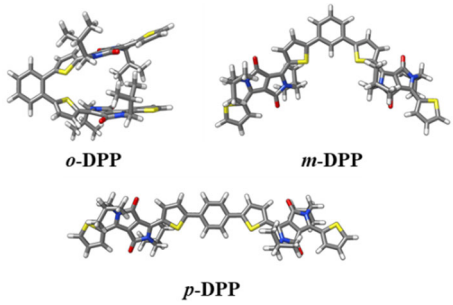

Figure 1. Optimized structures of ***o*-DPP**, ***m*-DPP**, and ***p*-DPP**.

An approximation of the SF thermodynamics of the DPP dimers was obtained by calculating TD-DFT VE (S_1, T_1, T_2) at the M06-2X/def2-TZVP level of theory (**Table S5**). The $S_0 - S_1$ vertical excitations were found to be in the order of 2.61 – 2.27 eV, and tended towards lower energies in the order **DPP-Ref** > ***o*-DPP** > ***m*-DPP** > ***p*-DPP**, in agreement with the steady-state absorption – *vide infra*. Subsequently, the SF process was predicted to be exothermic for all dimers, with S_1/T_1 (VE) ratios of 2.34, 2.40 and 2.38 for ***o*-DPP**, ***m*-DPP**, and ***p*-DPP**, respectively. In contrast, the triplet-triplet annihilation up-conversion (TTA-UC) process was found to be endothermic, with T_2/T_1 ratios of 2.52, 2.50 and 2.44, respectively, in turn ruling out the presence of delayed fluorescence. Both S_1/T_1 and T_2/T_1 for all dimers were found to be of a similar value, and should therefore not impact on the SF dynamics of the dimers differently.

The charge transfer/resonance character of SF dimers has recently been highlighted to enhance the formation of the correlated triplet pair significantly.[79] Studying the spin distribution in DPP linked pentacene

dimers revealed that strong charge transfer/resonance character of the S_1 state correlated with $^1(T_1T_1)$ exciton formation and subsequent triplet quantum yields (TQY). The DPP dimers investigated were found to have stable ground-state wave-functions, namely, non-biradicals with satisfactory closed-shell description of the singlets. Subsequent analysis of the TD-DFT S_0-S_1 VE in all dimers indicated S_1 to be a linear combination of the frontier molecular orbitals (FMOs) ± 1 (**Figures S37 – S40**).

The FMOs in all dimers were delocalized over both DPPs and only subtle differences were noted. Briefly, the ***o*-DPP** highest occupied molecular orbitals (HOMOs) and lowest occupied molecular orbitals (LUMOs) were equally and unequally distributed across the subunits, respectively, with minimal delocalization onto the benzene linker. In contrast, ***m*-DPP** and ***p*-DPP** FMOs were equally distributed and included the orbitals of the benzene linker. In addition, analysis of the FMO's contributions to the TD-DFT S_0-S_1 VE indicated minimal redistribution of electron density, even in the case of ***o*-DPP**, where the multiple contributions were almost equally distributed, minimizing the electron density localization. As a result, the $S_0 – S_1$ VE can primarily be described as π–π* in character, with a minimal degree of charge transfer/resonance, and should hinder the $^1(T_1T_1)$ exciton formation, resulting in the low TQYs observed – *vide infra*.

2.3 Photophysical Characterization

3.1.1. 2.3.1. Steady-State Characterization

Steady-state absorption measurements were performed to explore the ground-state of the DPPs. Measurements were conducted in solvents of different polarity, that is, toluene and benzonitrile, to investigate the influence of polarity on the SF-mechanism and its dynamics. The **DPP-Ref** absorptions in toluene included a set of well-resolved maxima between 400 and 600 nm, which represent the 0-*0 and 0-*1 transitions to the lowest singlet excited states. In addition, maxima were seen between 300 and 400 nm, representing the corresponding transitions to higher singlet excited states. Extinction coefficients as high as 30,000 $M^{-1}cm^{-1}$ were found in toluene. Changing the solvent to benzonitrile led to no significant differences.

Analysis of ***o*-DPP**, ***m*-DPP**, and ***p*-DPP** revealed significant differences between them. Notably, in **DPP-Ref** the intensities of the 0-*0 to 0-*1 transitions decreased, while in ***o*-DPP** they were reminiscent of the absorption pattern of *H*-aggregates, i.e. of equal intensity, suggesting sizeable interactions between the DPPs. Other differences included a red-shift of about 20 nm and an increase of the extinction coefficient to about 65,000 $M^{-1}cm^{-1}$. ***m*-DPP** features are much closer to those of **DPP-Ref**, despite the observation of a 30 nm red-shift and an extinction coefficient of nearly 93,000 $M^{-1}cm^{-1}$. Lastly, ***p*-DPP** exhibits broad and featureless absorption peaks, which are roughly 60

nm red-shifted compared to **DPP-Ref** with extinction coefficients as large as 96,000 $M^{-1}cm^{-1}$. Overall, the steady-state absorption measurements (**Figurea**) reveal increasing red shifts and extinction coefficients in the order ***o*-DPP** < ***m*-DPP** < ***p*-DPP**. It is safe to postulate that the electronic couplings, which differ in the DPP-dimers, are sufficient to govern *i*-SF – *vide infra*.[80] Steady-state fluorescence measurements provided first indications of differences in the excited states. For **DPP-Ref**, the fluorescence maximum lies between 500 and 750 nm and the fluorescence quantum yield (FQY) between 69.5% in toluene and 66.7% in benzonitrile. Common to ***o*-DPP**, ***m*-DPP**, and ***p*-DPP** are hypsochromic-shifts, which coalesced with the corresponding shifts seen in the absorption measurements (**Figureb**), and significant FQY quenching. Starting with ***m*-DPP**, a 46.6% FQY suggested moderate inter-DPP interactions. ***o*-DPP** is subject to a much stronger fluorescence quenching with an FQY of 12.1% and the strongest quenching is found for ***p*-DPP** with a 1.4% FQY. In contrast to **DPP-Ref**, changing the solvent from toluene to benzonitrile resulted in further FQY-quenching: 5.3% (***m*-DPP**), 2.1% (***o*-DPP**), 1.2% (***p*-DPP**) (**Figure S1**, **Table S1**).

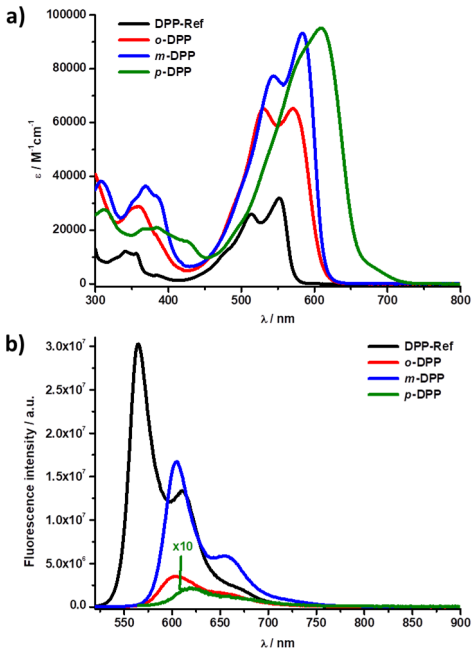

Figure 2. (a) Room-temperature absorption spectra of **DPP-Ref** (black), ***o*-DPP** (red), ***m*-DPP** (blue), and ***p*-DPP** (green) in toluene. (b) Respective fluorescence spectra in toluene following photoexcitation at 545 nm for ***o*-DPP** and ***m*-DPP**, 550 nm for ***p*-DPP**, and 505 nm for **DPP-Ref** with optical densities of 0.025.

The steady-state absorption and fluorescence measurements indicated that for ***o*-DPP** the intensity increase of the 0-*1 absorption is accompanied by a quenched FQY, when compared to **DPP-Ref**. Such trends are in line with intramolecular forces between slightly displaced, parallel arranged DPPs, as in *H*-type aggregates. Concentration independence underlines the intra- rather than intermolecular nature of the DPP interactions in ***o*-DPP**. The solvent-dependent FQYs suggest an excited-state deactivation involving the formation of either charge transfer (CT) state, relating to the

partial transfer of electron density, or symmetry-breaking charge separated (SBCS) state, relating to the full transfer of electron density and, in turn, the full separation of electrons and holes. Involvement of a CT/SBCS state induces red-shifts in the *H*-type aggregates, which usually feature blue-shifts.[81–83] Similarly, a deactivation *via* a CT state and/or a SBCS state in *H*-aggregates was reported for the case, in which a xanthene bridge was used in DPP-dimers.[50] For ***p*-DPP**, the broadened absorption goes hand-in-hand with the most strongly quenched fluorescence among the DPP-dimers. Again, the quenched and, more importantly, the solvent-dependent, albeit weak, FQYs suggest the involvement of either CT state or SBCS state. The broadening of the absorption features is attributed to the free and unhindered rotation of the DPPs, due to the minimal steric interaction of the *para*-position, which was supported by theory. Finally, for ***m*-DPP** both absorption and fluorescence resemble what is seen for the reference. The overall strength of the interaction is expected to be the weakest among the DPP-dimers, as the phenyl linker affords better electronic communication in case of *ortho*- and *para*-substitutions.[84,85]

Inlow-temperature measurements with **DPP-Ref** at 80 K in 2-methyltetrahydrofuran (MeTHF) and in the presence of ethyl iodide (EtI) to enhance the triplet formation, a 1185 nm feature was ascribed to phosphorescence. Correspondingly, a triplet excited state (T_1) energy of 1.04 eV was derived – **Figure S2**. Comparing a T_1 energy of 1.04 eV with S_1 energies as high as 2.22 eV in **DPP-Ref** and as low as 2.08 eV in ***m*-DPP** renders *i*-SF thermodynamically feasible.

2.3.2. Electrochemical and Spectroelectrochemical Characterization

Electrochemical properties of the three dimers were examined by cyclic voltammetry (CV) using CH_2Cl_2 as solvent containing 0.1 M tetrabutylammonium hexafluorophosphate ($TBAPF_6$) as supporting electrolyte (**Figure 3**, **Table 1**). The three dimers present a similar band-gap owing to the fact that the electron donor and the acceptor fragments are the same. However, ***p*-DPP** presents the lowest E_g^{cv} among the three different dimers. Based on a push-pull structure, the LUMO energy level is controlled by the electron accepting (deficient) unit, while the HOMO energy level is governed by the electron rich (donating) unit. **DPP-Ref** has the largest band-gap with a value of 2.2 eV when compared to the DPP-dimers, which are between 2.0 and 2.1 eV.

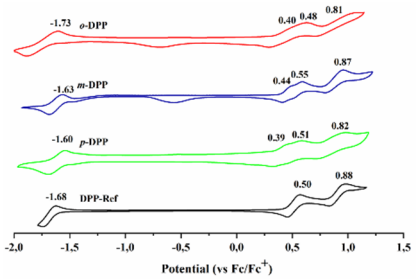

Figure 3. Cyclic voltammograms of ***o*-DPP**, ***m*-DPP**, ***p*-DPP**, and **DPP-Ref** in CH_2Cl_2 containing 0.1 M $TBAPF_6$ as supporting electrolyte and measured against Fc/Fc^+.

Table 1. Optical and electrochemical parameters *of o*-DPP, *m*-DPP, *p*-DPP, and DPP-Ref.

Compound	E_{red1} (eV)	E_{oxi1} (eV)	$E_{g,opt}$[a]/$_{EC}$[b] (eV)	HOMO[c]	LUMO[d]
***p*- DPP**	-1.60	0.39	2.02/1.99	-5.19	-3.20
***m*-DPP**	-1.63	0.44	2.09/2.07	-5.24	-3.17
***o*-DPP**	-1.73	0.40	2.11/2.03	-5.20	-3.17
DPP-Ref	-1.68	0.50	2.23/2.18	-5.30	-3.12

The energy positions of the HOMOs were estimated from the onset values for the oxidation potentials through the equation: a) $E_{g,opt}$ (eV) was determined from the intersection of normalized absorption and emission spectra registered in CH_2Cl_2. b) $\mathbf{E_{g,EC}} = \mathbf{E_{red1}} - \mathbf{E_{oxi1}}$. c) HOMO=-|$E_{ox1}$(vs. Fc/Fc$^+$) + 4.8|. d) The LUMO values were calculated by LUMO=HOMO+$\mathbf{E_{g,EC}}$(eV).

Spectroelectrochemical (SEC) measurements were conducted to register the optical features of both the one-electron reduced and oxidized forms of the DPP-dimers and to use them to interpret the time resolved transient absorption measurements. Experiments were conducted in a toluene/acetonitrile mixture (4/1 v/v) with 0.1 M $TBAPF_6$ as supporting electrolyte. In the case of ***o*-DPP**, applying +1.0 V resulted in fully reversible spectroscopic features of its one-electron oxidized form in the 650 to 1000 nm range with maxima at 780 and 900 nm (**Figure 4a**). In contrast, a potential of -1.5 V resulted in the formation of its semi-stable one-electron reduced form with only a single maximum at approximately 480 nm. Unfortunately, the ground state absorption superimposes the feature of the one-electron reduced form, which, in turn, could not be fully resolved (**Figure 4b**). Similar results were gathered for ***m*-DPP** and ***p*-DPP** (**Figures S4** and **S5**).

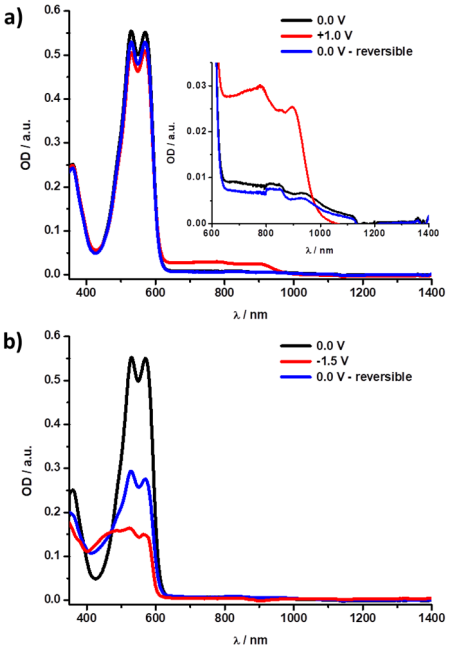

Figure 4. a) Spectroelectrochemical features of the (a) one-electron oxidized and (b) one-electron reduced forms of ***o*-DPP** in a toluene/acetonitrile solution (4/1 v/v) with 0.1 M $TBAPF_6$ as supporting electrolyte.

2.3.3. Time-Resolved Characterization

Time-correlated single photon counting (TCSPC) measurements, with a 530 nm excitation wavelength, revealed for **DPP-Ref** a single fluorescent component with a lifetime of 5.5 ns in toluene. ***o*-DPP**, ***m*-DPP**, ***p*-DPP** gave rise to two fluorescent components, a short-lived one on the picosecond timescale and a long-lived one on the nanosecond timescale.[86] In detail, the lifetimes in toluene are 832 ps and 2.4 ns for ***o*-DPP**, 490 ps and 3.6 ns for ***m*-DPP**, and <200 ps and 2.5 ns for ***p*-DPP**. A change to benzonitrile only affected the short-lived component without, however, impacting the long-lived one (**Figure S6**). A summary is given in

Table 2. Subsequently, time-resolved transient absorption spectroscopy on the femto- (fsTAS) and nanosecond (nsTAS) timescales were performed following 530 nm excitation. Lifetimes were obtained by means of GloTarAn target analyses. In **DPP-Ref**, excitation is immediately followed by the formation of the singlet excited state (S_1). In toluene, maxima are found at 435, 710, and 885 nm, while minima evolved at 513, 562, and 616 nm (**Figures S8a** and **S8c**). The former minima relate to ground-state bleaching (GSB) and the latter to stimulated emission (SE). All of these features were replaced within 4.5 ps (**Figures S8b** and **S8d**) by an intermediate state, which was characterized by subtle shifts of the 885 nm maximum and the 562 and 616 nm minima. The underlying process corresponds to solvent reorganization, which was due to increasing the solvation energy of the excited state leading to $(S_1)_{Sol}$.[29,87] From $(S_1)_{Sol}$, the complete reinstatement of the ground state (S_0) is reached within 6.0 ns (**Figure S10**). Similar results were gathered for **DPP-Ref** in benzonitrile (**Figures S9** and **S11**).

An initial analysis of ***o*-DPP**, ***m*-DPP**, and ***p*-DPP** showed that all of them featured in toluene the same initial singlet excited state (S_1S_0) with lifetimes of 9.9, 7.8, and 15.5 ps, respectively. Common to all (S_1S_0) was the solvent reorganization to afford $(S_1S_0)_{Sol}$. The underlying lifetimes of 576 ps (***o*-DPP**), 372 ps (***m*-DPP**), and 77 ps (***p*-DPP**) were, however, shorter than what was seen for **DPP-Ref**. It was also noted that the lifetimes reflected the strength of intramolecular DPP-interactions. In stark contrast to the conclusions drawn for **DPP-Ref**, ***o*-DPP**, ***m*-DPP**, and ***p*-DPP** populate yet another, third state, whose lifetimes are 2.3, 3.7, and 1.8 ns, respectively, and lead to the quantitative ground-state recovery. Interesting is the fact that the third species bears similarities with the aforementioned $(S_1S_0)_{Sol}$ signatures. In other words, it has still some singlet excited state character. Next to the $(S_1S_0)_{Sol}$ signatures, transients at 460, 650, and 1000 nm resemble the fingerprints seen in SEC (**Figures 4**, **S4**, and **S5**). We postulate in line with recent work mixing of the singlet excited state with a CT state and defining the third species as $(S_1S_0)_{CT}$.[25,29,88] Noteworthy, the lifetimes of $(S_1S_0)_{Sol}$ and $(S_1S_0)_{CT}$ match those of the short- and long-lived fluorescent components detected in the TCSPC measurements – *vide supra* (**Table 2**). The only notable differences between ***o*-DPP**, ***m*-DPP**, and ***p*-DPP** are the expected shifts in the GSB and SE features. Importantly, no appreciable

population of any triplet excited state is observed in toluene (**Figures S12-S15**, **S18-S19**).

The strong impact of solvent polarity changes on the FQYs suggested a subtle interplay between the different states in the excited state deactivation of ***o*-DPP**, ***m*-DPP**, and ***p*-DPP**. A comparison with toluene corroborates that the first, second, and third species are still involved in the excited-state deactivation. The longer (S_1S_0) lifetimes in benzonitrile are due to the higher viscosity, which slows down solvent reorganization.

Analysis of the results for ***o*-DPP** showed that, after solvent reorganization $(S_1S_0)_{Sol}$, a stronger CT contribution in $(S_1S_0)_{CT}$ is derived from the positive transient at 650 nm (**Figure 5a** and **5c**). Likewise, a shorter $(S_1S_0)_{CT}$ lifetime relative to toluene stems from the CT-stabilization in more polar solvents. $(S_1S_0)_{CT}$ also experienced a stronger CT-mixing, which is manifested in an intense peak at 480 nm and depletion of GSB. Both characteristics are in line with the SEC features seen for the one-electron reduced form of ***o*-DPP** (**Figure 4b**). Lifetimes of $(S_1S_0)_{Sol}$ and $(S_1S_0)_{CT}$ (**Figure 5b** and **5d** and **Table 2**) match the corresponding TCSPC lifetimes in benzonitrile (**Table 2**) – *vide supra*. Contrary to the results in toluene, the $(S_1S_0)_{CT}$ deactivation is linked to the population of two additional states. Of great importance is the fact that none of these two additional states resemble the CT-character seen, for example, in $(S_1S_0)_{CT}$, or the $(S_1S_0)_{Sol}$ features. In particular, maxima are found at 470 (broad) and 555 nm, which are complemented by minimum at 585 nm. Of equal importance is the fact that they are spectrally nearly identical.

To clarify the nature of these two additional states, we turned to triplet-triplet sensitization measurements with *N*-methylfulleropyrrolidine (***N*-MFP**, **Figure S23**) as a triplet-triplet energy transfer (TTET) donor and ***o*-DPP** as TTET acceptor. Photoexcitation was performed at 430 nm. In the case of ***o*-DPP**, again a maxima at 470 (broad) and 555 nm and minimum at 585 nm were seen to grow in at the expense of the triplet excited state maximum of ***N*-MFP** at 700 nm. The correspondingly formed (T_1S_0) decays with approximately 20 µs to the ground state. Considering the appreciable resemblance between the (T_1S_0) signature in TTET and the spectroscopic signature of the first of the two additional states, we infer the population of $^1(T_1T_1)$ in ***o*-DPP**, that is, two triplet excited states are formed (**Figures 6a** and **6c**). The re-intensification of the GSB was emphasized in **Figure S22**. In contrast to the approximately 20 µs lifetime of (T_1S_0), $^1(T_1T_1)$ is short-lived. It is within 42.0 ns that $^1(T_1T_1)$ transforms in the second of the two additional states.[89] We rationalize the transformation to the decoherence of $^1(T_1T_1)$ (**Figures 6b**, **6d**, and **Table 2**) and the formation of the uncorrelated triplet excited state ($T_1 + T_1$) (**Figures 6a** and **6c**). The lifetime of the latter is 15.0 µs and agrees well with that derived for (T_1S_0) (**Figures 6b**, **6d**, and **Table 2**). In short, the existence of these two triplet-based species, inferred by a reasonable coupling of the thiophene-phenyl-thiophene bridges due to

rotational freedom / heteroatom effect, corroborated *i*-SF, as conventional ISC would lead to only one triplet excited state. Despite the lack of CT-character in $^1(T_1T_1)$ and $(T_1 + T_1)$, an alternative deactivation route should be mentioned; two subsequently formed CTs with singlet and triplet spin, respectively.

The triplet quantum yield (TQY) was calculated using the method, which incorporates the singlet (ε_{S1*}) and triplet (ε_{T1*}) excited state molar extinction coefficients. As such, a value of 40% was derived (**Figure S28a**, **Table S2**).[28,29,31] Note that the spectroscopic features stemming from the one-electron reduced form superimpose those of $^1(T_1T_1)$ and $(T_1 + T_1)$ making an accurate calculation of the TQYs difficult.

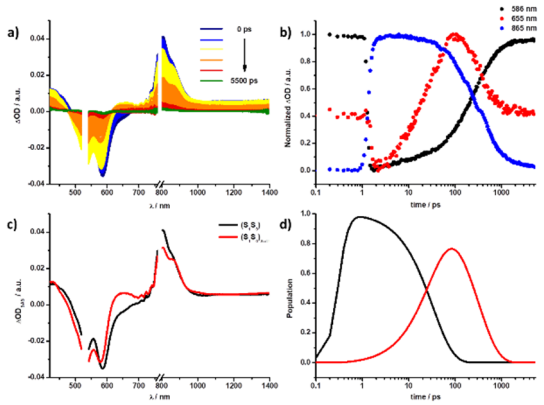

Figure 5. (a) Differential femtosecond transient absorption spectra (λ_{ex} = 530 nm, 400 nJ) of ***o*-DPP** in benzonitrile with time delays between 0 and 5500 ps, following the indicated color gradient. (b) Respective time absorption profiles at 586, 655, and 865. (c) Deconvoluted femtosecond transient absorption spectra of the singlet excited state (S_1S_0) (black) and intermediate state $(S_1S_0)_{Sol}$ (red) of ***o*-DPP** in benzonitrile as obtained by target analysis, using the kinetic model shown in **Figure *1.20***. (d) Respective population kinetics. Note that the subsequent species is omitted as a complete deconvolution failed on this time scale.

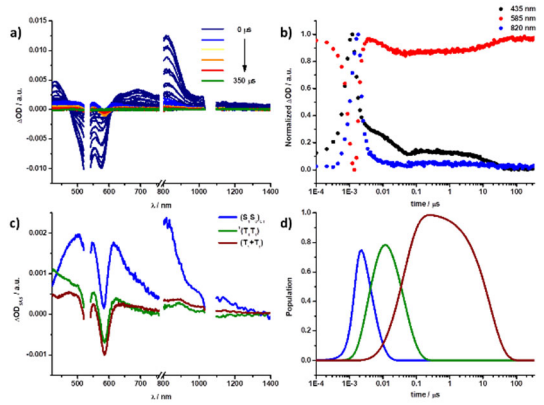

Figure 6. (a) Differential nanosecond transient absorption spectra (λ_{ex} = 530 nm, 400 nJ) of ***o*-DPP** in benzonitrile with time delays between 0 and 350 µs, following the indicated color gradient. (b) Respective time absorption profiles at 435, 585, and 820 nm. (c) Deconvoluted nanosecond transient absorption spectra of the intermediate singlet excited state with CT character $(S_1S_0)_{CT}$ (blue),

correlated triplet excited state $^1(T_1T_1)$ (green), and uncorrelated triplet excited state (T_1+T_1) (brown) of ***o*-DPP** in benzonitrile as obtained by target analysis, using the kinetic model shown in **Figure *1.20***7. (d) Respective population kinetics. Note that the intermediate $(S_1S_0)_{Sol}$, which was seen in femtosecond transient absorption, is omitted as the complete deconvolution failed on this time scale.

Table 2. Lifetimes obtained from GloTarAn target analysis of the time-resolved fluorescence (TCSPC) and transient absorption measurements, together with the calculated triplet quantum yields (TQY) in toluene and benzonitrile.

Sol	Compound	$\tau(S_1S_0)$ / ps	$\tau(S_1S_0)_{Sol}$ / ps	$\tau(S_1S_0)_{Sol}$ τ(SBCS) / ns	$\tau^1(T_1T_1)$ / ns	$\tau(T_1+T_1)$ / µs	TQY / %	τ_{TCSPC} ps	ns
Tol	**DPP-Ref**	4.5	6.0 ns	-	-	-	-	-	5.5
	***o*-DPP**	9.9	576	2.3	-	-	-	832	2.4
	***m*-DPP**	7.8	372	3.7	-	-	-	490	3.6
	***p*-DPP**	15.5	77.0	1.8	-	-	-	<200	2.5
BN	**DPP-Ref**	8.0	6.4 ns	-	-	-	-	-	5.9
	***o*-DPP**	33.7	313	3.9	42.0	15.0	40	389	3.9
	***m*-DPP**	14.0	298	4.4	86.5	98.9	11	298	3.8
	***p*-DPP**	18.2	56.8	2.2	-	-	-	<200	2.5

***m*-DPP** acts like ***o*-DPP** with a biphasic decay of $(S_1S_0)_{CT}$ via $^1(T_1T_1)$ and $(T_1 + T_1)$, but with a shorter $(S_1S_0)_{Sol}$ lifetime of 298 ps (**Figures S16a**, **S16c**, **S17a**, **S17c**, and **Table 2**). Overall, the CT-character in ***m*-DPP** is weaker than in ***o*-DPP** and the TQY is 11%. A likely rationale implies that the inter-DPP electronic coupling is weaker in ***m*-DPP** across the *meta*-position of the phenyl linker than across the *ortho*-position in ***o*-DPP** and, in turn, reduces TQY.[84,85]

Finally, for ***p*-DPP** the shortest $(S_1S_0)_{Sol}$ lifetime and subsequent population of $(S_1S_0)_{CT}$ was observed. Despite this finding, no evidence for any significant triplet excited-state population was gathered. At first glance, $(S_1S_0)_{CT}$ revealed an even stronger CT-character for ***p*-DPP** than for ***o*-DPP**. A closer look reveals, however, that the feature of the one-electron reduced form covers the range from 400 to 650 nm and, in turn, masks the GSB at around 600 nm (**Figures S20a**, **S20c**, **S21a**, **S21c**, and **Table 2**). From the strong resemblance of the transient with the SEC fingerprint and the low FQYs in the steady-state assays, a symmetry-breaking charge separation (SBCS) rather than $(S_1S_0)_{CT}$ formation with a significant CT-

character is inferred.[50] Minimizing the spatial overlap in ***o*-DPP**, ***m*-DPP**, and ***p*-DPP** enables SBCS. SBCS is, however, detrimental to SF. Therefore, the *i*-SF-efficiency follows the trend of ***o*-DPP** > ***m*-DPP** >>> ***p*-DPP** and a schematic diagram of the kinetic models is shown in **Figure 7**.

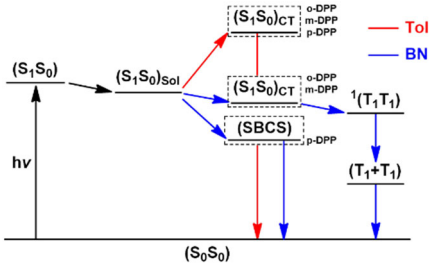

Figure 7. Kinetic models used to fit the transient absorption data of ***o*-DPP**, ***m*-DPP**, and ***p*-DPP** in toluene (red) and benzonitrile (blue).

3. Conclusion

A novel set of three different dimers of diketopyrrolopyrroles (DPPs), linked via dithienylphenylene spacers (***o*-DPP**, ***m*-DPP**, and ***p*-DPP**) was synthesized, characterized, and examined in light of intramolecular singlet fission (*i*-SF). Steady-state absorption and fluorescence measurements indicated the involvement of a charge-transfer (CT) and/or symmetry-breaking charge separated (SBCS) state as part of the SF-cascade. Solvent polarity plays the most important role in either CT or SBCS state population. Time-resolved transient absorption spectroscopy revealed two limiting scenarios. On one hand, CT mediated *i*-SF. Here, non-polar solvents such as toluene were found to be detrimental to the population of any triplet excited states. It is only that polar solvents such as benzonitrile, which enabled the population of $^1(T_1T_1)$ and subsequent $(T_1 + T_1)$. On the other hand, the spatial arrangement of the DPPs, which was important to govern *i*-SF. ***o*-DPP** had the highest *i*-SF efficiency with a TQY of 40% in benzonitrile. The TQYs were as low as 11% for ***m*-DPP** and 0% for ***p*-DPP** when benzonitrile was used as a solvent. As such, the electronic coupling between the two DPPs is in ***o*-DPP** strong enough to promote *i*-SF and, at the same time, weak enough to ensure $^1(T_1T_1)$ decoherence and avoid quantitative triplet-triplet annihilation. An alternative mechanism, which is based on the unlikely transient population of two subsequent CT states, namely of singlet and triplet spin ^{1}CT and ^{3}CT, respectively, before just one T_1 is formed, cannot entirely be ruled out. The *i*-SF was quantitatively suppressed in ***p*-DPP**, where the lack of spatial overlap resulted in a SBCS and shut down the population of $^1(T_1T_1)$ and $(T_1 + T_1)$. Therefore, this study has highlighted that the strength of the CT character, controlled by the solvent polarity, is decisive in balancing the electronic coupling and determining whether it mediates *i*-SF in DPP-dimers or blocks *i*-SF due to trapping.

Supporting Information

Supporting Information is available from the Wiley Online Library or from the author.

Acknowledgements

Ángela Sastre Santos thanks the Ministerio de Economía, Industria y Competitividad of Spain and FEDER funds by finantial support (CTQ2017-

87102-R). Maria João Álvaro-Martins thanks to "Beca Santiago Grisolia Grisolia 20177153" Comunidad Valenciana. Desiré Molina thanks the European Union through the "Programa Operativo del Fondo Social Europeo (FSE) de la Comunitat Valenciana 2014-2020". This work was supported by the Solar technologies Go Hybrid (SolTech) initiative of the Bavarian State Government. Ilias Papadopoulos and Maria João Álvaro-Martins contributed equally to this work (‡).

Received: ((will be filled in by the editorial staff))
Revised: ((will be filled in by the editorial staff))
Published online: ((will be filled in by the editorial staff))

References

[1] M. B. Smith, J. Michl, *Chem. Rev.* **2010**, *110*, 6891–6936.
[2] M. B. Smith, J. Michl, *Annu. Rev. Phys. Chem.* **2013**, *64*, 361–386.
[3] K. Miyata, F. S. Conrad-Burton, F. L. Geyer, X.-Y. Zhu, *Chem. Rev.* **2019**, *119*, 4261–4292.
[4] D. Casanova, *Chem. Rev.* **2018**, *118*, 7164–7207.
[5] B. S. Basel, I. Papadopoulos, D. Thiel, R. Casillas, J. Zirzlmeier, T. Clark, D. M. M. Guldi, R. R. R. Tykwinski, *Trends Chem.* **2019**, *1*, 11–21.
[6] S. Ito, T. Nagami, M. Nakano, *J. Photochem. Photobiol. C Photochem. Rev.* **2018**, *34*, 85–120.
[7] N. Monahan, X.-Y. Zhu, *Annu. Rev. Phys. Chem.* **2015**, *66*, 601–618.
[8] C. Hetzer, D. M. Guldi, R. R. Tykwinski, *Chem. - A Eur. J.* **2018**, *24*, 8245–8257.
[9] M. Tuan Trinh, A. Pinkard, A. B. Pun, S. N. Sanders, E. Kumarasamy, M. Y. Sfeir, L. M. Campos, X. Roy, X. Y. Zhu, *Sci. Adv.* **2017**, *3*, e1700241.
[10] W. Shockley, H. J. Queisser, *J. Appl. Phys.* **1961**, *32*, 510–519.
[11] M. C. Hanna, A. J. Nozik, *J. Appl. Phys.* **2006**, *100*, 074510.
[12] S. R. Yost, J. Lee, M. W. B. Wilson, T. Wu, D. P. McMahon, R. R. Parkhurst, N. J. Thompson, D. N. Congreve, A. Rao, K. Johnson, et al., *Nat. Chem.* **2014**, *6*, 492–497.
[13] J. C. Johnson, T. H. Reilly, A. C. Kanarr, J. van de Lagemaat, *J. Phys. Chem. C* **2009**, *113*, 6871–6877.
[14] H. Marciniak, I. Pugliesi, B. Nickel, S. Lochbrunner, *Phys. Rev. B - Condens. Matter Mater. Phys.* **2009**, *79*, 235318.
[15] M. W. B. Wilson, A. Rao, J. Clark, R. S. S. Kumar, D. Brida, G. Cerullo, R. H. Friend, *J. Am. Chem. Soc.* **2011**, *133*, 11830–11833.
[16] B. J. Walker, A. J. Musser, D. Beljonne, R. H. Friend, *Nat. Chem.* **2013**, *5*, 1019–1024.
[17] P. M. Zimmerman, C. B. Musgrave, M. Head-Gordon, *Acc. Chem. Res.* **2013**, *46*, 1339–1347.
[18] J. C. Johnson, A. J. Nozik, J. Michl, *Acc. Chem. Res.* **2013**, *46*, 1290–1299.
[19] X. Feng, A. V. Luzanov, A. I. Krylov, *J. Phys. Chem. Lett.* **2013**, *4*, 3845–3852.
[20] S. M. Parker, T. Seideman, M. A. Ratner, T. Shiozaki, *J. Phys. Chem. C* **2014**, *118*, 12700–12705.
[21] G. B. Piland, J. J. Burdett, R. J. Dillon, C. J. Bardeen, *J. Phys. Chem. Lett.* **2014**, *5*, 2312–2319.
[22] W. L. Chan, M. Ligges, A. Jailaubekov, L. Kaake, L. Miaja-Avila, X. Y. Zhu, *Science (80-.).* **2011**, *334*, 1541–1545.
[23] S. Lukman, K. Chen, J. M. Hodgkiss, D. H. P. Turban, N. D. M. Hine, S. Dong, J. Wu, N. C. Greenham, A. J. Musser, *Nat. Commun.* **2016**, *7*, 13622.
[24] S. Lukman, A. J. Musser, K. Chen,

S. Athanasopoulos, C. K. Yong, Z. Zeng, Q. Ye, C. Chi, J. M. Hodgkiss, J. Wu, et al., *Adv. Funct. Mater.* **2015**, *25*, 5452–5461.
[25] M. Chen, Y. J. Bae, C. M. Mauck, A. Mandal, R. M. Young, M. R. Wasielewski, *J. Am. Chem. Soc.* **2018**, *140*, 9184–9192.
[26] C. Mauck, K. Brown, N. Horwitz, M. R. Wasielewski, *J. Phys. Chem. A* **2015**, *119*, 5587–5596.
[27] J. C. Johnson, A. Akdag, M. Zamadar, X. Chen, A. F. Schwerin, I. Paci, M. B. Smith, Z. Havlas, J. R. Miller, M. A. Ratner, et al., *J. Phys. Chem. B* **2013**, *117*, 4680–4695.
[28] J. Zirzlmeier, R. Casillas, S. R. Reddy, P. B. Coto, D. Lehnherr, E. T. Chernick, I. Papadopoulos, M. Thoss, R. R. Tykwinski, D. M. Guldi, *Nanoscale* **2016**, *8*, 10113–10123.
[29] I. Papadopoulos, J. Zirzlmeier, C. Hetzer, Y. J. Bae, M. D. Krzyaniak, M. R. Wasielewski, T. Clark, R. R. Tykwinski, D. M. Guldi, *J. Am. Chem. Soc.* **2019**, *141*, 6191–6203.
[30] B. S. Basel, R. M. Young, M. D. Krzyaniak, I. Papadopoulos, C. Hetzer, Y. Gao, N. T. La Porte, B. T. Phelan, T. Clark, R. R. Tykwinski, et al., *Chem. Sci.* **2019**, *10*, 11130–11140.
[31] J. Zirzlmeier, D. Lehnherr, P. B. Coto, E. T. Chernick, R. Casillas, B. S. Basel, M. Thoss, R. R. Tykwinski, D. M. Guldi, *Proc. Natl. Acad. Sci.* **2015**, *112*, 5325–5330.
[32] B. S. Basel, J. Zirzlmeier, C. Hetzer, B. T. Phelan, M. D. Krzyaniak, S. R. Reddy, P. B. Coto, N. E. Horwitz, R. M. Young, F. J. White, et al., *Nat. Commun.* **2017**, *8*, 15171.
[33] E. Kumarasamy, S. N. Sanders, M. J. Y. Tayebjee, A. Asadpoordarvish, T. J. H. Hele, E. G. Fuemmeler, A. B. Pun, L. M. Yablon, J. Z. Low, D. W. Paley, et al., *J. Am. Chem. Soc.* **2017**, *139*, 12488–12494.
[34] S. N. Sanders, E. Kumarasamy, A. B. Pun, M. T. Trinh, B. Choi, J. Xia, E. J. Taffet, J. Z. Low, J. R. Miller, X. Roy, et al., *J. Am. Chem. Soc.* **2015**, *137*, 8965–8972.
[35] S. N. Sanders, E. Kumarasamy, A. B. Pun, M. L. Steigerwald, M. Y. Sfeir, L. M. Campos, *Chem* **2016**, *1*, 505–511.
[36] S. W. Eaton, L. E. Shoer, S. D. Karlen, S. M. Dyar, E. A. Margulies, B. S. Veldkamp, C. Ramanan, D. A. Hartzler, S. Savikhin, T. J. Marks, et al., *J. Am. Chem. Soc.* **2013**, *135*, 14701–14712.
[37] K. Nagarajan, A. R. Mallia, V. S. Reddy, M. Hariharan, *J. Phys. Chem. C* **2016**, *120*, 8443–8450.
[38] A. K. Le, J. A. Bender, S. T. Roberts, *J. Phys. Chem. Lett.* **2016**, *7*, 4922–4928.
[39] Y. V. Aulin, K. M. Felter, D. D. Günbas, R. K. Dubey, W. F. Jager, F. C. Grozema, *Chempluschem* **2018**, *83*, 230–238.
[40] A. K. Le, J. A. Bender, D. H. Arias, D. E. Cotton, J. C. Johnson, S. T. Roberts, *J. Am. Chem. Soc.* **2018**, *140*, 814–826.
[41] C. Schierl, A. Niazov-Elkan, L. J. W. Shimon, Y. Feldman, B. Rybtchinski, D. M. Guldi, *Nanoscale* **2018**, *10*, 20147–20154.
[42] K. M. Lefler, K. E. Brown, W. A. Salamant, S. M. Dyar, K. E. Knowles, M. R. Wasielewski, *J. Phys. Chem. A* **2013**, *117*, 10333–10345.
[43] E. A. Margulies, J. L. Logsdon, C. E. Miller, L. Ma, E. Simonoff, R. M. Young, G. C. Schatz, M. R. Wasielewski, *J. Am. Chem. Soc.* **2017**, *139*, 663–671.
[44] S. W. Eaton, S. A. Miller, E. A. Margulies, L. E. Shoer, R. D. Schaller, M. R. Wasielewski, *J. Phys. Chem. A* **2015**, *119*, 4151–4161.
[45] P. E. Hartnett, E. A. Margulies, C. M. Mauck, S. A. Miller, Y. Wu, Y.-L. Wu, T. J. Marks, M. R. Wasielewski, *J. Phys. Chem. B* **2016**, *120*, 1357–1366.
[46] C. M. Mauck, P. E. Hartnett, E. A. Margulies, L. Ma, C. E. Miller, G. C. Schatz, T. J. Marks, M. R. Wasielewski, *J. Am. Chem. Soc.* **2016**, *138*, 11749–11761.
[47] C. E. Miller, M. R. Wasielewski, G. C. Schatz, *J. Phys. Chem. C* **2017**, *121*, 10345–10350.

[48] T. Mukhopadhyay, A. J. Musser, B. Puttaraju, J. Dhar, R. H. Friend, S. Patil, *J. Phys. Chem. Lett.* **2017**, *8*, 984–991.
[49] C. M. Mauck, P. E. Hartnett, Y. L. Wu, C. E. Miller, T. J. Marks, M. R. Wasielewski, *Chem. Mater.* **2017**, *29*, 6810–6817.
[50] C. M. Mauck, Y. J. Bae, M. Chen, N. Powers-Riggs, Y.-L. Wu, M. R. Wasielewski, *ChemPhotoChem* **2018**, *2*, 223–233.
[51] L. Shen, Z. Tang, X. Wang, H. Liu, Y. Chen, X. Li, *Phys. Chem. Chem. Phys.* **2018**, *20*, 22997–23006.
[52] M. Grzybowski, D. T. Gryko, *Adv. Opt. Mater.* **2015**, *3*, 280–320.
[53] D. Chandran, K.-S. Lee, *Macromol. Res.* **2013**, *21*, 272–283.
[54] H. Langhals, T. Potrawa, H. Nöth, G. Linti, *Angew. Chemie Int. Ed. English* **1989**, *28*, 478–480.
[55] H. Bürckstümmer, A. Weissenstein, D. Bialas, F. Würthner, *J. Org. Chem.* **2011**, *76*, 2426–2432.
[56] J. Dhar, D. P. Karothu, S. Patil, *Chem. Commun.* **2015**, *51*, 97–100.
[57] J. Calvo-Castro, M. Warzecha, A. R. Kennedy, C. J. McHugh, A. J. McLean, *Cryst. Growth Des.* **2014**, *14*, 4849–4858.
[58] M. A. Naik, S. Patil, *J. Polym. Sci. Part A Polym. Chem.* **2013**, *51*, 4241–4260.
[59] B. Tieke, A. R. Rabindranath, K. Zhang, Y. Zhu, *Beilstein J. Org. Chem.* **2010**, *6*, 830–845.
[60] S. Qu, H. Tian, *Chem. Commun.* **2012**, *48*, 3039.
[61] C. B. Nielsen, M. Turbiez, I. McCulloch, *Adv. Mater.* **2013**, *25*, 1859–1880.
[62] Y. Li, P. Sonar, L. Murphy, W. Hong, *Energy Environ. Sci.* **2013**, *6*, 1684.
[63] M. Kaur, D. H. Choi, *Chem. Soc. Rev.* **2015**, *44*, 58–77.
[64] S. Loser, C. J. Bruns, H. Miyauchi, R. P. Ortiz, A. Facchetti, S. I. Stupp, T. J. Marks, *J. Am. Chem. Soc.* **2011**, *133*, 8142–8145.
[65] A. Tang, C. Zhan, J. Yao, E. Zhou, *Adv. Mater.* **2017**, *29*, 1600013.
[66] Y. Geng, A. Tang, K. Tajima, Q. Zeng, E. Zhou, *J. Mater. Chem. A* **2019**, *7*, 64–96.
[67] S. Masoomi-Godarzi, M. Liu, Y. Tachibana, L. Goerigk, K. P. Ghiggino, T. A. Smith, D. J. Jones, *Adv. Energy Mater.* **2018**, *8*, 1801720.
[68] D. Sahu, C.-H. Tsai, H.-Y. Wei, K.-C. Ho, F.-C. Chang, C.-W. Chu, *J. Mater. Chem.* **2012**, *22*, 7945.
[69] J. Yang, F. Zhu, W. Chen, B. Li, L. Zhang, R. Xie, *J. Chem. Res.* **2005**, *2005*, 184–186.
[70] E. Zhou, S. Yamakawa, K. Tajima, C. Yang, K. Hashimoto, *Chem. Mater.* **2009**, *21*, 4055–4061.
[71] A. T. Yiu, P. M. Beaujuge, O. P. Lee, C. H. Woo, M. F. Toney, J. M. J. Fréchet, *J. Am. Chem. Soc.* **2012**, *134*, 2180–2185.
[72] S.-Y. Liu, D.-G. Wang, A.-G. Zhong, H.-R. Wen, *Org. Chem. Front.* **2018**, *5*, 653–661.
[73] S. Grimme, J. Antony, S. Ehrlich, H. Krieg, *J. Chem. Phys.* **2010**, *132*, 154104.
[74] S. Grimme, S. Ehrlich, L. Goerigk, *J. Comput. Chem.* **2011**, *32*, 1456–1465.
[75] H. Kruse, S. Grimme, *J. Chem. Phys.* **2012**, *136*, 154101.
[76] L. Goerigk, N. Mehta, *Aust. J. Chem.* **2019**, *72*, 563.
[77] F. Jensen, *Wiley Interdiscip. Rev. Comput. Mol. Sci.* **2013**, *3*, 273–295.
[78] R. Ditchfield, W. J. Hehre, J. A. Pople, *J. Chem. Phys.* **1971**, *54*, 724–728.
[79] K. C. Krishnapriya, P. Roy, B. Puttaraju, U. Salzner, A. J. Musser, M. Jain, J. Dasgupta, S. Patil, *Nat. Commun.* **2019**, *10*, 33.
[80] A solvent change to benzonitrile did lead to no significant differences (**Figure S1**).
[81] N. J. Hestand, F. C. Spano, *Chem. Rev.* **2018**, *118*, 7069–7163.
[82] E. A. Margulies, L. E. Shoer, S. W. Eaton, M. R. Wasielewski, *Phys. Chem. Chem. Phys.* **2014**, *16*, 23735–23742.

[83] H. Yamagata, C. M. Pochas, F. C. Spano, *J. Phys. Chem. B* **2012**, *116*, 14494–14503.
[84] J. P. Mora-Fuentes, I. Papadopoulos, D. Thiel, R. Álvarez-Boto, D. Cortizo-Lacalle, T. Clark, M. Melle-Franco, D. M. Guldi, A. Mateo-Alonso, *Angew. Chemie Int. Ed.* **2020**, *59*, 1113–1117.
[85] N. V Korovina, J. Joy, X. Feng, C. Feltenberger, A. I. Krylov, S. E. Bradforth, M. E. Thompson, *J. Am. Chem. Soc.* **2018**, *140*, 10179–10190.
[86] Please note that the time resolution of our setup of 200 ps hampers accuracy in some cases.
[87] B. S. Basel, J. Zirzlmeier, C. Hetzer, S. R. Reddy, B. T. Phelan, M. D. Krzyaniak, M. K. Volland, P. B. Coto, R. M. Young, T. Clark, et al., *Chem* **2018**, *4*, 1092–1111.
[88] E. A. Margulies, C. E. Miller, Y. Wu, L. Ma, G. C. Schatz, R. M. Young, M. R. Wasielewski, *Nat. Chem.* **2016**, *8*, 1120–1125.
[89] ($T_1 + T_1$) formation of less than 100 ns hamper any meaningful investigations based on time-resolved EPR.

Subphthalocyanine-Diketopyrrolopyrrole Conjugates: 3D Star-Shaped Systems as Non-Fullerene Acceptors in Polymer Solar Cells with High Open-Circuit Voltage

Maria J. Álvaro-Martins,[a] José G. Sánchez,[b] Giulia Lavarda,[c] Desiré Molina,[a] Josep Pallarès,[b] Tomás Torres, * [c,d,e] Lluis F. Marsal*[b] and Ángela Sastre-Santos*[a]

Dedicated to Prof. Dr. Nazario Martín on the occasion of his 65th birthday.

[a] M. J. Álvaro-Martins, Dr. D. Molina, Prof. Á. Sastre-Santos
Instituto de Bioingeniería, Universidad Miguel Hernández,
03202 Elche, Spain,
E-mail: asastre@umh.es.
[b] Dr. J. G. Sánchez, Dr. J. Pallarès, Prof. Lluis Marsal
Departament d'Enginyeria Electronica Electrica i Automatica
Universitat Rovira i Virgili, 43007 Tarragona, Spain,
E-mail: lluis.marsal@urv.cat
[c] G. Lavarda, Prof. T. Torres
Departamento de Química Orgánica,
Universidad Autónoma de Madrid, Spain,
E-mail: tomas.torres@uam.es.
[d] Prof. T. Torres
IMDEA-Nanociencia
Campus de Cantoblanco, 28049 Madrid (Spain)
[e] Prof. T. Torres
Institute for Advanced Research in Chemical Sciences (IAdChem),
Universidad Autónoma de Madrid, Spain

Abstract: Four novel star-shaped electron acceptors [***C*$_1$-OPh 1**, ***C*$_3$-OPh 2**, ***C*$_1$-Cl 3** and ***C*$_3$-Cl 4**] based on a subphthalocyanine core bearing three diketopyrrolopyrrole wings linked by an acetylene bridge have been synthesized. These derivatives feature two different axial substituents [*i.e.*, 4-*tert*-butylphenoxy (OPh) or chlorine (Cl)] and for each of them, both the C_1 and the C_3 regioisomers have been investigated. The four compounds exhibit a broad absorption band in the 450-700 nm region, with bandgap values near to 2 eV. These materials were applied in the active layer of inverted bulk-heterojunction polymer solar cells in combination with the donor polymer PBDB-T. Derivatives bearing the OPh axial group showed the best performances, being ***C1-OPh 1*** the most intriguing of them with a PCE of 3.27% and a V_{oc} as high as 1.17 V. Despite presenting the widest absorption range, the photovoltaic results obtained with ***C1-Cl 3*** turned out to be the lowest (PCE = 1.01%).

Introduction

Bulk-heterojunction (BHJ) polymer solar cells have shown great potential for the fabrication of lightweight, flexible and transparent devices with low-cost manufacturing.[1] In conventional BHJ-polymer solar cells, indium tin oxide (ITO) is used as the anode, whereas poly(3,4-ethylenedioxy-thiophene):poly(styrenesulfonate) (PEDOT:PSS) and calcium are used as the hole-transporting layer (HTL) and the electron-transporting layer (ETL), respectively.[2] On the other hand, in BHJ-polymer solar cells with inverted structure, ITO acts as the cathode, calcium is replaced by titanium oxide (TiO_2), [3] zinc oxide (ZnO)[4] or poly[(9,9-bis(3-(*N,N*-dimethylamino) propyl)-2,7-fluorene)-alt-

2,7-(9,9 dioctylfluorene)] (PFN)[5] as ETL, meanwhile PEDOT:PSS is replaced by vanadium oxide (V_2O_5)[6] or molybdenum oxide (MoO_3)[7] as HTL. In the last years, electron-accepting fullerenes such as [6,6]-phenyl-C_{70}-butyric acid methyl ester ($PC_{70}BM$) or bis (1-[3-(methoxycarbonyl)propyl]-1-phenyl)-[6,6]C_{62} (Bis-PCBM) have led the polymer solar cells field since they allow for the preparation of highly efficient devices.[8] Nonetheless, the weak absorption in the visible region and poor ambient stability of fullerene materials limit the performance and lifetime of polymer solar cells. Moreover, the high electron affinity of fullerenes limits the open-circuit voltage to values below 1 volt.[9] To overcome these disadvantages, several non-fullerene acceptors (NFA) materials are being developed, which are attracting much attention by virtue of their low energy loss, strong absorption in the visible range, good thermal stability, and lower-cost synthesis with respect to fullerene acceptors.[10] A successful approach for the preparation of NFA materials consists in the synthesis of trimeric and tetrameric species to mimic the spherical shape of the fullerene π-system,[11 which is assumed to be capable of aligning with the donor π-plane in a three-dimensional (3D) way decreasing the Coulomb barrier for charge separation due to enhanced entropic effects, thus enabling isotropic charge transport compared to one-dimensional.[12]

Due to their unusual characteristics, subphthalocyanines (SubPcs) and diketopyrrolopyrroles (DPPs) stand out among other chromophores for the preparation of NFA materials.[13] SubPcs are aromatic chromophores with 14 delocalized π-electrons and a boron atom at their central cavity. These derivatives have been widely investigated in organic solar cells (OSCs) because of their interesting optical and electronic properties, such as strong optical absorptions in the 460–580 nm spectral region, and relatively high electron mobilities. Besides, their cone-shaped structure prevents aggregation in solution and even in the solid-state.[14] Traditionally, they have been applied as electron donors in BHJ organic solar cells,[15] although it has been shown that they can also act as electron acceptors in solution-processed BHJ devices.[11a,b,16] Thus, a 8.4% PCE record is held by Cnops when they fabricated three-layer vacuum-deposited devices, combining two[17] Regarding solution-processed devices, SubPc-cores funcionalized with three imide groups resulted in a maximum efficiency of 4.92%, using the polymer PM6 as donor counterpart.[18]

On the other hand, DPPs are well-known building blocks characterized by great synthetic versatility, high physical and chemical stability, and outstanding optoelectronic properties, such as intense radiation absorption in the visible spectrum and high fluorescence quantum yields.[19] The usual chemical structure of these moieties includes a central electron-attracting bicyclic-dilactam core flanked by two aromatic rings (*e.g.* benzene, thiophene, furan, selenophene, etc.). The flat structure of the DPP-core leads to significant π-π interactions and the dihedral angle that these rings form concerning the core influences the final morphology of the systems where they are integrated. By virtue of these characteristics, these moieties have also been extensively investigated in BHJ OSCs, as both donor and acceptor systems.[20] Herein, we have designed and synthesized four new NFAs that combine SubPcs and DPPs into 3D star-shaped structures (**Scheme 1**). The four acceptors present two main structural differences. First, two of them feature a *tert*-

butylphenoxy group (OPh) in the axial position of the SubPc macrocycle (*i.e.* ***C*$_1$-OPh 1** and ***C*$_3$-OPh 2**), whereas the other two bear a chlorine (Cl) atoms in the same position (*i.e.* ***C*$_1$-Cl 3** and ***C*$_3$-Cl 4**). Besides, for each axial ligand, both the C_1- and the C_3-symmetric regioisomers have been prepared. The solid-state morphology within the donor-acceptor blend and the optoelectronic properties of the materials are strongly influenced by these structural features (*vide infra*), which ultimately affect the photovoltaic performances of the devices based on these derivatives. With the aim to elucidate which structural features of the NFAs are the most favourable for their application in BHJ OSCs, we studied these acceptor systems blended with the electron-donating polymer poly[(2,6-(4,8-bis(5-(2-ethylhexyl)thiophen-2-yl)-benzo[1,2-b:4,5-b']dithiophene))alt-(5,5-(1',3'-di-2-thienyl-5',7'-bis(2-ethylhexyl)benzo[1',2'c:4',5'-c']dithiophene-4,8-dione)] (PBDB-T) in BHJ-inverted polymer solar cells. PBDB-T was chosen as donor material due to its complementary absorption band and deep HOMO level, which allow to obtain higher circuit current density (J_{SC}) and V_{OC}, respectively, in devices fabricated with subphthalocyanine acceptors. The BHJ-inverted polymer solar cells were fabricated using ITO as the cathode, TiO_2 as the ETL, V_2O_5 as the HTL, and silver (Ag) as the anode (ITO/TiO_2/PBDB-T:-SubPc(DPP)$_3$/V_2O_5/Ag). The effects of the 1,8-diiodooctane (DIO) additive concentration and annealing temperature on the performance of the devices were also analysed. Remarkably, compound ***C*$_1$-Cl 3** showed the lowest parameters, despite its wide absorbance range. On the other hand, ***C*$_1$-OPh 1** turned out to be the best the candidate among the series for application as NFA in BHJ solar cells. The J_{SC} trend calculated from the current density-voltage (*J*) curves is corroborated by the integrated J_{SC} calculated from the external quantum efficiency (EQE) spectrum for all devices.

Results and Discussion

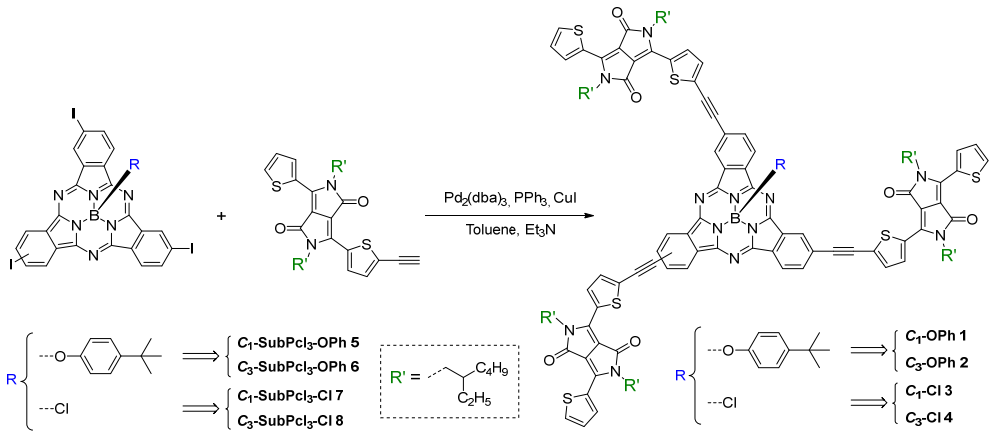

Scheme 1. Synthetic scheme for the preparation of SubPc-(DPP)$_3$ derivatives **1-4**.

The chemical structures of the four derivatives were confirmed by ^{1}H NMR, ^{11}B NMR and FT-IR spectroscopies as well as by MALDI-TOF mass spectrometry (see the supporting information, **Figure S1-16**). The ^{1}H NMR spectra of the C_1-symmetric

derivatives, *i.e.* ***C*$_1$-OPh 1** and ***C*$_1$-Cl 3**, have a similar profile. The same applies for C_3-symmetric derivatives ***C*$_3$-OPh 2** and ***C*$_3$-Cl 4.** A slightly shift towards lower fields of the protons around 8.0 ppm and 8.8-8.9 ppm corresponding to the SubPc ring was observed comparing the **SubPc-Cl 3** and **4** with their analogues with the phenoxy group in the axial position **1** and **2** (**Figure S15**). Spectra of ***C*$_1$-OPh 1** and ***C*$_3$-OPh 2** show slight differences in the aromatic region, namely for the signals between 8.84-8.80 ppm belonging to the DPP units, which appear for ***C*$_1$-OPh 1** in the form of two overlapping doublets centered at 8.83 ppm and 8.82 ppm and for **C$_3$-OPh 2** as two doublet of doublets centered at 8.81 ppm (Figure S13). Such unresolved signals in the spectrum of ***C*$_1$-OPh 1** are indicative of a rupture of the symmetry environment, which give rise to a more complex pattern.[21] In the case of the ***C*$_1$-Cl 3** and ***C*$_3$-Cl 4** spectra, the same behaviour was observed (Figure S14). Regarding to ^{11}B NMR spectra, a single singlet signal was observed in all spectra. Appearing at -14.60 ppm for OPh derivatives and-12.9 and -13.9 ppm for ***C*$_1$-Cl 3** and ***C*$_1$-Cl 4**, respectively.

Optical and electronic properties

The absorption features of all these SubPc-DPP derivatives measured in $CHCl_3$ solutions are shown in Figure 1a-1d and Table 1. All the acceptor materials show absorption bands in the ultraviolet (250-450 nm) and the visible/near IR (450-700 nm) regions of the spectra, **Figure 1a-1b**. The spectra of ***C*$_1$-OPh 1**, ***C*$_3$-OPh 2** and ***C*$_3$-Cl 4** present the characteristic shape typically observed for SubPc chromophores, showing maxima at 654, 623, 624 nm, respectively. Besides, all three spectra exhibit a shoulder attributable to the DPP units at 553, 550, and 554 nm, respectively. Differently, the UV-vis spectrum of ***C*$_1$-Cl 3** shows a broader Q-band at 592 nm with a molar extinction coefficient lower than the other derivatives (**Figure 1d, Table 1**). We infer that the existence of orbital overlap between the chromophoric units in ***C*$_1$-Cl 3** could lead to a strong interaction in the ground state. In comparison with the corresponding reference compounds (**DPP Ref**., **SubPc 5**, **6**, **7** and **8**) the four acceptors suffered a red-shift of the Q-band. ***C*$_3$-OPh 2** suffered the largest displacement (*i.e.* 54 nm) and ***C*$_1$-Cl 3** the smallest red-shift (*i.e.* 19 nm) (**Figure 1b-1c**). The bathochromic shift of the Soret and Q bands of the acceptors in comparison with the corresponding SubPc reference compounds is due to the increasing of the π-conjugation of the ring by the substitution of the peripheral positions of the SubPc core with three DPP units, **Figure 1b-1c**.[22] In films, the absorbance peaks of the four acceptors showed a broader shape due to the aggregation of the compounds in solid-state.

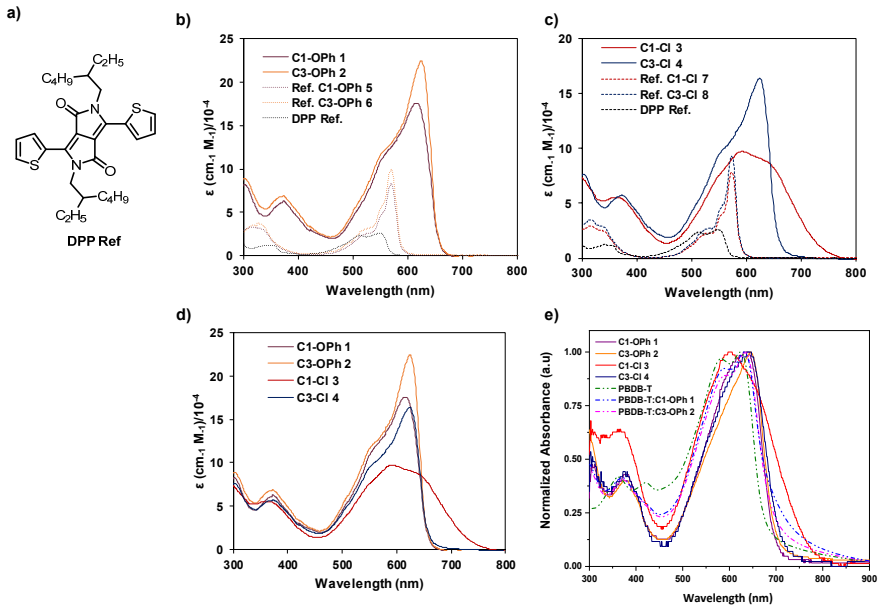

Figure 1. a) Chemical structure of DPP Ref. Absorption spectra of: b) ***C*1-OPh 1**, ***C*3-OPh 2** (solid lines) and the corresponding precursors ***C*1-SubPcl3-OPh 5** and ***C*3-SubPcl3-OPh 6** (dashed lines) in $CHCl_3$. c) ***C*1-Cl 3**, ***C*3-Cl 4** (solid lines) and the corresponding precursors ***C*1-SubPcl3-OPh 7** and ***C*3-SubPcl3-OPh 8** (dashed lines) in $CHCl_3$. d) Derivatives **1-4** in $CHCl_3$. e) Derivatives **1-4** and blend PBDb-T:**C1-OPh 1** y PBDB-T:**C3-OPh 2** in film .

Table 1- Optical and electrochemical parameters of the compounds under study.

	*C*X-R	Absorbance λ_{max} [nm]/ log(ε) [a]	Absorbance in film λ_{max} [nm]	Emission λ_{max} [nm] [a]	E_g^{opt} [eV][b]	E_{red1} [eV][c]	LUMO [eV] [d]	HOMO [eV] [e]	μ_e [$cm^2 V^{-1} s^{-1}$]
1	***C*1-OPh**	616/5.24	637	645	1.95	-1.01	-3.79	-5.74	$1.9x10^{-5}$
2	***C*3-OPh**	623/5.35	646	645	1.95	-1.06	-3.74	-5.69	$1.7x10^{-5}$
	***C*1-Cl 3**	592/4.99	602	615	2.04	-1.43	-3.37	-5.41	--
	***C*3-Cl 4**	624/5.21	642	641	1.96	-1.40	-3.40	-5.36	--

[a] Absorption and emission spectra were measured in $CHCl_3$. [b] E_g^{opt} was determined from the intersection of absorption and normalized emission spectra registered in $CHCl_3$ (E_g^{opt}= 1240/λ [eV]). [c] Redox potentials were measured in CH_2Cl_2 with 0.1 M Bu_4NPF_6 vs. Fc/Fc^+, with graphite counter electrode and $Ag/AgNO_3$ as reference electrode. [d] LUMO was calculated by LUMO= - $\left| E_{red1} \text{ (vs. } Fc/Fc^+) + 4.8 \right|$. [e] HOMO was calculated by HOMO= LUMO - E_g^{opt} (eV).

The absorption bands in films of ***C*1-OPh 1**, ***C*3-2**, ***C*1-Cl 3** and ***C*3-Cl 4** are centered at 637 nm, 646 nm, 602 nm and 642 nm, respectively, which result in a red-shift of 21 nm, 23 nm, 10 nm and 18 nm relative to the absorption peaks in solution. The bigger red-shift found for ***C*3-OPh 2** may be associated with a stronger intermolecular aggregation in the solid state**.** The steady-state photoluminescence spectra of the four new acceptors were measured in $CHCl_3$ (**FigureS16** and **Table 1**). As observed in absorption measurements, compound ***C*1-Cl 3** had a broader emission spectrum, suggesting

a higher tendency toward aggregation in solution than the other compounds. Stokes shift of all compounds vary between 17 and 29 nm, being ***C*$_3$-Cl 4** the compound with the lowest Stokes shift and ***C*$_1$-OPh 1** the one with the highest.

The HOMO and LUMO energy levels of the four acceptors were established by cyclic voltammetry (CV) and estimated using the onset values of reduction and oxidation potentials (**Figure S17**). To calculate LUMO levels, the following equation was used: LUMO= - $\left| E_{red1} \text{ (vs. Fc/Fc}^{+}) + 4.8 \right|$. HOMO was calculated as HOMO= LUMO- E_g^{opt}. The derivatives with a OPh group in the axial position did not show great differences between them. For ***C*$_1$-OPh 1** and ***C*$_3$-OPh 2** LUMO values of -3.79 eV and -3.74 eV and HOMO values of -5.74 eV and -5.69 eV were estimated, respectively. Something similar was observed for derivatives with Cl in the axial position, with LUMO values of -3.37 eV and -3.40 eV for ***C*$_1$-Cl 3** and ***C*$_3$-Cl 4,** respectively. HOMO values of -5.41 eV and -5.36 eV were estimated for ***C*$_1$-Cl 3** and ***C*$_3$-Cl 4**, respectively, **Figure 2a**. Cl derivatives showed higher reduction potential values in the module compared to OPh derivatives values.

Photovoltaics

To evaluate the photovoltaic properties of the SubPc(DPP)$_3$-based acceptors, OSCs based on SubPc(DPP)$_3$ derivatives were fabricated using the inverted structure ITO/TiO_2/PBDB-T:SubPc(DPP)$_3$/V_2O_5/Ag. The energy levels of the different constituents used in the fabrication of solar devices are compiled in **Figure 2a**. The LUMO levels of the new acceptor materials are well aligned with the LUMO value of the donor polymer PBDB-T (**Figure 2b**). Nevertheless, it appears that the HOMO values of the derivatives with chlorine atoms in the axial position could accept holes from the environment, which could lead to a higher probability of recombination phenomena. The PBDB-T:SubPc(DPP)$_3$ devices were optimized in terms of annealing temperature, spin-casting

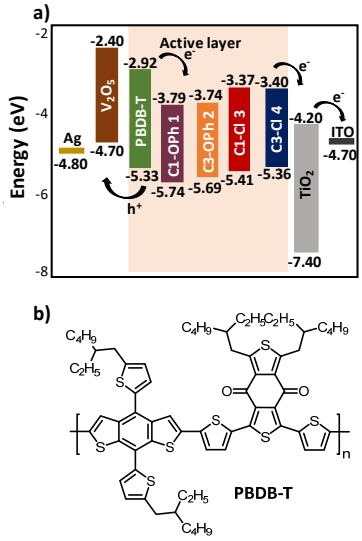

Figure 2. a) Energy levels diagram for the device layers. b) Donor polymer PBDB-T.

speed, DIO additive concentration, and donor/acceptor (D/A) ratio. ***C1-OPh 1*** and ***C3-OPh 2*** showed higher solubility in chlorobenzene comparing to ***C1-Cl 3*** and ***C3-Cl 4***. Among the four NFAs, ***C1-Cl 3*** had the poorest solubility in chlorobenzene, so that PBDB-T: ***C1-Cl 3*** was heated up to 80 °C till yielding a homogenous solution. The results of the OSCs optimization are summarized in Tables S1-S9 in the Supporting Information. The J_{SC} of OSCs increases when annealed up to 100 °C in comparison to devices without annealing. Nevertheless, by increasing the annealing temperature to 160 °C the J_{SC} of devices decreased. These results agree to the J_{SC} behaviour due to annealing temperature effect on inverted OSCs based on PBDB-T.[23] Li *et al*. reported that J_{SC} of PBDB-T:IT-M-based OSCs decreases because of a diffuse interface between PBDB-T and IT-M due to

the large correlation length of PBDB-T when annealed at 160 °C.[24]

On the other hand, the performance of the devices increased as the concentration of DIO in chlorobenzene decreased from 2 to 0.5 %. However, the devices made without DIO additive showed the lowest performance with respect to the devices with DIO. **Figure 3a** shows the current density-voltage *(J*-V*)* curves of the best-performing optimized devices, whereas the best and average (parenthesis) values of performance characteristics are summarized in **Table 2**. The devices parameters were averaged over eight devices.

The devices made with OPh derivatives exhibited higher performance parameters than those constituted by SubPc(DPP)$_3$-Cl, having obtained the best performance with ***C*$_1$-OPh 1** devices and the worst with ***C*$_1$-Cl 3** which presented an efficiency of 3.17% and 1.01%, respectively.

In detail, for the SubPc(DPP)$_3$-OPh based OSCs similar performances were obtained for the two regioisomers C_1 and C_3. Nevertheless, the devices made with ***C*$_1$-OPh 1**, with a J_{SC} of 6.42 mA cm^{-2}, a V_{OC} of 1.17 V and a FF of 42.16%, proved to be slightly better than those based on ***C*$_3$-OPh 2** derivative (3.17% *vs* 2.83%, respectively). However, this similarity was not gained with Cl derivatives since with the C_3 regioisomer an efficiency twice greater than that obtained with C_1 was achieved. This result indicates that the symmetry of the peripheral substitution pattern influences the performance of OSCs when using a chloride atom in the axial position. For comparison, the BHJ-inverted polymer solar cells device based on PBDB-T:PC60BM (PC60BM from Solenne BV) was fabricated in the same conditions than SubPc(DPP)$_3$-based devices. The *J*-V characteristic under the illumination of PBDB-T:PC60BM and its performance parameters are shown in **Figure S23**.
The devices based on the conventional PC60BM exhibited a V_{OC} of 0.80V, a J_{SC} of 12.99 mA/cm^2, a FF of 48.70%, and a PCE of 5.09%. PC60BM-based devices shown a higher PCE (which is attributed to its higher J_{SC} value), and a slightly improved FF. As expected, the PC60BM-based device exhibited lower V_{OC} than that of SubPc(DPP)$_3$-based devices due to its lower LUMO value.

A pertinent result of the study of SubPc(DPP)$_3$-derivatives in OSCs was the high V_{OC} values than were achieved. Excluding ***C*$_1$-Cl 3**, all the other derivatives presented V_{oc} values higher than 1 V. These values stand out in relation to other published in the literature although the efficiencies obtained were not so high as intended.[25] The external quantum efficiency (EQE) spectra of the best-performing optimized devices are displayed in **Figure 3b**. All the OSCs exhibited broad EQE spectra from 300 to 800 nm as a result of the absorption of PBDB-T and the SubPc(DPP)$_3$ acceptors. In the range of 450-500 nm the EQE spectra suffered a slightly decrease since the SubPc(DPP)$_3$ acceptors have a limited absorption over this range (**Figure 3b**). The J_{SC} values determined by integrating of the EQE spectra were 6.83 mA cm^{-2} for PBDB-T:***C*$_1$-OPh 1**, 6.03 mA cm^{-2} for PBDB-T:***C*$_3$-OPh 2**, 2.91 mA cm^{-2} and 4.43 mA cm^{-2} for PBDB-T:***C*$_1$-Cl 3** and PBDB-T:***C*$_3$-Cl 4**, respectively, agreeing with the J_{SC} calculated from the *J*-V characteristics (refers **Table 2**).

Since the morphology of the active layer plays an important role in the exciton dissociation and charge carrier transport performance of OSCs, the morphologies of the PBDB-T: SubPc(DPP)$_3$ films were

analyzed by atomic force spectroscopy (AFM). Thin films of active layers were deposited on TiO_2-covered ITO substrates in identical conditions to those of solar cell devices. **Figure 3c-3j** show the AFM images for the active layers from the different SubPc(DPP)$_3$ acceptors. As shown, all the blend thin films had a similarly smooth surface. The root-mean-square roughness (RMS) values, as well as the peak-to-peak height for the PBDB-T:SubPc thin films, are summarized in Table S10. The thin films showed an RMS in the range of 1.45–2.09 nm. However, thin films made with ***C*$_1$-Cl 3 and *C*$_3$-Cl 4** exhibited less roughness (1.45 nm and 1.54 nm, respectively) than thin films made with OPh derivatives (**1.98 nm** and **2.09 nm** for ***C*$_1$-OPh 1 and *C*$_3$-OPh 2, respectively). In addition, thin films** made with OPh derivatives presented higher peak-to peak values (17.57 nm and 15.34 nm for ***C*$_1$-OPh 1** and ***C*$_3$-OPh 2, respectively**) than that of thin films made with ***C*$_1$-Cl 3** and ***C*$_3$-Cl 4** (12.21 nm and 12.11 nm, respectively). Complementarily, the AFM 3D-images (**Figure S18**) revealed that all the PBDB-T: SubPc(DPP)$_3$ thin films have the similar "mountain and valley"-like aspect and no significant differences were found in the morphology of all thin films. Therefore, we assume that the reason for the limited efficiency of devices made with ***C*$_1$-Cl 3 and *C*$_3$-Cl 4** could lie on the degree of recombination dynamics and exciton dissociation.[26] Among the different SubPc(DPP)$_3$-derivative molecules, those with OPh-substituted species (i.e. ***C*$_1$-OPh 1** and ***C*$_3$-OPh 2**) demonstrated to be more promising acceptors for OSCs applications. To further investigate the electrical properties of the ***C*$_1$-OPh 1** and ***C*$_3$-OPh 2**, we carried out electron mobility measurements on electron-only devices with the structure ITO/ZnO/***C*$_1$-OPh 1** or ***C*$_3$-OPh 2**/Al. The *J*-V curves of electron-only devices are depicted in **Figure S20**. From the graph, we identified three characteristic space-charge-limited current (SCLC) regions[27]: i) the Ohmic region at low voltages, with slope SI = 1, ii) the trap-filled limited (TFL) region at medium voltages, with slope SII=2 and SII >2 when the current is limited by shadow and deep traps, respectively, and iii) the trap-free region at high voltages, with slope SIII = 2. In this last region, the trap-free electron mobility can be calculated using Mott-Gurney's law:

$$J_{SCLC} = \frac{9}{8}\,\mu\,\varepsilon_0\varepsilon_r\,\frac{V^2}{L^3} \qquad (1)$$

where μ is the charge carrier mobility, ε_0 is the permittivity of vacuum, ε_r is the relative permittivity of the SubPc derivatives, V is the voltage and L is the sample thickness. The calculated electron mobilities of the ***C*$_1$-OPh 1** and ***C*$_3$-OPh 2** acceptors were 1.9×10^{-5} cm^2 V^{-1} s^{-1} and 1.7×10^{-5} cm^2 V^{-1} s^{-1}, respectively. Despite the electron mobility of both acceptors is similar, Fig. S24 shows higher current density values for ***C*$_1$-OPh 1** devices at a voltage given which is in good agreement with their higher efficiency when used as active layer in solar cells. These results can be correlated with the electron trap-state density value, Nt, calculated using.[28]

$$V_{TFL} = \frac{eN_t L^2}{2\varepsilon_0\varepsilon_r} \qquad (2)$$

where V_{TFL} is the trap-filled limit voltage, e is the elementary charge, L is the thickness of ***C*$_1$-OPh 1** and ***C*$_3$-OPh 2** films, ε_0 is the vacuum permittivity, and ε_r is the relative dielectric constant of ***C*$_1$-OPh 1** and ***C*$_3$-OPh 2**. The calculated N_t of ***C*$_1$-OPh 1** was 4.5×10^{17} cm^{-3}, while the N_t of ***C*$_3$-OPh 2** is

slightly higher (5.7×10^{17} cm^{-3}). The combination of higher electron mobility and lower electron trap density of ***C*$_1$-OPh 1** could explain the enhanced performance of devices based on PBDB-T:***C*$_1$-OPh 1** in comparison to the those based on PBDB-T:***C*$_3$-OPh 2**.

Conclusion

The synthesis and characterization of four new star-shaped electron acceptors based on a SubPc core decorated with three DPP wings linked through an acetylene bridge are reported. The four compounds present a broad absorption in the 450-700 nm range. Unexpectedly, the absorption spectrum of ***C*$_1$-Cl 3** was found to slightly differ from that of the other derivatives, as it exhibits a broader Q-band with a lower molar extinction coefficient. All these materials were probed as acceptors in BHJ-inverted polymer solar cells, with the polymer PBDB-T as the donor counterpart. ***C*$_1$-OPh 1** produced the highest parameters, with a V_{oc} as high as 1.17 V, a PCE of 3.17%, a J_{sc} of 6.42 mA/cm^2 and a FF of 42.16%. These results can be attributed to the good electron mobility and low electron trap density of the ***C*$_1$-OPh 1** acceptor. Unlike, ***C*$_1$-Cl 3** gave rise to the lowest photovoltaic parameters, resulting in a discreet PCE of 1.01%. Although ***C*$_3$-Cl 4** reached a FF higher than ***C*$_3$-OPh 2** (42.16% *vs.* 41.35%), the latter afforded better PCE due to the higher V_{oc} and J_{sc} values. In summary, the conjugates featuring the OPh group in the axial position gave the best results as acceptors in the studied conditions. Whereas for the axially chlorinated derivatives it was found that the C_1 regioisomer present better photovoltaic parameters than the C_3 species, for the OPh-substituted species the two regioisomers afforded similar values. Despite the relatively low J_{SC} of OSCs based on our SubPc(DPP)$_3$-derivative acceptors, these devices exhibited exceptionally high V_{OC} (>1 V). For this reason, they are high promising NFAs for application in ternary OSCs in which a high V_{OC} is desired.

Experimental Section

Measurement and characterization

^{1}H NMR data were recorded at 25 °C with a Bruker AC300 and A400 spectrometer with chemical shifts referenced to residual TMS. Matrix-assisted laser desorption/ionization time-of-flight (MALDI-TOF) mass spectra were obtained on a Bruker Microflex LRF20 instrument using dithranol as a matrix. Cyclic voltammetry measurements were performed in 0.1 M tetrabutylammonium hexafluorophosphate dichloromethane solution as support electrolyte, a graphite working electrode, an Ag/Ag^+ reference electrode, and carbon counter electrode using a potentiostat/galvanostat μAutolab Type III. Ferrocene/ferrocenium redox couple (Fc/Fc^+) was used as an internal standard for all measurements, and 4.8 eV under vacuum was established as the reference level. UV-vis spectra in $CHCl_3$ solution were measured with a Helios Gamma spectrophotometer and the extinction coefficients were calculated using the Lambert-Beer Law. Emission measurements were recorded in Perkin Elmer LS 55 fluorometer. IR spectra were measured with a Nicolet Impact 400D spectrophotometer.

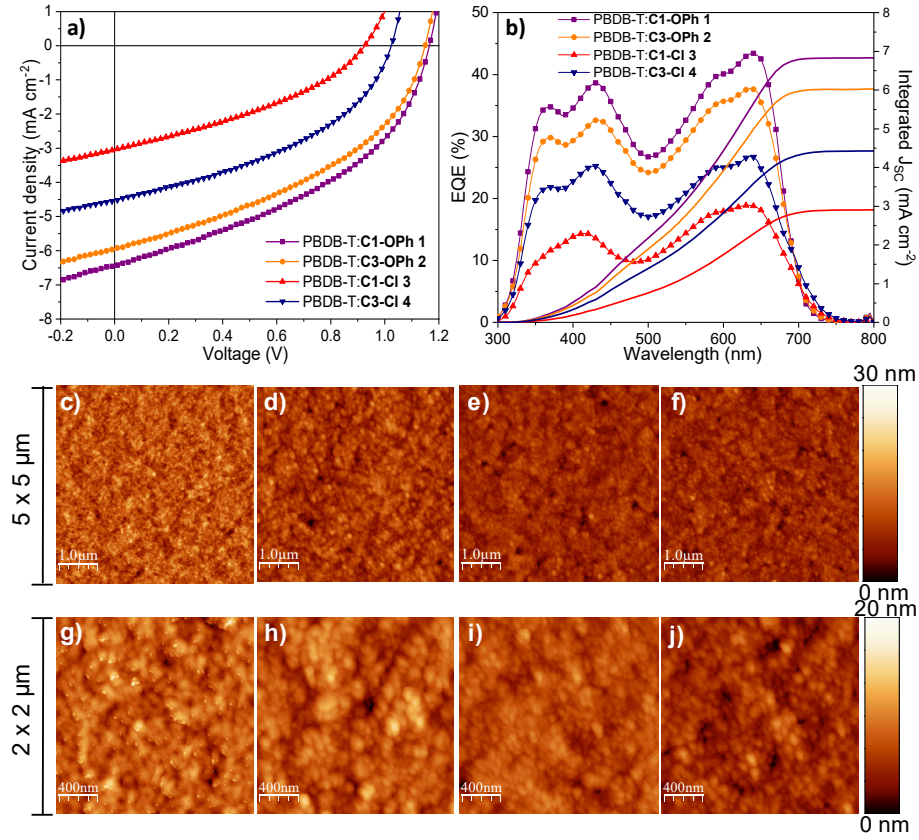

Figure 3. a) *J–V* curves and b) EQE spectra of the best-performing OSCs based on the optimized blends of PBDB-T blended with ***C1-OPh 1***, ***C3-OPh 2***, ***C*$_1$-Cl 3**, and ***C*$_3$-Cl 4** acceptors. AFM images for PBDB-T:***C*$_1$-OPh 1** (c, g), PBDB-T:***C*$_3$-OPh 2** (d, h), PBDB-T:***C*$_1$-Cl 3** (e, i), and PBDB-T:***C*$_3$-Cl 4** (f, j). The scan size is 5x5µm (a-d) and 2x2µm (e-h).

Table 2. Performance parameters of optimized OSCs based on PBDB-T blended with SubPc(DPP)$_3$-derivative acceptors.

Active Layer	V_{OC} [V]*	J_{SC} [mA cm^{-2}]*	J_{SC} (EQE) [mA cm^{-2}]	FF [%]*	PCE [%]*	R_S [Ω cm^2]*	R_{Sh} [Ω cm^2]*
PBDB-T:***C*$_1$-OPh 1**	1.17 (1.16)	6.42 (6.39)	6.83	42.16(41.63)	3.17 (3.08)	24.03 (24.80)	449.09 (439.76)
PBDB-T:***C*$_3$-OPh 2**	1.15 (1.14)	5.95 (5.91)	6.03	41.35 (38.98)	2.83 (2.62)	22.79 (26.34)	477.56 (417.48)
PBDB-T:***C*$_1$-Cl 3**	0.93 (0.89)	3.04 (2.89)	2.91	35.72 (36.07)	1.01 (0.91)	33.37 (27.50)	561.76 (621.95)
PBDB-T:***C*$_3$-Cl 4**	1.02 (0.99)	4.50 (4.23)	4.43	42.02 (39.58)	1.93 (1.68)	10.62 (12.54)	580.19 (547.45)

* Maximun value (average).

Materials

All chemicals and solvents were purchased from Sigma Aldrich (Merck) and TCI and were used without further purification unless otherwise stated. **DPP 9** was synthesized according to the literature.[29] Column chromatography was performed with SiO_2 (40–63 μm), and preparative TLC plate was used with 1 mm of silica gel 60 with indicator UV_{254}.

Synthesis

Synthesis of SubPc-$(DPP)_3$ derivatives. To a 25 mL round-bottom flask, the corresponding triiodide subphthalocyanine (50 mg, 0.055 mmol), tris(dibenzylideneacetone)dipalladium(0), $Pd_2(dba)_3$ (31 mg, 0.035 mmol), CuI (6.8 mg, 0.035 mmol), PPh_3 (75 mg, 0.288 mmol) and 1 mL of anhydrous toluene were added under nitrogen. Then, 2 mL of triethylamine were added, and the solution was deoxygenated. Finally, a degassed solution containing **DPP 9** (100 mg, 0.18 mmol) in 4 mL of toluene was added. After that, the crude was washed with 2M HCl and water and extracted with chloroform. The compounds were obtained in the form of dark blue solids.

- ***C*$_1$-OPh 1.** The compound was purified by silica gel column chromatography using different ratio of $CHCl_3$/ ethyl acetate as eluent. Yield: 17%. ^{1}H NMR (300 MHz, $CDCl_3$): δ (ppm) 9.04- 9.02 (m, 3H), 8.96-8.93 (m, 6H), overlapping doublets centered at 8.03 and 8.02 (d, 3H, J_1 =9 Hz), 8.04 (d, 3H, J_1 =6.0 Hz), 7.65 (d, 3H, J_1 =6.0 Hz), 7.51 (d, 3H, J_1 =3.0 Hz), 7.30-7.27 (m, 3H), 6.80 (d, 2H, J_1 =9.0 Hz), 5.35 (d, 2H, J_1 =9.0 Hz), 4.12-3.99 (m, 12H), 1.94-1.89 (m, 6H), 1.45-1.25 (m, 48H), 1.10 (s, 9H), 0.96-0.85 (m, 36H). FT-IR (KBr) ν: 2960, 2924, 2856, 2187, 1665, 1640, 1553, 1509, 1456, 1400, 1324, 1289, 1257, 1230, 1175, 1091, 1060, 1020, 856, 826, 761, 734, 707 cm^{-1}. UV/Vis ($CHCl_3$), λ_{max} (log ε):303 (4.91), 372 (4.80), 616 (5.24). MALDI-TOF (MS, dithranol): m/z=2184.2 $[M+H]^+$.
- ***C*$_3$-OPh 2.** The compound was purified by silica gel column chromatography using different ratio of $CHCl_3$/ ethyl acetate as eluent. Yield: 73%. ^{1}H NMR (300 MHz, $CDCl_3$): δ (ppm) 9.031-9.028 (m, 3H), 8.96-8.93 (m, 6H), 8.81 (dd, 3H, J_1 =8.82 Hz, J_2 =0.3 Hz), 8.03 (dd, 3H, J_1 =8.4 Hz, J_2 =1.2 Hz), 7.65 (dd, 3H, J_1 =5.0 Hz, J_2 =1.1 Hz), 7.50 (d, 3H, J_1 =6.0 Hz), 7.29-7.28 (m, 3H), 6.80 (d, 2H, J_1 =6.0 Hz), 5.35 (d, 2H, J_1 =6.0 Hz), 4.12-3.99 (m, 12H), 1.94-1.89 (m, 6H), 1.48-1.26 (m, 48H), 1.10 (s, 9H), 0.96-0.85 (m, 36H). FT-IR (KBr) ν: 2925, 1666, 1554, 1453, 1399, 1230, 1175, 1062, 827, 761, 134, 706 cm^{-1}. UV/Vis ($CHCl_3$), λ_{max} (log ε):302 (5.00), 369 (4.90), 553 (5.15), 623

(5.41). MALDI-TOF (MS, dithranol): m/z=2184.2 $[M+H]^+$.

- ***C*$_1$-Cl 3.** The compound was purified by preparative TLC plate using 2:1 $CHCl_3$/ ethyl acetate as eluent. Yield: 15%. ^{1}H NMR (400 MHz, $CDCl_3$): δ (ppm) 9.08-9.07 (m, 3H), 8.96 (d, 3H, J_1= 8 Hz), 8.94 (d, 3H, J_1= 4 Hz), overlapping doublets centered at 8.87 and 8.86 (d.3H, J_1=8 Hz), 8.09 (d, 3H, J_1=8 Hz), 7.66 (d, 3H, J_1= 4 Hz), 7.52 (d, 3H, J_1=8 Hz), 7.29 (t, 3H, J_1= 4 Hz), 4.11-4.00 (m, 12H), 1.94-1.89 (m, 6H), 1.45-1.25 (m, 57H), 0.96-0.85 (m, 38H). FT-IR (KBr) ν: 2956, 2927, 2858, 2188, 1730, 1666, 1613, 1555, 1509, 1455, 1401, 1327, 1292, 1264, 1231, 1179, 1096, 1021, 977, 890, 858, 827, 789, 766, 735, 709 cm^{-1}. UV/Vis (toluene), λ_{max} (log ε):373 (4.65), 595 (4.90). MALDI-TOF (MS, dithranol): m/z=2068.9 $[M]^+$.

- ***C*$_3$-Cl 4.** The compound was purified by preparative TLC plate using 100% CH_2Cl_2 as eluent. Yield: 8%. ^{1}H NMR (400 MHz, $CDCl_3$): δ (ppm) 9.05-9.04 (m, 3H), 8.97-8.94 (m, 6H), 8.82 (dd, 3H, J_1= 8.1 Hz, J_2=0.9 Hz), 8.05 (dd, 3H, J_1=8.0 Hz, J_2=1.6 Hz), 7.66 (dd, 3H, J_1=6.8 Hz, J_2=1.6 Hz), 7.51 (d, 3H, J_1= 8Hz), 7.31-7.28 (m, 3H), 4.08-4.05 (m, 12H), 1.94-1.85 (m, 6H), 1.45-1.25 (m, 60H), 0.96-0.85 (m, 36H). FT-IR (KBr) ν: 2954, 2954, 2856, 2189, 1731, 1666, 1613, 1554, 1509, 1453, 1400, 1381, 1305, 1264, 1230, 1178, 1095, 1065, 1021, 977, 891, 857, 827, 790, 734, 707, 663 cm^{-1}. UV/Vis (toluene), λ_{max} (log ε): 373 (4.73), 628 (5.19). MALDI-TOF (MS, dithranol): m/z=2068.9 $[M]^+$.

Synthesis of 4-*tert*-butylphenoxy-SubPc derivatives (*C*$_1$-SubPcI$_3$-OPh 5 and *C*$_3$-SubPcI$_3$-OPh 6). **SubPcI$_3$-OPh** was synthetized as a mixture of C_1 and C_3 regioisomers by substitution of the axial halide atom in **SubPcI$_3$-Cl** in a one-pot process, which was performed by treatment of the crude cyclotrimerization product with 4-*tert*-butylphenol in toluene at reflux for 16 h.[30] The purification of **SubPcI$_3$-OPh** was carried out by column chromatography on silica gel using toluene as solvent, which allowed to isolate the C_3 and C_1 regioisomers.

Synthesis of chloro-SubPc derivatives (*C*$_1$-SubPcI$_3$-Cl 7 and *C*$_3$-SubPcI$_3$-Cl 8). Chloro SubPcs **7** and **8** were obtained in the expected 3:1 statistical ratio by condensation of 4-iodophthalonitrile in the presence of boron trichloride in refluxing *p*-xylene according to a procedure previously reported by us.[31]The constitutional isomers were separated by column chromatography on silica gel employing toluene as eluent, as a variation of the conditions described in the literature.[32]

OSC devices fabrication and characterization.

The best performing of OSCs-based on ***C*$_1$-OPh 1**, ***C*$_3$-OPh 2**, and **C$_3$-Cl 4** was obtained under the optimized conditions with the weight ratio of PBDB-T:NFAs = 1:1, dissolved in chlorobenzene: DIO ratio of 99.5:0.5 v/v with a final concentration of 20 mg mL^{-1}. For OSCs based on PBDB-T: ***C*$_1$-Cl 3** the optimized weight ratio of was 1:1 dissolved in chlorobenzene: DIO ratio of 99:1 v/v with a final concentration of 20 mg mL^{-1}. All the PBDB-T:NFA solutions were deposited on top of TiO_2 film at 5000 rpm by 45 s, then PBDB-T:NFA films were thermally annealed at 100 °C by 10 min. The detailed devices fabrication is described in the Supporting Information. The *J*-V curves of the OSCs devices were recorded using a Keithley 2400 source-measure unit under 100 mW cm^2 AM 1.5G light illumination provided by a solar simulator (Abet Technologies model 11 000 class type A, Xenon arc). The EQE measurements were taken under forward wavelength sweep direction from 300 nm to 800 nm using Lasing IPCE-DC system with a serial number of LS1109-232.The AFM images of the samples were recorded in tapping mode on a Molecular Imaging model Pico SPM II (pico +). Images were collected in the air using silicon probes with a typical spring constant of 1–5 nN/m, and at a resonant frequency of 75 kHz.

Acknowledgements

ASS and TT thank to the Spanish Ministerio de Ciencia e Innovación (MICINN/FEDER) by financial support (CTQ2017-87102-R and CTQ2017-85393-P). Financial support from MINECO, Spain (PCI2019-111889-2) and ERA-NET/European Commission (UNIQUE, SOLAR-ERA.NET Cofound 2 N° 008), is also acknowledged (TT). MJAM thanks to "Beca Santiago Grisolia Grisoliap20177153" de la Comunidad Valenciana.

JGS, JP and LFM thank to the Spanish Ministerio de Ciencia e Innovación (MICINN/FEDER) RTI2018-094040-B-I00, the Agency for Management of University and Research Grants (AGAUR) ref 2017-SGR-1527, and the Catalan Institution for Research and Advanced Studies (ICREA) under the ICREA Academia Award.

IMDEA Nanociencia acknowledges support from the "Severo Ochoa" Programme for Centres of Excellence in R&D (MINECO, Grant SEV2016-0686).

Keywords: diketopyrrolopyrrole • subphthalocyanines • non-fullerene acceptor • organic solar cells • π-systems

Conflicts of interest

There are no conflicts to declare.

[1] a) A. M. Bagher, *Sustain. Energy.* **2014**, *2*, 85. a) G. Li, R. Zhu, and Y. Yang, *Nat. Photonics* **2012**, *6*, 153-161; b) Y. Sun, M. Chang, L. Meng, X. Wan, H. Gao, Y. Zhang, K. Zhao, Z. Sun, C. Li, S. Liu, H. Wang, J. Liang, Y. Chen, *Nat. Electron*. **2019**, *2*, 513-520.

[2] B. Ecker, J. C. Nolasco, J. Pallarés, L. F. Marsal, J. Posdorfer, J. Parisi, E. von Hauff, *Adv. Funct. Mater.* **2011**, *21*, 2705.

[3] K.-L. Ou, D. Tadytin, K. X. Steirer, D. Placencia, M. Nguyen, P. Lee and N. R. Armstrong, *J. Mater. Chem. A* **2013**, *1*, 6794-6803.

[4] J. G. Sánchez, V. S. Balderrama, S. I. Garduño, E. Osorio, A. Viterisi, M. Estrada, J. Ferré-Borrull, J. Pallarès, L. F. Marsal, *RSC Adv.* **2018**, *8*, 13094–13102.

[5] a) V. S. Balderrama, J. G. Sánchez, G. Lastra, W. Cambarau, S. Arias, J. Pallarès, E. Palomares, M. Estrada, Lluis F. Marsal, *J. Mater. Chem. A* **2018**, *6*, 22534-22544; b) Z. He, C. Zhong, S. Su, M. Xu, H. Wu, Y. Cao, *Nat. Photonics* **2012**, *6*, 593-595.

[6] a) R. C. I. MacKenzie, V. S. Balderrama, S. Schmeisser, R. Stoof, S. Greedy, J. Pallarès, L. F. Marsal, A. Chanaewa, E. von Hauff, *Adv. Energy Mater.* **2016**, *6*, 1501742; b) G. Terán-Escobar, J. Pampel, J. M. Caicedo, M. Lira-Cantú, *Energy Environ. Sci.* **2013**, *6*, 3088-3098.

[7] X. Li, F. Xie, S. Zhang, J. Hou, W. C. Choy, *Light Sci. Appl*. **2015**, *4*, e273.

[8] I. Etxebarria, J. Ajuria, R. Pacios, *J. Photonics Energy* **2015**, *5*, 057214-1-25.

[9] P. Cheng, G. Li, X. Zhan, Y. Yang, *Nat. Photonics* **2018**, *12*, 131-142.

[10] a) J. Zhang, H. S. Tan, X. Guo, A. Facchetti, H. Yan, *Nat. Energy* **2018**, *3*, 720-731; b) Y. Sun, H.-H. Gao, Y.-Q.-Q. Yi, X. Wan, H. Feng, X. Ke, Y. Zhang, J. Yan, C. Li, Y. Chen, *Sci. China Mater*. **2019**, *62*, 1210-1217.

[11] a) Y.-Q. Pan, G.-Y. Sun, *ChemSusChem* **2019**, *12*, 4570-4600; b) X. Huang, M. Hu, X. Zhao, C. Li, Z. Yuan, X. Liu, C. Cai, Y. Zhang, Y. Hu, Y. Chen, *Org. Lett*. **2019**, *21*, 3382-3386; c) H. Hang, X. Wu, Q. Xu, Y. Chen, H. Li, W. Wang, H. Tong, L. Wang, *Dyes Pigm.* **2019**, *160*, 243-251; d) Y. N. Luponosov, A. N. Solodukhin, A. L. Mannanov, P. S. Savchenko, Y. Minenkov, D. Y. Paraschuk, S. A. Ponomarenko, *Dyes Pigm.* **2020**, *177*, 108260; e) K. Wang, P. Xia, K. Wang, Xi. You, M. Wu, H. Huang, D. Wu, J. Xia, *ACS Appl. Mater. Interfaces* **2020**, *12*, 9528-9536; f) A. Stanculescua, C. Breazua, M. Socol, O. Rasoga, N. Preda, G. Petre, A.M. Solonaru, M. Grigoras, F. Stanculescu, G. Socol, G. Popescu-Pelin, M. Girtan, *Appl. Surf. Sci*. **2020**, *509*, 145351; g) J. Hu, X. Liu, K. Wang, M. Wu, H. Huang, D. Wu, J. Xia, *J. Mater. Chem. C* **2020**, *8*, 2135-2141.

[12] a) B. A. Gregg, *J. Phys. Chem. Lett.* **2011**, *2*, 3013; b) C. Zhan, X. Zhang, J. Yao, *RSC Adv*. **2015**, *5*, 93002. b) Q. Zhang, X. Xu, S. Chen, G. B. Bodedla, M. Sun, Q. Hu, Q. Peng, B. Huang, H. Ke, F. Liu, T. P. Russell, X. Zhu, ***Sustain. Energ. Fuels*** **2018**, ***2***, 2616-2624. c) C. Jiang, X. Huang, B. Sun, Y. Li, M. Gao, L. Ye, H. Ade, S. R. Forrest, J. Fan, *Organic Letters* **2020**, *84*, 105784.

[13] A. Wadsworth, M. Moser, A. Marks, M. S. Little, N. Gasparini, C. J. Brabec, D. Baran, I. McCulloch, *Chem. Soc. Rev.* **2019**, *48*, 1596-1625.

[14] a) T. M. Grant, D. S. Josey, K. L. Sampson, T. Mudigonda, T. P. Bender, B. H. Lessard, *Chem. Rec.* **2019**, *19*, 1093-1112; b) G. de la Torre, G. Bottari, T. Torres, *Adv. Energy Mater*. **2017**, *7*, 1601700; c) C.G. Claessens, D. Gonzalez-Rodriguez, M.S. Rodriguez-Morgade, A. Medina, T. Torres, *Chem. Rev*. **2014**, *114*, 2192-2277; d) G.E. Morse, T.P. Bender, *ACS Appl. Mater. Interfaces* **2012**, *4*, 5055-2068; e) A. Medina, C.G. Claessens, *J. Porphyr. Phthalocyanines* **2009**, *13*, 446-454.

[15] a) Y.-Q. Zheng, J.-L. Yu, W.-G. Li, J. Tang, B. Wei, X.-F. Li, J.-F. Shi, J.-H. Zhang, Y.-F. Wang; *J. Phys. D: Appl. Phys*. **2020**, *53*, 125102; b) M. Xiao, Y. Tian, S. Zheng, *Organic Electronics* **2018**, *59*, 279-287; c) . E. Jouad, E.M. El-Menyawy, G. Louarn, L. Arzel, M. Morsli, M. Addou, J.C. Bernède, L. Cattin, *J. Phys. Chem. Solids* **2020**, *136*, 109142; d) C.C. Lee, W.C. Su, Y.S. Shu, W.C. Chang, B.Y. Huang, Y.Z. Lee, T.H. Su, K.T. Chen, S.W. Liu, *RSC Adv*. **2015**, *5*, 5617-5626; e) N. Wang, X. Tong, Q. Burlingame, J. Yu, S.R. Forrest, *Sol. Energy Mater. Sol. Cells* **2014**, *125*, 170-175.

[16] a) B. Ebenhoch, N. B. A. Prasetya, V. M. Rotello, G. Cooke, I. D. W. Samuel, *J. Mater. Chem. A* **2015**, *3*, 7345-7352; b) T. M. Grant, D. S. Josey, K. L. Sampson, T.

Mudigonda, T. P. Bender, B. H. Lessard, *Chem. Rec*. **2019**, *19*, 1093–1112.
[17] K. Cnops, B. P. Rand, D. Cheyns, B. Verreet, M. A. Empl, P. Heremans, *Nat. Commun.* **2014**, *5*, 3406.
[18] X. Huang, M. Hu, X. Zhao, C. Li, Z. Yuan, X. Liu, C. Cai, Y. Zhang, Y. Hu, Y. Chen, *Org. Lett.* **2019**, *21*, 9, 3382–3386.
[19] a) Y. Patil, R. Misra, *J. Mater. Chem. C* **2019**, *7*, 13020; b) S. Loser, S. J. Lou, B. M. Savoie, C. J. Bruns, A. Timalsina, M. J. Leonardi, J. N. Smith, T. Harschneck, R. Turrisi, N. Zhou, C. L. Stern, A. A. Sarjeant, A. Facchetti, R. P. H. Chang, S. I. Stupp, M. A. Ratner, L. X. Chen, T. J. Marks, *J. Mater. Chem. A* **2017**, *5*, 13020-13031; c) M. Grzybowski, D. T. Gryko, *Adv. Optical Mater*. **2015**, *3*, 280-320.
[20] a) H.-H. Gao, Y. Sun, S. Li, X. Ke, Y. Cai, X. Wan, H. Zhang, C. Li and Y. Chen, *Dyes Pigm.* **2020**, *176*, 108250; b) M. Grzybowski, D. T. Gryko, *Adv. Optical Mater*. **2015**, *3*, 280-320; c) Q. Liu, S. E. Bottle, P. Sonar*, Adv. Mater*. **2020**, *32*, 1903882; d) K. Gao, S. B. Jo, X. Shi, L. Nian, M. Zhang, Y. Kan, F. Lin, B. Kan, B. Xu, Q. Rong, L. Shui, F. Liu, X. Peng, G. Zhou, Y. Cao, A. K.-Y. Jen, *Adv. Mater*. **2019**, *31*, 1807842.
[21] C. Yu, Z. Liu, Y. Yang, J. Yao, Z. Cai, H. Luo, G. Zhang, D. Zhang, ***J. Mater. Chem. C***, **2014**, ***2***, 10101-10109.
[22] C. G. Claessens, D. G.-Rodríguez, M. S. R.-Morgade, A. M., T. Torres, *Chem. Rev.* **2014**, *114*, 2192−2277
[23] J. G. Sanchez, A. A. A. Torimtubun, V. S. Balderrama, M. Estrada, J. Pallares, L. F. Marsal, *IEEE J. Electron Devices Soc.*, **2019**, *8*, 421–428.
[24] W. Li, J. Cai, Y. Yan, F. Cai, S. Li, R.S. Gurney, D. Liu, J.D. McGettrick, T.M. Watson, Z. Li, A.J. Pearson, D.G. Lidzey, J. Hou, T. Wang, *Sol. RRL*, **2018**, *2*, 1800114.
[25] a) Y. Cui, H. Yao, J. Zhang, K. Xian, T. Zhang, L. Hong, Y. Wang, Y. Xu, K. Ma, C. An, C. He, Z. Wei, F. Gao, Jianhui Hou*, Adv. Mater. **2020**, 32*,

1908205; b) Y. Lin, Y. Firdaus, F. H. Isikgor, M. I. Nugraha, E. Yengel, G. T. Harrison, R. Hallani, A. E.-Labban, H. Faber, C. Ma, X. Zheng, A. Subbiah, C. T. Howells, O. M. Bakr, I. McCulloch, S. D. Wolf, L. Tsetseris, Thomas D. Anthopoulos, *ACS Energy Lett.* **2020**, *5*, 2935−2944.
[26] H. Cha, S. Wheeler, S. Holliday, S. D. Dimitrov, A.Wadsworth, H. H. Lee, D. Baran, I. McCulloch, J. R. Durran, *Adv. Funct. Mater.*, **2018**, *28*, 1704389.
[27] a) H. F. Haneef, A. M. Zeidell, O. D. Jurchescu, *J. Mater. Chem. C* **2020**, 3, 759–787. b) F. C. Chiu, *Adv. Mater. Sci. Eng*. **2014**, *2014*, 1-18.
[28] .- a) B. Wang, Y. Fu, C. Yan, R. Zhang, Q. Yang, Y. Han, Z. Xie, *Front. Chem.* **2018**, *6*, 1. b) X.Meng, C. H. Y. Ho, S. Xiao, Y. Bai, T. Zhang, C. Hu,H. Lin, Y. Yang, S. K. So, S. Yang, *Nano Energy*, 52 **2018**, 300–306.
[29] C. Yu, Z. Liu, Y. Yang, J. Yao, Z. Cai, H. Luo, G. Zhang, D. Zhang, ***J. Mater. Chem. C*** **2014**, ***2***, 10101-10109.
[30] a) C. G. Claessens, M. J. Vicente-Arana, T. Torres, *Chem. Commun.*, **2008**, 6378–6380; b) I. Sanchez-Molina, B. Grimm, R. M. Krick Calderon, C. G. Claessens, D. M. Guldi, T. Torres, *J. Am. Chem. Soc.* **2013**, *135*, 10503−10511.
[31] C. G. Claessens, D. González-Rodríguez, B. del Rey, T. Torres, G. Mark, H.-P. Schuchmann, C. von Sonntag, J. G. MacDonald, R. S. Nohr, *Eur. J. Org. Chem.* 2003, 2547-2551.
[32] C. G. Claessens, T. Torres, *Tetrahedron Lett.* **2000**, *41*, 6361-6365.